APPLICATIONS OF NUMERICAL MODELS FOR ROUGH SURFACE SCATTERING

by

JOEL TIDMORE JOHNSON

B.E.E. Elec. Eng., Georgia Inst. of Technology, Atlanta
June 1991

S.M. Elec. Eng., Massachusetts Inst. of Technology, Cambridge
February 1993

Submitted to the Department of
Electrical Engineering and Computer Science
in Partial Fulfillment of the Requirements for the Degree of

DOCTOR OF PHILOSOPHY

at the

MASSACHUSETTS INSTITUTE OF TECHNOLOGY

February 1996

© Massachusetts Institute of Technology, 1996
All rights reserved

Signature of Author _____
Department of Electrical Engineering and Computer Science
February 1, 1996

Certified by _____
Professor Jin Au Kong
Thesis Supervisor

Accepted by _____
Frederic R. Morgenthaler
Chairman, Departmental Committee on Graduate Students

MASSACHUSETTS INSTITUTE OF TECHNOLOGY
Eng.
APR 11 1996
LIBRARIES

APPLICATIONS OF NUMERICAL MODELS FOR ROUGH SURFACE SCATTERING

by

JOEL TIDMORE JOHNSON

Submitted to the Department of Electrical Engineering and Computer Science
on February 1, 1996 in partial fulfillment of the requirements for the
Degree of Doctor of Philosophy

ABSTRACT

This thesis provides new computational models for electromagnetic surface scattering which allow large one and two dimensional problems to be considered through the use of efficient numerical algorithms and parallel computing techniques. This is in contrast with previous numerical studies that have been limited to relatively small surfaces rough in one dimension only. The new numerically exact models are applied to several problems of current interest, and allow studies of phenomena not predicted by any available analytical theories. In addition, comparisons are made with predictions of standard analytical models to obtain an assessment of their performance.

A one dimensional model for VHF propagation is the first numerical model considered. Comparisons with measurement data show the model to produce accurate results, and conclusively demonstrate the importance of terrain measurements in propagation predictions. Comparisons with approximate models allow their appropriate regions of validity to be determined.

Polarimetric thermal emission from two dimensional periodic surfaces is studied using an extended boundary condition (EBC) numerical solution. The model is applied to generate the only numerically exact results for two dimensional surface polarimetric thermal emission currently available, and demonstrates that properties of U_B, the third Stokes emission parameter, remain similar to those observed previously for one dimensional periodic surfaces. The response of U_B to level of medium anisotropy is also investigated.

A Monte Carlo study of backscattering enhancement from two dimensional perfectly conducting random rough surfaces follows, using a recently developed more efficient version of the method of moments which allows the large two dimensional surfaces investigated to be treated. Comparisons with bistatic scattering data from machine fabricated random surfaces taken at the University of Washington illustrate the first such validation of a two dimensional numerical scattering model to date. Backscattering enhancement is observed in both theoretical and experimental results, and theory and experiment are in good agreement.

Scattering from the surface of the ocean is studied using a two dimensional perfectly conducting surface Monte Carlo simulation. A simple power law spectrum model is chosen for the ocean surface, and variations with spectrum low frequency cutoffs are illustrated in the simulation. Both forward and back scattering from the ocean are considered, and comparisons are made with the standard composite surface model of ocean scattering which indicate appropriate choices of the "cutoff" wavenumber in the composite model. The validated composite surface theory is then used with more realistic ocean surface models to compare with measured ocean backscattering data.

Polarimetric thermal emission from the ocean is studied using a penetrable two dimensional surface Monte Carlo simulation. An extension to the standard penetrable surface method of moments is made to avoid greatly increasing the required number of surface unknowns for a highly lossy surface such as the ocean. Comparisons are made with the SPM and composite surface models for ocean scattering, and with available experimental data.

Thesis Supervisor: Professor Jin Au Kong
Professor of Electrical Engineering

ACKNOWLEDGEMENTS

I wish to express my sincerest thanks to Prof. J. A. Kong, my thesis supervisor, for his guidance on the studies of this thesis, and for his advice and insights into many other aspects of electromagnetics research. His excellence in teaching has enabled me to obtain the skills necessary for this work, and the research group he has created has provided an enriching environment in which to develop research skills.

I also wish to express thanks to Dr. Robert T. Shin, for his unending enthusiasm for surface scattering studies, which has provided great motivation, and for his willingness to address all technical issues in a clear and thorough fashion, which has helped immensely in handling technical issues along the way. I am grateful for the access I have had to Dr. Shin's technical expertise and to his solid grounding in real world problems and expectations. Thanks also to Prof. F. R. Morgenthaler for serving as a thesis reader, area exam member, and TA advisor.

I also wish to acknowledge collaborations with the University of Washington, particularly with Profs. Leung Tsang, Chi Chan, and Y. Kuga and with Kyung Pak. I appreciate the opportunity to have worked with Prof. Tsang while he was at MIT on sabbatical, and thank him for his willingness to collaborate in development and application of the SMFSIA approach. Collaborations with Groups 101 and 106 of Lincoln Laboratory are also acknowledged, with John Eidson of Group 106 providing a great deal of assistance with the propagation simulations of this thesis.

In the EWT group at MIT, I would like to acknowledge all of the former members I have had the pleasure of interacting with, especially Drs. Ali Tassoudji, Murat Veysoglu, Simon Yueh, Son Nghiem, and Kevin Li. I would like to acknowledge the efforts of Dr. Eric Yang and Chih Chien Hsu in maintaining the group's computers, and the help of Kit Lai as the group's secretary. Many technical discussions with Dr. K. H. Ding are also appreciated.

To all the current members of the EWT group, Chih Chien Hsu, Lifang Wang, Sean Shih, Yan Zhang, C. P. Yeang, Jerry Akerson, Fabio del Frate, and Nayon Tomsio, I wish you good luck in your continuing work and look forward to future collaborations. I appreciate the camaraderie we have shared, and acknowledge your

help in many areas.

Finally, I wish to thank my family for their continuing support through my graduate studies. This thesis is dedicated to my girlfriend Monica, who has shared every aspect of my life through the three years of this Ph.D. research with love, understanding, and thoughfulness. I look forward to our new future together.

The support of ONR contract N00014-92-J-4098, NASA contract 958461, and a National Science Foundation graduate fellowship are acknowledged. Sponsorship was also provided by the U.S. Air Force, under contract no. F19628-95-C-0002. Use of the Maui High Performance Computing Center is acknowledged, sponsored by Phillips Laboratory, Air Force Material Command under cooperative agreement F29601-93-2-001. The views and conclusions contained in this document are those of the author, and should not be interpreted as necessarily representing the official policies or endorsements, expressed or implied, of the US Air Force, Phillips Laboratory or the US Government.

To Monica

Contents

List of Figures

Chapter 1

Introduction

1.1 Background and Motivation

Rough surface scattering plays an important role in many electromagnetic applications, including both active and passive remote sensing, wave propagation, and optical and radar system design. Although approximate analytical techniques exist and work well for certain types of surfaces, a general analytical solution to the rough surface scattering problem remains to be discovered. At present, scattering from surfaces whose properties render the analytical theories invalid can be accurately calculated only through the use of numerical methods. Although numerical models are usually too computationally complex for general use in most practical applications, they provide a valuable means for evaluating other approximate scattering models and for decoupling uncertainties in the electromagnetic theories applied from uncertainties in other areas, especially in specification of input surface properties. Additionally, physical insight gained from numerical solutions can potentially aid in the development of future extended analytical theories. The ever increasing speed of moden computers also motivates the development of numerical models, since practical problems can be

solved with more reasonable amounts of computational time than in the past, and potentially with even less time in the future. The research of this thesis involves numerically exact models for surface scattering and their application in remote sensing and propagation problems.

A canonical rough surface scattering problem is illustrated in Figure 1.1, where an incident time harmonic electromagnetic plane wave impinges upon a boundary, described by the function $z = f(x)$, between two semi-infinite linear, homogeneous, isotropic, and time-invariant media. Such LHITI materials are the only electromagnetic media considered in this thesis. Determination of the resulting electromagnetic fields in the space above and below the surface profile defines the problem to be investigated. The configuration of Figure 1.1 could represent a wave from a radar system incident upon an ocean surface, for example, from which measurements of scattered fields or power could potentially be used to determine physical properties of the ocean. Alternatively, knowledge of the same scattered fields could be used to derive brightness temperatures of an ocean surface observed by an airborne or spaceborne radiometer. The configuration of Figure 1.1 could also model a laser beam incident upon a optical grating, a VHF field propagating over Earth like terrain, a synthetic aperture radar system observing soil moisture, or any number of other applications. This wide range of possibilities motivates the study of rough surface scattering and the desire for accurate and useful solutions to the rough surface scattering problem.

A well known solution to the problem of Figure 1.1 exists in the special case $z = 0$ or z a linear function of x, for which the fields consist of a specularly reflected wave above the surface profile and a specularly transmitted wave below. However,

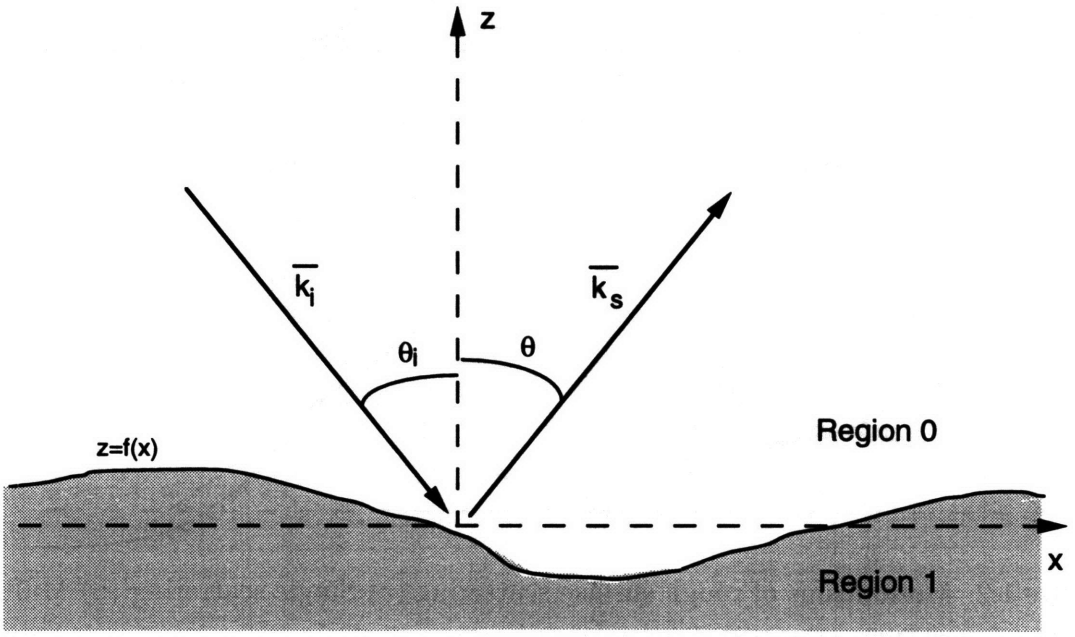

Figure 1.1: Geometry of a canonical rough surface scattering problem

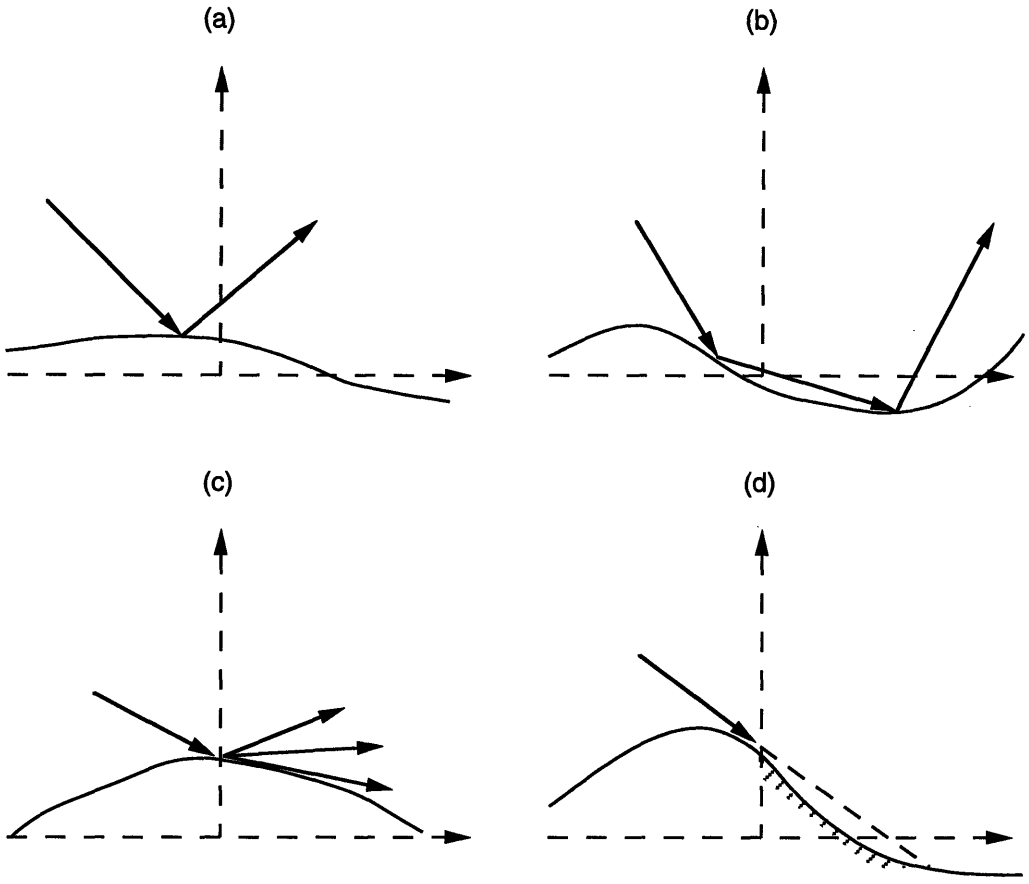

Figure 1.2: Mechanisms of rough surface scattering (a) Single scattering (b) Multiple scattering (c) Diffraction (d) Shadowing

solution of the boundary value problem for more general surface profiles is much more difficult, given the many possible scattering mechanisms which can exist on a rough surface. Heuristically, effects such a multiple scattering, diffraction, and shadowing, all illustrated in Figure 1.2, can exist singly or in combination, thereby making the prediction of scattered fields very difficult. These scattering mechanisms can also exist either locally (within an isolated region of the surface) or non-locally (coupling distant regions of the surface), further complicating the physics involved.

The above discussion considered surface profiles to be functions of coordinate x alone. This type of surface is known in the literature as a one dimensional (1-D) surface. More general surface profiles are functions of two spatial directions, $z = f(x, y)$, and are classified as two dimensional. Scattering behavior of rough surfaces can be very different in the one and two dimensional cases, especially given the decoupling of TE and TM polarizations associated with in-plane incidence in a 1-D problem. Due to the wider angular range over which scattered fields can exist in a 2-D problem, scattered fields at specific in-plane angles are usually expected to be lower than their 1-D counterparts. In addition, polarization coupling is inherent in 2-D scattering and further reduces copolarized fields compared to 1-D. For reasons to be discussed later, numerical models for 1-D surface scattering have received much more study in the past. This thesis is concerned with both 1-D and 2-D numerical models, but greater emphasis is placed upon the less studied 2-D case.

A final distinction exists between the random surface and deterministic surface cases. Figure 1.1 illustrates the deterministic case, for which a fields are calculated for a specified function describing the surface profile. However, since an exact functional description of surfaces observed may not always be available, many applications require a random surface model. In the random surface case, the surface profile function is modeled only in terms of its statistical properties as a stochastic process. Figure 1.1 could then be considered only to represent scattering from one realization of this stochastic process, with an ensemble average of scattered fields or power over surface realizations required to obtain statistical information about scattered field random variables. A statistical rather than deterministic description of scattered field quanti-

ties is clearly more useful in some instances, for example the ocean scattering problem mentioned above. Information about scattered fields from one specific configuration of the ocean surface is of little use since the surface itself changes both in time and with observation location. However, statistical properties of these observations when averaged over several observation times or locations are much less sensitive to such variations.

Statistical description of the surface profile stochastic process involves specification of the joint probability density function for an infinite number of random variables describing the height of the surface profile at individual values of coordinate x. However, if the stochastic process is assumed to be a Gaussian process, meaning that each of the individual surface height variables has a Gaussian height distribution, and to be stationary, meaning that its statistical properties are invariant with respect to a shift of origin, a complete description of the process is given by knowledge of its covariance function alone. Although realistic rough surface profiles are not necessarily well described as stationary Gaussian stochastic processes, the immense reduction in statistical complexity associated with such processes makes them highly advantageous. Both deterministic and random surface profiles are considered in this thesis, but only Gaussian process models are used in the random surface case.

The remaining sections of this chapter provide a brief overview of the theory of rough surface scattering. In Section 1.2.1, integral equation formulations of surface scattering are reviewed, and notations for scattered field, power, and brightness temperatures to be used throughout the thesis are introduced. Three commonly used approximate theories for surface scattering are then discussed in Section 1.3, and a

review of numerical methods for electromagnetics follows in Section 1.4. Finally, an overview of the chapters of the thesis is provided in Section 1.5.

1.2 Basic Surface Scattering Formulation

1.2.1 Integral equations for surface scattering

The standard dyadic Green's function formulation of Huygens' principle [1] states that time harmonic fields of frequency ω in a source-less volume V' bounded by a surface S' can be related to the equivalent tangential electric and magnetic fields on surface S' by

$$\overline{E}(\overline{r}) = \int dS' \left\{ i\omega\mu \overline{\overline{G}}(\overline{r},\overline{r}') \cdot [\hat{n}' \times \overline{H}(\overline{r}')] + \nabla \times \overline{\overline{G}} \cdot [\hat{n}' \times \overline{E}(\overline{r}')] \right\} \quad (1.1)$$

$$\overline{H}(\overline{r}) = \int dS' \left\{ -i\omega\epsilon \overline{\overline{G}}(\overline{r},\overline{r}') \cdot [\hat{n}' \times \overline{E}(\overline{r}')] + \nabla \times \overline{\overline{G}} \cdot [\hat{n}' \times \overline{H}(\overline{r}')] \right\} \quad (1.2)$$

where $\hat{n}$ is a unit normal vector to surface S'. The above equation assumes the medium inside volume V' to be a homogeneous, isotropic medium described by electric permittivity ϵ and magnetic permeability μ, and a time dependency of $e^{-i\omega t}$ is implied. In addition, the observation point $\overline{r}$ is assumed to lie inside volume V' but not on surface S'. The dyadic Green's function of the above equations is given by

$$\overline{\overline{G}} = \left[\overline{\overline{I}} + \frac{1}{k^2} \nabla\nabla \right] \frac{e^{ik|\overline{r}-\overline{r}'|}}{4\pi|\overline{r}-\overline{r}'|} \quad (1.3)$$

where $\overline{\overline{I}}$ represents the unit dyadic and k is the electromagnetic wave number $\omega\sqrt{\mu\epsilon}$. For observation points lying on surface S', so that a singularity at $\overline{r} = \overline{r}'$ is encountered

in the integral equations, an infinitesimal spherical exclusion zone around the point $\overline{r}$ is applied [2] and a limiting process yields

$$\frac{\overline{E}(\overline{r})}{2} = \int dS' \left\{ i\omega\mu\overline{\overline{G}}(\overline{r},\overline{r}') \cdot [\hat{n}' \times \overline{H}(\overline{r}')] + \nabla \times \overline{\overline{G}} \cdot [\hat{n}' \times \overline{E}(\overline{r}')] \right\} \quad (1.4)$$

$$\frac{\overline{H}(\overline{r})}{2} = \int dS' \left\{ -i\omega\epsilon\overline{\overline{G}}(\overline{r},\overline{r}') \cdot [\hat{n}' \times \overline{E}(\overline{r}')] + \nabla \times \overline{\overline{G}} \cdot [\hat{n}' \times \overline{H}(\overline{r}')] \right\} \quad (1.5)$$

where the integral $\int dS'$ is now performed as a principal value integration.

For semi-infinite half spaces separated by a surface boundary as in Figure 1.1, a radiation condition argument can be applied which illustrates that the surface at infinity does not contribute to the electromagnetic fields [1]. Thus, the above integral equations state that knowledge of tangential electric and magnetic fields on the surface profile bounding two semi-infinite half spaces determines fields throughout all of space. For observation points on the surface profile, equations (1.4) and (1.5) constitute coupled Fredholm integral equations of the second kind, whose solution yields the unknown tangential fields which can then be used to determine fields throughout all of space.

The problem of Figure 1.1 can be cast into an integral form by separately considering the regions of space above and below the surface profile respectively. For region 0 above the surface profile, a vector product of $\hat{n}$ with equations (1.4) and (1.5) yields

$$\frac{\hat{n} \times \overline{E}_0(\overline{r})}{2} = \hat{n} \times \overline{E}_{inc} + \hat{n} \times \int dS' \left\{ i\omega\mu\overline{\overline{G}}(\overline{r},\overline{r}') \cdot [\hat{n}' \times \overline{H}(\overline{r}')] + \nabla \times \overline{\overline{G}} \cdot [\hat{n}' \times \overline{E}(\overline{r}')] \right\} \quad (1.6)$$

$$\frac{\hat{n} \times \overline{H}_0(\overline{r})}{2} = \hat{n} \times \overline{H}_{inc} + \hat{n} \times \int dS' \left\{ -i\omega\epsilon \overline{\overline{G}}(\overline{r}, \overline{r}') \cdot [\hat{n}' \times \overline{E}(\overline{r}')] \right.$$

$$\left. + \nabla \times \overline{\overline{G}} \cdot [\hat{n}' \times \overline{H}(\overline{r}')] \right\} \tag{1.7}$$

where the contribution of the source fields, $\overline{E}_{inc}$ and $\overline{H}_{inc}$ are now included. For region 1 below the surface profile, the equations are

$$\frac{\hat{n} \times \overline{E}_1(\overline{r})}{2} = -\hat{n} \times \int dS' \left\{ i\omega\mu_1 \overline{\overline{G}}_1(\overline{r}, \overline{r}') \cdot [\hat{n}' \times \overline{H}(\overline{r}')] \right.$$

$$\left. + \nabla \times \overline{\overline{G}}_1 \cdot [\hat{n}' \times \overline{E}(\overline{r}')] \right\} \tag{1.8}$$

$$\frac{\hat{n} \times \overline{H}_1(\overline{r})}{2} = -\hat{n} \times \int dS' \left\{ -i\omega\epsilon_1 \overline{\overline{G}}_1(\overline{r}, \overline{r}') \cdot [\hat{n}' \times \overline{E}(\overline{r}')] \right.$$

$$\left. + \nabla \times \overline{\overline{G}}_1 \cdot [\hat{n}' \times \overline{H}(\overline{r}')] \right\} \tag{1.9}$$

where the incident field is no longer included since there is no source distribution in the space below the surface profile, medium properties are modified to ϵ_1 and μ_1, and the minus sign results from an assumed upward pointing definition for $\hat{n}'$. Note that the continuity of tangential electric and magnetic fields is implicit in the above equations, since the same sources produce the total fields above and below the surface profile. Equations (1.6-1.9) are the equations that will be solved for surface profile tangential fields throughout this thesis. These four vector equations, however, are not independent, as the magnetic field integral equations can be derived by taking a curl of the electric field equations. Thus, use of one or a combination of equations (1.6-1.7) along with one or a combination of equations (1.8-1.9) is required in order to model the rough surface scattering problem. Chapters 3 and 6 of this thesis follow

this procedure to formulate the problem of scattering from a penetrable rough surface.

In the limit that the medium below the surface profile is perfectly conducting, tangential electric fields on the surface profile vanish and the relavent equations become

$$0 = \hat{n} \times \overline{E}_{inc} + \hat{n} \times \int dS' \left\{ i\omega\mu \overline{\overline{G}}(\overline{r}, \overline{r}') \cdot [\hat{n}' \times \overline{H}(\overline{r}')] \right\} \quad (1.10)$$

$$\frac{\hat{n} \times \overline{H}_0(\overline{r})}{2} = \hat{n} \times \overline{H}_{inc} + \hat{n} \times \int dS' \left\{ \nabla \times \overline{\overline{G}} \cdot [\hat{n}' \times \overline{H}(\overline{r}')] \right\} \quad (1.11)$$

known in the literature as the electric field integral equation (EFIE) and the magnetic field integral equation (MFIE) respectively [3]. Either of these equations can be used to solve the perfectly conducting halfspace medium problem, although there are some important distinctions for thin conductors [4] which are not considered here. Since the MFIE formulation usually results in a better conditioned numerical solution [3], it is applied in Chapters 4 and 5 of this thesis to the perfectly conducting surface problem.

Another simplification of integral equations (1.6-1.9) is possible in the 1-D surface case. The symmetries associated with a 1-D problem allow knowledge of all field components to be obtained from knowledge of the transverse electric and magnetic field components, E_y and H_y in Figure 1.1. Thus, solution of the surface scattering problem requires knowledge of these field components alone on the surface profile. Furthermore, for fields incident in the $x-z$ plane alone, there is no coupling between these TE and TM fields, so that two sets of three field components exist independently. Following [1], the Huygens' principle integral equations above can be manipulated into

the vector Kirchhoff diffraction integrals,

$$\frac{\overline{E}(\overline{r})}{2} = \overline{E}_{inc} + \int dS' \left\{ \overline{E}(\overline{r}') \frac{\partial g(\overline{r}, \overline{r}')}{\partial n} - g(\overline{r}, \overline{r}') \frac{\partial \overline{E}(\overline{r}')}{\partial n} \right\} \tag{1.12}$$

for the electric field in region 0 and similar equations for the electric and magnetic fields in regions 0 and 1. Since fields in the 1-D problem are determined by knowledge of E_y and H_y alone, equations for the 1-D problem become

$$\frac{E_y(\overline{r})}{2} = E_{inc_y} + \int dS' \left\{ E_y(\overline{r}') \frac{\partial g(\overline{r}, \overline{r}')}{\partial n} - g(\overline{r}, \overline{r}') \frac{\partial E_y(\overline{r}')}{\partial n} \right\} \tag{1.13}$$

$$\frac{H_y(\overline{r})}{2} = H_{inc_y} + \int dS' \left\{ H_y(\overline{r}') \frac{\partial g(\overline{r}, \overline{r}')}{\partial n} - g(\overline{r}, \overline{r}') \frac{\partial H_y(\overline{r}')}{\partial n} \right\} \tag{1.14}$$

$$\frac{E_y(\overline{r})}{2} = -\int dS' \left\{ E_y(\overline{r}') \frac{\partial g_1(\overline{r}, \overline{r}')}{\partial n} - g_1(\overline{r}, \overline{r}') \left(\frac{\partial E_y(\overline{r}')}{\partial n} \right)_1 \right\} \tag{1.15}$$

$$\frac{H_y(\overline{r})}{2} = -\int dS' \left\{ H_y(\overline{r}') \frac{\partial g_1(\overline{r}, \overline{r}')}{\partial n} - g_1(\overline{r}, \overline{r}') \left(\frac{\partial H_y(\overline{r}')}{\partial n} \right)_1 \right\} \tag{1.16}$$

where continuity of tangential field components yields

$$\frac{\partial E_y(\overline{r}')}{\partial n} = \alpha \left(\frac{\partial E_y(\overline{r}')}{\partial n} \right)_1 \tag{1.17}$$

$$\frac{\partial H_y(\overline{r}')}{\partial n} = \beta \left(\frac{\partial H_y(\overline{r}')}{\partial n} \right)_1 \tag{1.18}$$

where $\alpha = 1$ for the TE case (non-magnetic medium) and $\beta = \frac{\epsilon_1}{\epsilon_2}$ for TM and in-plane incidence is assumed. Furthermore, integration of these equations can be performed over y, along which tangential field components are constant, to obtain a Green's

function of

$$g_j(\overline{\rho},\overline{\rho}') = \frac{i}{4}H_0^{(1)}(k_j|\overline{\rho}-\overline{\rho}'|) \tag{1.19}$$

where $H_0^{(1)}$ indicates the zeroth order Hankel function of the first kind and $\overline{\rho}$ reflects the $x-z$ plane distance as opposed to the three dimensional distance $\overline{r}$. One dimensional surfaces are studied in Chapter 2, and the above equations are used to determine surface profile tangential field components.

1.2.2 Definition of field vectors

In this thesis, a spherical coordinate system will often be used to describe incident and scattered field directions. For an incident electromagnetic plane wave, $\hat{e}_i e^{i\overline{k}_i\cdot\overline{r}}$, propagating in direction $\overline{k}_i$, the following definitions are used:

$$\begin{aligned} k_{ix} &= k\sin\theta_i\cos\phi_i \\ k_{iy} &= k\sin\theta_i\sin\phi_i \\ k_{iz} &= -k\cos\theta_i \end{aligned} \tag{1.20}$$

where θ_i refers to the incident polar angle, ϕ_i to the incident azimuthal angle. Two unit vectors labeled $\hat{h}_i$ and $\hat{v}_i$, for horizontal and vertical polarizations respectively, orthogonal to this direction are defined as

$$\hat{h}_i = \frac{\hat{z}\times\overline{k}_i}{|\hat{z}\times\overline{k}_i|} = -\hat{x}\sin\phi_i + \hat{y}\cos\phi_i$$

$$\hat{v}_i = \hat{h}_i \times \overline{k}_i = -\hat{x}\cos\theta_i\cos\phi_i - \hat{y}\cos\theta_i\sin\phi_i - \hat{z}\sin\theta_i$$

Scattered fields are observed in the far field, where they consist of outward propagating spherical waves, and scattered field propagation and polarization vectors are defined as

$$\begin{aligned} k_{sx} &= k\sin\theta_s\cos\phi_s \\ k_{sy} &= k\sin\theta_s\sin\phi_s \\ k_{sz} &= k\cos\theta_s \end{aligned} \tag{1.21}$$

$$\begin{aligned} \hat{h}_s &= \frac{\hat{z}\times\overline{k}_s}{|\hat{z}\times\overline{k}_s|} = -\hat{x}\sin\phi_s + \hat{y}\cos\phi_s \\ \hat{v}_s &= \hat{h}_s \times \overline{k}_s = \hat{x}\cos\theta_s\cos\phi_s + \hat{y}\cos\theta_s\sin\phi_s - \hat{z}\sin\theta_s \end{aligned}$$

where θ_s refers to the scattered polar angle, ϕ_s to the scattered azimuthal angle. In this notation, the forward scattering direction corresponds to $\theta_s = \theta_i$ and $\phi_s = \phi_i$, while backscattering is represented by either $\theta_s = -\theta_i$, $\phi_s = \phi_i$ or $\theta_s = \theta_i$, $\phi_s = \phi_i + \pi$.

1.2.3 Definition of active remote sensing quantities

Knowledge of the electric and magnetic fields throughout all of space implies a complete solution of the problem of Figure 1.1 in the deterministic surface case. Knowledge of the statistical properties of electric and magnetic field random variables is implied in the random surface case. However, many systems used in active and pas-

sive remote sensing measure only a small fraction of this information, and often report scattered field amplitudes alone with no phase information. The specific terminology used to describe scattered powers received in active remote sensing is reviewed in this section.

Active remote sensing involves use of a radar system to transmit an incident electromagnetic wave onto the medium under view and measurements of scattered fields or power are reported. The power received in an ideal monostatic radar system for a power transmitted P_t is given by the radar equation as

$$P_{rec} = P_t \frac{G_t^2 \lambda^2 \sigma}{(4\pi)^3 R^4} \tag{1.22}$$

where G_t represents the gain of the radar antenna, λ is the wavelength, R the range from transmitter to target, and σ is a quantity describing the target known as the radar cross section. Radar cross section σ is defined as the area of an equivalent isotropic radiator that would produce the same scattered power at the receiver as the target, and is a function of frequency, incidence and scattered angles, polarization, and target physical properties. In the remote sensing of geophysical media, radar cross sections are usually reported as normalized cross sections, σ^0, defined as $\frac{\sigma}{A}$ where A is the area illuminated by the transmitted antenna pattern. Only normalized radar cross sections will be reported in this thesis, so the σ notation will be used to indicate σ^0 only henceforth.

A specific definition for the far-field normalized bistatic cross section is given by

$$\sigma_{\alpha\beta}(\theta_s, \phi_s, \theta_i, \phi_i) = \lim_{R\to\infty} \frac{4\pi R^2 |E^s_{\alpha\beta}|^2}{A|E^{(i)}_\beta|^2} \tag{1.23}$$

where $\alpha, \beta = h, v$ represent the polarization of the scattered and incident waves respectively, R is the range from the target to the observation point, E^s is the scattered field amplitude, E^i is the amplitude of the field incident from direction (θ_i, ϕ_i), and A is the geometric area of the target. The above cross section is defined so that integration of $\sigma_{h\beta} + \sigma_{v\beta}$ over all of space should give $4\pi \cos\theta_i$ for power conservation. Monostatic radar systems measure the radar cross section only in the backscattering direction. Both monostatic and bistatic radar system configurations are considered in this thesis.

An alternate quantity $\gamma_{\alpha\beta} = \frac{\sigma_{\alpha\beta}}{\cos\theta_i}$ is also commonly used and will be defined as the normalized bistatic scattering coefficient in this thesis. This scattering coefficient is normalized by the integration of $\hat{n} \cdot \overline{S}_{inc}$, where $\overline{S}_{inc}$ is the Poynting flux density of the incident wave, over the surface profile rather than $\overline{S}_{inc}A$ used for σ. The factor of $\cos\theta_i$ above results for plane wave incident fields.

For random surfaces, $\sigma_{\alpha\beta}$ is defined in terms of the ensemble average scattered intensity as

$$\sigma_{\alpha\beta}(\theta_s, \phi_s, \theta_i, \phi_i) = \lim_{R\to\infty} \frac{4\pi R^2 \left\langle |E^s_{\alpha\beta}|^2 \right\rangle}{A|E^{(i)}_\beta|^2} \tag{1.24}$$

where the $< \cdot >$ notation above indicates an ensemble average over realizations of the surface stochastic process. Furthermore, the above quantities can be separated into

a coherent and incoherent part, defined as

$$\sigma^i_{\alpha\beta}(\theta_s, \phi_s, \theta_i, \phi_i) = \lim_{R\to\infty} \frac{4\pi R^2 \left\langle |E^s_{\alpha\beta} - < E^s_{\alpha\beta} > |^2 \right\rangle}{A|E^{(i)}_\beta|^2} \tag{1.25}$$

and

$$\sigma^c_{\alpha\beta}(\theta_s, \phi_s, \theta_i, \phi_i) = \lim_{R\to\infty} \frac{4\pi R^2 | < E^s_{\alpha\beta} > |^2}{A|E^{(i)}_\beta|^2} \tag{1.26}$$

where the sum of the incoherent, $\sigma^i_{\alpha\beta}$, and coherent, $\sigma^c_{\alpha\beta}$, parts is the same as (1.24). This distinction will prove useful in Chapter 5 when comparing finite size surface simulations with infinite size surface theories.

In polarimetric active remote sensing, measurements are made of correlations between polarization amplitudes in addition to the power measurements discussed above. The most commonly used additional parameter in polarimetric active remote sensing is the σ_{hh}, σ_{vv} correlation parameter, ρ, defined as

$$\rho = \lim_{R\to\infty} \frac{< E^s_{hh} E^{s*}_{vv} >}{|E^s_{hh}||E^s_{vv}|} \tag{1.27}$$

Measurement of rho implies a radar system capable of measuring phase differences between received polarization amplitudes. The rho parameter has been shown useful in identifying the similarity of hh and vv scattering mechanisms, since large values of rho imply similar phases in these scattered fields.

1.2.4 Definition of passive remote sensing quantities

In passive remote sensing, radiometers are used to measure thermal noise power emitted from the object under view. The level of noise power measured is described in terms of a brightness temperature, which is again a function of frequency, observation angle, polarization, and medium properties. In addition, correlations between horizontally and vertically polarized brightnesses are measured in polarimetric passive remote sensing. The brightness temperature Stokes vector measured in polarimetric passive remote sensing is defined as

$$\bar{T}_B = \frac{1}{C}\bar{I} = \frac{1}{C}\begin{bmatrix} I_h \\ I_v \\ U \\ V \end{bmatrix} = \frac{1}{\eta C}\begin{bmatrix} \langle E_h E_h^* \rangle \\ \langle E_v E_v^* \rangle \\ 2\mathrm{Re}\langle E_v E_h^* \rangle \\ 2\mathrm{Im}\langle E_v E_h^* \rangle \end{bmatrix} \tag{1.28}$$

In the above equation, E_h and E_v are the emitted electric fields received from the horizontal and vertical polarization channels of the radiometer, η is the characteristic impedance, and $C = K/\lambda^2$ with K denoting Boltzmann's constant, λ the wavelength. The first two parameters of the brightness temperature Stokes vector correspond to received powers for horizontal and vertical polarizations, respectively. The third and fourth parameters correspond to the complex correlation between electric fields received by the horizontal and vertical channels. These four parameters are labeled T_{Bh}, T_{Bv}, U_B, and V_B respectively in this thesis.

It is shown in [5] that the third and fourth Stokes parameters may be related to the brightness temperature in a 45 degree linearly polarized measurement (T_{Bp}) and

a right-hand-circularly polarized measurement (T_{Br}) as follows:

$$U_B = 2T_{Bp} - T_{Bh} - T_{Bv} \tag{1.29}$$

$$V_B = 2T_{Br} - T_{Bh} - T_{Bv} \tag{1.30}$$

Thus, to compute all four parameters of the Stokes vector, the brightness temperatures in horizontal, vertical, 45 degree linear, and right-hand-circular polarizations are first calculated, and the above equations are used to obtain U_B and V_B.

The emissivity of an object is defined as the ratio of the brightness temperature emitted by an object to its actual physical temperature, under the assumption that the object is at a constant physical temperature, T_{phys},

$$T_{Ba} = e_a(\theta, \phi) T_{phys} \tag{1.31}$$

In the above equation, the subscript a refers to the polarization of the brightness temperature, θ to the polar observation angle, and ϕ to the azimuthal observation angle. Through the principles of energy conservation and reciprocity, Kirchhoff's Law relates this emissivity to the reflectivity of the surface [6]:

$$e_a(\theta, \phi) = 1 - r_a(\theta, \phi) \tag{1.32}$$

The reflectivity $r_a(\theta, \phi)$ for the given incident polarization a is defined as the fraction of the power incident from direction (θ, ϕ) that is rescattered and can be evaluated by integrating the bistatic scattering coefficients $\gamma_{ba}(\theta', \phi'; \theta, \phi)$ over all

scattering angles in the upper hemisphere and summing the results of both orthogonal scattering polarizations:

$$r_a(\theta,\phi) = \frac{1}{4\pi}\sum_b \int_0^{\pi/2} d\theta' \sin\theta' \int_0^{2\pi} d\phi' \, \gamma_{ba}(\theta',\phi';\theta,\phi) \tag{1.33}$$

In the expression of the bistatic scattering coefficient, (θ,ϕ) and (θ',ϕ') represent the incident and the scattered directions, respectively, and the subscripts a and b represent the polarizations of the incident and the scattered waves, respectively.

Thus, to calculate the fully polarimetric emission vector, the bistatic scattering coefficient for each of four polarizations is first calculated and integrated over the upper hemisphere to obtain the reflectivity for that particular polarization. Multiplication of the corresponding emissivity by the physical temperature of the object under view yields the brightness temperature for this polarization. The fully polarimetric brightness vector is then calculated as described previously.

1.3 Review of Approximate Theories

The solution of integral equations (1.6-1.9) is very difficult, given the arbitrary surface profile S'. Analytical solutions to date have only been possible through the use of approximations to reduce problem complexity. The approximations made are valid for certain types of surfaces and scattering mechanisms, but neglect the contribution of other scattering mechanisms and thus are not accurate in general. A variety of such approximations have been studied in the literature for 1-D and 2-D, perfectly conducting or penetrable surfaces [6]-[27]. Two of the most commonly used approximate

theories are the physical optics approximation, or Kirchhoff approach, and the small perturbation method. Each of these approximations are discussed in more detail below, followed by brief sections on the composite surface model to be investigated in Chapter 5 and on other surface scattering theories proposed in the literature.

1.3.1 Physical optics approximation

In the physical optics (PO) approximation, discussed in [8], tangential fields on the surface profile are assumed to be the same as those that would exist on a plane tangent to each point on the surface, as shown in Figure 1.3. Thus, given an incident field and the height and first derivatives of the surface at a given point, the tangent plane can be constructed, the incident field resolved into its locally TE and TM components, and the total field calculated as the sum of the incident and reflected fields on the interface. This procedure is repeated for every point of the surface profile to generate tangential fields over the entire surface, which constitutes solution of equations (1.6-1.9). The solution process is simple for a deterministic surface, and can be applied in a Monte Carlo simulation for randomly rough surfaces. However, the simplicity of the physical optics approximation also lends itself well to analytical averaging techniques in the randomly rough case, especially for a Gaussian stochastic process.

For a perfectly conducting 2-D Gaussian process surface, the PO approximation yields [6]

$$\sigma_{aa}(\theta_i,\theta_s) = \frac{k^2}{\pi}\left|\frac{1+\cos\theta_i+\cos\theta_s-\sin\theta_i\sin\theta_s}{\cos\theta_i+\cos\theta_s}\right|^2 \int dx' \int dy' e^{-\sigma^2 k_{dz}^2}\left\{e^{\sigma^2 k_{dz}^2 C(x',y')}-1\right\} e^{ik_{dx}x'+ik_{dy}y'} \qquad (1.34)$$

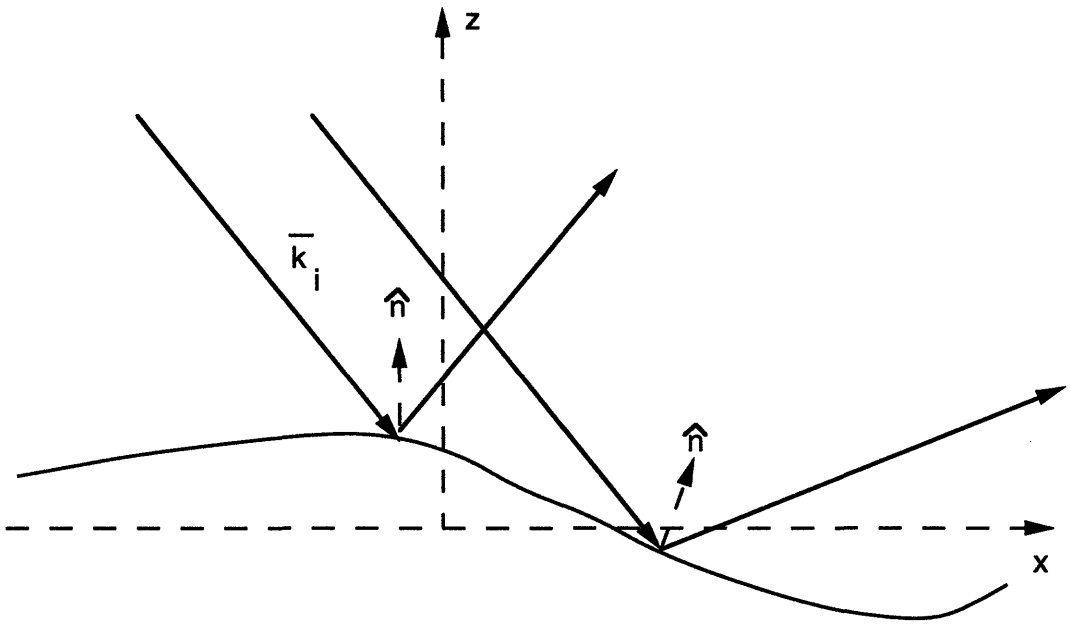

Figure 1.3: Physical optics approach to surface scattering

for the normalized incoherent co-polarized bistatic cross section in the plane of incidence $\phi = 0$, where $\overline{k}_d = \overline{k}_i - \overline{k}_s$, σ^2 is the variance of the rough surface, and $C(x', y')$ is the surface correlation function. A numerical evaluation of this integral will be used in Chapter 5 to determine PO cross sections for an ocean surface model. However, an examination of this equation reveals it to be an integration of a rapidly decaying function in the large σk_{dz} case, making numerical evaluation of this integral difficult for arbitrary $C(x', y')$ and σ. An analytical evaulation of the above integral is possible for some specific correlation functions, including a Gaussian correlation function, and results in an infinite series expression. A stationary phase integration method can also be used in the large σk_{dz} case, which results in the geometric optics (GO) limit to equation (1.34) [8]:

$$\begin{aligned} \sigma_{aa}(\theta_i, \theta_s) &= \frac{k^2}{\pi} \left| \frac{1 + \cos\theta_i + \cos\theta_s - \sin\theta_i \sin\theta_s}{\cos\theta_i + \cos\theta_s} \right|^2 \\ & \frac{4\pi}{2k_{dz}^2 \sigma^2 |C''(0)|} exp\left[-\frac{k_{dx}^2 + k_{dy}^2}{2\sigma^2 |C''(0)| k_{dz}^2} \right] \end{aligned} \tag{1.35}$$

The GO expression above can be interpreted as the cross section of a flat plane multiplied by the probability of obtaining a tilt angle such that the plane is normal to the incident plane wave. The $\sigma^2|C''(0)|$ terms above can be shown to be equal to the variance of the slope of the Gaussian stochastic process describing the surface.

Note that both the PO or GO solutions above predict no differences between hh and vv results for perfectly conducting surfaces, and both also predict no cross polarized fields in the backscattered direction. These results can be explained due to the single scattering nature of the PO and GO solutions [28]. Effects such as shadow-

ing and feature diffraction are also neglected, although attempts have been made to include shadowing through the use of "shadowing functions" in the analytical averaging procedure [10]. Physical optics solutions are therefore expected to be accurate only when multiple scattering, shadowing, and diffraction do not contribute significantly to the final field solution. Thus, surfaces with fairly small slopes and large radii of curvature, which limit multiple scattering effects, and near-forward scattering observations, which limit the effects of shadowing, are required. No restrictions are placed on overall surface rms variations however, as long as slopes remain small. Studies of the validity of the PO and GO approximations have been performed for 1-D surfaces through comparison with numerical methods [29]-[33], primarily for surfaces with Gaussian correlation functions, and have quantified the above conditions somewhat. However, comparisons for 2-D surfaces are much more limited.

1.3.2 Small perturbation method

A second approximate method for solving the rough surface scattering problem involves a perturbation theory originally proposed in [7]. Field solutions are expanded in perturbation series assuming that $k_{iz}f(x',y')$, $k_{1zi}f(x',y')$, $\frac{\partial f(x',y')}{\partial x'}$ and $\frac{\partial f(x',y')}{\partial y'}$ are small parameters, where k_{1zi} is the $\hat{z}$ component of the transmitted wave vector. Thus, the small perturbation method (SPM) requires that surface heights be much smaller than a wavelength and small surface slopes in order for the series to converge, as shown in Figure 1.4. The zeroth order solution consists of the specularly reflected and trasmitted coherent waves, and the first order term contributes only to the incoherent scattered fields. The second and higher order solutions modify both

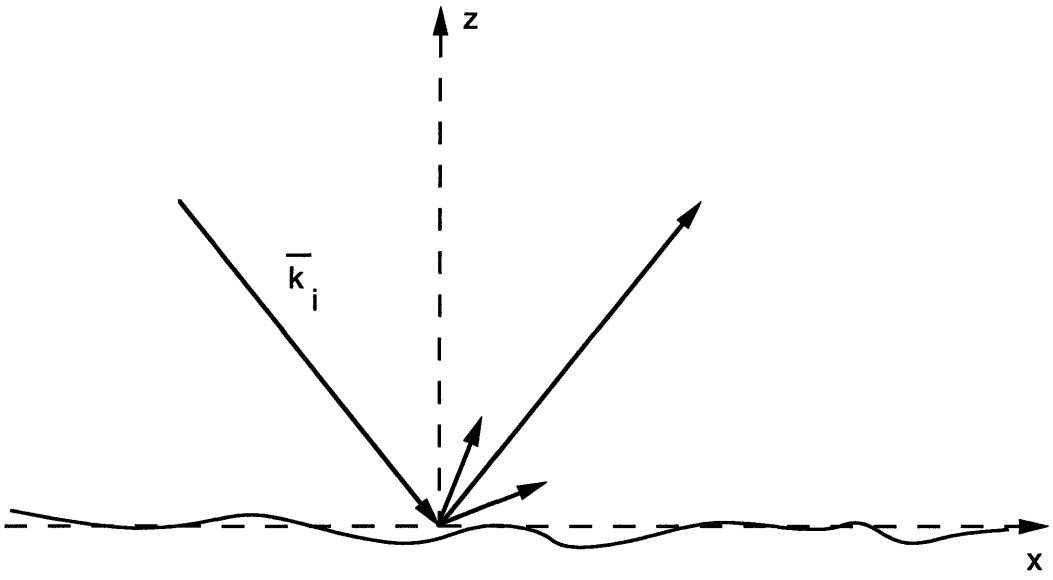

Figure 1.4: Small perturbation approach to surface scattering

the coherent and incoherent fields, but are much more computationally complex.

For a perfectly conducting 2-D Gaussian process surface, the SPM approximation yields

$$\sigma_{ab}(\theta_i, \theta_s) = 16\pi \cos^2\theta_s \cos^2\theta_i f_{ab} W(k_{xs} - k_{xi}, k_{ys} - k_{yi}) \tag{1.36}$$

for the normalized incoherent bistatic cross section in the plane of incidence to first order, where

$$f_{hh} = 1$$

$$f_{vv} = \frac{(1+\sin^2\theta_i)^4}{\cos^4\theta_i} \tag{1.37}$$

$$f_{hv} = f_{vh} = 0. \tag{1.38}$$

and $W(k_x, k_y)$ is the power spectral density (or "spectrum") of the surface,

$$W(k_x, k_y) = \frac{1}{4\pi^2}\int_{-\infty}^{\infty}\int_{-\infty}^{\infty} dx\, dy\, e^{ik_x x + ik_y y}\, \sigma^2 C(x,y) \tag{1.39}$$

The SPM result above illustrates the "Bragg" scattering response in rough surface scattering, which approximates the cross section as proportional to the spatial frequency in the surface which would cause a periodic surface Floquet mode to propagate in the observation direction. Note the polarization dependence of the above cross sections which contrasts with the physical optics result obtained above. The discrepancy between PO and SPM cross sections in the small surface height limit, for which both theories should apply, has been addressed in the literature [28] and eliminated through an iteration of the PO result. Thus, the predicted SPM polarization difference is accurate for small surface heights and slopes. Although the first order solution predicts no depolarization in the plane of incidence, second order incoherent fields yield a cross polarized contribution [34].

While the SPM is an exact perturbation solution, and therefore includes contributions from all possible scattering mechanisms for surfaces for which it converges, it clearly is limited by the accuracy of its zeroth order solution. For surfaces where significant scattering occurs, energy in the specularly reflected and transmitted waves is extinguished and spread into other propagation directions, invalidating the zeroth

order fields and increasing the number of required terms in the perturbation solution. Studies of the validity of the SPM approximations have been performed for 1-D surfaces through comparison with numerical methods [31]-[33], [35], again primarily for surfaces with Gaussian correlation functions. Comparisons for 2-D surfaces again are much more limited.

1.3.3 Two scale model

A third approximate method in surface scattering is used for surfaces which contain a large range of spatial scales, so that small surface variations can be considered to overly larger scale variations as shown in Figure 1.5. An ocean surface is an example of such a "composite" surface, due to presence of both long gravity type ocean waves and short capillary type waves simultaneously. Theories for composite surfaces have been considered by a number of authors [36]-[43] and involve a combination of the PO or GO solutions, which model the large spatial variations, and the SPM solution, which models the small spatial scale contributions. Additionally, the SPM contribution is averaged over a distribution of tilt angles due to the tilting effect of the larger spatial scales. The composite surface, or two scale, model has had great success in matching experimental backscattering data from the ocean at a variety of frequencies [42]. However, the theoretical basis of this model remains unclear, as the separation between "small" and "large" scales in the ocean requires choice of a spectral parameter. The composite surface model will be considered in more detail in Chapter 5 when a numerical study of two dimensional ocean scattering is performed.

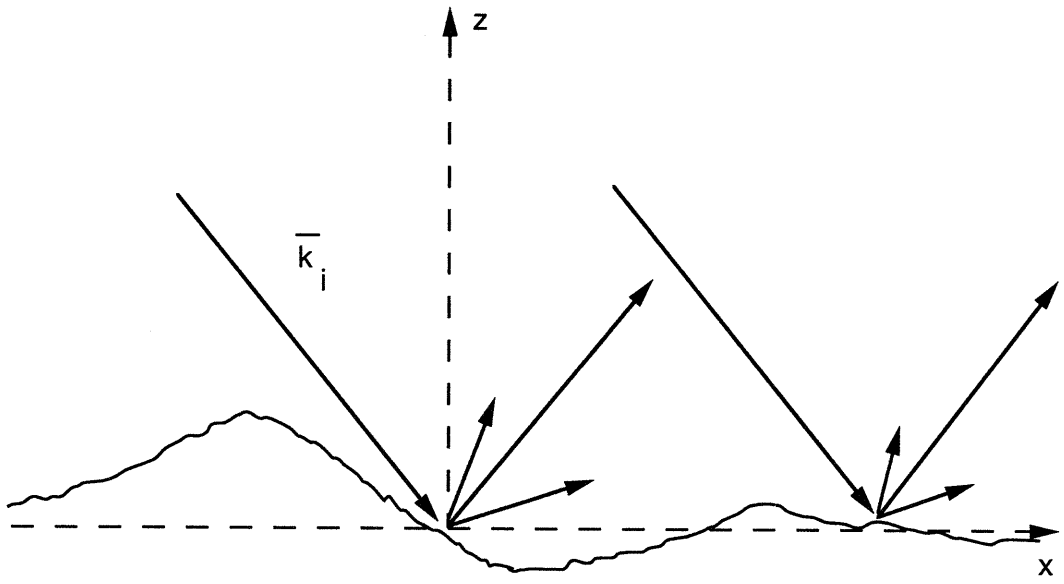

Figure 1.5: Composite surface approach to surface scattering

1.3.4 Other methods

A number of additional analytical theories have also been proposed for the rough surface scattering problem, especially within the last decade, based on alternate approximate methods [17]-[27]. None of these approaches, however, have been as generally accepted or as widely used as the three theories mentioned previously. There is currently a great deal of interest in evaluation of these new approaches and in comparison of their predictions with numerical and other analytical solutions. However, since the primary concern of this thesis involves the application of numerical models to physical problems of interest, an evaluation of these alternate scattering theories will not be pursued. Future studies of the new analytical models should be possible with the numerical methods developed in this thesis, however, and could potentially lead to a better understanding of the usefulness of these approaches.

1.4 Numerical Methods for Surface Scattering

Many numerical methods have been applied to the solution of Maxwell's equations, each with its own distinct advantages and disadvantages. The method of moments (MOM), developed in the mid 1960's [44]-[45], was the first widely used exact numerical technique for electromagnetics. The method of moments solves an integral equation at a single frequency for the unknown fields in a volume or on a surface by discretizing the integral equation into a matrix equation and then solving the matrix equation. Also proposed in the 1960's was the finite difference time domain (FDTD) algorithm of Yee [46], which solves Maxwell's equations in the time domain using a

centered difference, time marching approach. Since the 1960's, numerical methods for solving Maxwell's equations have greatly proliferated to include finite element, boundary element, multipole, transmission line, and a number of other methods [47]. Although many numerical methods have been applied to the rough surface scattering problem [48]-[51], the most widely used has been the method of moments. The method of moments is particulary advantageous for single frequency surface scattering problems because it requires discretization in a maximum of two dimensions compared to the three dimensional discretization needed in finite element and finite difference techniques, resulting in a much smaller number of unknowns to be determined by the numerical method.

Numerical surface scattering models based on the method of moments have been previously applied in a number of areas [29]-[33], [35], [52]-[56] and have been successful in predicting many phemonena. Standard approaches to the MOM perform the required matrix inversion using a direct matrix solver, for which computational time scales as the third power of the number of unknowns in the matrix. This rapid increase in computational requirements with number of unknowns limited previous simulations to relatively small surfaces rough in one direction only. However, more efficient approaches to the method of moments have recently been developed [57]-[60] which enable the solution of much larger problems, so that surfaces rough in two dimensions or very long surfaces rough in one dimension can be studied. These more efficient algorithms and parallel computing techniques will be applied in this thesis to investigate very large scale one dimensional and two dimensional rough surface problems.

The next section reviews the derivation of the method of moments, and a brief discussion of matrix equation solution methods follows. A more detailed description of the method of moments can be found in reference [3].

1.4.1 Method of moments

As mentioned previously, a method of moments solution to equations (1.6-1.9) involves discretizing these equations into a matrix equation which is then solved to obtain the expansion coefficients of unknown surface tangential fields. Unknown tangential fields are expanded into a set of "basis" functions as

$$\hat{x} \cdot \left[\hat{n} \times \overline{H}(\overline{r})\right] = \sum_n a_n P_n(\overline{r}) \tag{1.40}$$

$$\hat{y} \cdot \left[\hat{n} \times \overline{H}(\overline{r})\right] = \sum_n b_n P_n(\overline{r}) \tag{1.41}$$

$$\hat{x} \cdot \left[\hat{n} \times \overline{E}(\overline{r})\right] = \sum_n c_n P_n(\overline{r}) \tag{1.42}$$

$$\hat{y} \cdot \left[\hat{n} \times \overline{E}(\overline{r})\right] = \sum_n d_n P_n(\overline{r}) \tag{1.43}$$

where a_n, b_n, c_n, and d_n are the unknown constant expansion coefficients of these fields and $P_n(\overline{r})$ is a user selected basis function, which should in some sense provide a good approximation to the expected behavior of surface fields. Basis functions $P_n(\overline{r})$ can be chosen to be non-zero only over a small portion of the domain of interest ("subdomain" basis functions), or may range over the entirety of the domain ("entire domain" basis functions). An exact expansion of arbitrary fields into a specified set of basis functions is possible only for a very limited set of solutions, and may

often require a large set of expansion functions to achieve high accuracy. However, the advantage of the method of moments lies in the fact that its solutions can be shown to satisfy a variational principle, so that they are stationary to first order with respect to basis function variations [3]. A demonstration of convergence of method of moments solutions with respect to the number of unknown basis functions used is still always required, however, to insure that an accurate representation of tangential fields is being obtained. Common choices for basis functions include pulse (equal to one only over a small portion of the domain, equal to zero elsewhere), triangular (piecewise linear over a small portion of the domain, zero elsewhere), and sinusoidal (entire domain) functions.

Substitution of equations (1.40-1.43) into (1.6-1.9) converts the surface integrals of these equations into sums of constants times integrals involving vector products of the Green's and basis functions. However, evaluation of these integrals is not possible since the observation coordinate of the Green's function is still unspecified. An inner product approach is used to solve this problem, where another user specified set of functions, known as the "weighting" functions $w_n(\bar{r})$, is multiplied into each equation, and an integral over the domain of the weighting function is performed. This procedure leads to the aforementioned matrix equation, since inner products with each weighting function result in a single equation, or row of the matrix, involving sums of the unknown expansion coefficients, which make up the column vector multiplied by the matrix:

$$\overline{\overline{Z}}\bar{x} = \bar{b} \tag{1.44}$$

The right hand side column vector, $\bar{b}$ results from the inner product of the weighting functions with the source terms of $\overline{E}_{inc}$ and $\overline{H}_{inc}$ in the integral equations. Individual matrix elements of $\overline{\overline{Z}}$ correspond to double surface integrations over the domains of the weighting and basis functions respectively which involve vector products of the weighting, basis, and Green's functions. Evaluation of these integrals can be performed either analytically, numerically, or through the use of approximations. Solution of this matrix equation yields the expansion coefficients a_n to d_n which can then be used in a Huygens' priciple integral to evaluate scattered fields for any specified observation location.

The moment method codes of this thesis will use exclusively pulse basis functions and delta weighting functions, so that integral equations (1.6-1.9) are satisfied at a discrete set of points on the surface profile. This technique, known as "point matching", has been applied successfully to a number of problems in the literature [3] and found to require a sampling rate ranging from 4 to 10 points per electromagnetic wavelength to obtain reasonable accuracy. Although pulse basis functions represent a low order expansion of surface tangential fields, the reduction in complexity associated in matrix element integrals makes the iterative matrix equation solution techniques to be discussed in the next section possible. Higher order basis and weighting functions have been found in the literature to reduce the number of unknowns required to solve a given problem, but the complex integration of matrix elements required can sometimes be much more time consuming. Such integrations make the matrix equation solution techniques of this thesis more difficult, and therefore are not considered. Demonstration of model convergence with respect to the

number of unknowns used will be performed throughout the thesis to indicate that an accurate solution is indeed being obtained by the point matching method. Note that sampling is strictly required on the scale of the shortest electromagnetic wavelength in the problem, so that problems involving high dielectric constant materials can potentially cause a great increase in the number of unknowns. Chapter 6 will discuss a method for avoiding this problem for the case of a highly lossly dielectric medium.

1.4.2 Matrix equation solution methods

The solution of matrix equations such as (1.44) is a standard mathematical procedure which is often required in numerical methods. However, for matrix equations which involve more than a few thousand unknowns, standard direct inversion techniques become very limited [61]. Given the very large matrix equations to be studied in this thesis, more efficient techniques are required if solutions are to be obtained with reasonable amounts of computational time. Higher efficiency in solving matrix equations is obtainable through the use of iterative, instead of direct, solutions [62]. Iterative matrix equation solutions have been studied extensively, and have greatly proliferated within the past decade to include a wide range of techniques. Most of the commonly used iterative approaches are based on variants of the conjugate gradient algorithm of [63], which minimizes matrix equation residual error at each iteration by expanding the solution into a set of orthogonal vectors. For the non-symmetric, complex matrices of this thesis, a variant known as the bi-conjugate gradient-stabilized algorithm (BiCGSTAB) is used [62],[64], which has no guarantee of convergence, but

has been observed to converge more rapidly than other techniques for these matrices. The BiCGSTAB algorithm is

Initialize, for an initial guess x_0:

$$\overline{r}_0 \leftarrow \overline{b} - \overline{\overline{Z}}\overline{x}_0$$

$$\overline{r}' \leftarrow \overline{r}_0$$

$$n \leftarrow 1$$

begin loop:

$$\rho_{n-1} = (\overline{r}', \overline{r}_{n-1})$$

$$if\ n = 1\ then$$

$$\overline{p}_n \leftarrow \overline{r}_{n-1}$$

$$else$$

$$\beta_{n-1} \leftarrow \frac{\rho_{n-1} w_{n-1}}{\rho_{n-2} \alpha_{n-1}}$$

$$\overline{p}_n \leftarrow \overline{r}_{n-1} + \beta_{n-1} \left(\overline{p}_{n-1} - w_{n-1} \overline{v}_{n-1} \right)$$

$$endif$$

$$\overline{v}_n \leftarrow \overline{\overline{Z}}\overline{p}_n$$

$$\alpha_n \leftarrow \rho_{n-1} / (\overline{r}', \overline{v}_n)$$

$$\overline{s}_n \leftarrow \overline{r}_{n-1} - \alpha_n \overline{v}_n$$

$$\overline{t}_n \leftarrow \overline{\overline{Z}}\overline{s}_n$$

$$w_n \leftarrow (\overline{t}_n, \overline{s}_n) / (\overline{t}_n, \overline{t}_n)$$

$$\overline{x}_n \leftarrow \overline{x}_{n-1} + \alpha_n \overline{p}_n + w_n \overline{s}_n$$

$$\overline{r}_n \leftarrow \overline{s}_n - w_n \overline{t}_n$$

$$n \leftarrow n + 1$$

$$test\ for\ convergence$$

exit if converged

end loop

where the $\left(\overline{a}, \overline{b}\right)$ notation refers to the complex inner product $\sum_n a_n^* b_n$. Convergence is tested for in the complex norm of the $\overline{r}_n$ vector, which is the residual error of the matrix equation at a given iteration.

The BiCGSTAB algorithm requires two matrix multiplications on each iteration, and therefore is an order N^2 algorithm. Although this represents a great improvement over the order N^3 direct methods when the iterative solution converges rapidly, even order N^2 techniques can be prohibitive for large matrices. Chapters 2 and 4 of this thesis describe recently developed iterative techniques, known as the banded matrix flat surface iterative approach (BMFSIA) [57] and the sparse matrix flat surface iterative approach (SMFSIA) [59] which further improve the efficiency of the BiCGSTAB algorithm by peforming matrix multiplies more rapidly. It is these new algorithms which enable the large scale surface scattering simulations of this thesis to be performed.

1.4.3 Computational facilities

All of the numerical results to be presented were generated using either a DEC AXP 3000 - M800 workstation with 416 megabytes of onboard RAM, capable of approximately 375 MFLOP operation, or the IBM SP2 400 node parallel computer at the Maui High Performance Computing Center (MHPCC) [65], where access has been allowed in the initial startup phase on this new center. The IBM SP2 is a collection of 400 RS-6000 (based on a POWER2 CPU) workstations, capable of around

250 MFLOP operation individually, networked through a high performance communication system to allow groups of nodes to operate in combination as a parallel processor. Software libraries are available at the center to implement inter-process communications using simple routine calls, so that development of parallel codes is relatively efficient. The codes of this thesis implemented with the MHPCC used the parallel virtual machine (PVM) message passing library [66], which is a public domain package for UNIX communications. Since many of these codes involved Monte Carlo simulations, inter-process communication was often limited to simple process starting and monitoring routines. However, the codes of Chapters 2 and 6 make use of parallel computations and therefore involve more process communications. The parallel algorithms used will be described further in their respective chapters.

1.5 Overview of Thesis

The remaining portion of this thesis consists of five distinct applications of numerical methods to surface scattering problems followed by a concluding chapter.

In Chapter 2, a 1-D numerical model for VHF propagation is developed using the BMFSIA. VHF fields are used for both radio and television broadcasting, and also for low resolution radar measurements, and understanding field strengths produced by transmitting sources over inhomogeneous terrain is important in both commercial and military applications. Model predictions are compared with experimental data from Lincoln Laboratory and with other approximate methods. Results of the study indicate the level of sensitivity of propagation models to input terrain profiles, and validate use of the parabolic wave equation technique for further propagation

predictions.

Chapter 3 presents a numerical model for the prediction of 2-D periodic surface polarimetric brigthness temperatures. An extended boundary condition (EBC) approach is adopted based on the electric field integral equations, resulting in a mode matching type solution for the Fourier expansion coefficients of tangential surface fields. A study of pyramidal surface polarimetric passive remote sensing is performed, and illustrates the sensitivity of the third Stokes parameter, U_B, to medium azimuthal asymmetry. The model developed can also potentially be applied for treatment of grazing angle scattering problems and for microwave absorber design.

Backscattering enhancement from 2-D perfectly conducting randomly rough surfaces is studied in Chapter 4. Backscattering enhancement is primarily a multiple scattering effect which can occur for surfaces with large slopes, and therefore is not predicted by any of the analytic theories. A numerical model using the SMFSIA in a Monte Carlo simulation is developed in Chapter 4, and simulation results are compared with millimeter wave laboratory data from the University of Washington. Gaussian surface processes are assumed, and a Gaussian correlation function is further specified. Simulations are performed for surfaces with rms heights of one wavelength and correlation lengths of 1.41, 2, and 3 wavelengths, and clearly show backscattering enhancement effects.

Active remote sensing of the ocean is studied in Chapter 5, again with the 2-D perfectly conducting randomly rough surface SMFSIA model applied in a Monte Carlo simulation. The SMFSIA approach is extended using a canonical grid expansion of weak matrix terms so that the very large surface sizes required to eliminate

edge effects in backscattering simulations can be treated. Both forward and backscattering are investigated, and an assessment of the analytical approximations in both of these regions is obtained. In addition, the physical optics approximation for ocean scattering is investigated through Monte Carlo simulation and used to validate the method through comparison with the analytically evaluated physical optics integral. Comparisons with experimental data are made using the composite surface model suggested by comparison with numerical simulations.

Chapter 6 studies passive remote sensing of the ocean with a penetrable surface SMFSIA formulation applied again in a Monte Carlo simulation. A modification of the SMFSIA which enables efficient calculation of fields scattered from a highly lossly surface such as the ocean without increasing the number of unknowns is developed. The modified SMFSIA approach is based on the observation that any rapidly varying fields in the ocean medium are effectively averaged when multiplied by the slowly varying free space Green's function, so that an averaging of matrix elements in the ocean medium to free space scale is reasonable. The code is applied to provide some initial results in a study of ocean polarimetric thermal emission, although computational limitations prevent a detailed assessment, and the small azimuthal variations of ocean brightness temperatures obtained make accurate calculations difficult. Results concerning the influence of different ocean wavelength regions on azimuthal variations are found to agree with those of the approximate models, and further simulations using the composite surface model emphasize the importance of an accurate ocean spectral model in the prediction of ocean polarimetric brightness temperatures.

Chapter 2

A Method of Moments Model for VHF Propagation

2.1 Introduction

Site specific VHF propagation models remain a subject of continuing interest. A number of approximate methods exist and have been applied successfully in specific cases, but the limitations of the approximations of these models remain unclear. One such model, known as SEKE (Spherical Earth with Knife Edges) [67], uses a weighted average of analytic solutions for the multipath, spherical earth, and knife edge diffraction contributions which depends on the transmitter, receiver, and terrain geometries. Although SEKE has been shown to have good general agreement with experimental data, some cases exist for which SEKE's predictions are substantially different from measurements. Another approach which has been studied extensively involves the use of the parabolic approximation to the Helmholtz equation [68]-[70]. Methods based on the parabolic wave equation (PWE) neglect the contribution of backscattered fields, which can become significant when obstacles are near the transmitter. Again, com-

parisons with measurement data show good general agreement with problems in some specific cases. For both the SEKE and PWE models, clarification of discrepancies is difficult given uncertainties both in the underlying approximations and in the input terrain profiles.

Numerically exact methods have also been investigated for small obstacles [71]-[72], but the large electromagnetic distances involved in more general propagation problems makes numerical methods impractical. Given that at 150 MHz, one kilometer of terrain corresponds to 500λ, and that typical VHF propagation problems involve distances in the tens of kilometers, a numerical model needs to be able to solve problems with profiles the order of tens of thousands of wavelengths long. Such electromagnetic distances are usually considered too large for numerical methods. A numerically exact model is desirable because it avoids any approximations in the solution and can therefore be used to validate other non-exact methods and to demonstrate conclusively the sensitivity of the true solution to input terrain parameters.

In this chapter, a numerically exact model based on the recently developed banded matrix iterative approach (BMIA) [57]-[60] to the method of moments is presented which enables the solution of practical propagation problems. Although this model remains computationally complex, the iterative method used results in greater efficiency in the method of moments solution, so that predictions can be generated from a single DEC AXP 3000 workstation in approximately two CPU days for a ten thousand wavelength problem. Section 2.2 describes the basic propagation configuration and reviews the formulation of the method of moments solution. The method is then validated in Section 2.3 through comparison with exact solutions

for some simple geometries, and a parallel implementation which allows the solution of larger problems in reasonable amounts of time is discussed in Section 2.4. A comparison of model predictions with experimental data in Section 2.5 shows overall agreement between the model and measurements to be good, and demonstrates the sensitivity of terrain based propagation models to input terrain parameters. Section 2.6 compares these predictions with the SEKE and PWE methods, and Section 2.7 presents final conclusions.

2.2 Review of Formulation and Numerical Method

A typical VHF propagation problem involves predicting the power measured by a receiver as a function of altitude at a given distance away from a like polarized transmitter and above an inhomogeneous terrain profile, as shown in Figure 2.1. When distances separating the transmitter and receiver are very large and the terrain is not rapidly varying on an electromagnetic scale, a Fresnel zone argument can be applied which illustrates that terrain outside of the plane of incidence has little effect, so that a two dimensional model is sufficient to capture the physics of the problem. Thus, the method of moments formulation will assume a surface profile which is rough only in the plane of incidence (taken to be the $x-z$ plane) and constant perpendicular to the plane of incidence (the y direction).

As discussed in Chapter 1, for in-plane incidence in a two dimensional problem, Maxwell's equations decouple into dual equations for TE and TM waves, and a scalar Kirchhoff diffraction integral in terms of E_y for the TE case and H_y for the TM case can be applied using the two dimensional Hankel function form of the Green's

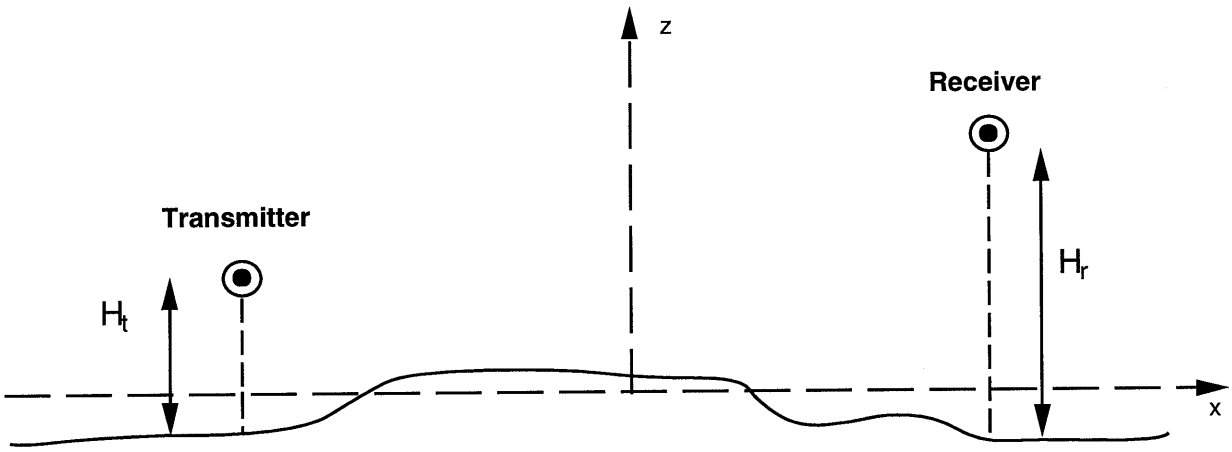

Figure 2.1: Geometry of propagation problem

function. Equations for a dielectric surface medium are [58]

$$h_2\Psi_{in}(\overline{\rho}_s) - \int_S d\sigma' \left\{G_j(\overline{\rho}_s, \overline{\rho}'_s)\hat{n}\cdot\nabla'_s\Psi_j(\overline{\rho}'_s) - \Psi_j(\overline{\rho}'_s)\hat{n}\cdot\nabla'_s G_j(\overline{\rho}_s, \overline{\rho}'_s)\right\} \;=\; h_1\Psi_j(\overline{\rho}_s)$$

where $\Psi = E_y$ for the TE case and H_y for the TM case, $j = 1, 2$ signifies regions 1 (free space) or 2 (dielectric), $h_1 = 0.5, -0.5$ and $h_2 = 1, 0$ for $j = 1, 2$ respectively. Also, in the above equation

$$d\sigma'\hat{n} = \left[\hat{z} - \hat{x}\frac{df(x')}{dx'}\right]dx' \tag{2.1}$$

$$\overline{\rho}_s = \hat{x}x + \hat{y}y \tag{2.2}$$

and

$$G_j(\overline{\rho}_s, \overline{\rho}'_s) = \frac{i}{4}H_0^{(1)}(k_j|\overline{\rho}_s - \overline{\rho}'_s|) \tag{2.3}$$

where $k_j = \omega\sqrt{\mu_0\epsilon_j}$ is the propagation constant in medium j. Boundary conditions at the interface between region 1 and 2 are

$$\Psi_1(\overline{\rho}') = \Psi_2(\overline{\rho}') \tag{2.4}$$

for both the TE and TM cases and

$$\hat{n}\cdot\nabla'_s\Psi_1(\overline{\rho}'_s) = \alpha\hat{n}\cdot\nabla'_s\Psi_2(\overline{\rho}'_s) \tag{2.5}$$

where $\alpha = 1$ for the TE case (non-magnetic medium) and $\frac{\epsilon_1}{\epsilon_2}$ for TM.

The above formulation gives two integral equations in two unknowns (Ψ_1 and $\hat{n} \cdot \nabla'_s \Psi_1$) on the surface profile. Applying a point matching method of moments technique as in reference [58] results in a matrix equation in terms of the unknown pulse basis function expansion coefficients of these fields, which can be written as

$$\overline{\overline{Z}}\,\overline{I} = \overline{V} \tag{2.6}$$

where $\overline{I}$ is a vector containing the expansion coefficients, and $\overline{V}$ contains the incident field evaluated at points on the surface profile. Elements of the impedance matrix $\overline{\overline{Z}}$ are proportional to Hankel functions of order zero or order one evaluated at arguments corresponding to distances between individual points on the surface profile. Tables of the zero and first order Hankel functions are stored in the computer code implemented to avoid multiple calls to Hankel routines.

In the banded matrix iterative approach (BMIA) of reference [58], the above matrix equation is solved iteratively by expressing the matrix $\overline{\overline{Z}}$ as the sum of a strong matrix $\overline{\overline{Z}}^{(s)}$, which contains the elements of $\overline{\overline{Z}}$ to within a specified bandwidth from the diagonal, and a weak matrix, $\overline{\overline{Z}}^{(w)}$, which contains the remaining elements. The weak matrix contribution is included iteratively, so that the solution is obtained by solving

$$\overline{\overline{Z}}^{(s)}\overline{I}^{(1)} = \overline{V} \tag{2.7}$$

initially and then iterating

$$\overline{\overline{Z}}^{(s)}\overline{I}^{(n+1)} = \overline{V} - \overline{\overline{Z}}^{(w)}\overline{I}^{(n)} \tag{2.8}$$

until convergence is observed in $\overline{I}^{(n)}$. The BMIA requires solution of the banded matrix equation on each iteration and then a weak matrix multiply, so that the overall method is $O(N^2)$ for an N by N matrix, but convergence is typically faster than other $O(N^2)$ methods. Direct solution of the banded matrix equation is practical when enough memory resources are available to store the banded matrix. However, in the case of propagation problems, even storage of the banded matrix is impossible if a reasonable bandwidth is desired in the computations. Also, relatively large bandwidths are required in the BMIA due to the fact that weak terms are neglected entirely in the banded matrix equation solution.

In this chapter, a method similar to those applied for surfaces rough in two dimensions [59]-[60] is adopted in an attempt to alleviate some of the problems associated with the BMIA. In this method, known as the banded matrix flat surface iterative approach (BMFSIA), the original matrix $\overline{\overline{Z}}$ is decomposed into the sum of the same BMIA strong matrix $\overline{\overline{Z}}^{(s)}$, a new 'flat surface' matrix, $\overline{\overline{Z}}^{(fs)}$, which contains an approximation to the terms of the BMIA weak matrix, and a new weak matrix, $\overline{\overline{Z}}^{(w)}$, which contains the difference between BMIA weak matrix elements and elements of the flat surface matrix. The flat surface matrix approximates coupling between points on the surface by assuming that they lie at the same elevation, so

that matrix elements are evaluated using

$$G_j^{(fs)}(\overline{\rho}_s, \overline{\rho}_s') = \frac{i}{4} H_0^{(1)}(k_j|x - x'|) \tag{2.9}$$

and

$$\hat{n} \cdot \nabla_s' G_j^{(fs)}(\overline{\rho}_s, \overline{\rho}_s') = 0 \tag{2.10}$$

instead of G_j and $\hat{n} \cdot \nabla_s' G_j$ as in the BMIA weak matrix.

Again, the weak matrix contribution is included iteratively, so that the solution is obtained by solving

$$(\overline{\overline{Z}}^{(s)} + \overline{\overline{Z}}^{(fs)})\overline{I}^{(1)} = \overline{V} \tag{2.11}$$

initially and then iterating

$$(\overline{\overline{Z}}^{(s)} + \overline{\overline{Z}}^{(fs)})\overline{I}^{(n+1)} = \overline{V} - \overline{\overline{Z}}^{(w)}\overline{I}^{(n)} \tag{2.12}$$

until convergence is observed in $\overline{I}^{(n)}$. However, in the BMFSIA another iterative method is used to solve the strong plus flat surface matrix equation on each weak iteration, resulting in nested iterative methods analogous to those of reference [59]. The advantage of the 'inner' iterative technique, which uses BiCGSTAB solver discussed in Chapter 1, is that inclusion of flat surface terms is not computationally expensive since flat surface matrix multiplies can be performed using the FFT. Also, the conjugate gradient solver of the inner iteration is more easily parallelizable than

a direct banded matrix solver with no storage, as will be described in Section 2.4.

Once the induced fields on the surface are obtained, the Kirchhoff diffraction integral can again be used to calculate the scattered field at the receiver and therefore the total power received. Transmitting antennas are modeled as either electric or magnetic line sources for the TE and TM cases respectively, so that a zero order Hankel function incident field is produced on the surface. Although a vertical electric dipole antenna does not have the same pattern as a horizontal magnetic dipole, the long distances involved in propagation problems again result in only minor effects due to differences in antenna patterns.

2.3 Model Validation

To validate the model, comparisons with published results and with exact solutions for some simple geometries were performed. Issues to be considered in the method of moments model are the discretization level required, the effect of finite surface size on the simulations, the importance of retaining all weak iterations in the BMFSIA, and the necessity of modeling surface medium dielectric properties.

Figure 2.2 compares predicted excess one-way propagation loss (defined as the ratio of power at the receiver over terrain to the power at the receiver if it were in free space) at a range of 236 wavelengths for a horizontally polarized (TE) line source above a flat perfectly conducting plane with the analytical solution. Surface currents were sampled at four points per electromagnetic wavelength, and the model is seen to accurately capture the multipath interference effects of this problem. Surface currents

for a TM line source above a flat impedance plane and for a TE line source in front of a perfectly conducting semi-cylinder were also compared with references [71] and [73] respectively and found to be in excellent agreement. Four points per wavelength sampling was again found sufficient for the TM line source case, but a higher sampling rate of twenty points per wavelength was required in the TE comparison due to the need to accurately sample the geometry of a 0.5λ radius semi-cylinder. The simple point matching method of moments used requires high sampling in cases where surface structures are rapidly varying on an electromagnetic scale. However, since terrain profiles to be studied with the model are extremely undersampled on an electromagnetic scale, and therefore very slowly varying, four points per wavelength sampling is sufficient to model the obtained field variations.

To investigate the effect of finite surface size on model predictions, simulations were run for the perfectly conducting wedge geometry of reference [74], shown in Figure 2.3, at 100 MHz and TE polarization. Results for total surface sizes, L, of 5 km ($1,666\lambda$) and 10 km ($3,333\lambda$) are plotted in Figure 4, and demonstrate that finite surface size has little effect on model predictions. Predictions for a surface size of 5 km were also compared with the GTD approach of reference [74] and again found to be in excellent agreement.

Since typical propagation problems involve very large distances, an initial consideration of the BMFSIA technique suggests that complete neglect of the weak matrix might be reasonable. This issue is studied in Figure 2.5, where the results of Figure 2.4 for a surface size of $1,666\lambda$ are plotted at each weak iteration of the BMFSIA, using a bandwidth of 1000 points or 250λ. These curves clearly demonstrate the im-

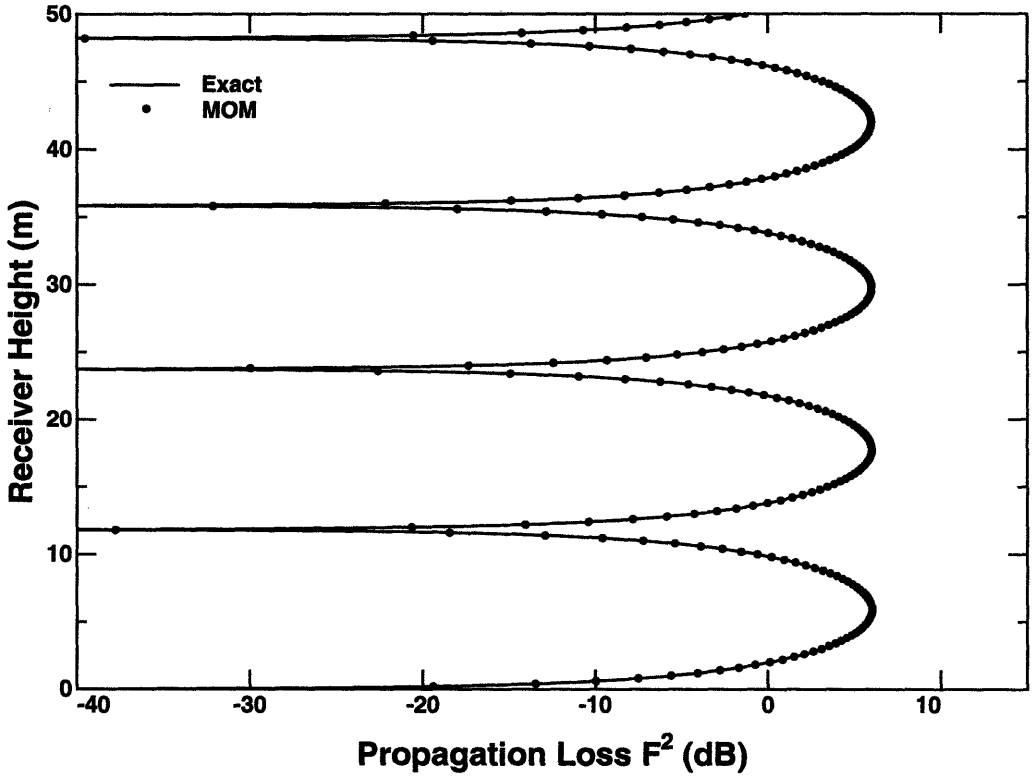

Figure 2.2: Excess one way propagation loss over a flat perfectly conducting plane - TE polarization: Comparison of MOM predictions with analytical solution

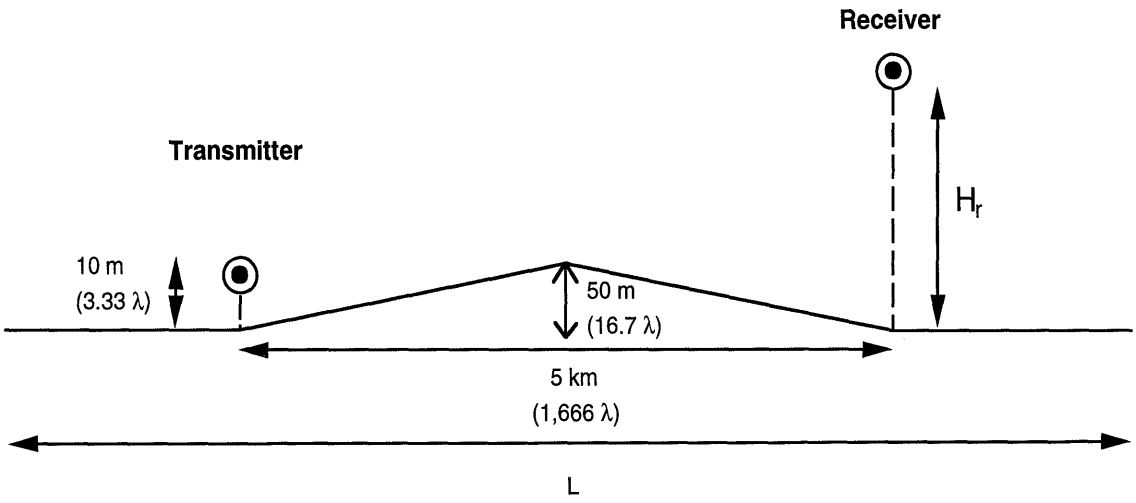

Figure 2.3: Wedge geometry for surface size tests

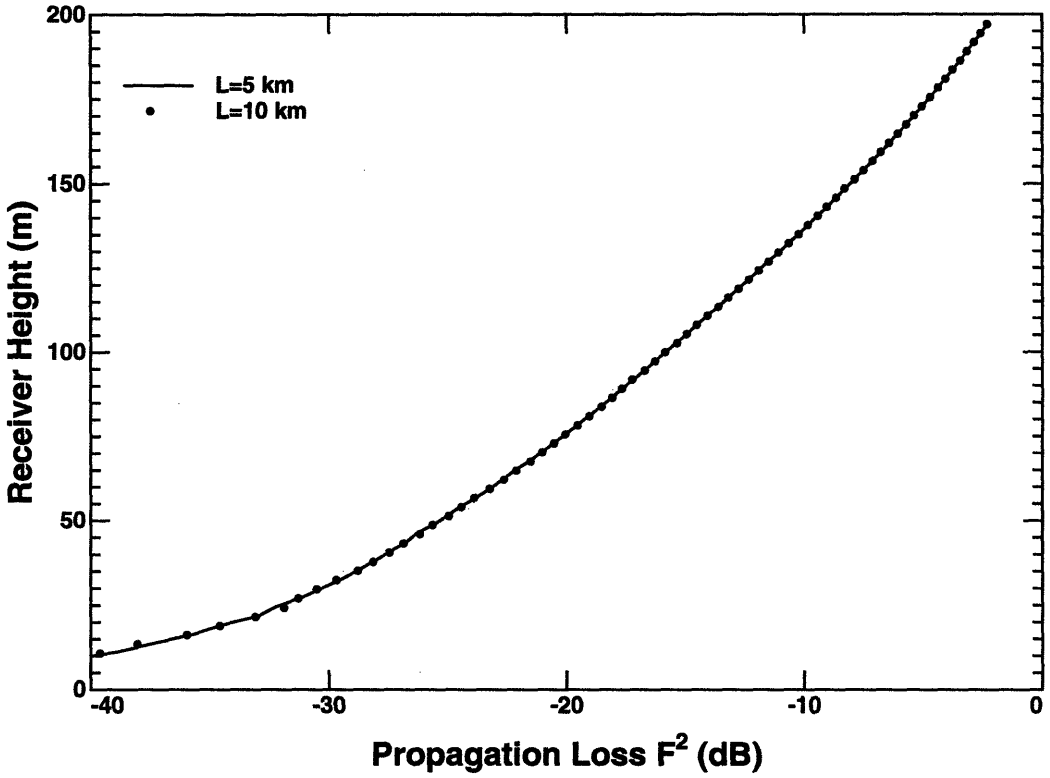

Figure 2.4: Predicted excess one way propagation loss for perfectly conducting wedge - TE polarization: Comparison of results for varying total surface size

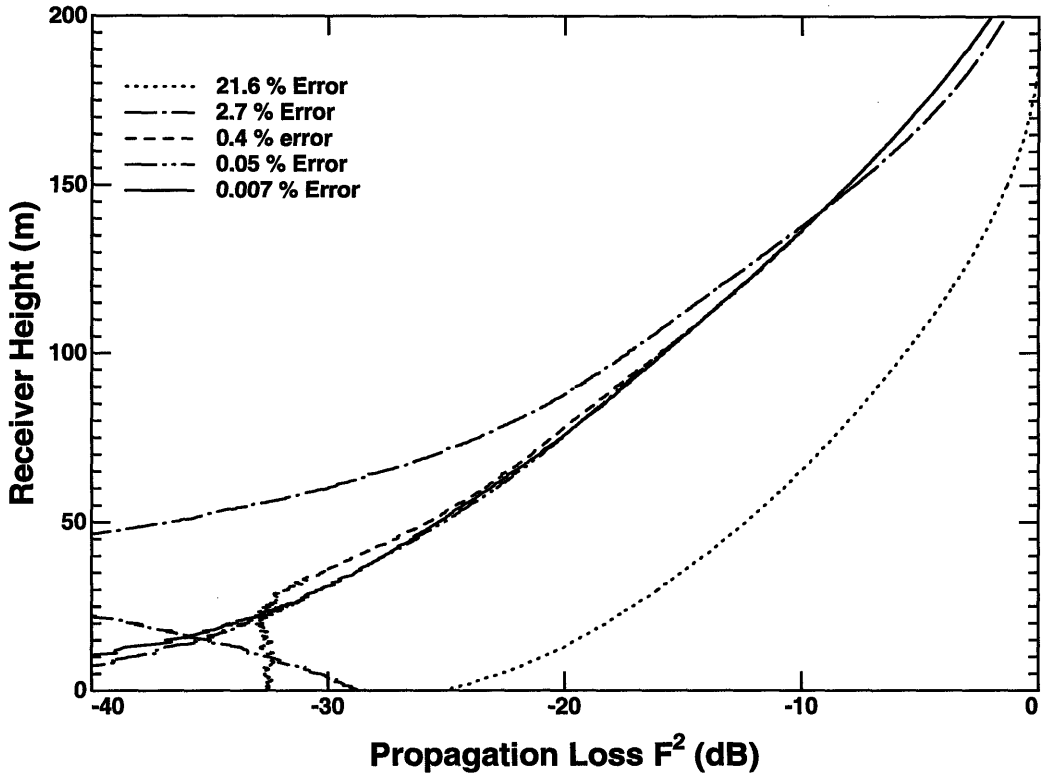

Figure 2.5: Predicted excess one way propagation loss for perfectly conducting wedge - TE polarization: Model predictions on each BMFSIA weak iteration

portance of including weak matrix contributions, especially in the diffraction region, where a convergent result is not obtained until an error of less than 0.1 % is reached in the BMFSIA.

A final issue in the method of moments model involves the importance of modeling surface medium dielectric properties. As is discussed in [69], both TE and TM polarized model predictions are usually fit well by assuming a TE polarized transmitter and a perfectly conducting surface. This is demonstrated in measurement data as well, where little difference is observed for the same profiles measured in TE or TM polarizations. Modeling the surface as being perfectly conducting is advantageous since one of the two unknown fields on the surface vanishes and the matrix equation

reduces in size by a factor of two. In addition, the need to sample surface fields on the scale of the wavelength inside the medium is eliminated. To investigate this point, simulations were run for the wedge geometry of Figure 2.3, using both perfectly conducting and penetrable media in TE and TM polarizations. A dielectric constant of $\epsilon = (6., 0.63)$ was assumed for the penetrable case for matrix sizes of $6,664$ in the perfectly conducting code, and $32,768$ in the penetrable code. The additional factor of $\sqrt{6}$ in penetrable matrix size results from sampling surface field unknowns on approximately the scale of the wavelength in the surface medium.

Predicted one way propagation losses are shown in Figures 2.6 for TE and TM polarizations. The comparison shows little difference between the penetrable surface TE and TM predictions and the perfectly conducting TE prediction. The perfectly conducting TM prediction is seen to differ, as can be explained by observing that for TM polarization, the Brewster angle effect results in a reflection coefficient of $+1$ in the perfectly conducting case as one approaches grazing, but -1 in the penetrable case for angles closer to grazing than the Brewster angle. Due to similarity of the TE and TM predictions, simulations in the following sections were run only for TE polarization and a perfectly conducting surface profile.

2.4 Parallel Implementation

One particular terrain profile of interest, Magrath NW37, which will be described in more detail in the next section, has a length of 37 km, or $20,600\lambda$ at the 167 MHz frequency where measurement data were taken. An additional 14 km buffer zone was added to the terrain profile to avoid any potential edge effects, for a total of $113,500$

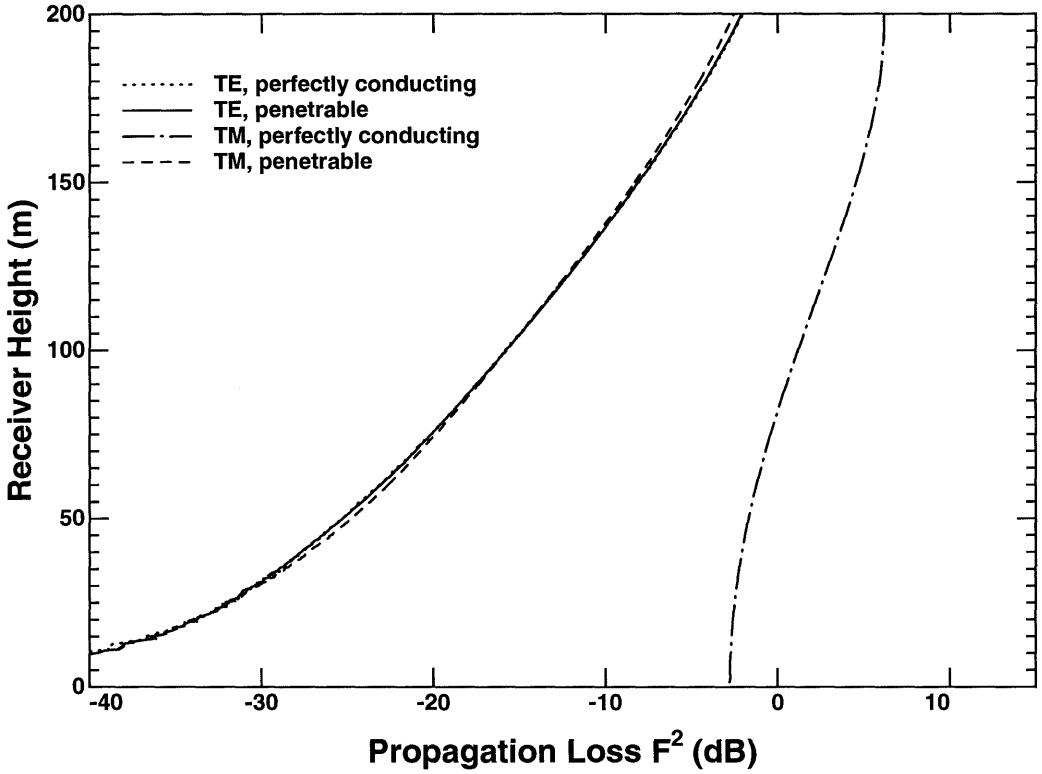

Figure 2.6: Predicted excess one way propagation loss for perfectly conducting wedge - TE and TM polarizations: Comparison of perfectly conducting and penetrable surfaces

unknowns in the BMFSIA solution. The BMFSIA code was run for this case on a DEC AXP 3000 Alpha workstation and was found to require approximately one week of CPU time. To reduce this large time requirement, a parallel implementation of the BMFSIA was developed and is described in this section.

Since the BMFSIA is composed of two iterative methods which both require matrix multiplies with a vector, parallelization of the code is achieved by performing these multiplies in parallel. A simple master-slave configuration is used, in which the master program broadcasts the vector to be multiplied to S slave programs, which then perform the multiplication for N/S rows of the matrix. These slaves then broadcast their individual solutions back to the master program, which adds up the results to obtain the matrix vector product. This code was implemented on 16 nodes of the IBM SP/2 parallel computer at the Maui High Performance Computing Center, using the public domain Parallel Virtual Machine (PVM) code described in Chapter 1 as the message passing library. Due to the large size of the problem and the need for recalculation of all matrix elements on every iteration, communication costs represent relatively little of the overall program time, so that the parallelization for this code is relatively efficient. Comparison of the workstation and parallel versions showed a parallel speed-up factor of approximately 70% of the number of nodes used in the calculations.

Several additional methods were used to reduce computational time as well. A physical optics initial guess was used to begin the iterative process and found to reduce the number of conjugate gradient iterations required in the first order solution. A diagonal block pre-conditioner was used in the conjugate gradient method,

and matrix multiplies made use of the semi-symmetric properties of the impedance matrix. Finally, an asymptotic expansion of the Hankel function was used in the slave program weak matrix multiply routines, so that storing the Hankel function table at large distances was not required.

2.5 Comparison with Experimental Data

A large database of propagation measurements for sites in Canada has been compiled by Lincoln Laboratory, as is described in [67], for both TE and TM polarizations. Terrain profile data were obtained from both hand-read Canada Map Office (CMO) maps and Defense Mapping Agency (DMA) digital files at resolutions of 30 and 100 m, respectively. Three locations (called Beiseker N15, Magrath NW27, and Magrath NW37, respectively) for which SEKE predictions deviated from measured data were selected for use in the method of moments simulation. Measurements were taken at 167 MHz with a transmitting antenna height of 18.3 m above ground level. Atmospheric and Earth curvature effects were included in the model by assuming the standard 4/3 Earth radius approximation for a linear atmospheric refractive index profile, so that specified terrain elevation data were fit to a sphere of radius 4/3 times the true Earth radius.

Figures 2.7 to 2.9 show comparisons between model predictions and measurement data for the three locations using CMO terrain profiles. Overall agreement is observed to be very good for these cases, and the method of moments model is seen to capture the multipath and diffraction contributions accurately both in the interference and shadowed regions. However, some discrepancies, particularly in the location

of the first multipath null, exist which require clarification.

One possible source of these differences is the accuracy of input terrain profiles. Figures 2.10 to 2.12 compare the CMO and DMA profile method of moments predictions for the same three locations. Results are seen to be very sensitive to input terrain data, especially in the Beiseker N15 case (Figure 2.10), where profile differences close to the transmitter location influence the specular point slope and significantly alter predictions. Predictions using the higher resolution CMO profiles are seen to be closer to measurements for all three cases. Figures 2.10 to 2.12 demonstrate that accurate terrain profile measurements are required in order to obtain accurate predictions of propagation loss.

2.6 Comparison with Other Propagation Models

Figures 2.13 to 2.15 compare SEKE, PWE, and method of moments predictions for both CMO and DMA profiles of the three locations. The 1994 beta version of SEKE was used in these comparisons, which is a revision of the 1986 version described in reference [67] with improvements to the four basic SEKE propagation loss algorithms for single- and multiple- specular multipath, knife edge diffraction and spherical Earth diffraction. PWE results were generated using a split-step Fourier algorithm similar to reference [69] developed at MIT [75], and assumed a standard atmospheric profile and a Gaussian beam initial field distribution. Terrain profile inputs to the PWE code were smoothed with a five point averaging filter to avoid large second derivatives, and calculations were performed for 1 m and 25 m step increments in height and range respectively. Figures 2.13 to 2.15 show a good overall level of agreement between the

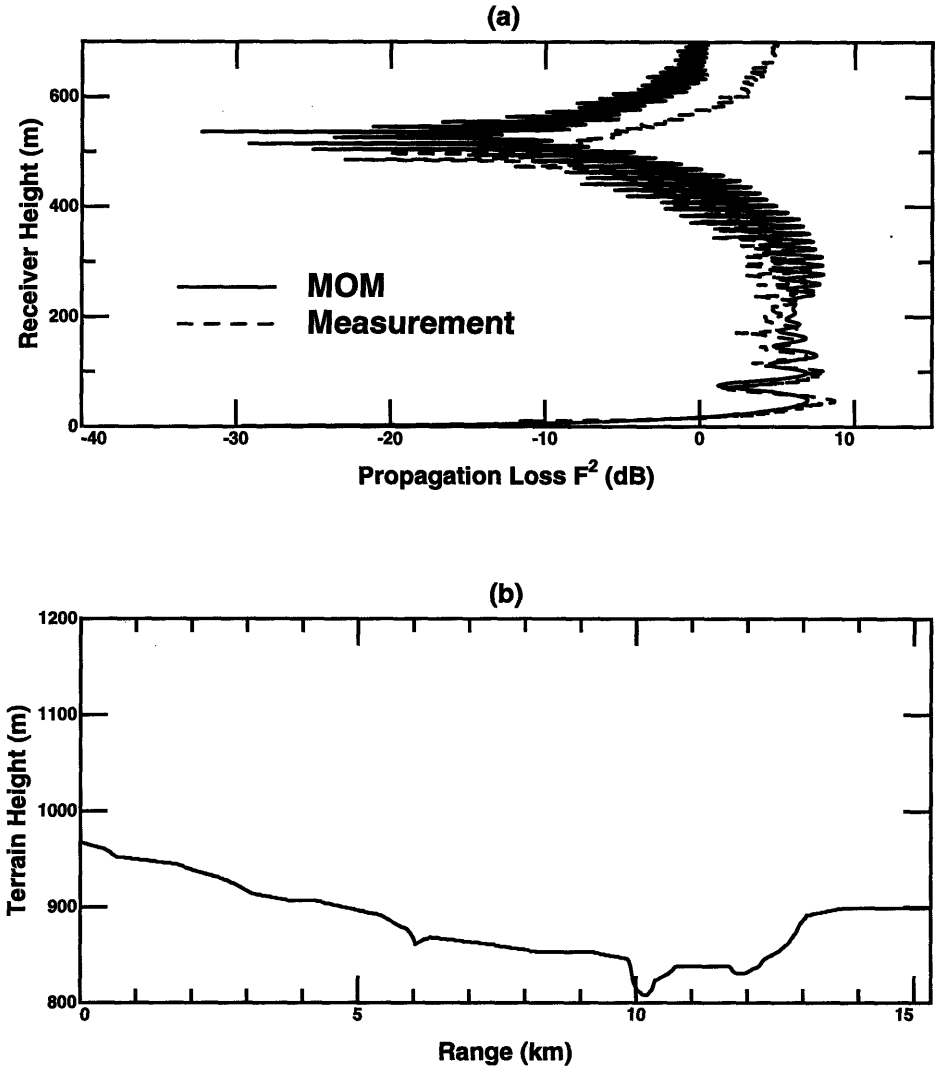

Figure 2.7: Comparison of MOM predictions with measurement data (a) excess one way propagation loss (b) Beiseker N15 terrain profile

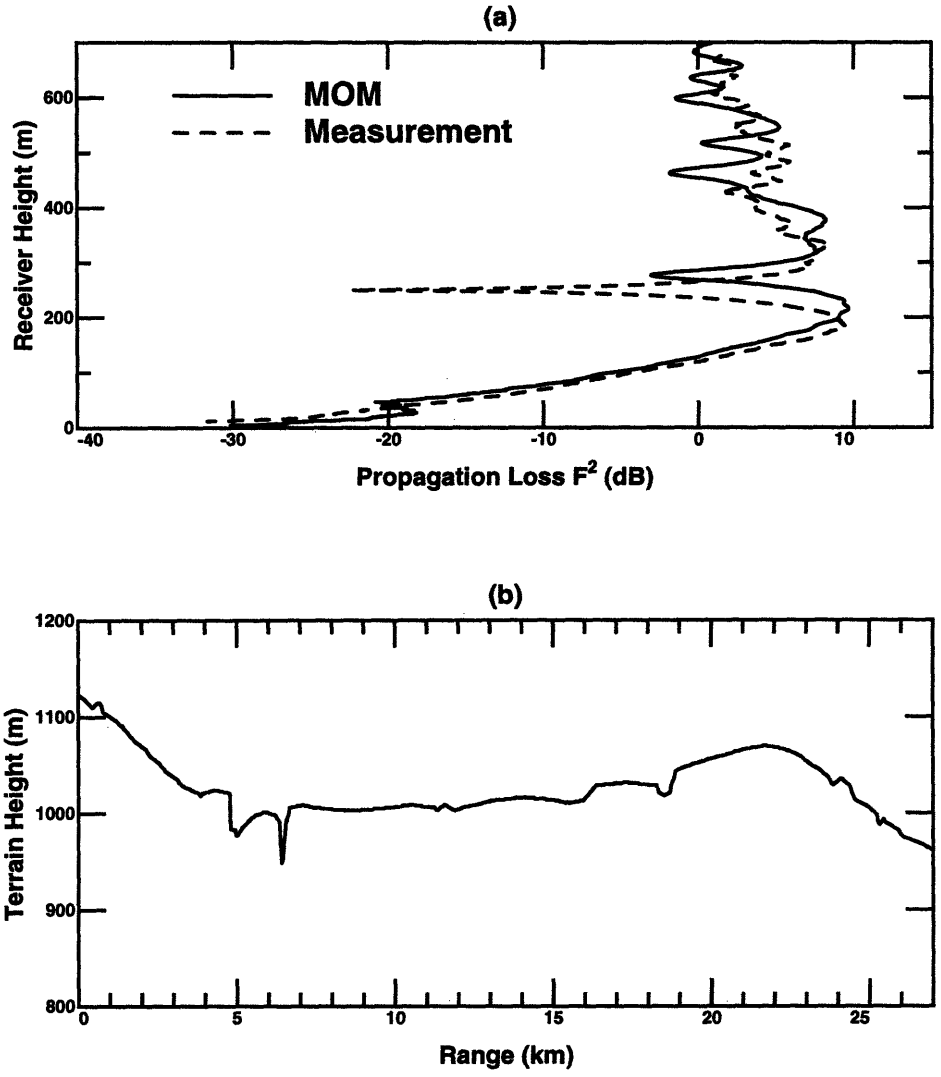

Figure 2.8: Comparison of MOM predictions with measurement data (a) excess one way propagation loss (b) Magrath NW27 terrain profile

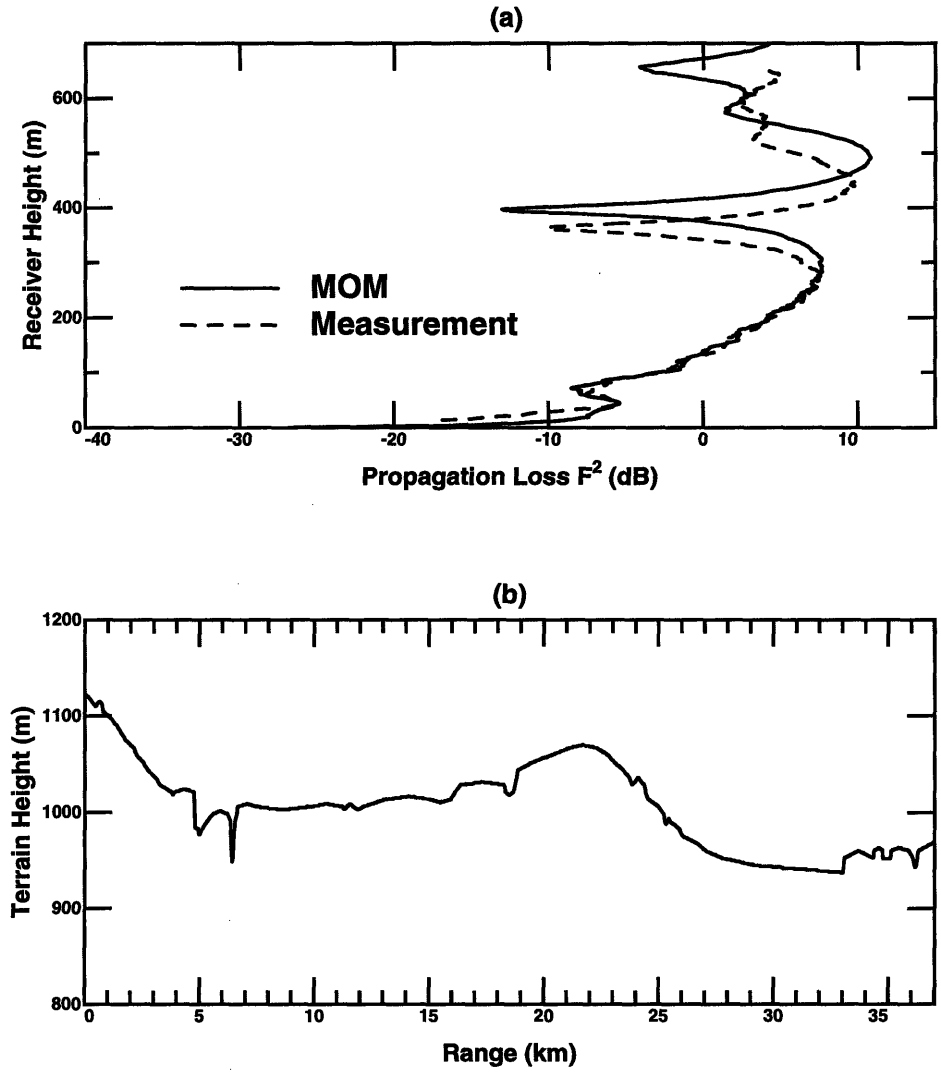

Figure 2.9: Comparison of MOM predictions with measurement data (a) excess one way propagation loss (b) Magrath NW37 terrain profile

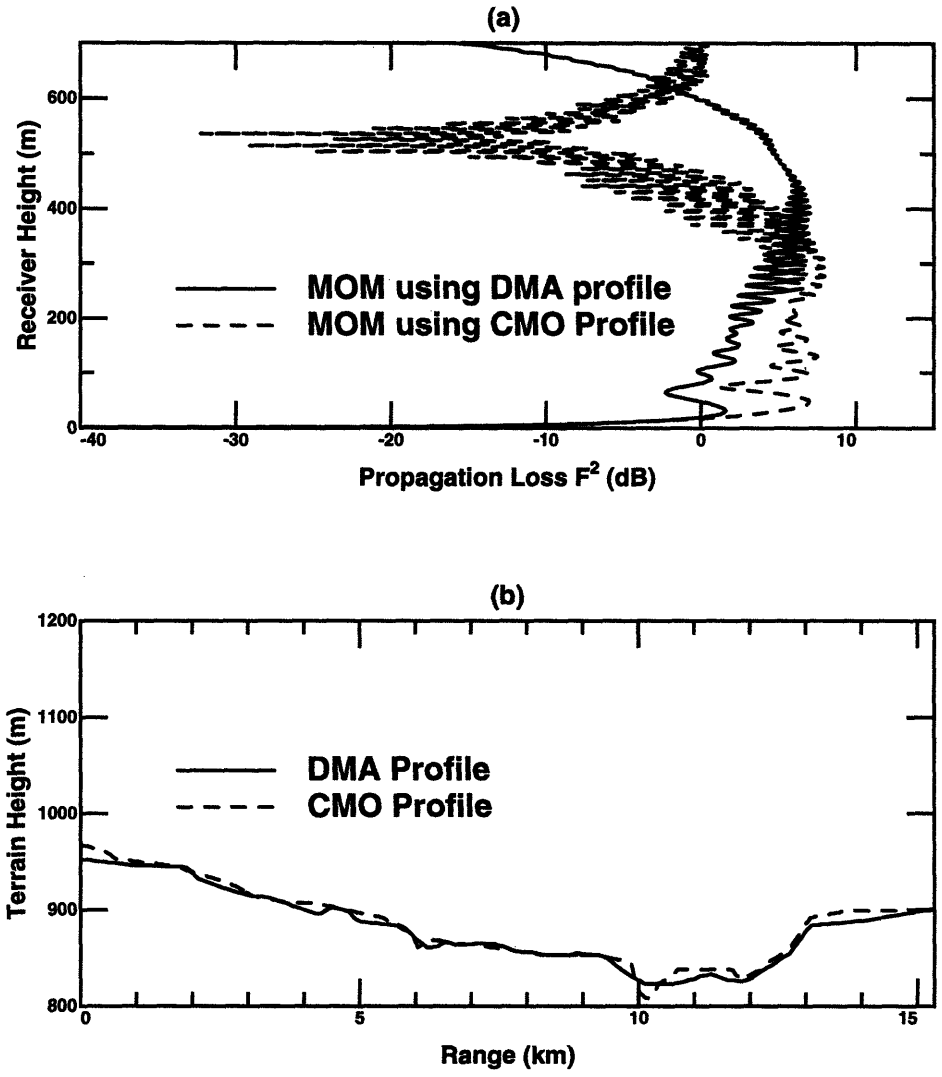

Figure 2.10: Variation of predictions with input terrain profile (a) excess one way propagation loss (b) Beiseker N15 terrain profiles

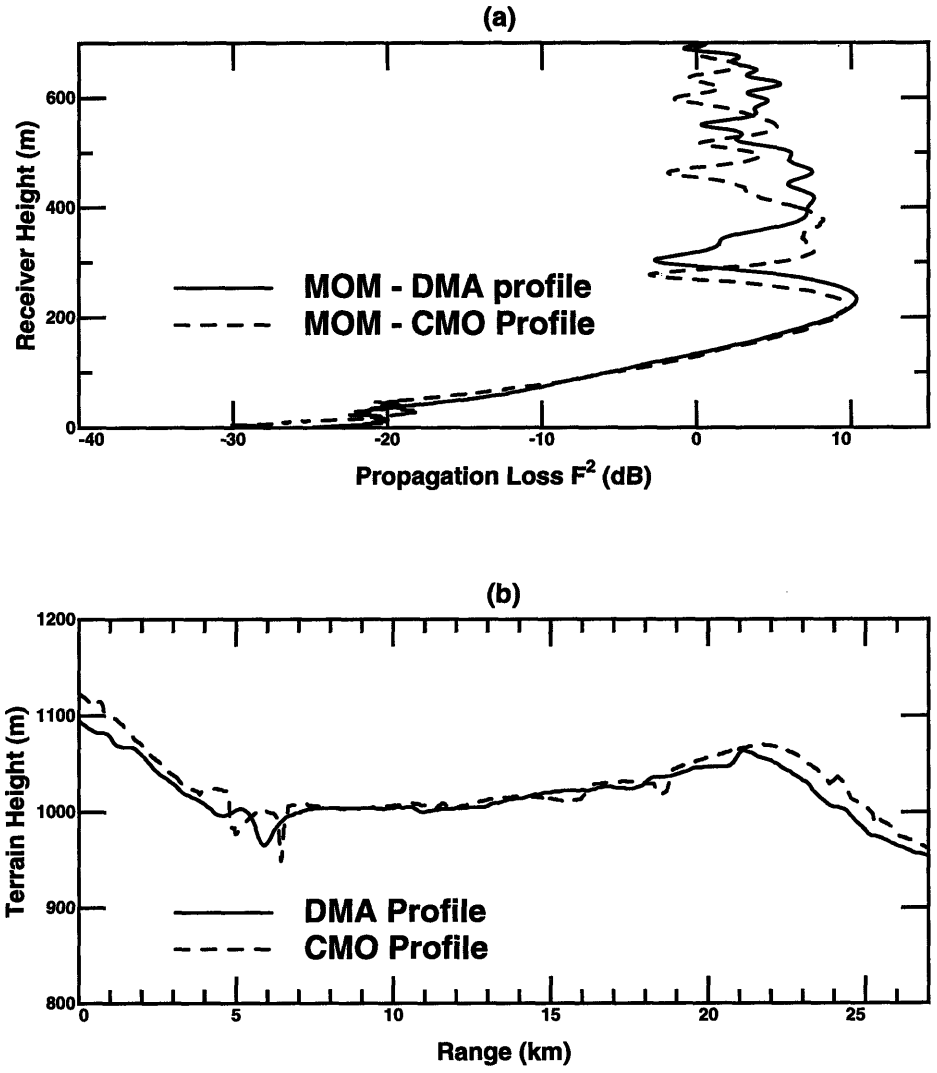

Figure 2.11: Variation of predictions with input terrain profile (a) excess one way propagation loss (b) Magrath NW27 terrain profiles

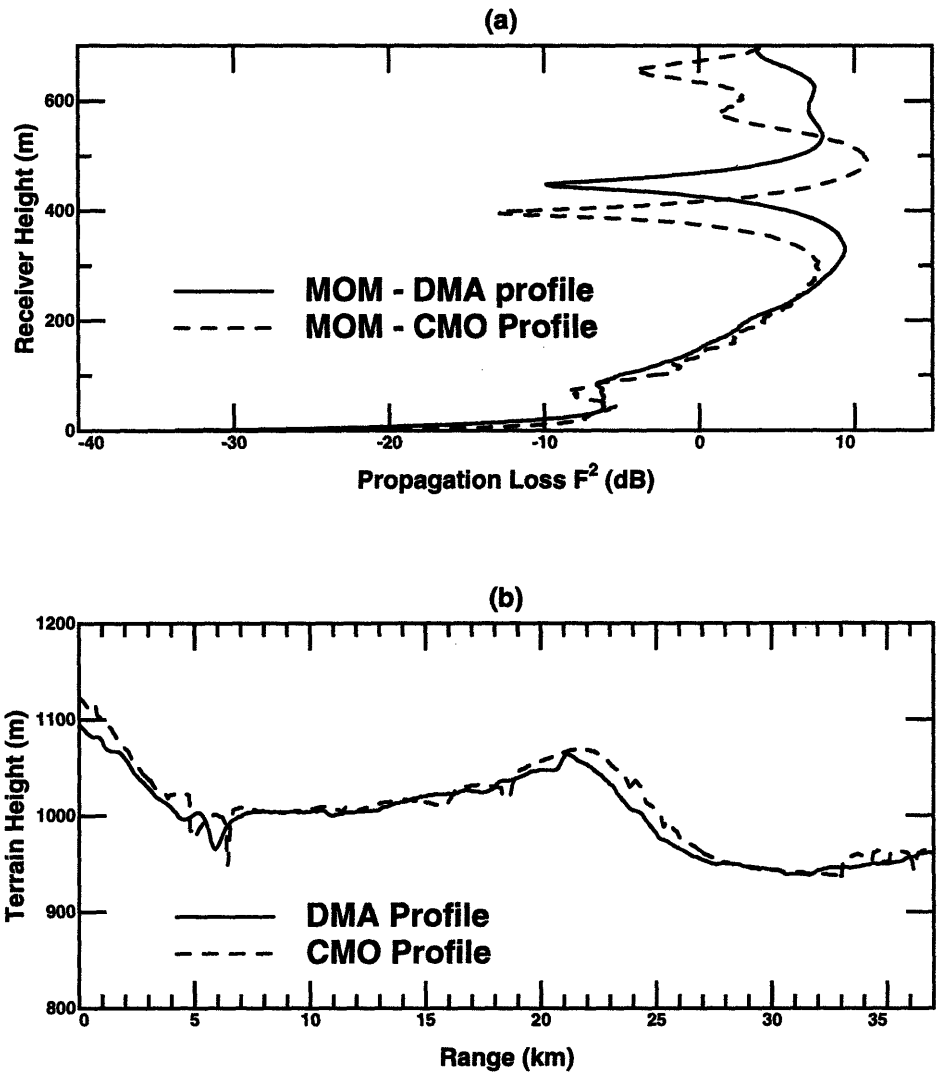

Figure 2.12: Variation of predictions with input terrain profile (a) excess one way propagation loss (b) Magrath NW37 terrain profiles

three methods, demonstrating that the PWE and SEKE models are giving an accurate prediction for the terrain profile input. However, some differences are observed which illustrate the limitations of the SEKE and PWE methods.

SEKE predictions become inaccurate in cases where both multipath and diffraction contributions are significant, and underestimate the strength of the first maximum above the shadowed region in particular as shown in Figures 2.14 and 2.15. Similar underestimations are observed for knife edge diffraction routines in reference [74] when compared to wedge diffraction. Inaccuracies in SEKE's spherical and knife edge diffraction weighting algorithm are seen in low altitude regions (less than 20 m) as well, although improvements to SEKE for clutter modeling in this region have been studied and are currently being implemented [76]. SEKE also fails to obtain the small maximum at receiver height approximately 50 m in Figures 2.14 and 2.15, which the PWE shows to be due to a bounce from a wave diffracted by the hill in the Magrath profile. Finally, the discrete nature of SEKE's routines is evident in Figure 2.13 (a), where the multiple specular contribution abruptly begins at receiver height 200 m and is neglected below.

Agreement between PWE and MOM predictions is remarkable throughout Figures 2.13 to 2.15, and illustrates the accuracy of the paraxial approximation for the terrain profiles investigated. The high accuracy of PWE results and their additional ability in modeling atmospheric structure clearly favors use of the PWE for propagation predictions. One disadvantage associated with the PWE is sensitivity to parameters used in the numerical simulation such as computational domain size, width of the initial field distribution, and properties of the upper absorbing bound-

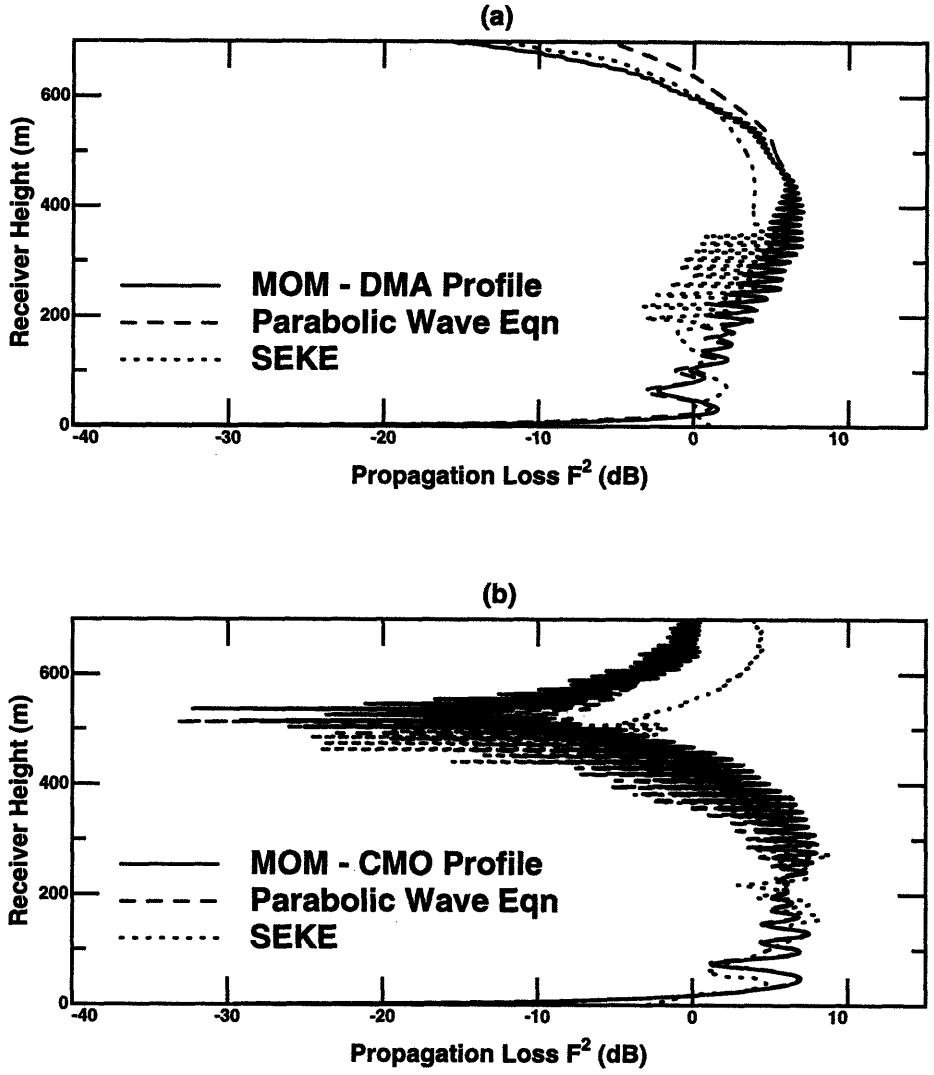

Figure 2.13: Comparison with analytic models - Beiseker N15 (a) DMA terrain profile (b) CMO terrain profile

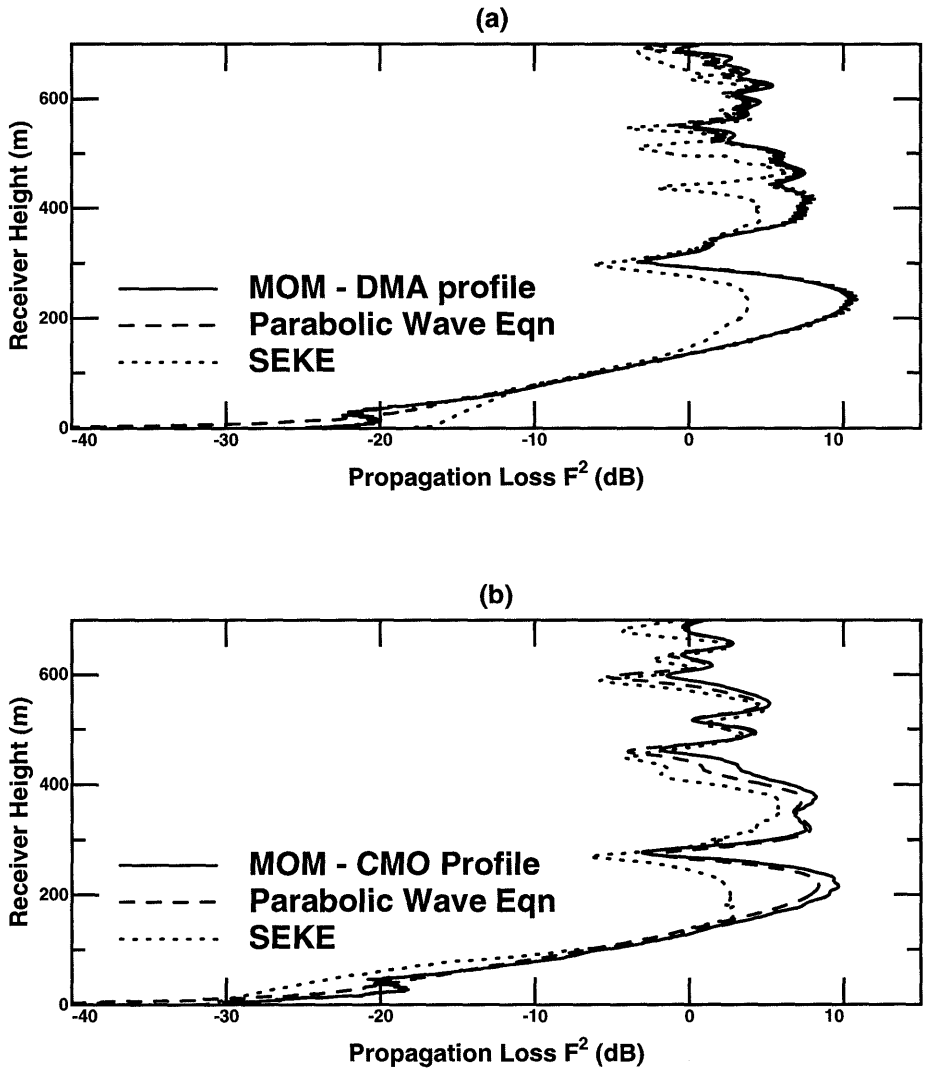

Figure 2.14: Comparison with analytic models - Magrath NW27 (a) DMA terrain profile (b) CMO terrain profile

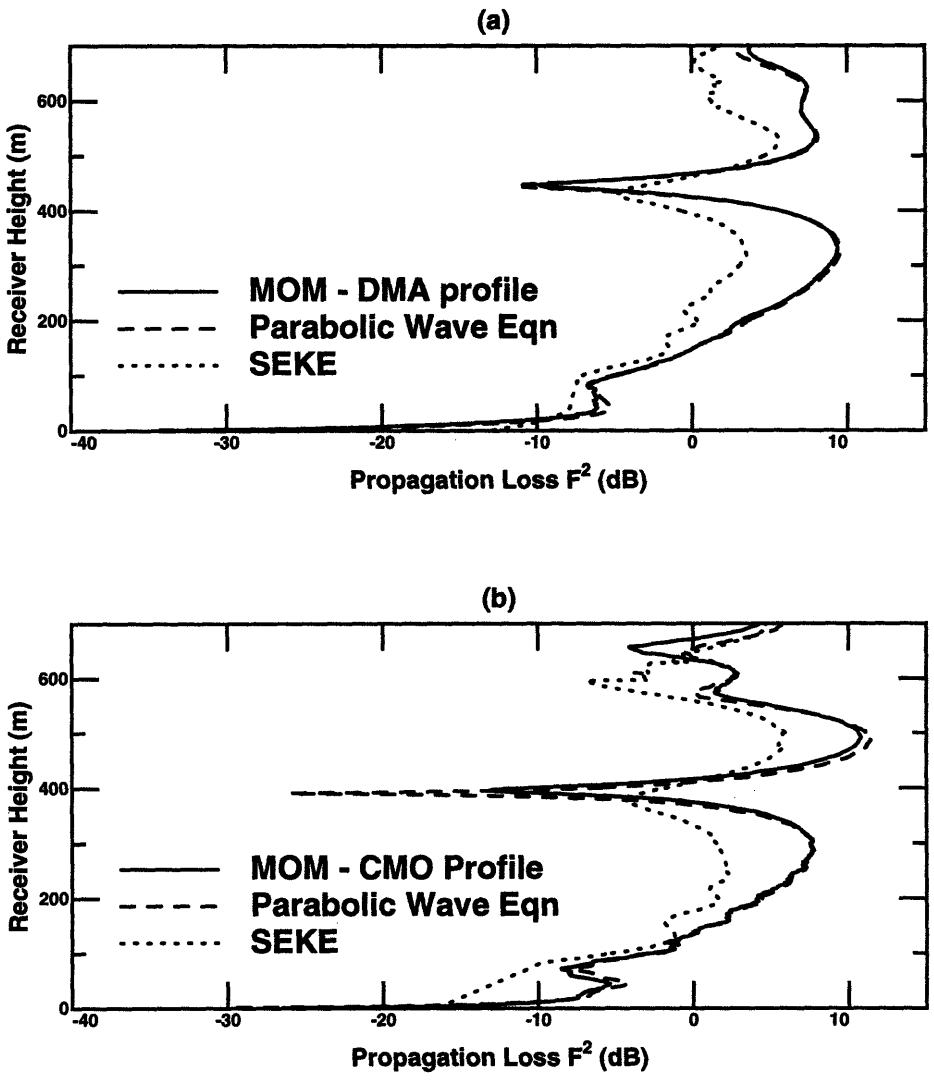

Figure 2.15: Comparison with analytic models - Magrath NW37 (a) DMA terrain profile (b) CMO terrain profile

ary. For example, predictions generated for the Beiseker N15 profile of Figure 2.13 were originally found inaccurate when a fairly narrow initial beam was used. Use of a wider initial field distribution eliminated these problems, but caused errors due to spurious reflections from the 500 m fixed Gaussian taper computational domain upper boundary in longer range problems such as Magrath NW37. Although these errors were subsequently eliminated by doubling computational domain height from 8192 to 16384 m for Magrath NW37, an appropriate choice of numerical simulation parameters is clearly required if reliable predictions are desired from the PWE. However, the relatively small amount of computational time required for the PWE makes an iterative procedure to determine simulation parameters feasible, and the results of this study show that an iterated PWE technique should be a very accurate and practical tool for propagation prediction.

2.7 Conclusions

A numerically exact model for VHF propagation based on an iterative version of the method of moments has been developed. While this model remains computationally intense, its usefulness has been demonstrated in validating and studying the limitations of other approximate methods. Results have been shown which illustrate the accuracy of the numerical method, and which show the sensitivity of propagation models to input terrain profiles. Comparisons with the SEKE and PWE models showed that these models overall give reliable predictions except in cases where underlying approximations become invalid. SEKE was found to follow the overall trends of the method of moments in all cases, but to have problems in predicting propagation

loss in regions where multiple phenomena were important. Agreement with the PWE was found to be excellent in all cases after steps were taken to insure that initial field distributions and computational domain sizes were appropriate.

Chapter 3

Scattering and Thermal Emission From a Two Dimensional Periodic Surface

3.1 Introduction

Scattering from a one dimensional periodic surface has been studied extensively with a large number of techniques, including both approximate [7]-[8],[77], and numerically exact [78]-[85] methods. Models for one dimensional periodic surface scattering have found application in a wide range of areas, ranging from optical grating design [82] to the prediction of wave propagation over the ocean [84]. In a more recent application, theories and experiments involving passive remote sensing of one dimensional periodic surfaces [85]-[90] have conclusively demonstrated the existence of a third Stokes parameter component of the thermal emission, U_B. Assumed to be non-zero only in polarimetric passive remote sensing, U_B is known to respond to the azimuthal anisotropy of the medium under view [5] and thus is currently being investigated for application to remote sensing of wind direction over the ocean [91]-[94].

The one dimensional periodic surface studies previously performed allow surfaces to be rough in one spatial direction only. Surface profiles do not vary perpendicular to this direction, so that a "row" type structure results as shown in Figure 3.1. While there are many interesting surfaces which do have a row structure, more general surfaces vary in two spatial directions as shown in Figure 3.2 and therefore render the one dimensional models invalid. Scattering from two dimensional periodic surfaces has previously been studied in reference [95], in which a volume equivalent current moment method was applied to investigate the reflection characteristics of microwave absorbing materials. However, to date no numerically exact results for two dimensional surface polarimetric thermal emission have been presented, so that the extension of U_B properties observed in the one dimensional case to the two dimensional case remains uncertain. For example, a one dimensional periodic surface model allows no insight into the effect of varying levels of surface azimuthal anisotropy on U_B signatures since a one dimensionally rough surface represents only a limiting case of anisotropy.

In this chapter, a numerically exact model for scattering from a two dimensional dielectric periodic surface is presented, based upon an extension of the extended boundary condition (EBC) technique for one dimensional periodic surfaces [81] to the two dimensional case. Although the limitations of the EBC method for surfaces with deep corrugations are well known [96], previous one dimensional periodic surface studies showed the EBC to perform efficiently for non-steep surfaces when compared to a method of moments approach [90]. Use of the EBC method for two dimensional surface profiles is motivated by the fact that computational requirements are much

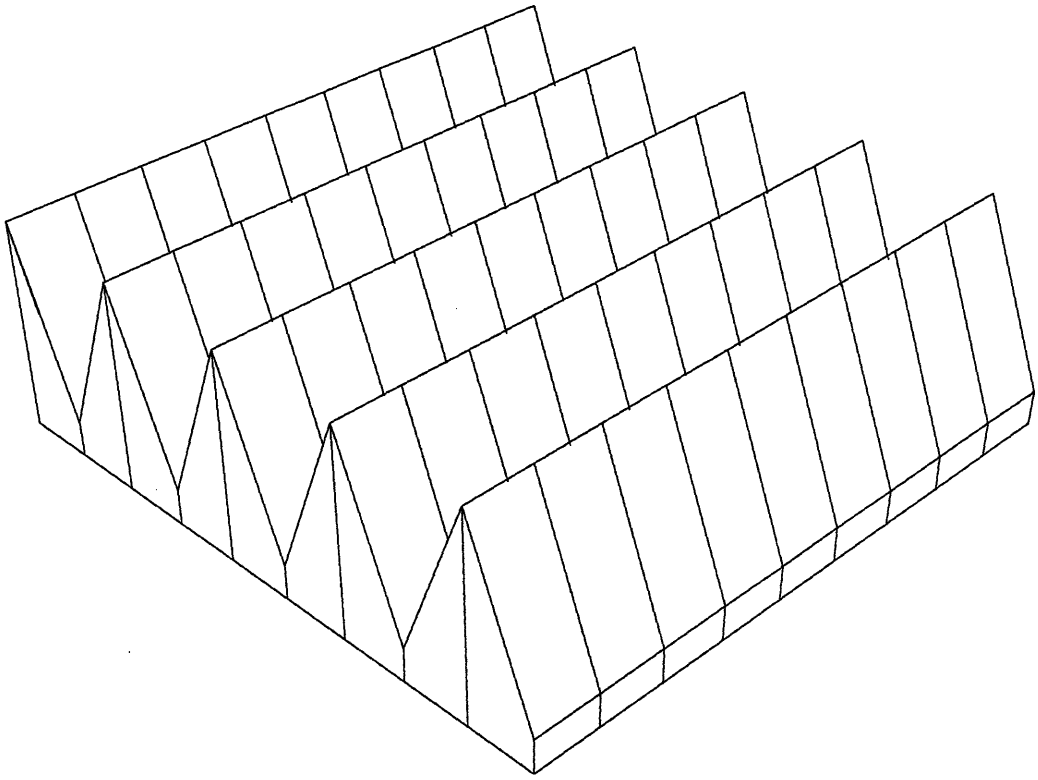

Figure 3.1: Geometry of a one dimensional periodic surface

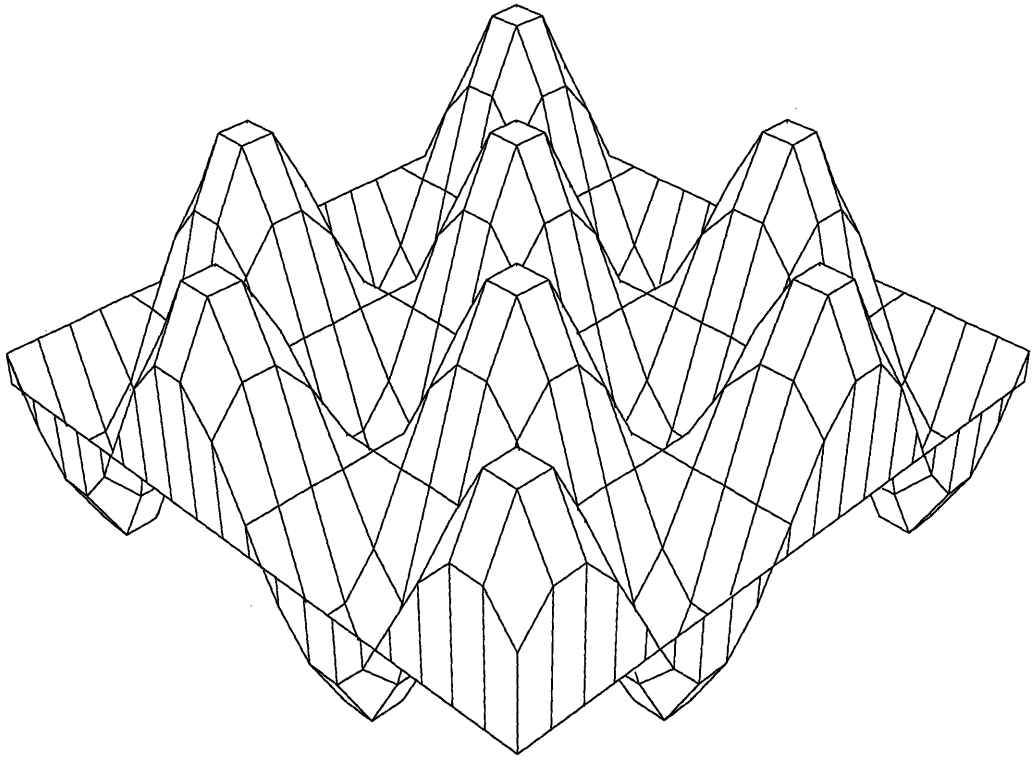

Figure 3.2: Geometry of a two dimensional periodic surface

greater than in the one dimensional case, so that efficiency becomes an even more important issue if a thorough study is to be performed. Since properties of U_B for two dimensional surfaces can be studied within the limitations of the EBC, the method is adequate for the goals of this chapter. Computational efficiency is further improved by performing required integrals analytically over an arbitrary faceted surface profile.

The model is applied in a study of the response of U_B to the level of anisotropy of the medium under view. Calculations are performed for simple pyramidal surfaces, which reduce computational complexity and provide physical insight into the mechanisms which generate third Stokes parameter emission. Sensitivities of U_B to observation angle, pyramidal surface heights and lengths, and surface dielectric constants are studied, and illustrate that properties of U_B observed for one dimensional periodic surfaces remain similar in the two dimensional case.

The formulation of the extended boundary condition method is detailed in the next section, followed by a discussion of required integral evaluation in Section 3.3. The model is validated in Section 3.4 through reduction to the one dimensional periodic surface case, and convergence of predicted brightnesses with the number of surface field unknowns is discussed for two dimensional surfaces. A study of pyramidal surface polarimetric thermal emission in Section 3.5 is followed by conclusions in Section 3.6.

3.2 Formulation and Numerical Method

The extended boundary condition technique for periodic surface scattering involves solution of the Huygens' principle type integral equations for unknown tangential electric and magnetic fields on a surface separating two homogeneous dielectric regions of space, labeled regions 0 and 1, as discussed in Chapter 1. The standard electric field integral equation (EFIE) can be written as

$$\int_{-\infty}^{\infty} dS' \left\{ i\omega\mu \left(\overline{\overline{I}} + \frac{\nabla\nabla}{k_0^2} \right) g_0(\overline{r},\overline{r}')[\hat{n}' \times \overline{H}(\overline{r}')] + \nabla g_0(\overline{r},\overline{r}') \times [\hat{n}' \times \overline{E}(\overline{r}')] \right\}$$

$$+\overline{E}_{inc}(\overline{r}) = \begin{cases} \overline{E}_0(\overline{r}) & z > z_s(x,y) \\ 0 & z < z_s(x,y) \end{cases} \tag{3.1}$$

where $\overline{E}_{inc}$ represents the incident electric field, taken to be a single incident plane wave with propagation vector $\overline{k}_i = \hat{x}k_{xi} + \hat{y}k_{yi} + \hat{z}k_{zi}$ in the following discussions, and $z_s(x,y)$ is a function describing the surface profile separating regions 0 and 1. It is assumed that the observation point $\overline{r}$ does not coincide with any of the source points $\overline{r}'$ in the integral equation, so that no singularities are encountered. The scalar Green's function in the above equation is

$$g_j(\overline{r},\overline{r}') = \frac{e^{ik_j|\overline{r}-\overline{r}'|}}{4\pi|\overline{r}-\overline{r}'|} \tag{3.2}$$

where k_j represents the electromagnetic wave number in regions $j = 0$ or $j = 1$ respectively. A similar integral equation can be written for the electric field in the

region below the surface,

$$-\int_{-\infty}^{\infty} dS' \left\{ i\omega\mu \left(\overline{\overline{I}} + \frac{\nabla\nabla}{k_1^2} \right) g_1(\overline{r},\overline{r}')[\hat{n}' \times \overline{H}(\overline{r}')] + \nabla g_1(\overline{r},\overline{r}') \times [\hat{n}' \times \overline{E}(\overline{r}')] \right\}$$
$$= \begin{cases} \overline{E}_1(\overline{r}) & z < z_s(x,y) \\ 0 & z > z_s(x,y) \end{cases} \tag{3.3}$$

If the surface height function is assumed to be periodic in both the x and y directions, so that $z_s(x+P_x,y) = z_s(x,y)$ and $z_s(x,y+P_y) = z_s(x,y)$, integration regions in the above integral equations can be reduced to a single period through the use of a periodic Green's function. Such Green's functions are well known and have been derived elsewhere [3] as

$$g_{Pj} = \frac{i}{P_x P_y} \sum_{m=-\infty}^{\infty} \sum_{n=-\infty}^{\infty} \frac{1}{2k_{zj_{mn}}} e^{i[k_{xn}(x-x')+k_{ym}(y-y')+k_{zj_{mn}}|z-z'|]} \tag{3.4}$$

where the spectral form of the periodic Green's function has been used, $k_{xn} = k_{xi} + \frac{2\pi n}{P_x}$, $k_{ym} = k_{yi} + \frac{2\pi m}{P_x}$ and $k_{zj_{mn}} = \sqrt{k_j^2 - k_{xn}^2 - k_{ym}^2}$. The branch cut of the square root function for $k_{zj_{mn}}$ is defined so that $\sqrt{-1} = +i$. Upon substitution of this Green's function into the integral equations, and assuming observation points above or below the points of maximum and minimum surface height respectively, integral equations (3.1) and (3.3) become

$$\overline{E}_{inc}(\overline{r}) + \sum_{m=-\infty}^{\infty} \sum_{n=-\infty}^{\infty} \overline{a}_{mn} e^{i\overline{k}_{mn0}^{+}\cdot\overline{r}} = \overline{E}_0(\overline{r}) \qquad z > z_s(x,y)_{max} \tag{3.5}$$

$$\overline{E}_{inc}(\overline{r}) + \sum_{m=-\infty}^{\infty} \sum_{n=-\infty}^{\infty} \overline{b}_{mn} e^{i\overline{k}^{-}_{mn0}\cdot\overline{r}} = 0 \qquad z < z_s(x,y)_{min} \tag{3.6}$$

$$\sum_{m=-\infty}^{\infty} \sum_{n=-\infty}^{\infty} \overline{c}_{mn} e^{i\overline{k}^{-}_{mn1}\cdot\overline{r}} = -\overline{E}_1(\overline{r}) \qquad z < z_s(x,y)_{min} \tag{3.7}$$

$$\sum_{m=-\infty}^{\infty} \sum_{n=-\infty}^{\infty} \overline{d}_{mn} e^{i\overline{k}^{+}_{mn1}\cdot\overline{r}} = 0 \qquad z > z_s(x,y)_{max} \tag{3.8}$$

where

$$\bar{a}_{mn} = \frac{i}{2P_xP_yk_{z0_{mn}}} \int_P dS' e^{-i\overline{k}^{+}_{mn0}\cdot\overline{r}} \left\{ i\omega\mu \left(\overline{\overline{I}} - \hat{k}^{+}_{mn0}\hat{k}^{+}_{mn0}\right) [\hat{n}' \times \overline{H}(\overline{r}')] + i\overline{k}^{+}_{mn0} \times [\hat{n}' \times \overline{E}(\overline{r}')] \right\} \tag{3.9}$$

$$\bar{b}_{mn} = \frac{i}{2P_xP_yk_{z0_{mn}}} \int_P dS' e^{-i\overline{k}^{-}_{mn0}\cdot\overline{r}} \left\{ i\omega\mu \left(\overline{\overline{I}} - \hat{k}^{-}_{mn0}\hat{k}^{-}_{mn0}\right) [\hat{n}' \times \overline{H}(\overline{r}')] + i\overline{k}^{-}_{mn0} \times [\hat{n}' \times \overline{E}(\overline{r}')] \right\} \tag{3.10}$$

$$\bar{c}_{mn} = \frac{i}{2P_xP_yk_{z1_{mn}}} \int_P dS' e^{-i\overline{k}^{-}_{mn1}\cdot\overline{r}} \left\{ i\omega\mu \left(\overline{\overline{I}} - \hat{k}^{-}_{mn1}\hat{k}^{-}_{mn1}\right) [\hat{n}' \times \overline{H}(\overline{r}')] + i\overline{k}^{-}_{mn1} \times [\hat{n}' \times \overline{E}(\overline{r}')] \right\} \tag{3.11}$$

$$\bar{d}_{mn} = \frac{i}{2P_xP_yk_{z1_{mn}}} \int_P dS' e^{-i\overline{k}^+_{mn1}\cdot\overline{r}} \left\{ i\omega\mu \left(\overline{\overline{I}} - \hat{k}^+_{mn1}\hat{k}^+_{mn1} \right) [\hat{n}' \times \overline{H}(\overline{r}')] + i\overline{k}^+_{mn1} \times [\hat{n}' \times \overline{E}(\overline{r}')] \right\} \tag{3.12}$$

and

$$\overline{k}^{\pm}_{mnj} = \hat{x}k_{xn} + \hat{y}k_{ym} \pm \hat{z}k_{zj_{mn}}$$

From equations (3.5) and (3.7), it is clear that the scattered field in region zero above the surface profile and the transmitted field in region one below the surface profile consist of a sum of upgoing and downgoing plane wave fields respectively, known as Floquet modes, with unknown vector amplitudes $\overline{a}_{mn}$ and $\overline{c}_{mn}$. These unknown amplitudes can be determined from equations (3.9) and (3.11) once tangential electric and magnetic fields at the surface boundary are known.

The formulation of equations (3.1) to (3.12) is general for two dimensional periodic surfaces. The EBC approach is based upon solution of vector equations (3.6) and (3.8) for the unknown tangential electric and magnetic fields, which involve the regions of "no-interest" in the Huygens' formulation. Use of these equations is advantageous because a knowledge of both tangential fields on the surface profile and the total fields above or below the surface profile $\overline{E}_0$ and $\overline{E}_1$ is not required as in equations (3.5) and (3.7), and a simple mode matching technique can be applied to their solution. However, the non-local nature of equations (3.5) to (3.8) cause the

previously mentioned conditioning problems for steep surfaces, as evanescent waves generated within the surface profile are modeled only after having been exponentially attenuated.

Applying the orthogonality property for plane wave fields in equations (3.6) and (3.8) yields the following vector equations

$$\overline{b}_{mn} = -\hat{e}_i \delta_{mn0} \tag{3.13}$$

$$\overline{d}_{mn} = 0 \tag{3.14}$$

where δ_{mn0} is one for $m = n = 0$ and zero otherwise and a plane wave incident field of $\overline{E}_{inc} = \hat{e}_i e^{i\overline{k}_i \cdot \overline{r}}$ has been assumed. Next, unknown tangential fields on the surface profile are written as

$$\hat{n}' \times \overline{H} = \hat{x} J_x + \hat{y} J_y + \hat{z} \left(\frac{\partial z_s}{\partial x'} J_x + \frac{\partial z_s}{\partial y'} J_y \right)$$

$$-\hat{n}' \times \overline{E} = \hat{x} M_x + \hat{y} M_y + \hat{z} \left(\frac{\partial z_s}{\partial x'} M_x + \frac{\partial z_s}{\partial y'} M_y \right)$$

where

$$\hat{n}' = \left\{ \hat{z} - \frac{\partial z_s}{\partial x'} \hat{x} - \frac{\partial z_s}{\partial y'} \hat{y} \right\} / \sqrt{1 + \left(\frac{\partial z_s}{\partial x'} \right)^2 + \left(\frac{\partial z_s}{\partial y'} \right)^2}$$

and unknown surface field amplitudes are expanded in Fourier series as

$$J_x = \sum_o \sum_p q_{op} e^{ik_{xo}x' + ik_{yp}y'} \tag{3.15}$$

$$J_y = \sum_o \sum_p r_{op} e^{ik_{xo}x' + ik_{yp}y'} \tag{3.16}$$

$$M_x = -\sum_o \sum_p s_{op} e^{ik_{xo}x' + ik_{yp}y'} \tag{3.17}$$

$$M_y = -\sum_o \sum_p t_{op} e^{ik_{xo}x' + ik_{yp}y'} \tag{3.18}$$

Vector equations (3.13) and (3.14) each consist of one set of m times n equations for three Cartesian components. However, these six sets of equations are restricted to four by the divergenceless condition of plane wave fields. Using the x and y components of these equations and substituting in the Fourier series expansions (3.15-3.18) results in the following matrix equation:

$$\begin{bmatrix} \overline{\overline{A}}^{-}_{xx0} & \overline{\overline{A}}^{-}_{xy0} & \overline{\overline{B}}^{-}_{xx0} & \overline{\overline{B}}^{-}_{xy0} \\ \overline{\overline{A}}^{-}_{yx0} & \overline{\overline{A}}^{-}_{yy0} & \overline{\overline{B}}^{-}_{yx0} & \overline{\overline{B}}^{-}_{yy0} \\ \overline{\overline{A}}^{+}_{xx1} & \overline{\overline{A}}^{+}_{xy1} & \overline{\overline{B}}^{+}_{xx1} & \overline{\overline{B}}^{+}_{xy1} \\ \overline{\overline{A}}^{+}_{yx1} & \overline{\overline{A}}^{+}_{yy1} & \overline{\overline{B}}^{+}_{yx1} & \overline{\overline{B}}^{+}_{yy1} \end{bmatrix} \begin{bmatrix} q_{[op]} \\ r_{[op]} \\ s_{[op]} \\ t_{[op]} \end{bmatrix} = \begin{bmatrix} E_{x[mn]} \\ E_{y[mn]} \\ 0 \\ 0 \end{bmatrix} \tag{3.19}$$

where

$$\left[\overline{\overline{A}}^{\pm}_{\alpha\beta j}\right]_{[mn][op]} = \int_P dx'dy' \left\{ \frac{-\omega\mu}{2P_xP_yk_{zj_{mn}}} e^{-i(k_{xn}-k_{xo})x' - i(k_{ym}-k_{yp})y' - i(\pm k_{zj_{mn}})z'} \right. \tag{3.20}$$
$$\left. \sqrt{1+\left(\frac{\partial z_s}{\partial x'}\right)^2 + \left(\frac{\partial z_s}{\partial y'}\right)^2}\, \hat{\alpha}\cdot\left(\overline{\overline{I}} - \hat{k}^{\pm}_{mnj}\hat{k}^{\pm}_{mnj}\right)\cdot\left(\hat{\beta} + \hat{z}\frac{\partial z_s}{\partial \beta}\right) \right\}$$

$$\left[\overline{\overline{B}}^{\pm}_{\alpha\beta j}\right]_{[mn][op]} = \int_P dx'dy' \left\{ \frac{i}{2P_xP_yk_{zj_{mn}}} e^{-i(k_{xn}-k_{xo})x' - i(k_{ym}-k_{yp})y' - i(\pm k_{zj_{mn}})z'} \right.$$
$$\left. \sqrt{1+\left(\frac{\partial z_s}{\partial x'}\right)^2 + \left(\frac{\partial z_s}{\partial y'}\right)^2}\, i\hat{\alpha}\cdot\left[\overline{k}^{\pm}_{mnj}\times\left(\hat{\beta} + \hat{z}\frac{\partial z_s}{\partial \beta}\right)\right] \right\} \tag{3.21}$$

and

$$E_{\alpha[mn]} = -\hat{\alpha} \cdot \hat{e}_i \delta_{mn0} \tag{3.22}$$

In the above notation, $[mn]$ references the row number of the matrix, while $[op]$ references the column. These indices actually are a single number, which is obtained by consecutively labeling the set of m times n scattered modes in two dimensions and the set of o times p Fourier series coefficients. The above matrix equation is infinitely large in theory, but must be truncated in order to be inverted. Convergence of model predictions with the number of equations retained will be discussed in Section 3.4. Matrix elements can be calculated once the surface profile is specified, and the matrix can be inverted to obtain Fourier series expansion coefficients of unknown surface fields, q_{op}, r_{op}, s_{op}, and t_{op}. These expansion coefficients can then be substituted into equations (3.9) and (3.11), which involve integrals similar to the matrices $\overline{\overline{A}}$ and $\overline{\overline{B}}$ above, to determine vector amplitudes of the reflected and transmitted Floquet modes, $\overline{a}_{[mn]}$ and $\overline{c}_{[mn]}$ respectively, as

$$\begin{bmatrix} \overline{\overline{A}}^{+}_{xx0} & \overline{\overline{A}}^{+}_{xy0} & \overline{\overline{B}}^{+}_{xx0} & \overline{\overline{B}}^{+}_{xy0} \\ \overline{\overline{A}}^{+}_{yx0} & \overline{\overline{A}}^{+}_{yy0} & \overline{\overline{B}}^{+}_{yx0} & \overline{\overline{B}}^{+}_{yy0} \\ \overline{\overline{A}}^{-}_{xx1} & \overline{\overline{A}}^{-}_{xy1} & \overline{\overline{B}}^{-}_{xx1} & \overline{\overline{B}}^{-}_{xy1} \\ \overline{\overline{A}}^{-}_{yx1} & \overline{\overline{A}}^{-}_{yy1} & \overline{\overline{B}}^{-}_{yx1} & \overline{\overline{B}}^{-}_{yy1} \end{bmatrix} \begin{bmatrix} q_{[op]} \\ r_{[op]} \\ s_{[op]} \\ t_{[op]} \end{bmatrix} = \begin{bmatrix} a_{x[mn]} \\ a_{y[mn]} \\ c_{x[mn]} \\ c_{y[mn]} \end{bmatrix} \tag{3.23}$$

Components of $\overline{a}_{[mn]}$ and $\overline{c}_{[mn]}$ in the $\hat{z}$ direction are obtained from the divergence condition as

$$a_{z[mn]} = -\frac{1}{k_{z0_{mn}}} \left(k_{xn} a_{x[mn]} + k_{ym} a_{y[mn]} \right)$$

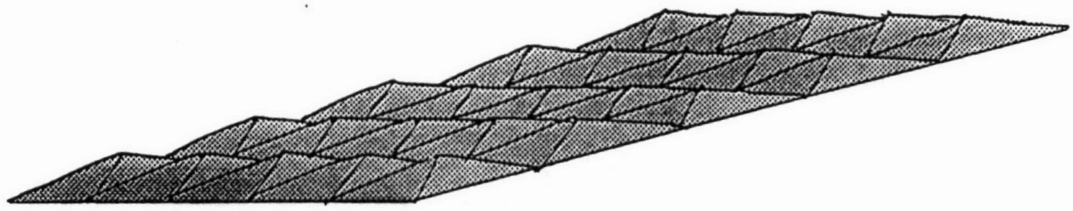

Figure 3.3: Geometry of a two dimensional pyramidal surface

$$c_{z[mn]} = \frac{1}{k_{z1_{mn}}} \left(k_{xn} c_{x[mn]} + k_{ym} c_{y[mn]} \right)$$

3.3 Evaluation of Required Integrals

Construction of matrix equation (3.19) requires evaluation of the integrals of (3.20) and (3.21) for each combination of $[mn]$ and $[op]$ indices. There are many options for evaluating these integrals, ranging from a fully numerical integration scheme to an FFT based method in which the $e^{-i(\pm k_{zj_{mn}})z'}$ term inside the integral is expanded in a Fourier series. In this chapter, a method in which the surface profile is assumed to be made up of triangular facets is adopted, and resulting integrals over individual surface facets are performed analytically. This approach should be an efficient technique for surfaces that are accurately described in terms of a small number of triangular facets, such as the pyramidal type surface illustrated in Figure 3.3.

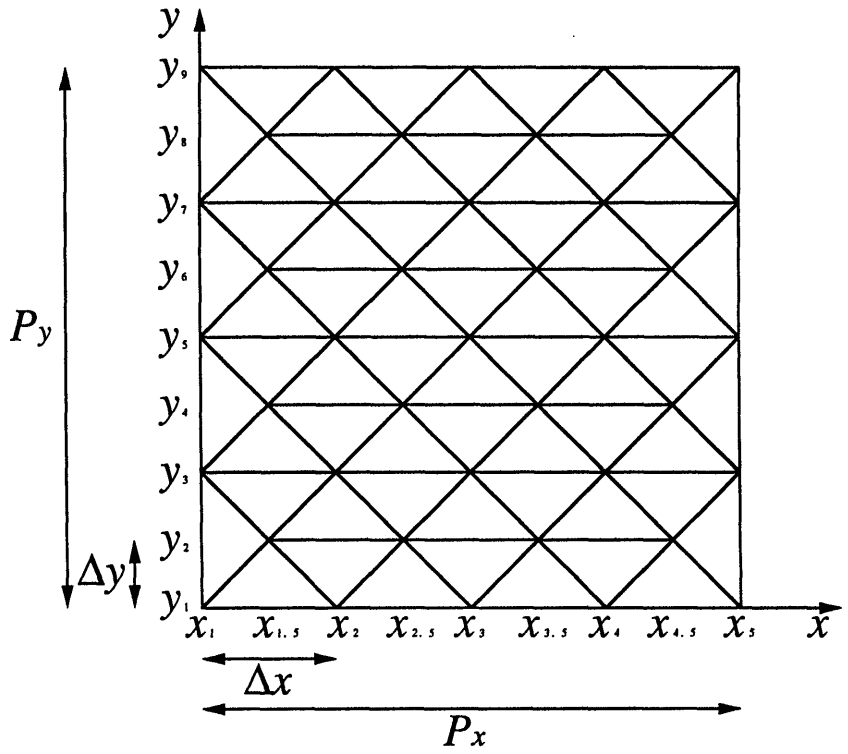

Figure 3.4: Triangular grid in $x-y$ plane for surface specification

Consider a triangular grid in the $x-y$ plane, shown in Figure 3.4, for which surface heights above the $x-y$ plane are specified at each of the points $x_\gamma = (\gamma-1)\Delta x$, $y_\delta = (\delta-1)\Delta y$ on the grid, with $\gamma = 1, 3/2, 2, \ldots$ and $\delta = 1, 2, 3, \ldots$. A 4×8 point grid is assumed in Figure 3.4, with the lines $x = x_5$ and $y = y_9$ equivalent to $x = x_1$ and $y = y_1$ respectively due to surface periodicities. The particular structure of the grid in Figure 3.4 is chosen to enable simple construction of pyramidal type surfaces, as will be discussed in the Section 3.5.

Since the integrals of (3.20) and (3.21) are over one period of the surface profile, matrix elements can be rewritten as a sum of the integrals over each individual triangular facet making up the profile. In addition, surface derivatives, $\frac{\partial z_s}{\partial x'}$ and $\frac{\partial z_s}{\partial y'}$

remain constant on an individual planar surface facet, so that vector product terms can be factored out of facet integrals. The resulting matrix elements are

$$\left[\overline{\overline{A}}^{\pm}_{\alpha\beta j}\right]_{[mn][op]} = \frac{-\omega\mu}{2P_xP_yk_{zj_{mn}}}\sum_f\left\{\sqrt{1+\left(\frac{\partial z_s}{\partial x'}\right)^2+\left(\frac{\partial z_s}{\partial y'}\right)^2}\left[\hat{\alpha}\cdot\left(\overline{\overline{I}}-\hat{k}^{\pm}_{mnj}\hat{k}^{\pm}_{mnj}\right)\cdot\right.\right.$$

$$\left.\left.\cdot\left(\hat{\beta}+\hat{z}\frac{\partial z_s}{\partial\beta}\right)\right]\int_{F_f}dx'dy'e^{-i(k_{xn}-k_{xo})x'-i(k_{ym}-k_{yp})y'-i(\pm k_{zj_{mn}})z'}\right\} \tag{3.24}$$

$$\left[\overline{\overline{B}}^{\pm}_{\alpha\beta j}\right]_{[mn][op]} = \frac{i}{2P_xP_yk_{zj_{mn}}}\sum_f\left\{\sqrt{1+\left(\frac{\partial z_s}{\partial x'}\right)^2+\left(\frac{\partial z_s}{\partial y'}\right)^2}\right.$$

$$\left.i\hat{\alpha}\cdot\left[\overline{k}^{\pm}_{mnj}\times\left(\hat{\beta}+\hat{z}\frac{\partial z_s}{\partial\beta}\right)\right]\int_{F_f}dx'dy'e^{-i(k_{xn}-k_{xo})x'-i(k_{ym}-k_{yp})y'-i(\pm k_{zj_{mn}})z'}\right\} \tag{3.25}$$

where F_f indicates the particular facet over which the integral is to be performed. From the above equations, it is clear that evaluation of the sixteen matrix elements for each $[mn]$ and $[op]$ combination actually requires calculation of only two integrals for each surface facet.

The surface profile of each triangular facet is simply a plane passing through the three points bounding the triangle. The equation of this plane is

$$z' = ax' + by' + c \tag{3.26}$$

where

$$a = \frac{z_2 - z_1}{\Delta x}$$

$$b = \frac{z_3 - (z_2 + z_1)/2}{\Delta y}$$

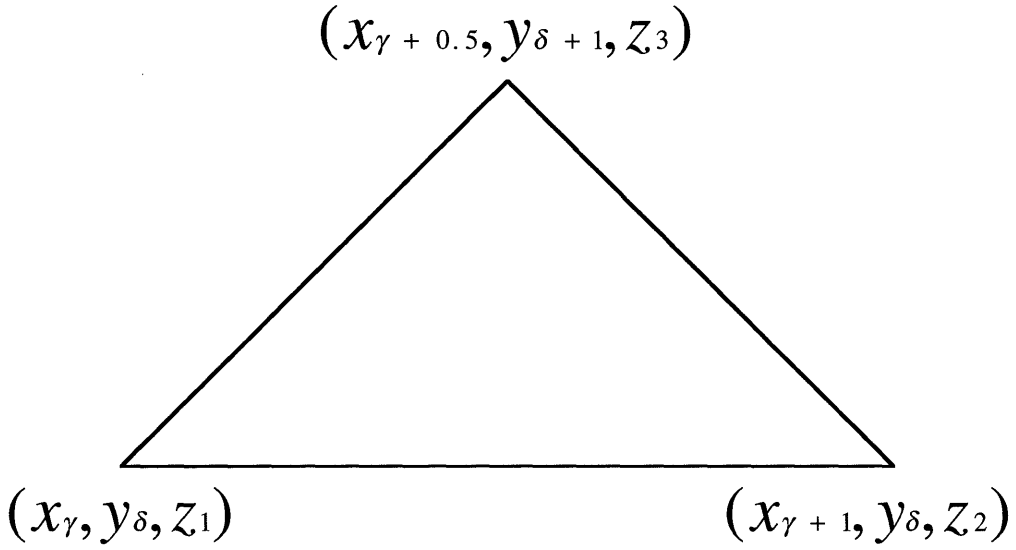

Figure 3.5: Definition of surface plane through triangle

$$c = z_1 - ax_\gamma - by_\delta$$

and z_1, z_2, z_3, x_γ, and y_δ are as defined in Figure 3.5.

Upon substitution of this equation for z' into (3.24) and (3.25), integrals over each surface facet can be performed analytically. The necessary integrals are

$$I^{\pm}_{\gamma\delta} = e^{-i(\pm k_{zjmn} c)} \int_{F_f} dx'dy' e^{-t_2 x' - t_1 y'} \tag{3.27}$$

where

$$t_1 = i(k_{ym} - k_{yp} \pm k_{zj_{mn}} b)$$

$$t_2 = i(k_{xn} - k_{xo} \pm k_{zj_{mn}} a)$$

and the domain of the integral corresponds to triangles on the grid of Figure 3.4. A closer examination of Figure 3.4 reveals that there are four types of triangular domains to be considered, isolated and referred to as triangles u, d, l, and r in Figure 3.6, each with a unique domain and definition of a, b, and c. Integrals for each of these triangles must be performed separately. In addition, integrals for the special cases of $t_1 = 0, t_2 \neq 0$ and $t_1 \neq 0, t_2 = 0$ must be considered. Results of these integrations are

Triangle u :

$t_1 = 0, t_2 \neq 0$

$$I^{\pm}_{\gamma\delta} = \frac{2\Delta y}{\Delta x}\frac{1}{t_2^2} e^{-t_2 x_\gamma}(1 - e^{-t_2 \Delta x/2})^2 \tag{3.28}$$

$t_1 \neq 0, t_2 = 0$

$$I^{\pm}_{\gamma\delta} = \frac{\Delta x}{t_1} e^{-t_1 y_\delta}\left(1 - \frac{1}{t_1 \Delta y}(1 - e^{-t_1 \Delta y})\right) \tag{3.29}$$

$t_1 \neq 0, t_2 \neq 0$

$$I^{\pm}_{\gamma\delta} = \frac{2\Delta y}{\Delta x}\frac{1}{t_2} e^{-t_2(x_\gamma + \frac{\Delta x}{2})} e^{-t_1(y_\delta + \Delta y)} \left\{ \frac{1 - e^{t_5 \Delta x/2}}{t_5} + \frac{1 - e^{-t_4 \Delta x/2}}{t_4} \right\} \tag{3.30}$$

Triangle d :

$t_1 = 0, t_2 \neq 0$

$$I^{\pm}_{\gamma\delta} = \frac{2\Delta y}{\Delta x}\frac{1}{t_2^2}e^{-t_2 x_\gamma}(1-e^{-t_2\Delta x/2})^2 \tag{3.31}$$

$t_1 \neq 0, t_2 = 0$

$$I^{\pm}_{\gamma\delta} = -\frac{\Delta x}{t_1}e^{-t_1 y_\delta}(1+\frac{1}{t_1\Delta y}(1-e^{-t_1\Delta y})) \tag{3.32}$$

$t_1 \neq 0, t_2 \neq 0$

$$I^{\pm}_{\gamma\delta} = \frac{2\Delta y}{\Delta x}\frac{1}{t_2}e^{-t_2(x_\gamma+\frac{\Delta x}{2})}e^{-t_1(y_\delta-\Delta y)}\left\{\frac{1-e^{-t_5\Delta x/2}}{t_5}+\frac{1-e^{t_4\Delta x/2}}{t_4}\right\} \tag{3.33}$$

Triangle l :

$t_1 = 0, t_2 \neq 0$

$$I^{\pm}_{\gamma\delta} = \frac{2\Delta y}{t_2}\left(1-\frac{2}{t_2\Delta x}(1-e^{-t_2\Delta x/2})\right) \tag{3.34}$$

$t_1 \neq 0, t_2 = 0$

$$I^{\pm}_{\gamma\delta} = \frac{\Delta x}{2\Delta y t_1^2}e^{-t_1(y_\delta+\Delta y)}\left((1-e^{t_1\Delta y})+e^{2t_1\Delta y}(1-e^{-t_1\Delta y})\right) \tag{3.35}$$

$t_1 \neq 0, t_2 \neq 0$

$$I^{\pm}_{\gamma\delta} = \frac{1}{t_1}e^{-t_1(y_\delta+\Delta y)}\left\{\frac{1-e^{t_5\Delta x/2}}{t_5}-e^{2t_1\Delta y}\frac{1-e^{t_4\Delta x/2}}{t_4}\right\} \tag{3.36}$$

Triangle r :

$t_1 = 0, t_2 \neq 0$

$$I^{\pm}_{\gamma\delta} = -\frac{2\Delta y}{t_2} e^{-t_2(x_\gamma + \Delta x/2)} \left(1 + \frac{2}{t_2 \Delta x}(1 - e^{t_2 \Delta x/2})\right) \tag{3.37}$$

$t_1 \neq 0, t_2 = 0$

$$I^{\pm}_{\gamma\delta} = \frac{\Delta x}{2\Delta y t_1^2} e^{-t_1(y_\delta - \Delta y)} \left((1 - e^{-t_1 \Delta y}) + e^{-2t_1 \Delta y}(1 - e^{t_1 \Delta y})\right) \tag{3.38}$$

$t_1 \neq 0, t_2 \neq 0$

$$I^{\pm}_{\gamma\delta} = \frac{1}{t_1} e^{-t_1(y_\delta + \Delta y)} e^{-t_2(x_\gamma + \Delta x/2)} \left\{ e^{2t_1 \Delta y} \frac{1 - e^{-t_5 \Delta x/2}}{t_5} - \frac{1 - e^{-t_4 \Delta x/2}}{t_4} \right\} \tag{3.39}$$

where

$$t_4 = -t_2 - t_1 2 \frac{\Delta y}{\Delta x}$$

$$t_5 = -t_2 + t_1 2 \frac{\Delta y}{\Delta x}$$

and $x_\gamma, y_\delta, \Delta x$, and Δy are as defined in Figure 3.4.

Thus, evaluation of the matrix elements for equation (3.19) requires summing the analytical expressions above for each facet of the surface profile multiplied by the appropriate vector products for each of the eight matrix elements involving this integral. This procedure is repeated for every combination of the $[mn]$ and $[op]$ indices, with the final number of operations proportional to $m \times n \times o \times p \times f \times 2$ where f is the number of facets making up the profile. Since integrals are performed analytically in this formulation, the only numerical approximation used involves truncation of the surface field unknown Fourier series.

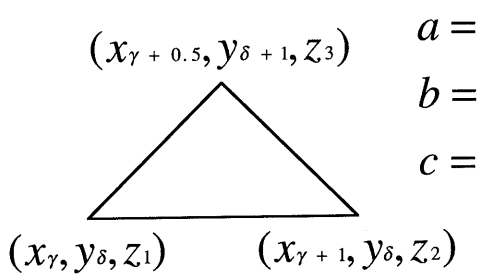

$$a = (z_2 - z_1) / \Delta x$$
$$b = (z_3 - (z_2 + z_1) / 2) / \Delta y$$
$$c = z_1 - a * x_\gamma - b * y_\delta$$

Triangle u

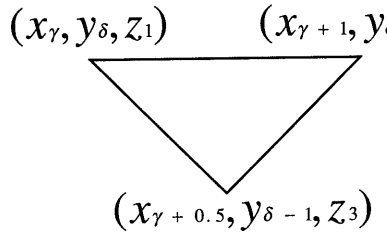

$$a = (z_2 - z_1) / \Delta x$$
$$b = -(z_3 - (z_2 + z_1) / 2) / \Delta y$$
$$c = z_1 - a * x_\gamma - b * y_\delta$$

Triangle d

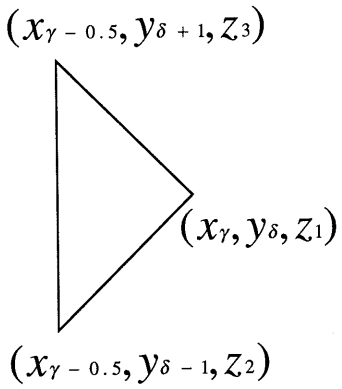

Triangle l

$$b = (z_3 - z_2) / \Delta y$$
$$a = 2(z_1 - (z_3 + z_2) / 2) / \Delta x$$
$$c = z_1 - a * x_\gamma - b * y_\delta$$

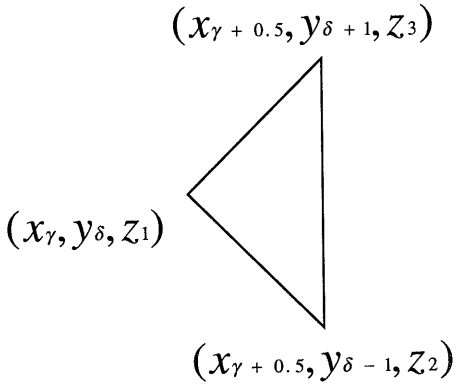

Triangle r

$$b = (z_3 - z_2) / \Delta y$$
$$a = -2(z_1 - (z_3 + z_2) / 2) / \Delta x$$
$$c = z_1 - a * x_\gamma - b * y_\delta$$

Figure 3.6: Types of triangles in surface grid

A direct LU inversion technique was used for the matrix equation (3.19), although more efficient methods could potentially be applied. Note that a direct inversion of the matrix equation requires retaining an equal number of $m \times n$ scattered modes and $o \times p$ Fourier series coefficients. Individual indices m, n, o, and p do not necessarily range over the same values, although a symmetric expansion about zero seems reasonable, especially for a normally incident plane wave field, and was adopted in the results to be presented. Although only direct solutions with square matrices are considered in this chapter, use of non-square matrices inverted with a singular value decomposition technique has been reported for one dimensional periodic surfaces in the literature [84] and has shown potential for avoiding the EBC's conditioning problems.

3.4 Model Validation

To validate the code developed, comparisons were made with both EBC [87] and moment method codes [85] for a one dimensional sawtooth surface profile as shown in Figure 3.1. The triangular grid of Figure 3.4, however, is unable to model a one dimensional surface profile due to the presence of triangles l and r along the lines $x = x_1$ and $x = P_x$ respectively. The modified triangular grid shown in Figure 3.7 is used instead, which now contains four new triangular domains, lu, ld, ru, and rd, for which the $I^{\pm}_{\gamma\delta}$ integrals must be evaluated. Results are

Triangle lu :

$t_1 = 0, t_2 \neq 0$

$$I^{\pm}_{\gamma\delta} = \frac{\Delta y}{t_2}\left(1 - \frac{2}{t_2\Delta x}(1 - e^{-t_2\Delta x/2})\right) \tag{3.40}$$

$t_1 \neq 0, t_2 = 0$

$$I^{\pm}_{\gamma\delta} = \frac{\Delta x}{2\Delta y t_1^2} e^{-t_1 y_\delta}\left(-(1 - e^{-t_1\Delta y}) + \Delta y t_1\right) \tag{3.41}$$

$t_1 \neq 0, t_2 \neq 0$

$$I^{\pm}_{\gamma\delta} = \frac{1}{t_1} e^{-t_1(y_\delta + \Delta y)}\left\{\frac{1 - e^{t_5\Delta x/2}}{t_5} + e^{t_1\Delta y}\frac{1 - e^{-t_2\Delta x/2}}{t_2}\right\} \tag{3.42}$$

Triangle ld :

$t_1 = 0, t_2 \neq 0$

$$I^{\pm}_{\gamma\delta} = \frac{\Delta y}{t_2}\left(1 - \frac{2}{t_2\Delta x}(1 - e^{-t_2\Delta x/2})\right) \tag{3.43}$$

$t_1 \neq 0, t_2 = 0$

$$I^{\pm}_{\gamma\delta} = -\frac{\Delta x}{2\Delta y t_1^2} e^{-t_1 y_\delta}\left(-e^{t_1\Delta y}(1 - e^{-t_1\Delta y}) + \Delta y t_1\right) \tag{3.44}$$

$t_1 \neq 0, t_2 \neq 0$

$$I^{\pm}_{\gamma\delta} = \frac{1}{t_1} e^{-t_1(y_\delta + \Delta y)}\left\{-e^{t_1\Delta y}\frac{1 - e^{-t_2\Delta x/2}}{t_2} - e^{2t_1\Delta y}\frac{1 - e^{t_4\Delta x/2}}{t_4}\right\} \tag{3.45}$$

Triangle ru :

$t_1 = 0, t_2 \neq 0$

$$I^{\pm}_{\gamma\delta} = -\frac{\Delta y}{t_2} e^{-t_2(x_\gamma + \Delta x/2)} \left(1 + \frac{2}{t_2 \Delta x}(1 - e^{t_2 \Delta x/2})\right) \tag{3.46}$$

$t_1 \neq 0, t_2 = 0$

$$I^{\pm}_{\gamma\delta} = \frac{\Delta x}{2\Delta y t_1^2} e^{-t_1(y_\delta - \Delta y)} \left(\Delta y t_1 e^{-t_1 \Delta y}) + e^{-2t_1 \Delta y}(1 - e^{t_1 \Delta y})\right) \tag{3.47}$$

$t_1 \neq 0, t_2 \neq 0$

$$I^{\pm}_{\gamma\delta} = \frac{1}{t_1} e^{-t_1 y_\delta} e^{-t_2 x_\gamma} \left\{ \frac{1 - e^{t_4 \Delta x/2}}{t_4} + \frac{1 - e^{-t_2 \Delta x/2}}{t_2} \right\} \tag{3.48}$$

Triangle rd:

$t_1 = 0, t_2 \neq 0$

$$I^{\pm}_{\gamma\delta} = -\frac{\Delta y}{t_2} e^{-t_2(x_\gamma + \Delta x/2)} \left(1 + \frac{2}{t_2 \Delta x}(1 - e^{t_2 \Delta x/2})\right) \tag{3.49}$$

$t_1 \neq 0, t_2 = 0$

$$I^{\pm}_{\gamma\delta} = \frac{\Delta x}{2\Delta y t_1^2} e^{-t_1(y_\delta - \Delta y)} \left(-\Delta y t_1 e^{-t_1 \Delta y}) + (1 - e^{-t_1 \Delta y})\right) \tag{3.50}$$

$t_1 \neq 0, t_2 \neq 0$

$$I^{\pm}_{\gamma\delta} = \frac{1}{t_1} e^{-t_1 y_\delta} e^{-t_2 x_\gamma} \left\{ \frac{e^{t_5 \Delta x/2} - 1}{t_5} - \frac{1 - e^{-t_2 \Delta x/2}}{t_2} \right\} \tag{3.51}$$

Construction of a sawtooth profile now requires only two points specified on the surface profile, (x_1, y_1) and $(x_{3/2}, y_2)$ which are set equal to 0 and h, the height of

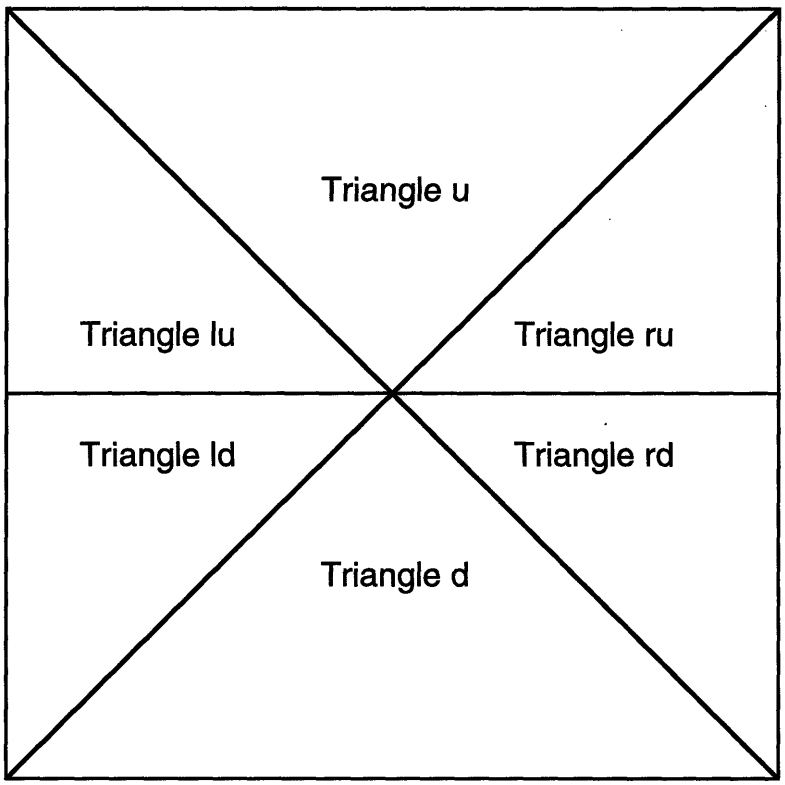

Figure 3.7: Modified triangular grid in $x - y$ plane for 1-D wedge profile

the sawtooth profile, respectively. Calculations were performed for a surface height of 0.5λ, period 3.01λ, dielectric constant $(6, 0)$ and a normally incident plane wave field. Predicted values for the induced currents on the surface profile are plotted in Figure 3.8 for the one dimensional EBC, one dimensional MOM, and two dimensional EBC codes. A total of 13 Fourier series terms were used with the one dimensional EBC, 169 terms with the two dimensional EBC (using $m = -6$ to 6 and $n = -6$ to 6 as the period in the x direction was set to 3.01λ also), and 50 pulse basis functions in the point matching MOM code, corresponding to 6 points per wavelength sampling in the dielectric medium. Surface currents M_y and J_x are plotted in Figures 3.8 (a) and (b) for a vertically polarized incident field, meaning that the unit magnitude incident electric field is directed along the row direction of the surface profile, while surface currents M_x and J_y are plotted in Figure 3.8 (c) and (d) for a horizontally polarized incident field. Power conservation for all three codes was within 1%, and predicted brightness temperatures as discussed in the next section differed by less than 0.5 K under the assumption of a 300 K surface temperature. These comparisons show that the two dimensional EBC model correctly reduces to the one dimensional surface case, and also that the extended boundary condition approach yields an accurate solution when compared to the method of moments for the sawtooth profile considered. Note that the accuracy of the EBC for this profile is not immediately obvious, as induced surface currents near the edges of the surface have potentially singular behavior. Moment method results were also generated using larger numbers of basis functions and showed that no strong singular behavior occurred near the edges of the wedge profile.

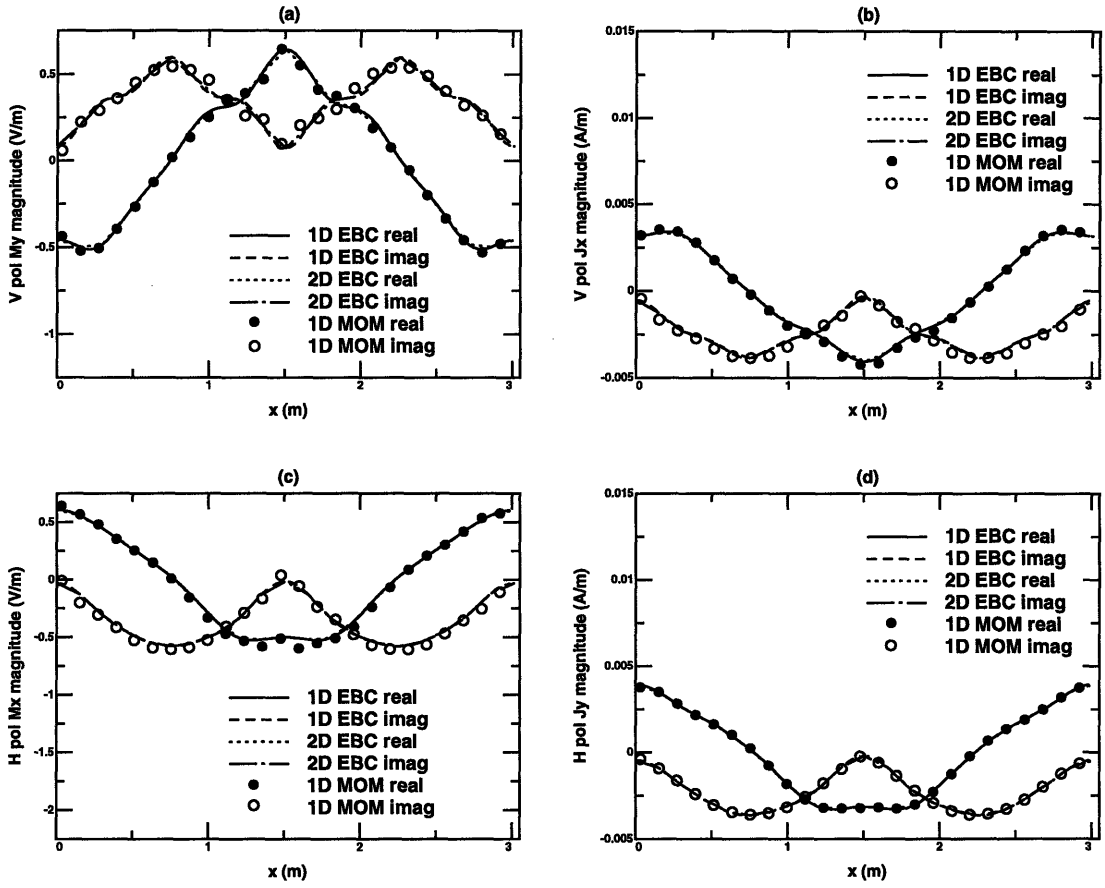

Figure 3.8: Comparison of induced currents on one dimensional wedge profile (a) M_y (b) J_x (c) M_x (d) J_y

Figure 3.9 illustrates the convergence of predicted reflectivities with the total number of surface field Fourier coefficients retained for a pyramidal type surface as shown in Figure 3.3. A surface height of 0.5λ, period in the x and y directions of 3 and 6 λ respectively and a dielectric constant of $(6, 0)$ is used, and total reflected powers are plotted in Figures 3.9 (a) and (b) for a normally incident plane wave in horizontal and vertical polarizations respectively. The resulting power conservation corresponding to Figures 3.9 (a) and (b) is also plotted in Figures 3.9 (c) and (d), and illustrates a clear convergence as the number of surface field mode amplitudes approaches and exceeds 121. Convergence of the predicted total reflected power is of primary concern since this quantity determines the brightness temperature as described in the next section. The results of Figure 3.9 indicate the accuracy of the EBC approach for the relatively smooth pyramidal surfaces to be considered in this chapter, and show that 169 surface field Fourier coefficients should be sufficient to model induced current variations. The remaining calculations of this chapter were generated using 169 coefficients, which results in a matrix size of 676 by 676, and required approximately 70 seconds of CPU time on a DEC AXP 3000-M800 for each brightness temperature point.

3.5 Pyramidal Surface Thermal Emission

To assess the response of the third Stokes brightness temperature to degree of surface azimuthal anisotropy, the two dimensionally periodic surface scattering model developed is applied in a study of polarimetric thermal emission from pyramidal surfaces, as shown in Figure 3.3, for which the faceted surface model approach should be very

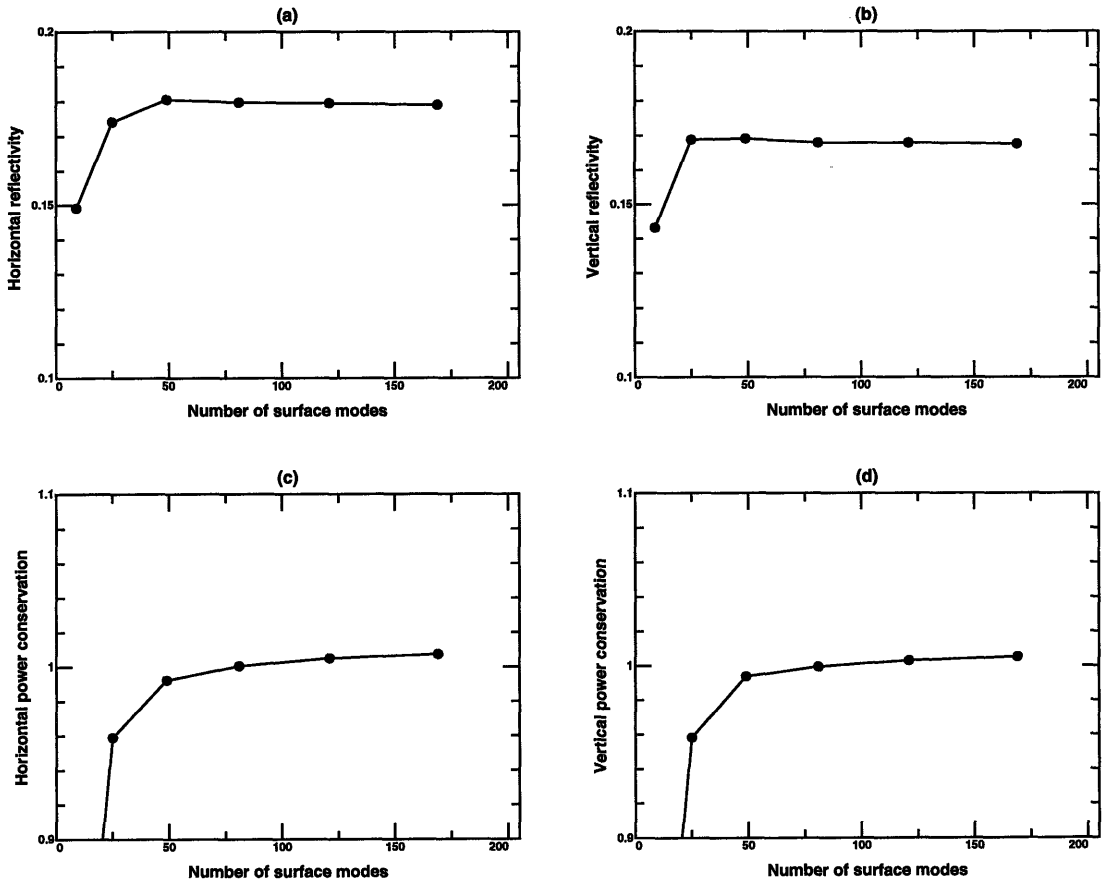

Figure 3.9: Convergence of total reflected power with number of Fourier coefficients (a) Horizontal incidence (b) Vertical incidence (c) Horizontal power conservation (d) Vertical power conservation

efficient. The pyramidal surfaces studied are made up of only 4 triangular facets, corresponding to including only the points (x_1, y_1) and $(x_{3/2}, y_2)$ in the surface profile description, with remaining surface facets generated by the required periodicities.

As discussed in Chapter 1, brightness temperatures corresponding to all four modified Stokes parameters are investigated in polarimetric passive remote sensing. The brightness temperature Stokes vector is defined as

$$\bar{T}_B = \frac{1}{C}\bar{I} = \frac{1}{C}\begin{bmatrix} I_h \\ I_v \\ U \\ V \end{bmatrix} = \frac{1}{\eta C}\begin{bmatrix} \langle E_h E_h^* \rangle \\ \langle E_v E_v^* \rangle \\ 2\mathrm{Re}\langle E_v E_h^* \rangle \\ 2\mathrm{Im}\langle E_v E_h^* \rangle \end{bmatrix} \tag{3.52}$$

and is calculated through evaluation of the total power reflected for each of four incident polarizations. The reflectivity $r_a(\theta, \phi)$ for the periodic surfaces of this chapter is evaluated through calculation of the scattered mode amplitudes $\overline{a}_{mn}$. Due to the periodic nature of the surface profile, the net power reflected from the surface travels only in the $\hat{z}$ direction, so that the total reflectivity of the surface can be written as

$$r_a(\theta, \phi) = \sum_m \sum_n \frac{Re\{k_{z0_{mn}}\}}{|k_{zi}|} |\overline{a}_{mn}|^2 \tag{3.53}$$

The total power transmitted into the surface medium can also be calculated similarly from the $\overline{c}_{mn}$ amplitudes, and a power conservation check can be performed to insure code accuracy.

Thus, to determine polarimetric thermal emission from a pyramidal surface, reflected mode amplitudes $\overline{a}_{mn}$ are calculated for an incident field polarized in each of four directions. Note that this requires only one matrix generation and inversion

procedure since only the right hand side of the matrix equation varies with different incident fields. Reflectivities, emissivities, and polarimetric brightness temperatures are then calculated from these modes as described previously. A physical temperature of 300 K is assumed for all of the surfaces studied in this section.

Figure 3.10 presents predicted polarimetric brightness temperatures for a pyramidal surface with a height of 0.5λ, period in the x direction of 3.01λ and a varying period in the y direction, ranging from 3.01 to 24.08λ. A dielectric constant of $(6, 0)$ is assumed for the surface medium, and the power conservation check was within 1 % for these calculations. Note that the slopes of this surface are no greater than those for which the wedge profile validation was performed in the previous section, so that the EBC approach should be valid for this surface. Brightness temperatures are plotted for a 0 degree polar observation angle, (nadir looking), and for azimuthal angle, ϕ, varying from 0 (along the $+x$ direction) to 90 degrees (along the $+y$ direction). The expected $\sin 2\phi$ variation of the U_B brightness required for nadir observation due to the reflection symmetries of the surface profile [92] is observed. Also, the $P_y = 3.01\lambda$ curve illustrates the small values of U_B obtained from a nearly azimuthally symmetric medium. The response of U_B to the level of anisotropy of the surface is clearly demonstrated in Figure 3.10, which shows that values of U_B predicted assuming a very large value of P_y significantly overestimate U_B values obtained in the $P_y = 2P_x$ case. However, the convergence of U_B results for $P_y > 4P_x$ illustrates that azimuthal anisotropy beyond this level has little effect.

The response of the polarimetric brightness temperatures to pyramidal surface height is plotted in Figure 3.11, for nadir observation, $P_x = 3.01\lambda$, $P_y = 6.02\lambda$, and a

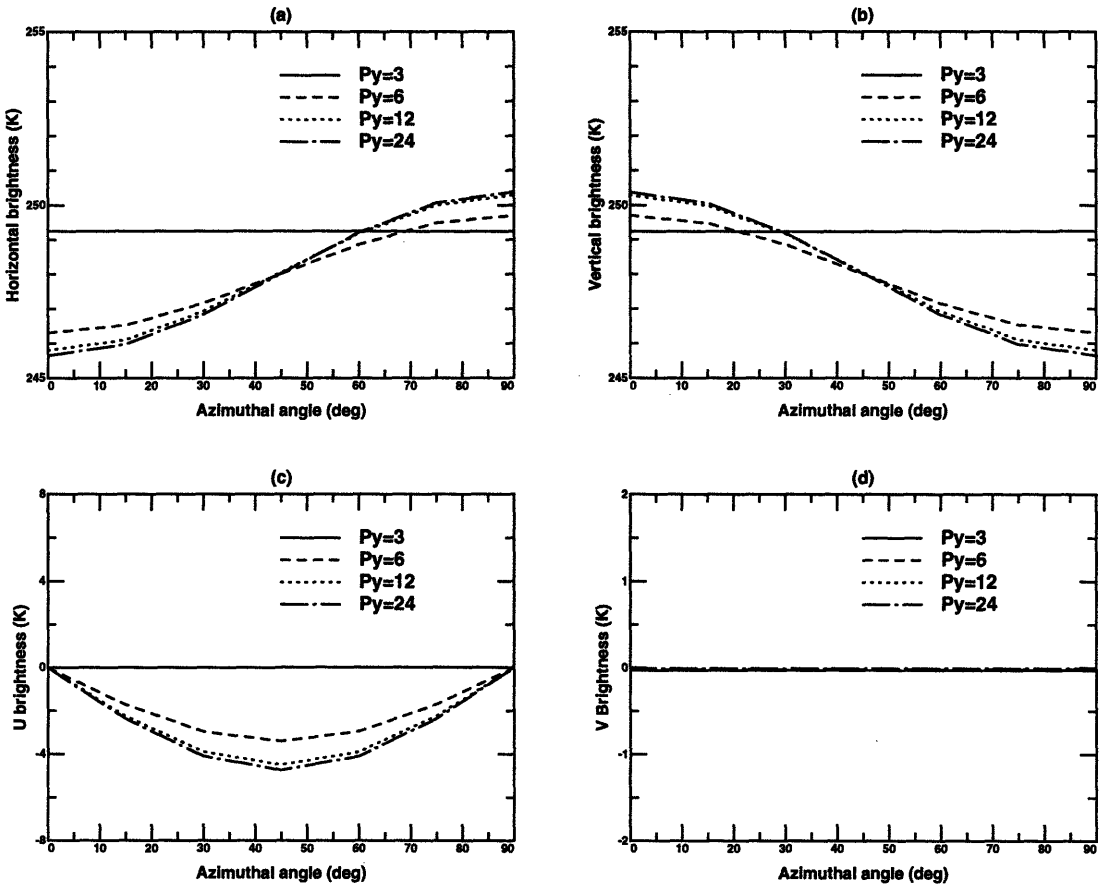

Figure 3.10: Predicted polarimetric brightness temperatures from a pyramidal surface: Variation with P_y (a) T_{Bh} (b) T_{Bv} (c) U_B (d) V_B

dielectric constant of $(6, 0)$. The response of U_B to surface slope, as indicated by higher U_B values for larger surface heights, is demonstrated in Figure 3.11. This response has been observed in the literature for 1-D periodic surfaces [85],[90]. Surfaces with heights less than 0.25λ and maximum slopes consequently less than 0.08 are seen to produce negligible U_B emission.

The response of the polarimetric brightness temperatures to polar observation angle is plotted in Figure 3.12, for pyramidal surfaces with height 0.5λ, $P_x = 3.01\lambda$, $P_y = 6.02\lambda$, and dielectric constant of $(6, 0)$. The response to polar angle variation is very strong for these relatively low dielectric constant materials, again as has been observed for 1-D surfaces [85]. However, simulations in the literature with much higher, ocean like dielectric constant media show smaller variations with polar observation angle in this range [90]. Also, V_B is observed to show some response to polar observation angle, although it is quite small.

The response of the polarimetric brightness temperatures to the real part of the surface dielectric constant is plotted in Figure 3.13, for pyramidal surfaces with height 0.5λ, $P_x = 3.01\lambda$, $P_y = 6.02\lambda$, and nadir viewing observation. Although the T_{Bh} and T_{Bv} brightnesses are influenced very strongly by variations in dielectric constant, U_B is affected less significantly and still shows the same azimuthal signature. Increasing U_B values obtained are observed to saturate in simulations performed with dielectric constants higher than $(12, 0)$.

The response of the polarimetric brightness temperatures to the imaginary part of the surface dielectric constant is plotted in Figure 3.14, for pyramidal surfaces with height 0.5λ, $P_x = 3.01\lambda$, $P_y = 6.02\lambda$, and nadir viewing observation. Again, the

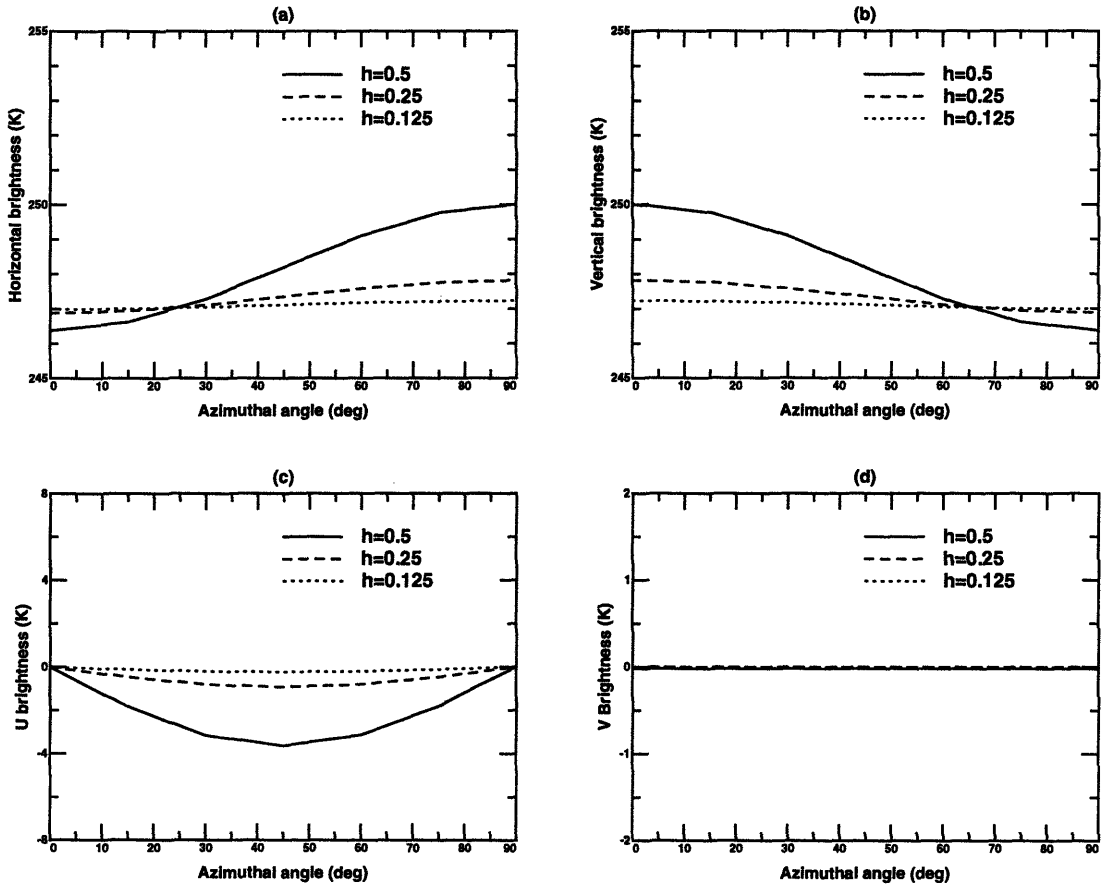

Figure 3.11: Predicted polarimetric brightness temperatures from a pyramidal surface: Variation with surface height (a) T_{Bh} (b) T_{Bv} (c) U_B (d) V_B

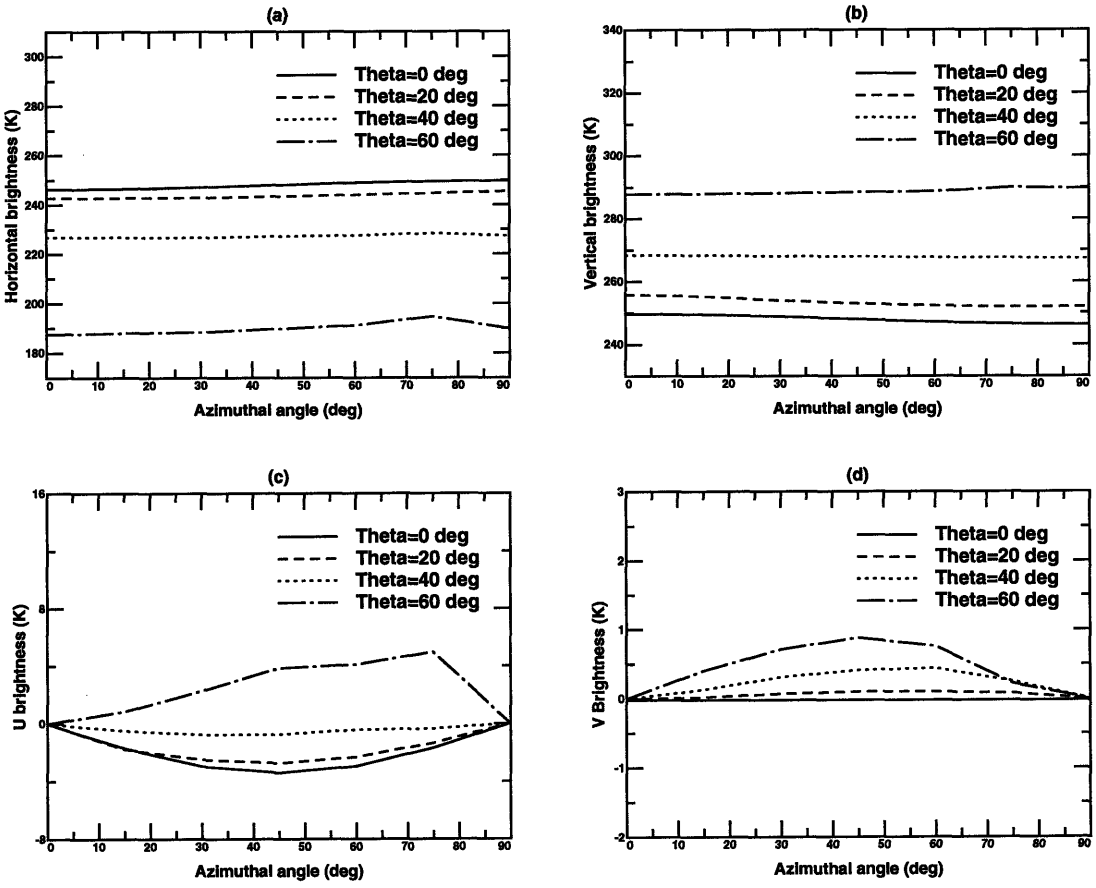

Figure 3.12: Predicted polarimetric brightness temperatures from a pyramidal surface: Variation with polar angle (a) T_{Bh} (b) T_{Bv} (c) U_B (d) V_B

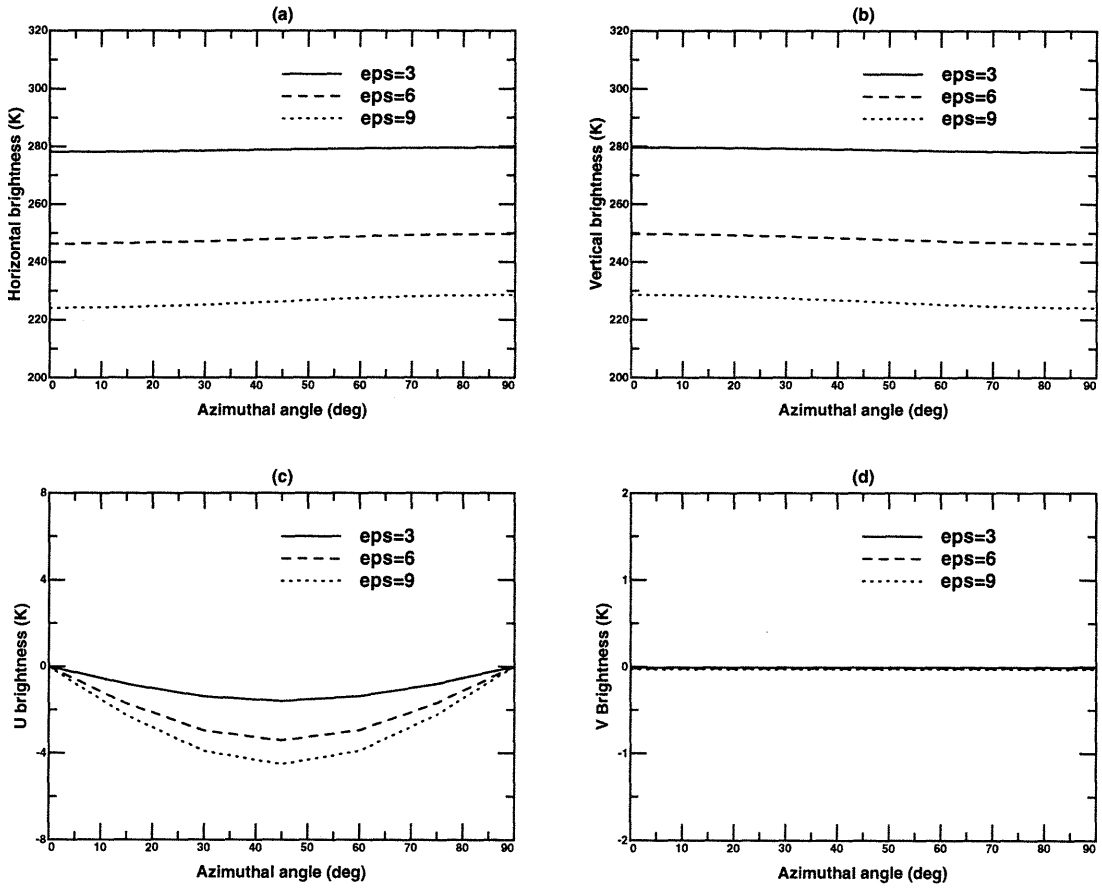

Figure 3.13: Predicted polarimetric brightness temperatures from a pyramidal surface: Variation with real dielectric constant (a) T_{Bh} (b) T_{Bv} (c) U_B (d) V_B

linearly polarized brightness temperatures show large variations as the imaginary part of the dielectric constant is increased, but U_B remains relatively unaffected, showing only slight increases with increasing imaginary part.

3.6 Conclusions

A model for the prediction of scattered Floquet mode amplitudes from a surface periodic in two spatial directions has been developed. This model applies the extended boundary condition approach, and uses an analytical evaluation of matrix elements over an assumed triangularly faceted surface profile. This method should be very accurate and efficient for surface profiles which are represented in terms of a small number of triangular facets, such as the pyramidal surfaces studied. The model was applied in a study of polarimetric passive remote sensing, and demonstrated that properties of U_B observed in the one dimensional periodic surface case are similar in the two dimensional rough surface case. Also, the response of U_B to the level of anisotropy of the medium under view was studied, and pyramidal surfaces with x to y period ratios greater than 4 were found to show little variation in predicted U_B brightnesses. Other applications of this model include the design of pyramidal type absorbing materials and simulation of scattering from two dimensional surfaces at low grazing angles, where the large surface sizes involved in a periodic surface simulation are required.

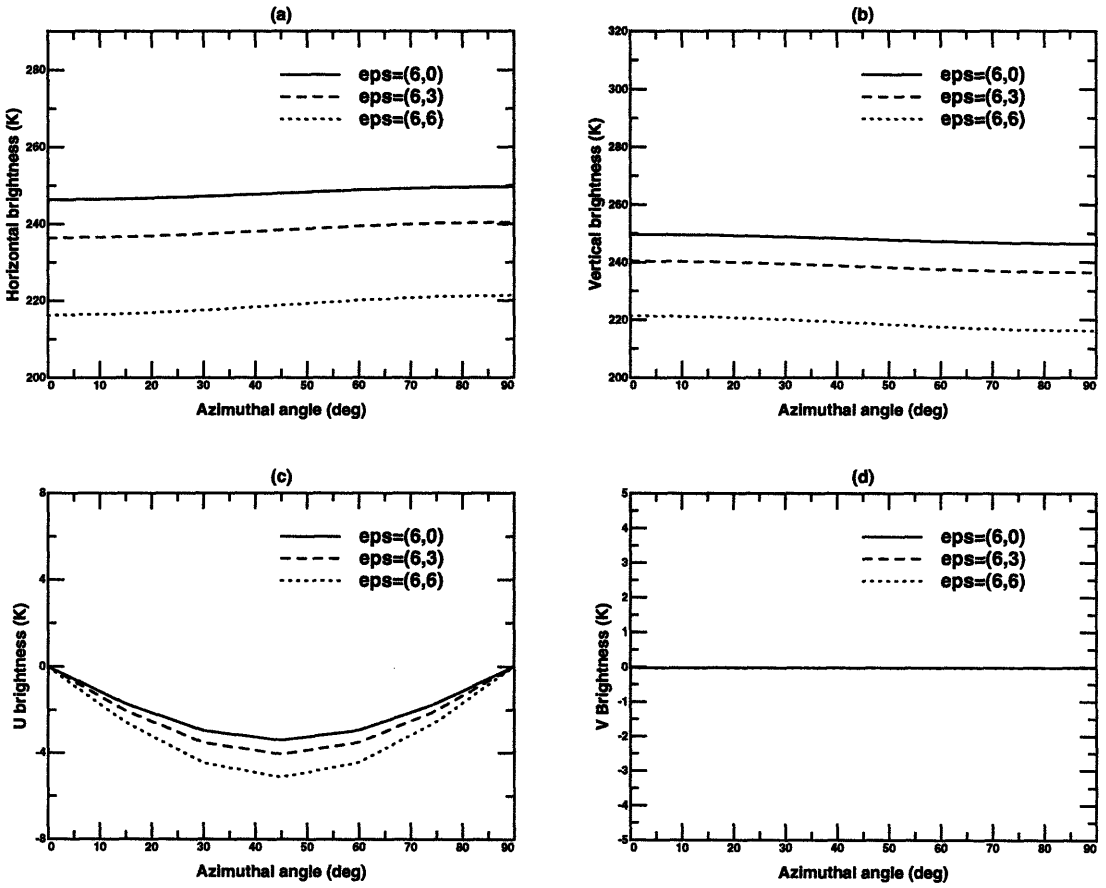

Figure 3.14: Predicted polarimetric brightness temperatures from a pyramidal surface: Variation with imaginary dielectric constant (a) T_{Bh} (b) T_{Bv} (c) U_B (d) V_B

Chapter 4

Backscattering Enhancement from Two-Dimensional Perfectly Conducting Rough Surfaces

4.1 Introduction

Backscattering enhancement from random rough surfaces is a topic which has been of recent interest in electromagnetics. Enhanced backscattering has been observed experimentally [97]- [103] from several rough surface types. One such type involves surfaces with relatively large slopes for which predictions of the standard Kirchhoff approach or small perturbation method are inaccurate due to the small slope limitations of these approximate theories [6]. The limitations of the analytic methods for large slope surfaces and the increasing power of modern computers have recently generated more interest in numerical approaches to the large slope surface problem based on Monte Carlo simulation of waves scattered from random rough surfaces. Monte Carlo simulations have been applied in the literature [54]-[56] and have been successful in predicting backscattering enhancement. As discussed in Chapter 1, the

most common of the numerical approaches previously used is the surface integral equation method and its solution by the method of moments, in which the integral equation is discretized into a matrix equation and then solved by matrix inversion. Because the matrix equation solving time scales as N^3 (where N is the number of surface field unknowns) for direct matrix inversion techniques, all of the previous simulations except for a few have been restricted to one-dimensional (1-D) random rough surfaces, as two dimensionally rough surfaces require a much larger number of surface field unknowns.

To increase computational efficiency so that 2-D surfaces could be treated, the Kirchhoff iteration method, also known in mathematics as the Neumann expansion, has been used [56], [104]-[106]. Recently, the Kirchhoff iteration technique has been applied in a Monte Carlo simulation of electromagnetic scattering at 0° incidence angle from a 2-D, randomly rough, perfectly conducting surface with 8192 surface field unknowns using 16 points per square wavelength (4 points per wavelength) sampling [105] and from a 2-D, randomly rough, metallic surface with 98,304 surface field unknowns using 100 points per square wavelength (10 points per wavelength) sampling [106]. However, it has been shown that the Neumann expansion has convergence problems for surfaces with large slopes and/or large incidence angles [104].

In the last few years, another efficient method called the sparse-matrix flat-surface iterative approach (SMFSIA) has been developed for the rough surface scattering problem [59]-[60]. The SMFSIA is similar to the BMFSIA of Chapter 2 in that interactions between two points on the surface are distinguished as either neighborhood strong interaction or far field interaction in the matrix equation of the method

of moments. As with the BMFSIA, this classification allows the original matrix to be separated into the sum of a strong matrix, a block Toeplitz flat-surface part, and a weak remainder. However, in the SMFSIA, the strong matrix is sparse instead of banded, due to the fact that points in a two dimensional grid cannot be labeled consecutively with all their nearest neighbors. An iterative procedure is again applied until convergence is achieved for the error norm of the matrix equation. The approach always converges since the neighborhood distance can be adjusted to insure convergence. Using this approach, scalar wave scattering from a 2-D random rough surface with a surface area of 81 square wavelengths (λ^2) and 4096 surface field unknowns was studied [59].

In this chapter, an extension of the method to vector electromagnetic wave scattering from a two-dimensional perfect electric conductor with a randomly rough surface profile is used [60]. Numerical results are illustrated for an incidence angle of 20°, up to 131,072 surface field unknowns, surface areas of 256 square wavelengths and 1024 square wavelengths, and up to 600 surface realizations. Surfaces with both a Gaussian height distribution and correlation function, rms height 1 wavelength, and correlation lengths 1.41, 2 or 3 wavelengths are considered. Backscattering enhancement is exhibited for both co-polarized and cross-polarized components. Comparisons with controlled laboratory millimeter wave experimental data at 20° incidence angle are also presented. The use of millimeter wave frequencies for the experiment allows a calibrated comparison of scattered power to incident power [100]-[101], so that the absolute value of the bistatic scattering cross section as normalized by the incident power is measured. Thus, absolute values of bistatic scattering cross sections

are compared between Monte Carlo simulations and experiments without the use of "arbitrary units". Results show numerical simulations to be in good agreement with experimental data in terms of both absolute magnitude and bistatic angular dependence and in view of the fact that there are no adjustable parameters.

In the next section, the numerical model used in the simulations is described. Section 4.3 reviews the experimental method, and in Section 4.4, results from theory and experiment are presented for a range of surface statistics.

4.2 Formulation and Numerical Method

The numerical model used for the comparison is a Monte Carlo method utilizing an exact numerical solution of the rough surface scattering problem. In Monte Carlo methods, a large number of finite area surface profiles with specified statistics are generated using a Fourier transform technique [100]. The scattering of an incident field from each surface realization is then computed using a numerical method, and the resulting bistatic scattering cross sections from all of the realizations are averaged to obtain the Monte Carlo estimate of bistatic scattering cross sections.

Consider an incident wave with magnetic field $\overline{H}_i(x,y,z)$ and time dependence $\exp(-i\omega t)$ impinging upon a 2-D perfectly conducting rough surface with a random height profile $z = f(x,y)$. The height function $z = f(x,y)$ has zero mean. Let $\overline{r}' = \hat{x}x' + \hat{y}y' + \hat{z}f(x',y')$ denote a source point and $\overline{r} = \hat{x}x + \hat{y}y + \hat{z}f(x,y)$ denote a field point on the rough surface. As discussed in Chapter 1, the magnetic field integral equation (MFIE) on the perfectly conducting rough surface for $\overline{r}$ and $\overline{r}'$ on

the surface is

$$\frac{\hat{n} \times \overline{H}_0(\overline{r})}{2} = \hat{n} \times \overline{H}_{inc} + \hat{n} \times \int dS' \left\{ \nabla g \times [\hat{n}' \times \overline{H}(\overline{r}')] \right\} \tag{4.1}$$

where the above integral $\int$ represents the principal-value integral,

$$\nabla g = (\overline{r} - \overline{r}')G(R) \tag{4.2}$$

$$G(R) = \frac{(ikR - 1)\exp(ikR)}{4\pi R^3} \tag{4.3}$$

and $R = \sqrt{(x - x')^2 + (y - y')^2 + (f(x,y) - f(x',y'))^2}$.

The SMFSIA, described in more detail in reference [60], solves this integral equation with a standard point matching method of moments technique, except that the matrix inversion is performed iteratively. In matrix notation,

$$\overline{\overline{Z}}\overline{x} = \overline{b} \tag{4.4}$$

is the exact matrix equation of the method of moments using pulse basis functions and delta testing functions. In the SMFSIA, the original matrix is decomposed into the sum of a strong matrix, a block Toeplitz flat-surface part, and a weak remainder:

$$(\overline{\overline{Z}}^{(s)} + \overline{\overline{Z}}^{(FS)} + \overline{\overline{Z}}^{(w)})\overline{x} = \overline{b} \tag{4.5}$$

In the above equation, $\overline{\overline{Z}}^{(s)}$ is a sparse matrix which contains the exact matrix elements up to a certain distance from the testing point, known as r_d, and zeros oth-

erwise. $\overline{\overline{Z}}^{(FS)}$, known as the "flat-surface" matrix, is a block Toeplitz matrix whose elements are the MOM integrals using the Green's function of a flat surface for distances larger than r_d from the testing point and zeros otherwise. This is based on the observation that for two points far away on the rough surface, the exact Green's function is well approximated by that of a flat surface. The weak remainder matrix, $\overline{\overline{Z}}^{(w)}$, contains the differences between the exact matrix elements and the flat surface approximated matrix elements for distances larger than r_d from the testing point and zeros otherwise, so that the sum of the three matrices is exactly the original matrix.

The matrix equation is then rearranged to take an iterative form. For the first-order and higher order solutions, the calculation procedure is

$$(\overline{\overline{Z}}^{(s)} + \overline{\overline{Z}}^{(FS)})\overline{x}^{(1)} = \overline{b} \tag{4.6}$$

$$(\overline{\overline{Z}}^{(s)} + \overline{\overline{Z}}^{(FS)})\overline{x}^{(n+1)} = \overline{b}^{(n+1)} \tag{4.7}$$

$$\overline{b}^{(n+1)} = \overline{b} - \overline{\overline{Z}}^{(w)}\overline{x}^{(n)} \tag{4.8}$$

The above matrix equations are solved using the BiCGSTAB technique, in which the required matrix multiplies are performed rapidly due to the decomposition of the matrix into a sparse matrix, which can be multiplied efficiently, and a block Toeplitz matrix, which can be multiplied using the FFT [107]. This iteration method is different from the Neumann iteration of references [56],[104]-[106] in that it can be shown to converge for arbitrarily large surface slopes and incidence angles, given

that the neighborhood interaction distance, r_d, is made large enough. Note that the simulations of this chapter do not use a parallelized BiCGSTAB routine as in Chapter 2, but rather achieve full parallelization by performing calculations for individual surface realizations in the Monte Carlo simulation on individual nodes of the parallel computer.

One issue in Monte Carlo simulations involves the effect of finite surface size. Experimental results to be compared with are both illuminated and observed by an antenna, whose pattern limits the spatial extent of the scattering surface. To model this pattern, incident fields in the simulation are "tapered" with a Gaussian beam amplitude pattern, which confines the illuminated rough surface to the surface area $L_x \times L_y$ so that surface edges do not contribute strongly to obtained scattered fields. For an incident field centered in direction $\hat{k}_i = \sin\theta_i \cos\phi_i \hat{x} + \sin\theta_i \sin\phi_i \hat{y} - \cos\theta_i \hat{z}$ with wave number k, the incident magnetic field of the tapered beam is

$$\overline{H}_i(x,y,z) = \frac{1}{\eta}\int_{-\infty}^{+\infty} dk_x \int_{-\infty}^{+\infty} dk_y \ \exp(ik_x x + ik_y y - ik_z z)\ \Psi(k_x,k_y) \left\{-E_h \hat{v}_i(kx,ky) + E_v \hat{h}_i(kx,ky)\right\} \qquad (4.9)$$

where

$$k_z \ = \ \sqrt{k^2 - k_x^2 - k_y^2}$$

, $\hat{h}_i$ and $\hat{v}_i$ are the incident polarization vectors defined in Chapter 1, and η is the impedance of free space [6]. In (4.9), $\Psi(k_x,k_y)$ is the spectrum of the incident wave,

defined as

$$\Psi(k_x, k_y) = \frac{1}{4\pi^2} \int_{-\infty}^{+\infty} dx \int_{-\infty}^{+\infty} dy \exp(-ik_x x - ik_y y) \exp(i(k_{ix}x + k_{iy}y)(1+w)) \exp(-t) \tag{4.10}$$

where

$$t = t_x + t_y = (x^2 + y^2)/g'^2 \tag{4.11}$$

$$t_x = \frac{(\cos\theta_i \cos\phi_i x + \cos\theta_i \sin\phi_i y)^2}{g'^2 \cos^2\theta_i} \tag{4.12}$$

$$t_y = \frac{(-\sin\phi_i x + \cos\phi_i y)^2}{g'^2} \tag{4.13}$$

and

$$w = \frac{1}{k^2}\left[\frac{(2t_x - 1)}{g'^2 \cos^2\theta_i} + \frac{(2t_y - 1)}{g'^2}\right] \tag{4.14}$$

The parameter g' controls the tapering of the incident wave and is set to $L_x/2 = L_y/2$ in the simulations of this chapter. While this tapering size does not correspond to that of the physical antennas in the experiment, the large number of surface correlation lengths contained within the pattern for the simulations performed insures that a reasonable result for the normalized backscattering cross section should be obtained. In addition, the chosen tapering lengths cause field amplitudes to be reduced by a factor of e^{-2} at surface edges compared to the center, so that any edge contributions to scattered fields are made less significant. The w and t terms are introduced to

approximate the tapered wave solution that was previously used for the scalar wave case [59]. However, in (4.9), a spectrum of vector plane waves is used so that the incident wave obeys Maxwell's equations exactly. For horizontally polarized incidence (meaning the electric field is polarized along $\hat{h}_i$), $E_h = 1$ and $E_v = 0$, while for vertically polarized incidence, $E_h = 0$ and $E_v = 1$. Variations with taper width in these simulations are discussed in [60] and were not found significant for the near normal incidence cases of this chapter. These variations become more significant as the incidence angle increases, however, as will be discussed in Chapter 5.

Numerical simulation results will be presented in terms of the normalized bistatic cross section, as defined in Chapter 1. For a scattered wave in α polarization and an incident wave in β polarization,

$$\sigma_{\alpha\beta}(\theta_s, \phi_s) = \frac{4\pi|\mathcal{E}_\alpha^s|^2}{2\eta P_{inc}} \cos\theta_i \tag{4.15}$$

where $\alpha, \beta = h, v$ and the observation direction is $\hat{k}_s = \sin\theta_s \cos\phi_s \hat{x} + \sin\theta_s \sin\phi_s \hat{y} + \cos\theta_s \hat{z}$. The incident power is

$$P_{inc} = \frac{2\pi^2}{\eta} \int\limits_{k_\rho < k} dk_x dk_y |\Psi(k_x, k_y)|^2 \frac{k_z}{k} (|E_h|^2 + |E_v|^2) \tag{4.16}$$

and $\mathcal{E}_\alpha^s$ for $\alpha = h, v$ are respectively

$$\mathcal{E}_h^s = \frac{\eta i k}{4\pi} \int_{S'} dx' dy' \exp(-ik\tau') \{F_x(x', y')(-\sin\phi_s) + F_y(x', y') \cos\phi_s\} \tag{4.17}$$

and

$$\mathcal{E}_v^s = \frac{\eta ik}{4\pi}\int_{S'} dx'dy' \exp(-ik\tau')\left\{F_x(x',y')\left[\frac{-\partial f(x',y')}{\partial x'}\sin\theta_s + \cos\theta_s\cos\phi_s\right]\right.$$
$$\left. + F_y(x',y')\left[-\frac{\partial f(x',y')}{\partial x'}\sin\theta_s + \cos\theta_s\sin\phi_s\right]\right\} \tag{4.18}$$

where

$$\tau' = x'\sin\theta_s\cos\phi_s + y'\sin\theta_s\sin\phi_s + f(x',y')\cos\theta_s \tag{4.19}$$

and, for $\overline{r}$ on rough surface S,

$$F_x(\overline{r}) = \sqrt{1 + \left(\frac{\partial f(x,y)}{\partial x}\right)^2 + \left(\frac{\partial f(x,y)}{\partial y}\right)^2}\,\hat{n}\times\overline{H}(\overline{r})\cdot\hat{x} \tag{4.20}$$

and

$$F_y(\overline{r}) = \sqrt{1 + \left(\frac{\partial f(x,y)}{\partial x}\right)^2 + \left(\frac{\partial f(x,y)}{\partial y}\right)^2}\,\hat{n}\times\overline{H}(\overline{r})\cdot\hat{y} \tag{4.21}$$

are the unknown functions proportional to the x and y components of the tangential magnetic field solved for in the method of moments. The above equations for scattered field amplitudes arise from use of the Huygens' principle integral in the far field, and from dot products with the $\hat{h}_s$ and $\hat{v}_s$ scattered field polarization vectors defined in Chapter 1.

4.3 Experimental Procedure

Experimental data is obtained from controlled laboratory millimeter wave experiments performed at the University of Washington Electromagnetics and Remote Sensing Laboratory, described in more detail in references [100]-[103]. Although millimeter wave systems have wider angular resolution when compared to the optical measurements previously performed, a millimeter wave system was chosen for these experiments due to a desire for accurate calibration of measured data with highly controlled surface statistical properties. The larger length scales associated with millimeter wave frequencies allowed surface profiles to be constructed in plastic by a computer controlled milling technique, so that their statistics were specifiable. Surfaces were then coated with several layers of nickel paint to make them highly conducting. The reflectivity of the nickel paint used is 0.95 with a relative phase of 175 degrees at the frequency of interest, and the transmittivity of a 0.2 mm layer is at least -40 dB down compared to air. Thus, the finite conductivity of this paint is expected to have only a minor effect on measured results. Surfaces with both a Gaussian height distribution function and correlation function were fabricated, so that their surface statistics were described by an rms height, chosen to be one wavelength, and a correlation length, chosen to be either 1.41, 2, or 3 wavelengths. The corresponding rms slopes of these surfaces range from 0.471 to 1.0 and contain regions where backscattering enhancement effects are known to exist. The 2-D surface spectrum is given by

$$W(K_x, K_y) = \frac{l_x l_y h^2}{4\pi} \exp\left(-\frac{K_x^2 l_x^2}{4} - \frac{K_y^2 l_y^2}{4}\right) \tag{4.22}$$

where l_x, l_y, are the correlation lengths in the x and y directions respectively, K_x and K_y are the spatial frequencies in the x and y directions respectively, and h is the surface rms height. Only isotropic surfaces with $l = l_x = l_y$ are considered in this chapter.

The experimental apparatus consists of a network analyzer and separate transmit and receive antennas, which can be oriented to measure the bistatic scattering pattern from an angle of -70 to +70 degrees in polar angle. Bistatic data for incidence angles of 0, 20, and 40 degrees from normal and both h and v polarizations was taken and is presented in [101]. A dual polarized receive antenna is used to measure both co- and cross polarized bistatic returns, and the single polarization transmit antenna is rotated to generate varying incident polarizations. Half power spot sizes of the transmit and receive antennas are approximately 50 and 32 wavelengths diameter at 97.5 GHz respectively at normal incidence. Since fabricated surfaces were much larger than the antenna spot sizes, experimental results were averaged over approximately 80 observations of varying surface locations. Additionally, results were averaged over a 5 GHz frequency band, for which the data showed little variation, centered at 97.5 GHz to provide a total of approximately 400 independent samples.

Calibration of experimental data is performed by comparison with a known radar cross section target, a flat metallic plate. This calibration enables the magnitude of the scattering cross sections as normalized by the incident power to be measured accurately in the experiment. An accuracy of better than 10% is expected for the cross section values presented in this chapter.

4.4 Comparison of Results

Previous simulations [60] have shown that a surface area of at least 16 x 16 wavelengths in numerical simulations is needed in order to obtain an accurate model of the experiments. The case of electromagnetic waves with a sampling rate of 8 points per wavelength will result in a 128 x 128 grid with 2 unknowns per point for a total of 32,768 surface field unknowns. This large number of unknowns is prohibitive for standard approaches to the method of moments. However, the use of the SMFSIA makes the solution of this problem possible. In this section, results from Monte Carlo simulations for an incidence angle of 20° are compared with the experimental data for a surface area of 256 square wavelengths using 8 points per wavelength sampling, and a surface area of 1024 square wavelengths using both 4 and 8 points per wavelength sampling. Bistatic scattering cross sections in the plane of incidence are compared. Numerical simulations were performed using the 400 node parallel IBM SP/2 at the Maui High Performance Computing Center and required approximately 4 CPU hours per node per realization for 32,768 unknowns.

Figure 4.1 (a)-(d) shows the comparison for surfaces with rms height one wavelength, correlation length two wavelengths for both h and v incidence and a surface area of 256 square wavelengths in the numerical simulation. The forward ($\phi_s = 0°$, $0° \leq \theta_s \leq 90°$) and backward direction ($\phi_s = 180°$, $0° \leq \theta_s \leq 90°$) are indicated in the plots as positive and negative angles, respectively, so that the backscattered direction corresponds to observation angle = $-20°$, indicated by the dashed line in the figures. The number of realizations averaged for a particular case are indicated in parenthesis in these figures and throughout the rest of this chapter. Backscat-

tering enhancement is clearly visible in both the numerical and experimental results for the hh co-polarized return, the vv co-polarized return, and for both the vh and hv cross-polarized returns. Overall, the agreement between experiment and theory is observed to be good, especially given that the absolute values of the normalized bistatic scattering cross sections are compared on a linear scale with no adjustable parameters. However, the predicted cross-polarized level seems to be slightly lower than the experimental data for both h and v incidence, and the forward scattering peak in hh returns is not reproduced in the simulations.

Figure 4.2 (a)-(d) presents the same comparison, but with a surface area of 1024 square wavelengths and 8 points per wavelength sampling for a total of 131,072 surface unknowns in the Monte Carlo simulation. The h incidence agreement is seen to be better for this case, especially in the cross polarized results, but vv co-polarized results are somewhat worse. The minor differences obtained between theory and experiments in Figures 4.1 and 4.2 are difficult to clarify, but could potentially be due to differences between the theoretical and experimental antenna patterns, the additional frequency averaging in the experimental data, and inaccuracies in the rough surface profiles that were fabricated.

Since the SMFSIA approach is effectively an order N^2 solution technique, the four fold increase in number of unknowns in Figure 4.2 results in sixteen times the computational requirements for this $131,072$ unknowns case. A comparison of the $131,072$ unknowns (8 points per wavelength sampling) results with the $32,768$ unknowns (4 points per wavelength sampling) results for the 1024 square wavelengths case in Figure 4.3 (a)-(d), however, shows that 4 points per wavelength sampling

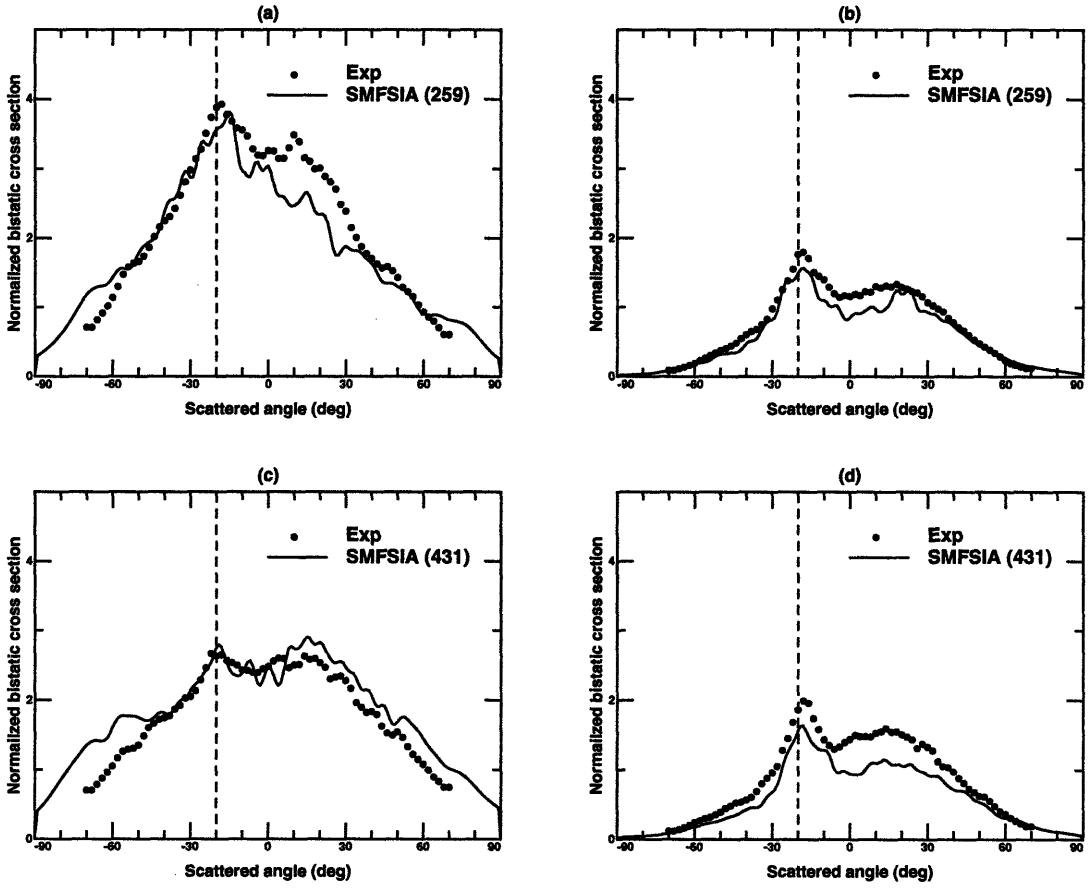

Figure 4.1: Comparison of Monte Carlo SMFSIA with experimental data. Surface area of 256 square wavelengths with an rms height of 1 wavelength and correlation length of 2 wavelengths. (a) σ_{hh} (b) σ_{vh} (c) σ_{hv} (d) σ_{vv}

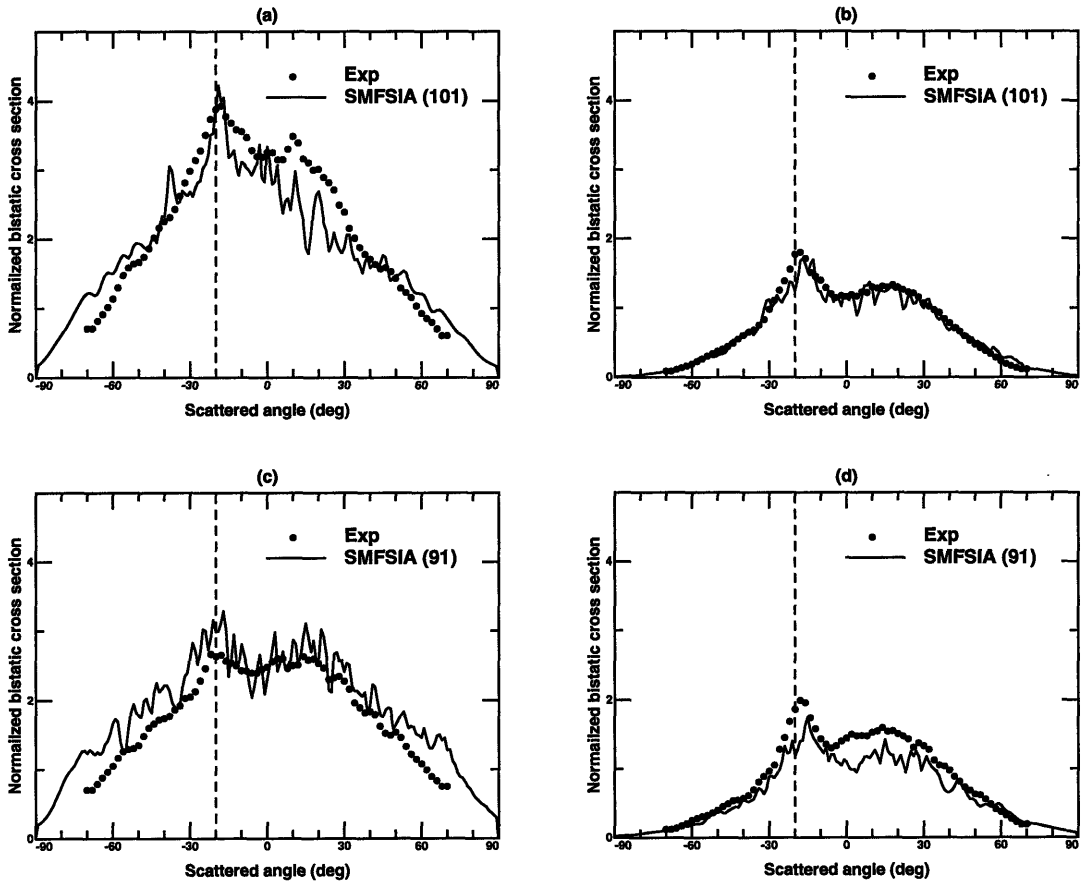

Figure 4.2: Comparison of Monte Carlo SMFSIA with experimental data. Surface area of 1024 square wavelengths with an rms height of 1 wavelength and correlation length of 2 wavelengths. (a) σ_{hh} (b) σ_{vh} (c) σ_{hv} (d) σ_{vv}

should be sufficient, at least for the surface statistics compared. Note the smoother 4 points per wavelength curve obtained due to the larger number of realizations run for this less computationally intensive case. Further Monte Carlo simulations were limited to 32,768 unknowns. In addition, the substantial agreement between 256 and 1024 square wavelength surface area results shows that a 256 square wavelength surface area should be sufficient in the numerical simulations for these surface statistics.

In Figure 4.4 (a)-(d), SMFSIA and experimental results are compared for surfaces with rms height one wavelength, correlation length 1.41 wavelengths and surface area 256 square wavelengths. In this very rough surface case, backscattering enhancement is observed for both h and v incidence co- and cross- polarized returns. Again, the agreement between experiment and theory is observed to be good, although the predicted cross-polarized level remains slightly lower than the experimental data and the forward scattering peak for hh is still not reproduced in the simulations. Predictions for this case using a sampling rate of 4 points per wavelength and surface area 1,024 square wavelengths were found significantly inaccurate due to the rougher surface statistics.

Figures 4.5 and 4.6 (a)-(d) illustrate the same comparisons for surfaces with rms height one wavelength, correlation length 3 wavelengths, and surface areas of 256 and 1024 square wavelengths respectively. For this smoother surface case, backscattering enhancement is not observed in the hh co-polarized experimental results, although some small effects are seen in both vh and vv cross-polarized components and in the vv co-polarized component. Also, the forward scattering peak in the hh experimental results is more pronounced. The Monte Carlo simulations are again shown to repro-

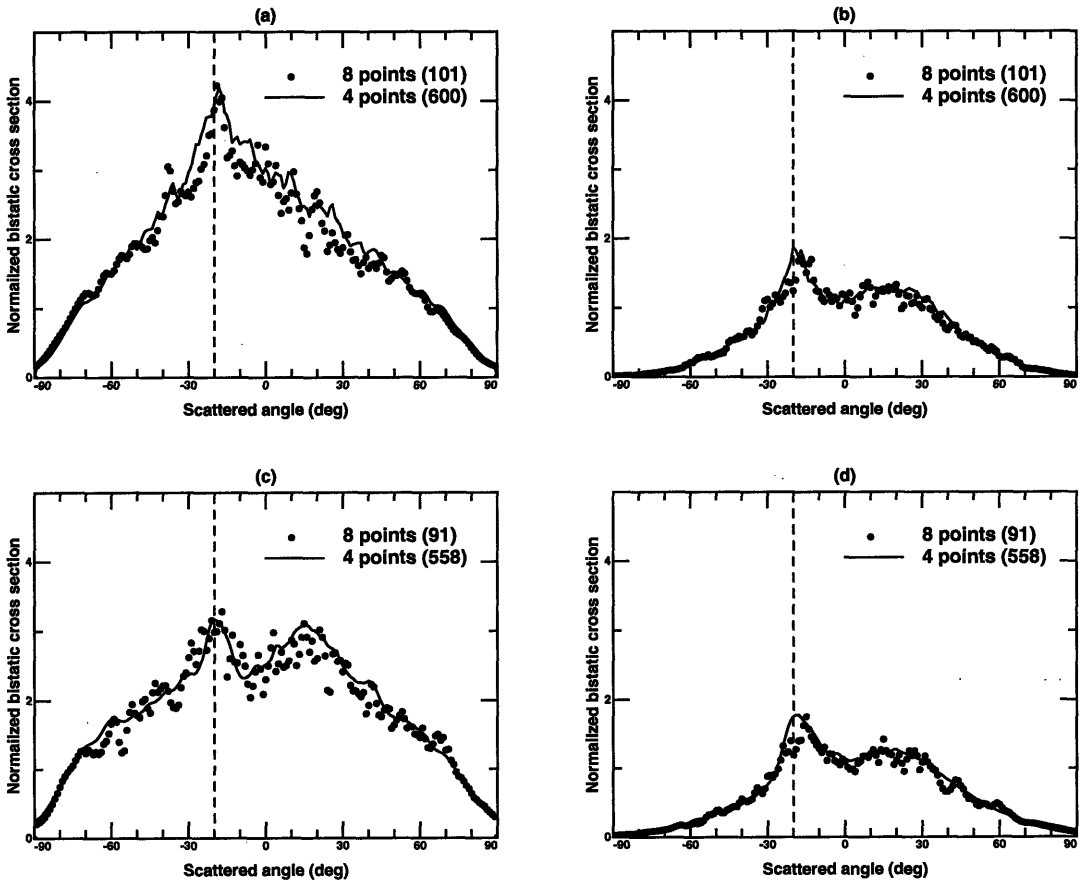

Figure 4.3: Comparison of Monte Carlo SMFSIA with varying sampling rates. Surface area of 1024 square wavelengths with an rms height of 1 wavelength and correlation length of 2 wavelengths. (a) σ_{hh} (b) σ_{vh} (c) σ_{hv} (d) σ_{vv}

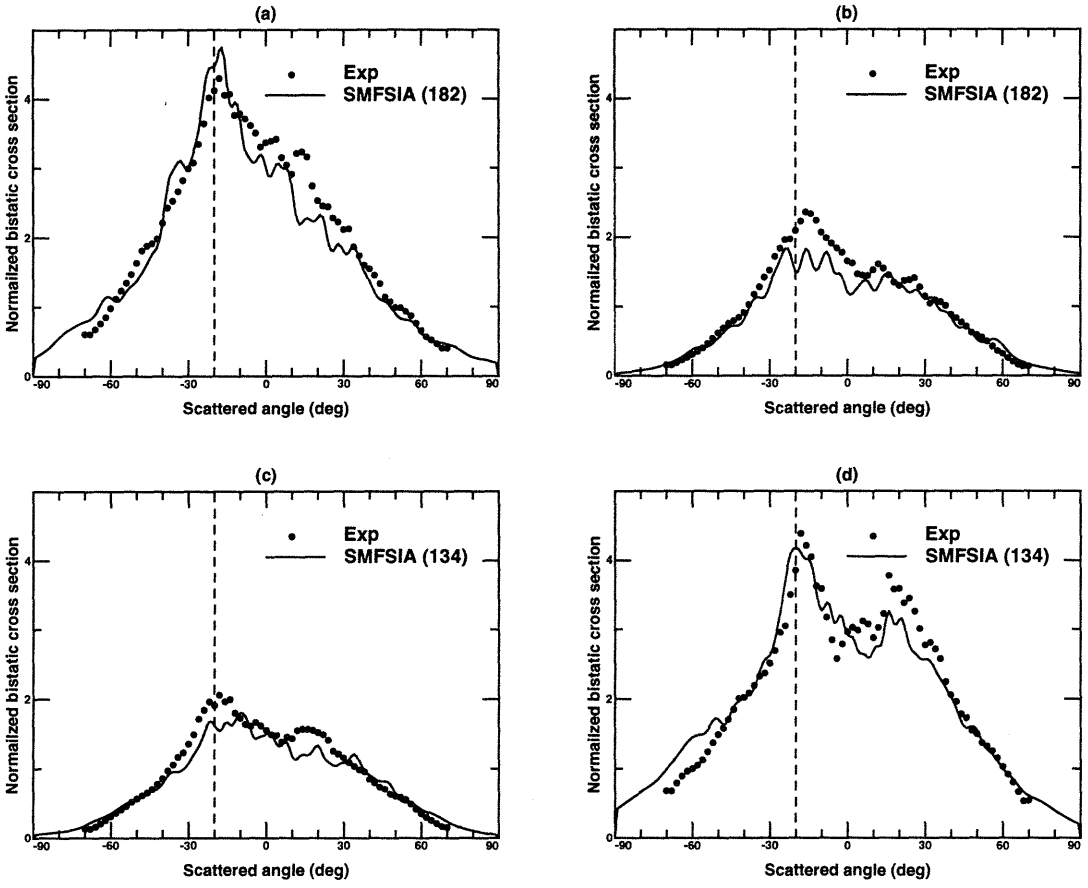

Figure 4.4: Comparison of Monte Carlo SMFSIA with experimental data. Surface area of 256 square wavelengths with an rms height of 1 wavelength and correlation length of 1.41 wavelengths. (a) σ_{hh} (b) σ_{vh} (c) σ_{hv} (d) σ_{vv}

duce the overall trends and level of the experimental data, with the larger surface area results giving better overall agreement due to the inclusion of more surface correlation lengths for this long correlation length case.

As discussed in Chapter 1, polarimetric active remote sensing involves measurement of correlations between scattered field amplitudes in addition to the power measurements illustrated in Figures 4.1-4.6. Although a polarimetric system was not used in the experiments, polarimetric calculations are possible with the SMFSIA. Figure 4.7 presents an example of such calculations, where the $hh - vv$ correlation coefficient, ρ, is plotted for the Monte Carlo simulations of Figures 4.1 and 4.6. Both the real and imaginary parts of ρ are illustrated in this figure, and are seen to have distinct variations between the rms height one, correlation length two wavelengths case (Figures 4.7 (a) and (b)) and the rms height one, correlation length three wavelengths case (Figures 4.7 (c) and (d)). The results of 4.7 are of interest because the standard analytical theories always predict $|\rho|$ values very close to one, which is clearly at variance with the small values of ρ predicted by the SMFSIA. Such small values of $|\rho|$ indicate a distinction between hh and vv scattering mechanisms, although the exact nature of this distinction is still unclear.

4.5 Conclusions

The results of this chapter clearly demonstrate the capability of Monte Carlo methods for simulating backscattering enhancement from surfaces randomly rough in two directions. The use of an efficient version of the method of moments, the SMFSIA, has enabled problems involving up to 131,072 unknowns to be treated so that an ac-

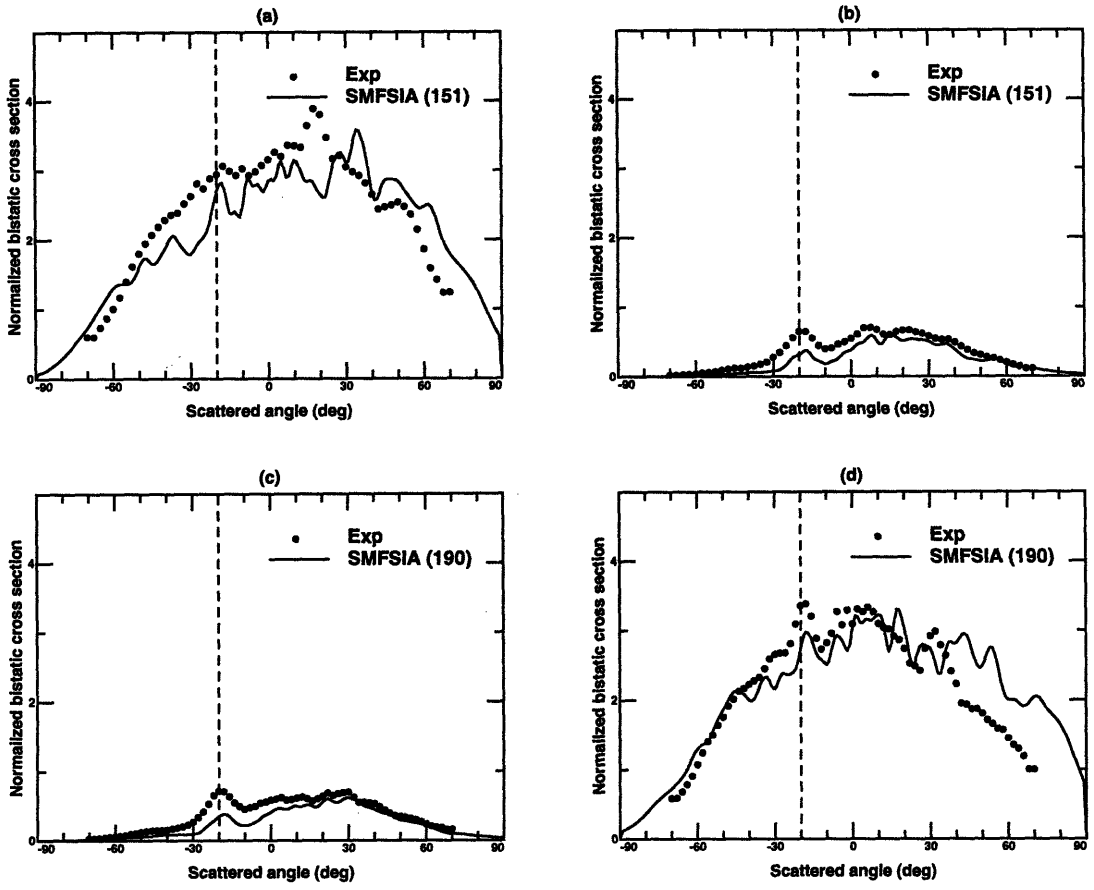

Figure 4.5: Comparison of Monte Carlo SMFSIA with experimental data. Surface area of 256 square wavelengths with an rms height of 1 wavelength and correlation length of 3 wavelengths. (a) σ_{hh} (b) σ_{vh} (c) σ_{hv} (d) σ_{vv}

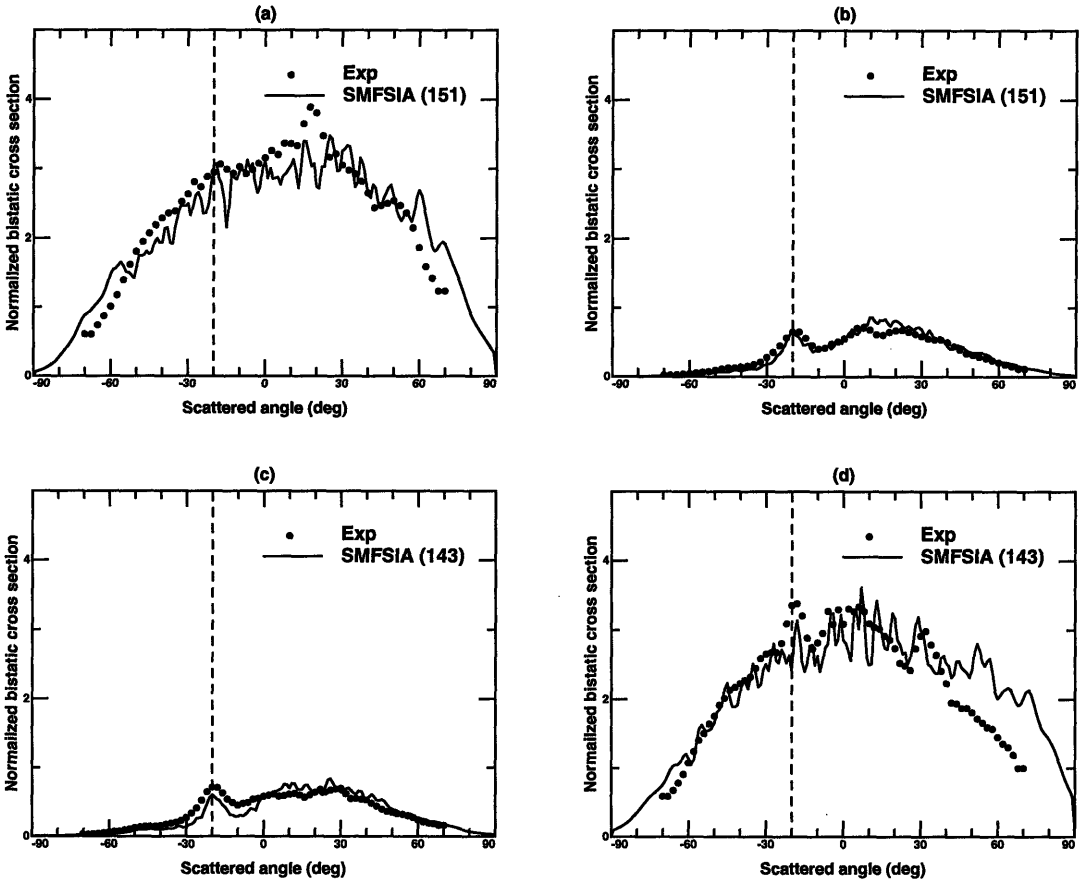

Figure 4.6: Comparison of Monte Carlo SMFSIA with experimental data. Surface area of 1024 square wavelengths with an rms height of 1 wavelength and correlation length of 3 wavelengths. (a) σ_{hh} (b) σ_{vh} (c) σ_{hv} (d) σ_{vv}

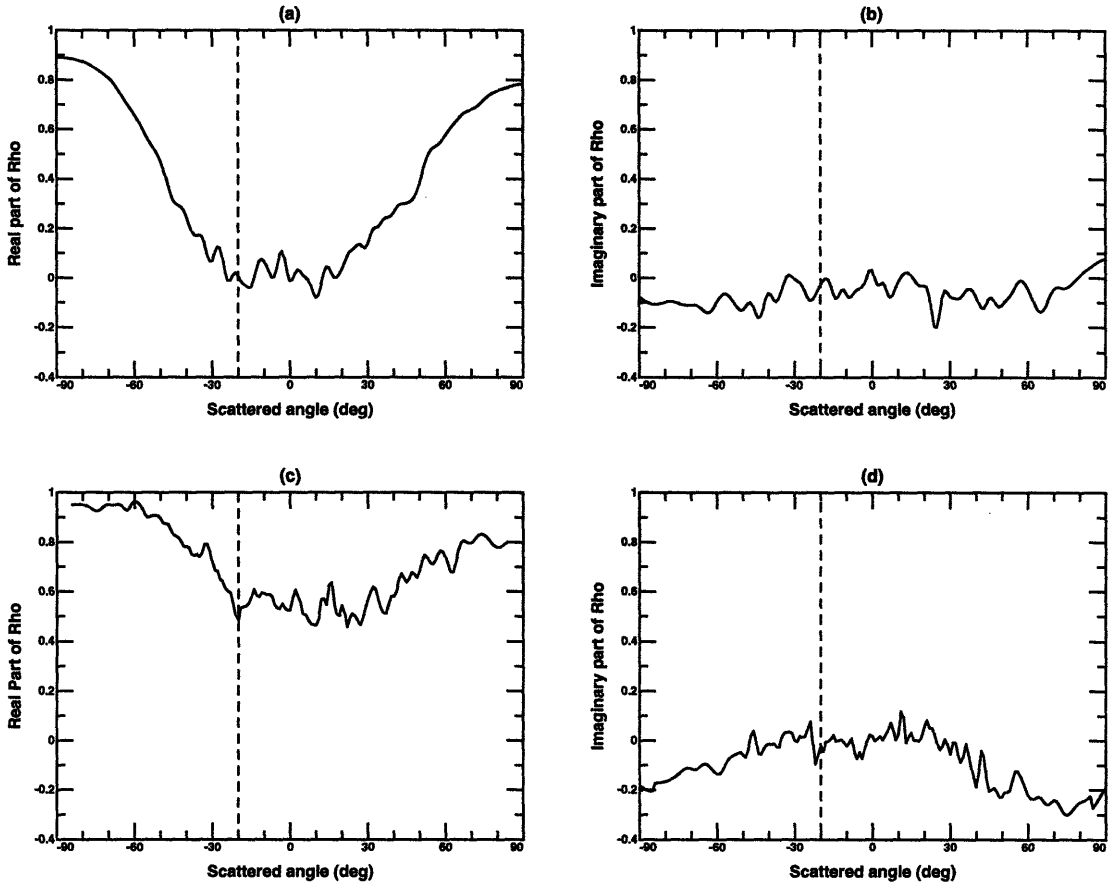

Figure 4.7: SMFSIA predictions of ρ (a) Real part of ρ for the simulations of Figure 4.1 (b) Imaginary part of ρ for Figure 4.7 (a) (c) Real part of ρ for the simulations of Figure 4.6 (d) Imaginary part of ρ for Figure 4.7 (c)

curate numerical model of scattering from these surfaces could be created. The close agreement between Monte Carlo predictions and results of a controlled laboratory experiment shows the accuracy of the Monte Carlo method. Polarimetric calculations of the $hh - vv$ correlation coefficient ρ were also illustrated, and showed that small values of ρ not predicted by the analytical theories can be obtained from the very rough surface types investigated.

Chapter 5

A Numerical Study of Ocean Scattering

5.1 Background and Motivation

Previous chapters of this thesis have dealt with surfaces whose properties were well known. The terrain profiles of Chapter 2, pyramidal surfaces of Chapter 3, and fabricated realizations of a Gaussian random process in Chapter 4 all allowed very accurate descriptions of the scattering surface to be included in the numerical model. Beginning in this chapter, a random surface whose statistical properties are much more difficult to describe is considered for use in a Monte Carlo simulation. The surface to be studied is that of the ocean, which has spatially and temporally varying properties affected by both local and non-local interactions that can be extrememly complex. Since this thesis is concerned primarily with electromagnetic scattering models and not with the physical forces that govern properties of the ocean surface, the description of the ocean surface used will be limited only to the relatively simple models currently available in the literature. The limitations of these descriptions

therefore also will limit the accuracy of the numerical simulation, so that this study can only be considered an initial investigation of scattering properties for an ocean-like surface model. The results, however, should allow some insight into the physics of ocean scattering which can be useful in future numerical studies with a more realistic ocean surface model.

Scattering from the ocean surface has been of interest since the development and application of radar in maritime environments in the 1940's [108]. Since backscatter from the ocean is the principle source of clutter for a monostatic radar operating at sea, its characterization is important for accurate radar system design and description. The backscattering cross section of the ocean also has been found to depend on local wind speed over the ocean, so that measurements allow wind speed and also direction over the ocean surface to be detected remotely. Forward scattering from the ocean is important for communication or radar systems operating at sea since it governs the degree to which multipath interference is significant. Forward scattering has been less studied, however, since its measurement requires a bistatic sensor for non-normally incident configurations. Although the numerical model to be applied in this chapter is able to provide scattered field predictions for all possible bistatic scattering angles, only the backscatter and forward scatter regions will be considered due to the above motivations and to the immense amount of information contained in a full bistatic scattering pattern.

A review of previous studies of ocean scattering follows in the next section. More detailed reviews can be found in [109] and [110].

5.1.1 Previous studies of ocean scattering

Although many studies of sea scattering were performed in the late 1940's to early 1950's [108], little progress in understanding the mechanisms of sea clutter was made until the mid 1950's, when it was observed that ocean backscatter at mid range incidence angles seeemed to be determined by waves in the ocean surface whose wavelengths were half that of the incident electromagnetic wavelength [111]. This phenomenon, known as Bragg scattering, agreed qualitatively with the predictions of the SPM, and created a link between electromagnetic scattering models and a power spectrum description of the ocean surface as discussed in Chapter 1. Interest in verification of this idea led to a series of measurements performed by the Naval Research Laboratory in the mid-late 1960's [112]-[115], and eventually to the development of a composite surface model for ocean backscatter in which SPM predictions are averaged over a slope probability density function which models the long wavelength portion of the ocean spectrum's influence on short wavelength Bragg scattering [36]-[43]. Initial comparisons between composite surface model predictions and the NRL's measurements showed a good quantitative agreement overall after some adjustments to account for variations in the assumed probability density functions in the data processing [115].

The initial success of these studies led to further interest in refining models for ocean scattering and to more detailed experimental campaigns. One such campaign was that of the NASA AAFE airborne K_u band sensor, whose circular flights over the ocean revealed a wind direction dependent signal which showed a maximum cross section in the upwind direction with minima in the cross wind direction and a lesser

maximum in the downwind direction [116]. The accurate measurements of observation direction relative to wind direction of this data allowed new models of the ocean spectrum to be proposed which included an anisotropic high frequency portion [41]. In addition, the AAFE campaign clearly showed the potential for remote measurement of ocean wind speed and direction using microwave wavelengths.

Many other experimental campaigns have been carried out since 1977, including flights of a K_u band scatterometer on the SEASAT satellite and a number of airborne and platform measurements [117]-[123]. More recently, the availability of larger data sets of spaceborne ocean SAR imagery have increased interest in the phenomena which govern formation of these images [109],[124]-[127]. However, these campaigns have primarily been used to refine empirical models of ocean scattering at specified frequencies and polarizations, with no significant variations in the composite surface model used in theoretical comparisons having been proposed. Although the composite surface model has been successful in producing a qualitative agreement with most available ocean scattering data, its basis remains a heuristic one, as the division of the ocean surface into a "small" and "long" scale remains an unclear process. This chapter, therefore, is primarily concerned with investigation of the composite surface model

The next section gives an overview of the ocean surface models to be applied in this chapter. A desciption of the numerical scattering model used follows, and a brief review of approximate theories for ocean scattering is given in Section 5.4. Studies of ocean backscattering and forward scattering are described in Sections 5.5 and 5.6 respectively for a power law ocean spectrum. Section 5.7 considers the composite sur-

face model for more realistic ocean spectra, and conclusions are presented in Section 5.8. A method for evaluating the physical optics integral for an isotropic power law ocean spectrum is described in the appendix.

5.2 Description of the Ocean Surface

Although the equations of fluid dynamics allow some basic relationships to be derived between the forces which produce ocean surface waves and their character [128], the overall process by which rough ocean surfaces are created remains too complicated for present theories. Interactions between different scales of roughness, the presence of non-locally generated waves which propagate into the region of interest, and the forces of wind stress and surface tension combine to make ocean surfaces difficult to characterize. A statistical description of the ocean surface has been a subject of research in oceanography for quite some time, especially given the motivation of its importance in the composite surface model. The work of Cox and Munk [129] in 1954 provided such a description through analysis of the speckle patterns produced by optical glare off the ocean surface. Cox and Munk found their data to be well fit by modeling the ocean as a skewed Gaussian process, whose slope probability density function was that of a Gaussian function times a polynomial. In addition, Cox and Munk derived relationships between the local wind speed and the slope variance of this process, which effectively determines the width of the optical glare pattern. The Cox and Munk data provides enough information to model scattering from the ocean in the geometrical optics limit, which requires only a slope variance for the ocean to produce predictions. However, the SPM portion of the composite surface model

requires description of the ocean spectrum or correlation function as well.

Measurements of the ocean spectrum have been pursued extensively, primarily through the use of wave height recording buoys on the ocean and measurements made in indoor wave tanks [110]. These measurements actually record wave heights versus time, which then determines the temporal frequency spectrum of the ocean. Under an assumption of a particular dispersion relation for ocean waves (which is non-linear and varies between gravity and capillary type waves [128]), the temporal frequency spectrum can be transformed into the spatial frequency spectrum desired. It should be noted that the portion of the spatial frequency spectrum of most interest in the composite surface model corresponds to the same spatial scales as that of the electromagnetic wavelength. Therefore, at microwave frequencies, accurate measurements of ocean waves of decimeter sizes or less are required. Such measurements are not usually possible in a real ocean environment, given the presence of much larger waves which mask these smaller variations, but instead have been performed almost exclusively through the use of wave tanks. Extrapolation of wave tank spectra to ocean spectra remains an uncertain proposition, but at present wave tank measurements comprise the only reliable data for the high frequency portion of the spectrum needed.

Although the ocean random process itself is clearly not a purely Gaussian random process, its deviation from a Gaussian process is relatively small and as such may be neglected in an initial model [130]. The reduction in complexity associated with a purely Gaussian surface model further motivates this simplification. Note that use of a stationary Gaussian ocean process removes any potential upwind-downwind

assymetry in predicted ocean scattering behavior, as such a process must have symmetric properties when viewed in opposite directions [131]. Variations between up wind and cross wind scattering behaviors are still retained however. Third and higher order statistics of an ocean process have been incorporated in an approximate scattering model in [27], again primarily to obtain the relatively small up-down wind assymetry observed in ocean backscattering.

A number of different models for the ocean spectrum have been proposed, based either on ocean or wave tank measurements or on empirical fits to radar backscattering data through the composite surface model [128],[130]-[138]. These models also are based on an equilibrium assumption, which implies that the wind forces which generate the spectrum have been applied for a sufficient time and over sufficient distances to cause an equilibrium to be reached between the applied wind forces and the dissipation mechanisms of friction and breaking. A brief description of three recent models for the ocean spectrum available in the literature and applied in this thesis follows.

5.2.1 Power law spectrum

One of the simplest models available for the ocean spectrum and applied in the literature [42] is that of a power law

$$\Psi(k,\phi) = a_0 k^{-4} \tag{5.1}$$

where Ψ represents the ocean spectrum amplitude in m^4, k represents the spatial wavenumber of the ocean, ϕ represents the azimuthal angle of the two dimensional

spectrum, and a_0 is a specified constant. A k^{-4} dependence for the ocean spectrum has been proposed by a number of authors based on purely physical requirements [130], although other authors have proposed slight deviations from this form [118]. Also, the proposed power law spectrum is only valid for a specified portion of the ocean spectrum given by $k_{dl} < k < k_{du}$, as evidenced by the singularity of the spectrum at $k = 0$. Measured ocean spectra are well fit qualitatively by a truncated k^{-4} spectrum near the Bragg scattering portion for microwave frequencies, although variations with wind speed and azimuth angle are not included in this description. For such a truncated power law spectrum, the surface variance is given by

$$\sigma^2 = \int_{k_{dl}}^{k_{du}} dk\ k \int_0^{2\pi} d\phi\ \Psi(k,\phi) \tag{5.2}$$

$$= \pi a_0 \left(\frac{1}{k_{dl}^2} - \frac{1}{k_{du}^2} \right) \tag{5.3}$$

since the ocean spectrum is defined by

$$\Psi'(k_x, k_y) = \frac{1}{(2\pi)^2} \int_{-\infty}^{\infty} dx \int_{-\infty}^{\infty} dy\ R(x,y)\ e^{ik_x x + ik_y y} \tag{5.4}$$

where $R(\alpha,\beta) =< f(x,y) f(x+\alpha, y+\beta) >$ is the covariance function of the Gaussian process, $f(x,y)$ represents one realization of this process, and a change from polar to rectangular coordinates has been made in the spectrum for convenience. Similarly, the total slope variance of the k^{-4} spectrum can be obtained from

$$s^2 = \int_{k_{dl}}^{k_{du}} dk\ k^3 \int_0^{2\pi} d\phi\ \Psi(k,\phi) \tag{5.5}$$

$$= 2\pi a_0 \log |k_{du}/k_{dl}| \tag{5.6}$$

From these relationships, it is clear that the variance of a power law spectrum ocean is dominated by its low frequency components since they comprise the highest amplitude portions of the spectrum, while the slope variance is determined by the width of the spectrum. Note that this slope variance dependence emphasizes the need for a cutoff wavelength in the composite surface model, as the slope variance of such a surface could be made very large by extending the spectrum into very short wavelegths beyond the Bragg scatter region which are known to have almost no real effect on ocean scattering.

5.2.2 Durden-Vesecky spectrum

A second model for the ocean spectrum from the literature is that of Durden and Vesecky [135]. This spectrum is based on empirical fits to radar backscattering data under an assumed composite surface model, and has been applied in the literature to match passive ocean measurements as well [92]-[93]. The Durden-Vesecky spectrum is given by

$$\Psi(k,\phi) = \frac{a_0}{2\pi k^4}\left(1 + c(1 - e^{-(k/89.44)^2})\cos 2\phi\right)\begin{cases} e^{-0.74(\frac{9.81}{U_{19.5}^2 k})^2} & k < 2 \\ \left(\frac{1.25 k u_*^2}{9.81 + 7.25\times 10^{-5} k^2}\right)^{0.225\log_{10}(k/2)} & k > 2 \end{cases}$$

where u_* is the wind friction velocity at the ocean surface in m/s,

$$U_h = \frac{u_*}{0.4}\log\frac{h}{0.0000684/u_* + 0.00428u_*^2 - 0.000443} \tag{5.7}$$

is the windspeed in m/s at h meters above the ocean surface, and a_0 is a constant originally set equal to 0.004 in [135] but modified to 0.008 in [93] to achieve a better

fit to measured data. The constant c which determines the azimuthal dependence of the spectrum is given by

$$c = \frac{2(1-R)/(1+R)}{1-D} \tag{5.8}$$

where

$$R = \frac{0.003 + 1.92 \times 10^{-3} U_{12.5}}{3.16 \times 10^{-3} U_{12.5}} \tag{5.9}$$

$$D = \frac{\int_0^\infty dk\ k^2\ S(k)\ e^{-(k/89.44)^2}}{\int_0^\infty dk\ k^2\ S(k)} \tag{5.10}$$

and $S(k)$ is the spectrum divided by $\frac{1}{k^4}\left(1 + c(1 - e^{-(k/89.44)^2})\cos 2\phi\right)$.

Clearly, the Durden-Vesecky spectrum is much more complicated than the power law spectrum described previously, but contains variations with both azimuthal angle and wind speed. Note that the azimuthally varying portion of the spectrum is similar to that proposed in [43] and preserves the ratio of upwind to crosswind slope variances R measured by Cox and Munk. The degree of azimuthal anisotropy of the spectrum is a function of spatial wavenumber, with higher frequency (shorter) waves being more anisotropic as is needed in the composite surface model to reproduce measured azimuthal variations. The exponential rolloff of the spectrum for $k < 2$ represents a well studied portion of the ocean spectrum, as buoy measurements on the open ocean are possible for such large waves. However, the portion of the spectrum for $k > 2$ is based on fits to backscatter data alone and effectively represents a deviation from a pure power law spectrum (given by the k^{-4} portion of the spectrum) as a function

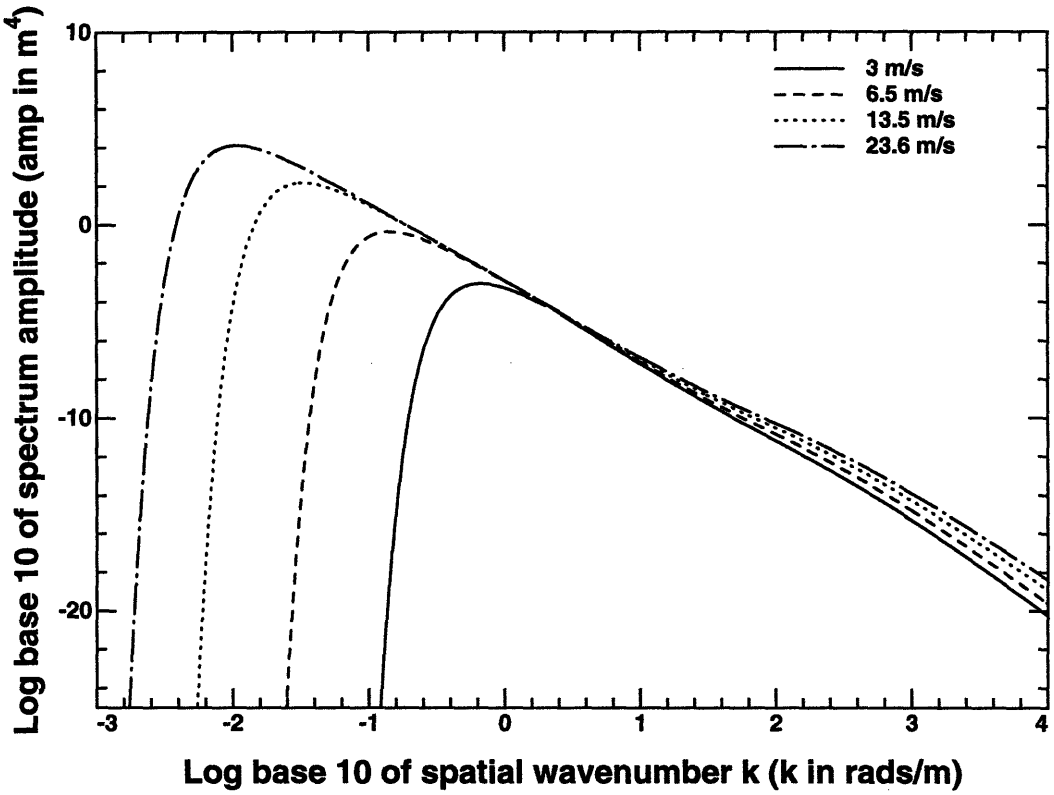

Figure 5.1: Amplitude of Durden-Vesecky spectrum for 4 wind speeds

of wind speed. Figure 5.1 plots the Durden-Vesecky spectrum for three wind speeds on a $\log \Psi$ versus $\log k$ scale to illustrate the k^{-4} dependence for $a_0 = 0.008$. Note the changes in the low frequency cutoff predicted by the spectrum, indicating a much larger surface rms height at the higher wind speeds, as well as the small increase in spectrum amplitude at the higher frequencies. This increase at the higher frequencies is important, since changes in high frequency amplitudes directly cause variations in the Bragg scatter ocean cross section with wind speed in the composite surface model.

5.2.3 Donelan-Banner-Jahne spectrum

A final model for the ocean spectrum presented in [130] is based upon empirical fits to the wave tank frequency spectrum measurements of Donelan, Banner, and Jahne (DBJ), and has also been applied with an SPM model to match vertically polarized backscattering data at several frequencies. The DBJ spectrum is given by

$$\Psi(k,\phi) = \frac{a_0}{k^4} e^{-(0.14+5(k_p/k)^{1.3})\phi^2} e^{-(k_p/k)^2-(k/6283)^2} 1.7^{\exp[-(k^{1/2}-k_p^{1/2})^2/(0.32k_p)]} \left\{ \frac{1}{1+(k/100)^2} + S(0.8k\ sech[(k-400)/450]) \right\} \tag{5.11}$$

where

$$k_p = \frac{9.81}{\sqrt{2}u^2} \tag{5.12}$$

$$S = 10^{(-4.95+3.45(1-e^{-u/4.7}))} \tag{5.13}$$

and u is the windspeed at 10 meters above the ocean surface in m/s. The DBJ spectrum is composed of several individually derived portions which determine its behavior in specific wavenumber regions, from its rolloff at both high and low frequencies to its eventual saturation with increasing wind speed. The amplitude a_0 is set equal to 0.000195 to insure a reasonable variance obtained for the ocean process when the spectrum is integrated as with the power law spectrum discussed previously. Again, the DBJ spectrum is based primarily upon a k^{-4} dependence for the ocean spectrum, with additional factors added to fit the observed variations with wind speed in certain spectral regions. Note also that the azimuthal variation of the DBJ spectrum, defined

for $-\pi < \phi < \pi$, makes the longer waves more anisotropic that the shorter waves, so that a Bragg scatter mechanism cannot explain observed azimuthal variations in ocean cross section for most microwave frequencies. The distinction between the Durden-Vesecky and DBJ spectra on this issue emphasizes the current lack of knowledge on true ocean spectra in the capillary wave region and the difficulty in measuring these spectra. Note also that the azimuthal dependence of the DBJ spectrum is not that of a stationary Gaussian process, as the exponential azimuth angle dependence is not origin symmetric. For use in stationary process scattering theories, the spectrum must be symmetrized as in [130] by using $\Psi'(k,\phi) = [\Psi(k,\phi) + \Psi(k,\phi+\pi)]/2$. Figure 5.2 plots the DBJ spectrum for three wind speeds, again on a $\log \Psi$ versus $\log k$ scale. Similar behavior to the Durden-Vesecky spectrum is observed, with the difference in azimuthal behavior not illustrated in this one dimensional plot. Figure 5.3 overlays both the Durden-Vesecky and DBJ spectra times k^4, known as the curvature spectrum, to compare the wind speed variations of the two descriptions. Overall, similar trends are observed in the two spectra, although the high frequency rolloff of the DBJ spectrum is not included in the Durden-Vesecky spectrum. This distinction is not expected to have effects on scattering below frequencies of 30 GHz ($k = 628.3$) since the corresponding Bragg wavenumbers lie below the beginning of the DBJ high frequency rolloff.

5.3 Numerical Model for Ocean Scattering

Given a choice of spectrum description for the ocean surface, a numerical model similar to that described in Chapter 4 can be applied to produce predictions of average

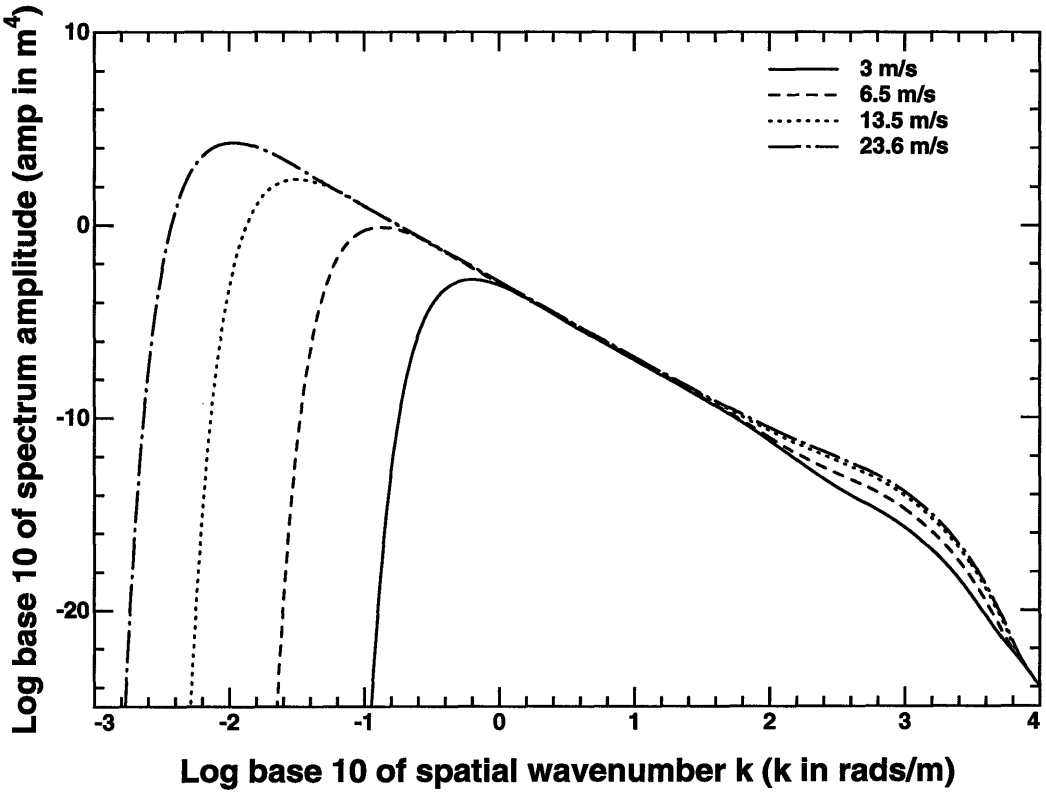

Figure 5.2: Amplitude of DBJ spectrum for 4 wind speeds

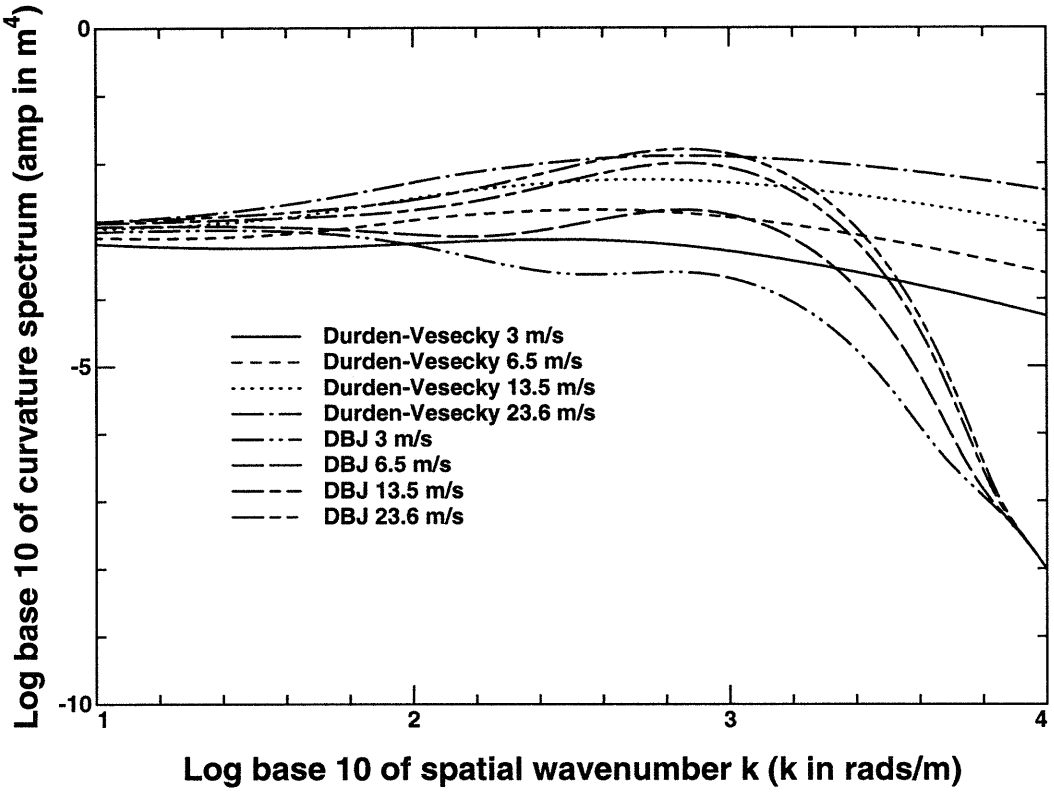

Figure 5.3: Comparison of Durden-Vesecky and DBJ curvature spectra

scattered electromagnetic power through a Monte Carlo simulation. In contrast to the narrow band Gaussian spectrum surfaces of Chapter 4 however, the ocean surface models to be investigated are comprised of a wide range of spatial scales ranging over several orders of magnitude both larger and smaller than the electromagnetic wavelength. Inclusion of all these scales in a numerical simulation is impossible, given their large range and the computational costs associated with two dimensional surface scattering problems. Use of a numerical simulation will inherently imply a low and high frequency cutoff wavenumber in the portion of the ocean spectrum simulated, since the finite size of surfaces used limits their low frequency content and the non-zero discretization size used limits their high frequency content. As a result, direct extrapolation of numerical model results to a full ocean spectrum is not immediately possible, and is warranted only if convergence with respect to the high and low frequency spectral cutoffs can be demonstrated. These variations are also of interest themselves, as they should illustrate some of the physical processes at work in ocean scattering, at least as described by the composite surface model. Since varying the low and high frequency cutoffs of the spectrum does not affect the Bragg spectral component (unless it is directly cutoff) but does affect the slope variance of the entire spectrum simulated (as given in equation (5.5)), these variations should illustrate any tilting affects due the "long" wavelength portion of the spectrum simulated.

The numerical model to be applied models the ocean surface as being perfectly conducting. Sea water actually is a fairly high loss medium, with a dielectric constant of approximately $(39.7, 40.2)$ at K_u band [139] which increases with decreasing frequency primiarily due to ionic conductivity. A model for ocean scattering which

includes the effect of this loss will be discussed in Chapter 6 when passive remote sensing is considered. However, in active remote sensing, the finite conductivity of the ocean surface is expected to have only a fairly small influence on ocean cross sections, especially when considered on a decibel scale. Given the much greater complexity associated with the penetrable surface numerical model of Chapter 6 and the fact that only perfectly conducting surface models will be compared in this chapter, use of a perfectly conducting surface for the ocean should not significantly influence the results of this study. Comparisons with experimental data made in Section 5.7 will include the effect of surface conductivity through the composite surface model.

5.3.1 Canonical grid approach

As stated previously, the numerical model of this chapter is essentially the same as that of Chapter 4: a method of moments solution for finite size realizations of the perfectly conducting ocean surface random process illuminated by a tapered beam incident wave. However, some problems with the model of Chapter 4 occur when simulating ocean surface back scattering which necessitate improvements. The problems are due to a desire for simulation of ocean surface backscattering cross section at incident polar angles ranging from 0 to 60 degrees, for which cross section values can vary by a scale of more than 40 dB. The very small values of ocean backscattered cross section at an incidence angle of 60 degrees make simulations very sensitive to any edge scattering effects due to the finite size of the surface modeled. Although these contributions can be reduced by increasing the tapering of the incident beam, such an increase has the effect of increasing the angular width over which scattered

cross sections are averaged and thereby reducing angular resolution of scattered field predictions. Edge contributions can also be reduced by increasing the simulated surface size while maintaining a constant incident beam size if the associated increase in computational domain size remains within computational limitations. It is this latter approach that motivates an increase in computational efficiency so that larger surface sizes can be included to reduce edge effects.

The method used to increase computational efficiency is a canonical grid (CAG) approach as described in [60]. Recall that the SMFSIA of Chapter 4 was composed of nested iterative methods for inversion of the method of moments matrix equation given by

$$(\overline{\overline{Z}}^{(s)} + \overline{\overline{Z}}^{(FS)})\overline{x}^{(1)} = \overline{b} \tag{5.14}$$

$$(\overline{\overline{Z}}^{(s)} + \overline{\overline{Z}}^{(FS)})\overline{x}^{(n+1)} = \overline{b}^{(n+1)} \tag{5.15}$$

$$\overline{b}^{(n+1)} = \overline{b} - \overline{\overline{Z}}^{(w)}\overline{x}^{(n)} \tag{5.16}$$

where solution of the above matrix equations was accomplished using a CG-FFT approach since flat surface multiplies could be performed with a fast Fourier transform. However, the above method remains an order N^2 technique, since the weak matrix multiplies of each iteration are order N^2. The canonical grid approach avoids this problem by expanding weak matrix elements into a translationally invariant Taylor series whose individual terms again can be multiplied using the FFT. This series can

be written as

$$G(R) - G_{FS}(\rho_R) = \frac{(ikR-1)\exp(ikR)}{4\pi R^3} - \frac{(ik\rho_R - 1)\exp(ik\rho_R)}{4\pi\rho_R^3} = \sum_{m=1}^{M} a_m(\rho_R)(\frac{z_d^2}{\rho_R^2})^m$$

where $z_d = f(x,y) - f(x',y')$, and the first few terms of this series are

$$a_1 = \frac{e^{ik\rho}}{4\pi\rho^3}\left(\frac{3}{2}\right)\left(1 - ik\rho - \frac{(k\rho)^2}{3}\right) \tag{5.17}$$

$$a_2 = \frac{e^{ik\rho}}{4\pi\rho^3}\left(\frac{-15}{8}\right)\left(1 - ik\rho - \frac{2(k\rho)^2}{5} + i\frac{(k\rho)^3}{15}\right) \tag{5.18}$$

$$a_3 = \frac{e^{ik\rho}}{4\pi\rho^3}\left(\frac{35}{16}\right)\left(1 - ik\rho - \frac{3(k\rho)^2}{7} + i\frac{2(k\rho)^3}{21} + \frac{(k\rho)^4}{105}\right) \tag{5.19}$$

with higher order terms easily derived using a symbolic mathematical program. Note that this expansion is similar to an expansion of the Fresnel term $e^{i\frac{kz_d^2}{2\rho}}$ which occurs in standard diffraction problems as $1 + i\frac{kz_d^2}{2\rho} - \ldots$. Clearly such an expansion is useful only for surfaces with relatively small slopes, as the power series above converges reasonably only for fairly small values of $\frac{kz_d^2}{2\rho}$. It is this convergence requirement that eliminated the possibility of the more efficient canonical grid approach for the terrain profiles of Chapter 1, which often had variations of several hundred wavelengths within reasonably short horizontal distances. However, the ocean spectra to be considered in this chapter have relatively small variations compared to the electromagnetic wavelength given that only the portion of the spectrum near this wavelength is able to be simulated. The number of terms necessary in the CAG series to retain accuracy will be considered in the following sections.

5.3.2 Neumann iteration

A second approach which can be applied to increase program efficiency is that of Neumann iteration, which essentially is a Born series solution to the MFIE

$$\hat{n} \times \overline{H}(\overline{r}) = 2\hat{n} \times \overline{H}_{inc} + 2\hat{n} \times \int dS' \left\{ \nabla \times \overline{\overline{G}} \cdot [\hat{n}' \times \overline{H}(\overline{r}')] \right\} \tag{5.20}$$

which approximates tangential magnetic fields on the surface as

$$\left[\hat{n} \times \overline{H}(\overline{r})\right]^{(j)} = 2\hat{n} \times \overline{H}_{inc} + 2\hat{n} \times \int dS' \left\{ \nabla \times \overline{\overline{G}} \cdot \left[\hat{n}' \times \overline{H}(\overline{r}')\right]^{(j-1)} \right\} \tag{5.21}$$

with $\left[\hat{n} \times \overline{H}\right]^{(0)} = 2\hat{n} \times \overline{H}_{inc}$, the physical optics approximation. Equation (5.21) above can be iterated to achieve higher order Neumann solutions, each of which corresponds to given order of scattering. Note that a discretized version of equation (5.21) results in expressing higher order tangential magnetic fields as proportional to the same matrix as the method of moments times present order tangential magnetic fields. Thus, the same techniques for more efficient matrix multiplication as in the method of moments can be applied to the Neumann iteration, with the result being effectively the same procedure as the SMFSIA except that the conjugate gradient solution step of the SMFSIA is replaced by a Neumann iterative solution.

A comparison of the SMFSIA and the Neumann iterative approach clearly shows the SMFSIA to produce superior convergence properties. As discussed in Chapter 4, the Neumann series approach has been shown to have convergence problems when used at large incidence angles or for surfaces with large slopes. This is due to the fact that the Neumann series uses the same coefficient weightings for the contribu-

tion of each previous order of scattering regardless of how significant each of those contributions may be for a given surface. In contrast, a conjugate gradient solution adjusts these coefficients in an attempt to minimize the current residual of the matrix equation, so that its convergence properties are almost by definition superior. However, the Neumann series is appealing in that its terms correspond physically to the contributions of individual multiple scattering terms, and as such may indicate the possibility of eventually obtaining improved analytical approximations through inclusion of these terms. In addition, a single Neumann iteration requires only one matrix multiplication while a single conjugate gradient iteration requires two. Thus, for surfaces for which the Neumann iteration technique converges to a desired accuracy after one iteration, the method has a computational advantage as well.

Comparisons between full method of moment results and single Neumann iteration results will be made in Section 5.5.

5.3.3 Separation of coherent and incoherent terms

For an infinitely large ocean surface, reflected and transmitted coherent fields consist of individual propagating plane waves whose amplitude is reduced as the surface height fluctuations increase. However, surfaces simulated numerically are of finite size, and the coherent field is no longer a plane wave but rather spreads over a range of scattered angles. Since scattering from the ocean is primarily incoherent at microwave frequencies, only incoherent scattered powers are of interest in the numerical simulation. Thus, the removal of any coherent fields which remain due to finite surface size effects is required in the Monte Carlo simulation. This removal is

performed by calculating incoherent scattered powers as

$$< P_s^{inc} >=< |\bar{E}_s - < \bar{E}_s > |^2 > \tag{5.22}$$

where, in the Monte Carlo simulation, $< \cdot >$ indicates averaging over the number surface realizations simulated, and P_s^{inc} represents the incoherent scattered power for a specific configuration. In the simulation results presented in Sections 5.5 and 5.6, surface rms heights ranging from 0.02 to 0.64 wavelengths are considered, so that coherent fields are clearly present in the lower rms height cases. The above procedure allows their influence to be removed so that only incoherent scattered powers can be compared.

5.4 Approximate Models for Ocean Scattering

Standard approximate theories scattering from the ocean are based on either a physical optics (PO), geometric optics (GO), SPM, or composite surface approximation as discussed in Chapter 1. The PO approximation results in an expression for bistatic cross sections which requires integration of an exponential function involving the surface correlation function. Since this integral is usually difficult to perform, especially for surfaces with large rms variations on an electromagnetic scale, a further stationary phase approximation can be made which defines the geometric optics approximation. Both the PO and GO approximations predict no polarization dependence to co-polarized cross sections for perfectly conducting surfaces, which is at strong variance with observed off-normal backscattered cross sections but in agreement with observed forward scatter cross sections. Thus, PO and GO results are expected to be

more accurate for forward scattering.

The physical optics approximation can also be used in a Monte Carlo simulation. Although the ensemble average calculated in the Monte Carlo simulation can be obtained analytically with PO approximated surface currents, difficulties associated with evaluation of the resulting expression limit use of the analytical solution. The appendix of this chapter discusses a method for calculation of the analytical PO solution, but the approach is limited to a power law ocean spectrum and relatively small rms height surfaces. Monte Carlo simulations of PO approximated scattering can be performed for arbitrary ocean spectra or rms height surfaces. One clear distinction between Monte Carlo ensemble averages and analytically calculated ensemble averages is the finite number of realizations inherent in the Monte Carlo approach. Also, Monte Carlo PO results are calculated for finite size surface realizations as opposed to the infinitely large surfaces of the analytical solution. Comparison of Monte Carlo PO results with their analytically evaluated counterparts will provide a useful tool for assessing the influence of these factors on Monte Carlo predictions. A good agreement between the Monte Carlo and analytical PO results indicates that a sufficient number of realizations has been used in the simulation and that the effects of finite surface size are not important.

The SPM predicts incoherent scattering from the ocean surface to be proportional to one spatial frequency component of the ocean spectrum alone to first order as discussed in Chapter 1. The SPM also predicts a strong polarization dependence to co-polarized scattering coefficients which increases as the incident observation angle increases. It is this polarization dependence which favors use of the SPM at

higher observation angles, where observed ocean backscattering data shows a large polarization difference, with vertically polarized cross sections exceeding horizontally polarized cross sections by 10 dB or more in some cases at 60 degree observation. However, the small surface height assumptions of the SPM derivation are not applicable to an ocean spectrum in general, so that the theoretical basis for using the SPM in ocean scattering is unclear [110].

The final ocean surface scattering model considered is the composite surface model, which expresses scattering from the ocean surface to be the combination of the geometric optics results in the near forward scattering direction and SPM results away from forward scattering. SPM results, however, are now tilted over an underlying Gaussian slope distribution as described in [39]-[40], for which the primary result is an increase in hh cross sections at large incidence angles. The slope distribution used to tilt SPM contributions and in GO predictions models the "long" wavelength portion of the spectrum, while SPM predictions contain only the "short" wavelength portion. Division between these two regions is made at a specific wavenumber, labeled K_d, which effectively is a parameter of the model. Note, however, that the rms surface height contained in the SPM portion of the spectrum increases as K_d is decreased so that strictly speaking SPM predictions become less valid. References from the literature [15] suggest choice of this wavenumber as approximately $k/3$ where k is the electromagnetic wavenumber, corresponding to a 3 wavelength spatial scale cutoff. Numerical simulations have also been performed for one dimensional surfaces [140] which indicate that backscattering errors can be minimized for a range of incidence angles by choosing K_d as $k/2$. Appropriate choices for K_d which provide minimum

error when compared to the two dimensional surface simulations performed will be considered in the following sections.

5.5 Backscattering

As mentioned previously, numerical calculation of backscattered cross sections from an ocean surface model is difficult due to low scattered field strengths in the backscatter direction. The contribution of edge effects can significantly affect model predictions for non-normal angles where scattered field strengths become extremely low. Numerical results will be presented in this section using the CAG approach, which allows the much larger surface sizes required to reduce edge effects to be simulated. Figure 5.4 illustrates the convergence of predicted normalized backscattered cross sections (as defined in Chapter 1) with surface size simulated for a power law spectrum with high and low frequency cutoffs of $k_{dl} = 73.3$ (4λ) and $k_{du} = 586.4$ $(\lambda/2)$ at a frequency of 14 GHz. An amplitude of $a_0 = 1.273 \times 10^{-3}$ was used for the power law spectrum, which corresponds to the $\frac{0.008}{2\pi}$ amplitude used for the Durden-Vesecky spectrum and results in a $k\sigma$ product of 0.25. The small rms height of this surface shows that SPM predictions should be valid, and should therefore provide a check on edge effects in the simulation. Numerical simulations were run with sampling rates of 8 unknowns per wavelength and surface sizes of $16\lambda \times 16\lambda$, $32\lambda \times 32\lambda$ and $64\lambda \times 64\lambda$ for total matrix sizes of $32,768$, $131,072$, and $524,288$ respectively. Incident fields in the simulations were kept constant as surface sizes were increased by increasing the g parameter correspondingly since the exponential taper width used for the incident field is $g' = L/g$. A taper width g' of 16λ was used in all of the simulations for

incidence angles of 20 degrees or greater, while a plane wave incident field was used for incidence angles less than 20 degrees to avoid a reduction in angular scattered field resolution in this high scattered power region where edge effects should not be significant. Results were generated using the CAG approach with a strong matrix bandwidth of 15 points and with a physical optics initial guess in the conjugate gradient solver, and tests with a single surface realization were performed to determine the importance of retaining CAG series terms. Contributions of the weak matrix CAG terms to the final predicted cross sections were found insignificant (within 0.1 dB), so the weak matrix was neglected entirely in subsequent realizations. Results plotted in Figure 5.4 are averaged over 20 realizations, and comparisons with SPM predictions clearly show that the model is yielding accurate results. Results for the three surface sizes are within $1-2$ dB of one another at all incidence angles except for 50 and 60 degree incidence, where significant differences are observed in the very small horizontally polarized cross sections. A surface size of $64\lambda \times 64\lambda$, however, is seen sufficient to reduce any edge contributions below the predicted SPM levels so that a good agreement can be obtained.

Further results in section 5.5.1 will be presented using a surface size of $64\lambda \times 64\lambda$ and 524,288 unknowns, for which single realization calculations require approximately 5 hours of SP2 node time at the Maui High Performance Computing Center. Surfaces with larger rms heights than those of Figure 5.4 will also be considered, so that weak matrix contributions potentially become more important. Single realization tests performed with the roughest surfaces showed that neglecting CAG series terms causes no greater than a 1 dB inaccuracy for all of the surfaces considered. The much

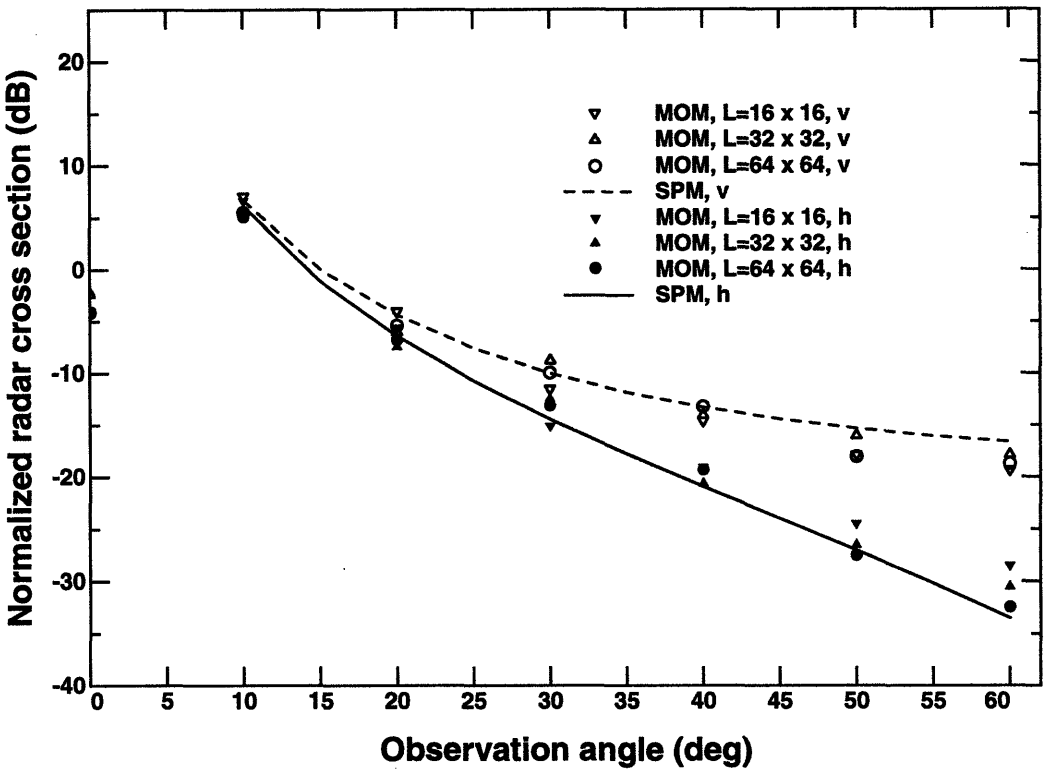

Figure 5.4: Comparison of MOM and SPM backscattering predictions for cutoff wavenumber $k_{dl} = 73.3$: Convergence with respect to surface size

greater computational time required to include CAG series terms makes a Monte Carlo simulation impossible. Therefore, all the results to be presented neglect CAG series terms with a resulting error of approximately 1 dB.

5.5.1 Backscattering from a power law spectrum ocean

Given the simplicity of the power law spectrum, the only spectral variations to be considered are those associated with varying the high and low frequency cutoff wavenumbers of the spectrum. Although amplitude variations are also possible, the $a_0 = 1.273 \times 10^{-3}$ value used previously roughly corresponds to the overall amplitude of the other spectrum models, and therefore will not be varied. Figures 5.5

(a) through 5.10 (a) compare simulation results with SPM predictions for low frequency cutoff wavenumbers varying from 146.6 (2λ) down to 4.58 (64λ), all with a high frequency cutoff of 586.4 ($\lambda/2$). Single realization simulations including surface frequencies above this high frequency cutoff showed no effect on predicted results, so only low frequency cutoff variations are considered. Rms heights of the simulated surfaces range from 0.02 to 0.64 electromagnetic wavelengths, and Figures 5.5 to 5.10 illustrate the effects of this increase on scattered cross sections for the power law surface considered. Note that SPM predictions vary only in the location of the cutoff region between figures, as Bragg scatter portions of the spectrum are not altered by changing the low frequency cutoff. Simulation results are plotted for both *hh* and *vv* cross sections, and both *hv* and *vh* cross sections, which differ by less than 1 dB and indicate the accuracy of the SMFSIA solution, are included as well. Figures 5.5 (b) through 5.10 (b) illustrate the corresponding comparison between Monte Carlo physical optics results (generated for the same set of surfaces as the results of Figures 5.5 (a) through 5.10 (a)) and analytical physical optics predictions evaulated by the method of Appendix A. The good comparison between Monte Carlo and analytical PO results in Figures 5.5 (b) to 5.10 (b) (within 1-2 dB at all incidence angles) demonstrates that the finite surface size and number of realizations in the Monte Carlo simulation are not having a large impact on model predictions. A slight underestimation at higher incidence angles is observed which is believed to be due to the tapered beam of the Monte Carlo simulation. A minimum of twenty surface realizations were averaged for each of the points of these figures, with simulations of independent sets of twenty surface profiles showing convergence to within 1.5 dB. While a larger number of realizations is desirable to reduce this uncertainty, computational limitations prohibited

further simulations, so that a final accuracy of approximately 2.5 dB results for this study.

An examination of Figures 5.5 to 5.10 reveals that overall, little change is observed in model predictions at large incidence angles as the low frequency cutoff frequency is varied, which is consistent with all of the approximate theories. The primary change in predicted cross sections is seen to occur near normal incidence, where the width of an angular cutoff region is seen to decrease as the rms height of the surface increases. This cutoff phenomenon is predicted by the SPM and composite surface models, which obtain a zero scattered power (minus infinity dB) at angles related to cutoff regions in the surface spectrum. Method of moments results, however, are non-zero and are well fit by the physical optics approximation. This can be explained by the fact that SPM predictions generated are first order only, with higher order SPM terms containing a convolution between scales in the spectrum which should produce some scattered power in the cutoff zone. Changing scattered field strengths near normal incidence illustrate the transfer of energy from coherent to incoherent fields as surface rms height increases. The lower rms height surfaces of Figures 5.5 to 5.7 still allow a large coherent reflected wave to exist, so that reduced incoherent powers are observed in the forward direction. However, Figures 5.8 to 5.10, where the $k\sigma$ product is 1 or greater, show no such cutoff phenomena since the coherent field strength is already significantly reduced.

Comparison of Figures 5.5 (b) to 5.10 (b) with Figures 5.5 (a) to 5.10 (a) shows that the physical optics approximation fits MOM results extremely well up to 20 degree incidence for all of the surfaces considered. Beyond 20 degree incidence, how-

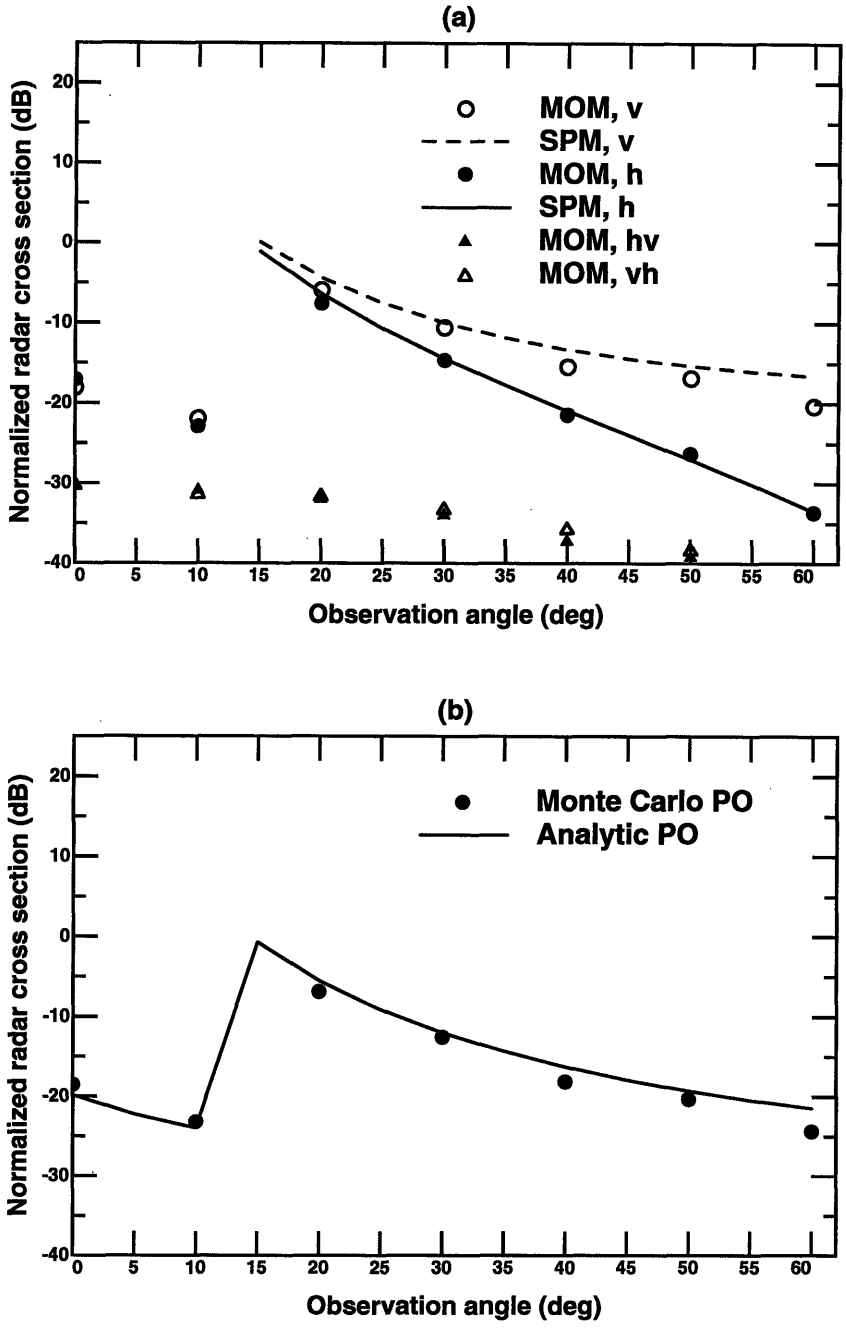

Figure 5.5: Cutoff wavenumber $k_{dl} = 146.6$, $k\sigma = 0.125$ (a) Comparison of MOM and SPM backscattering predictions (b) Comparison of Monte Carlo and analytical PO backscattering predictions

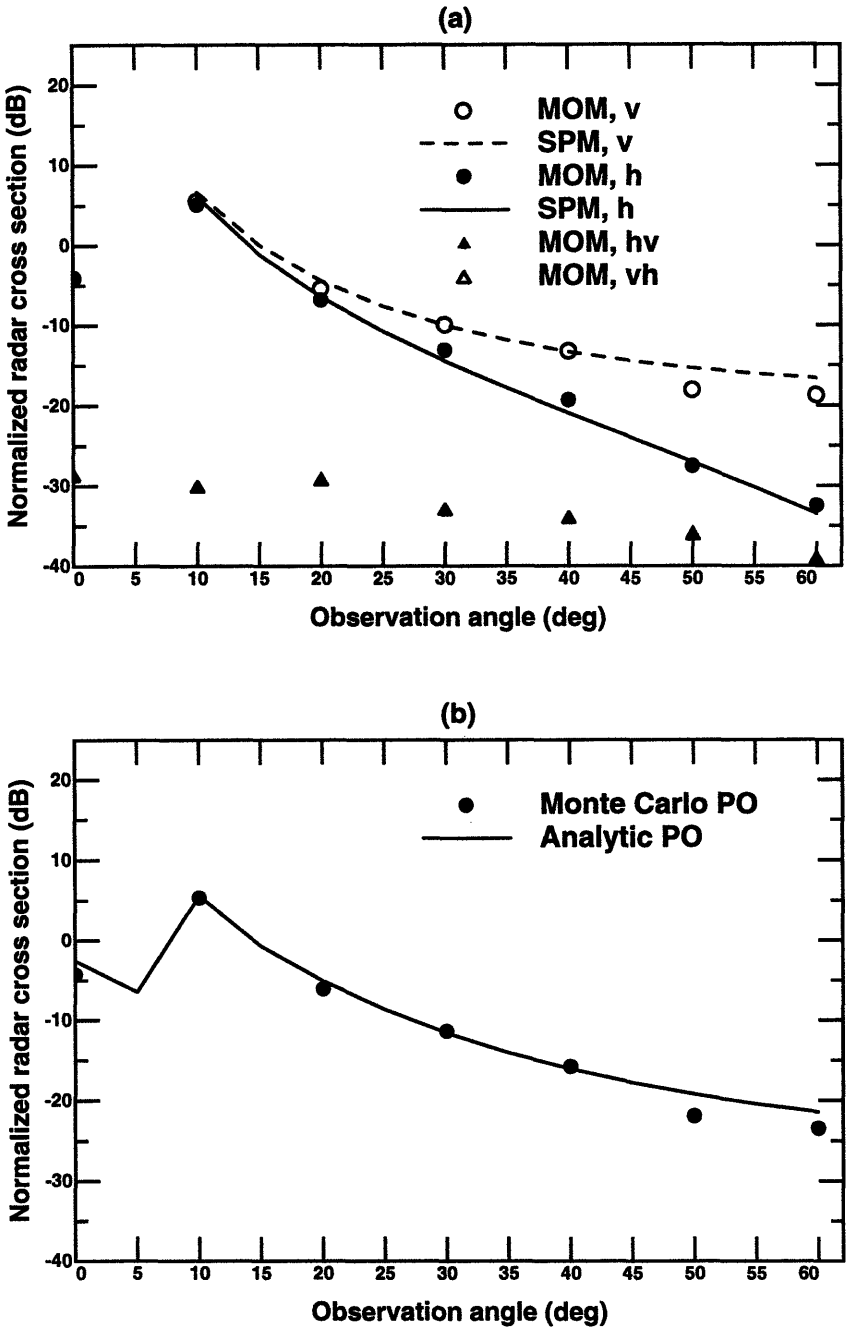

Figure 5.6: Cutoff wavenumber $k_{dl} = 73.3$, $k\sigma = 0.25$ (a) Comparison of MOM and SPM backscattering predictions (b) Comparison of Monte Carlo and analytical PO backscattering predictions

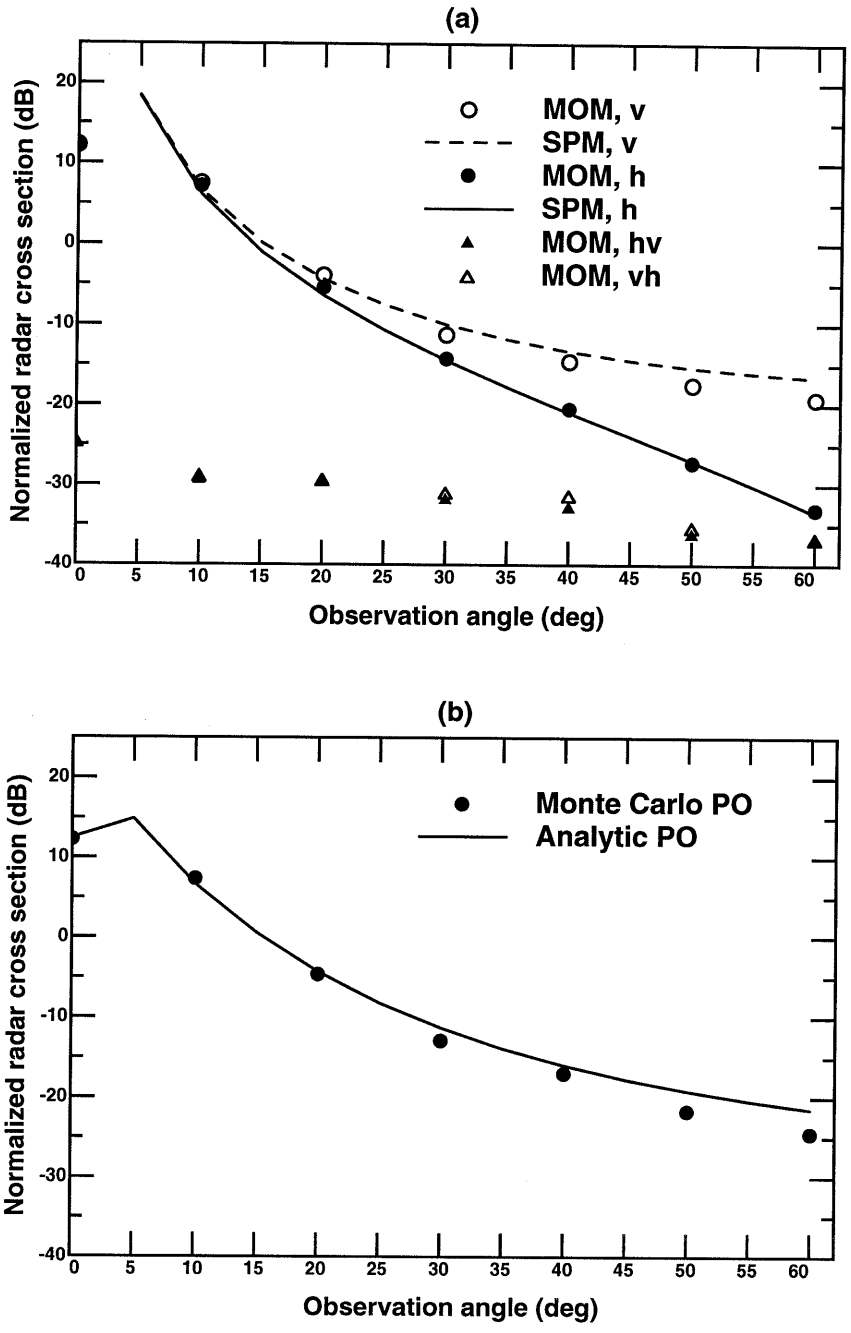

Figure 5.7: Cutoff wavenumber $k_{dl} = 36.6$, $k\sigma = 0.5$ (a) Comparison of MOM and SPM backscattering predictions (b) Comparison of Monte Carlo and analytical PO backscattering predictions

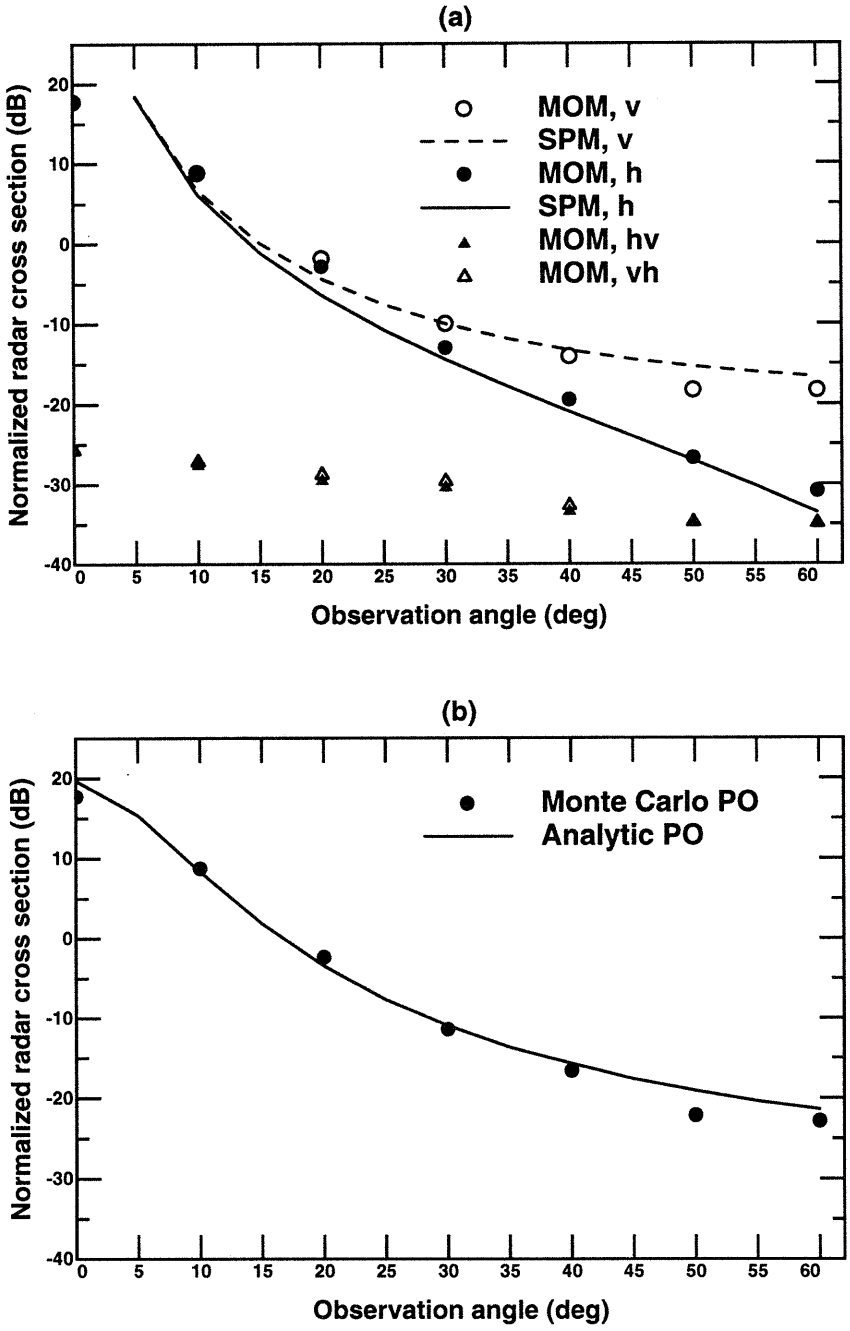

Figure 5.8: Cutoff wavenumber $k_{dl} = 18.3$, $k\sigma = 1.0$ (a) Comparison of MOM and SPM backscattering predictions (b) Comparison of Monte Carlo and analytical PO backscattering predictions

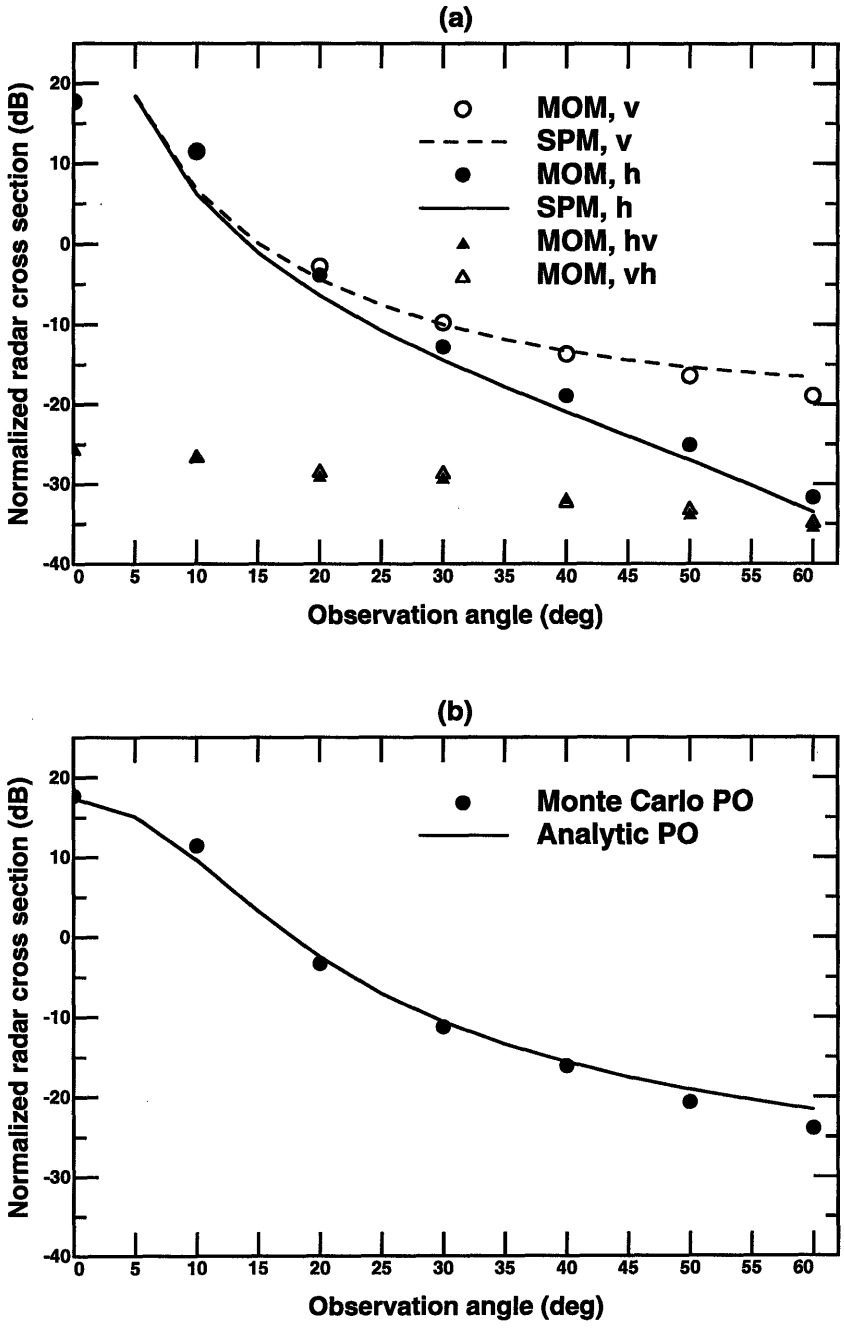

Figure 5.9: Cutoff wavenumber $k_{dl} = 9.16$, $k\sigma = 2.0$ (a) Comparison of MOM and SPM backscattering predictions (b) Comparison of Monte Carlo and analytical PO backscattering predictions

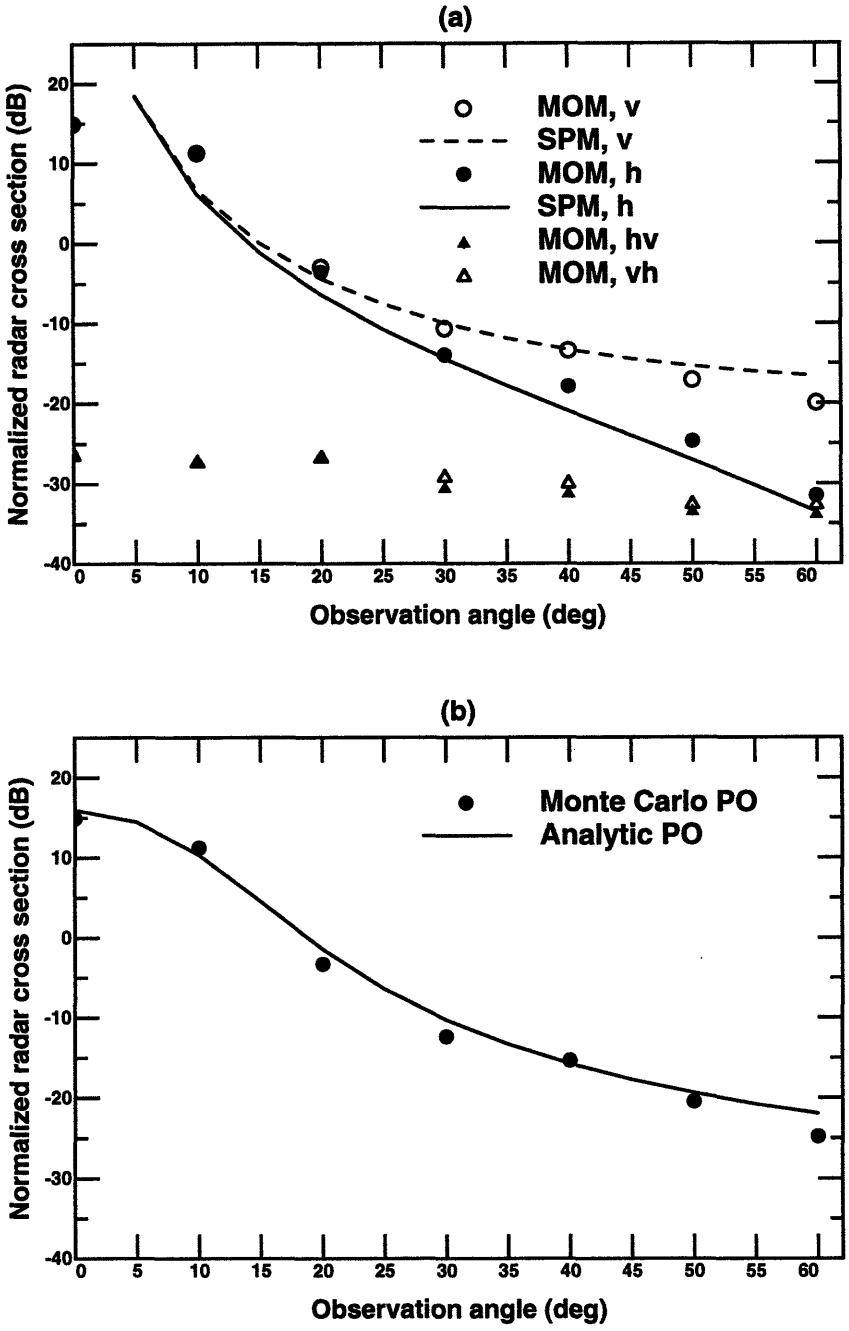

Figure 5.10: Cutoff wavenumber $k_{dl} = 4.58$, $k\sigma = 4.0$ (a) Comparison of MOM and SPM backscattering predictions (b) Comparison of Monte Carlo and analytical PO backscattering predictions

ever, PO results fall between vertically and horizontally polarized results and fail to reproduce the observed polarization dependence. Note that the physical optics approximation predicts almost no variation in cross sections for incidence angles greater than 40 degrees for the entire range of surface rms heights. This observation contrasts with the geometrical optics model, which predicts much smaller cross sections at high incidence angles which increase as surface rms heights (and slopes) increase.

To summarize, the results of Figures 5.5 to 5.10 illustrate that SPM predictions indeed remain qualitatively accurate for incidence angles larger than 20 degrees as surface rms heights are increased dramatically beyond regions where SPM predictions are expected to hold. In addition, physical optics predictions are observed to be accurate for incidence angles less than 20 degrees regardless of surface rms height. Both of these results favor general assumptions of the composite surface model. More specific aspects are considered in the next section.

5.5.2 Comparison with composite surface model

Although the theoretical basis of the composite surface model has been somewhat justified by the comparisons of the previous section, a more detailed comparison with composite surface model predictions should allow further insight into the choice of cutoff wavenumber inherent in the model. Figures 5.11 through 5.13 plot variations in vv, hh, and hv cross sections with low frequency cutoff for four of the cases previously studied. For incidence angles greater than 20 degrees, these figures show very little variation in vv, larger variations in hh, and the largest variation in hv cross sections. Variations in both vv and hh cross sections are small enough to make their distinction

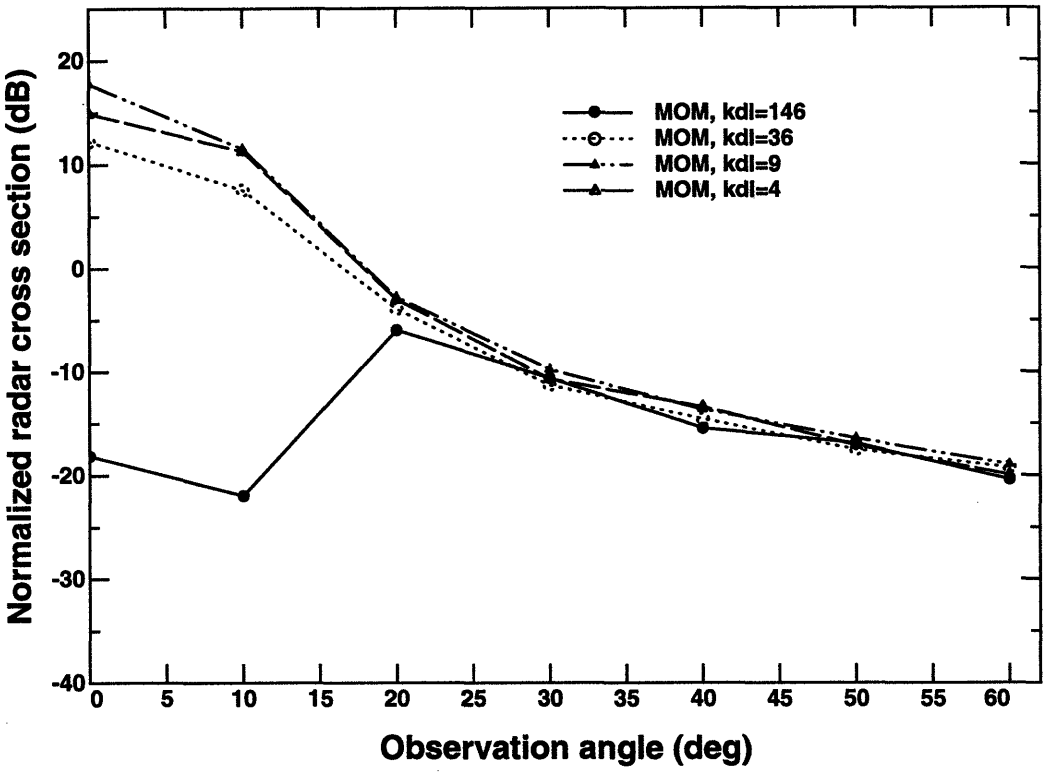

Figure 5.11: Variation in vv backscatter cross sections with low frequency cutoff

from the 2.5 dB model uncertainty difficult, but variations in hh are clearly larger than their vv counterparts. Only the variation in cross polarized cross sections is significant enough to provide a quantitative test of an approximate theory.

For comparison with the composite surface model, two separate angular backscattering regions will be considered: the region between 0 and 30 degrees, for which the physical/geometric optics models are primarily used, and the region between 30 and 60 degrees, for which tilted SPM predictions are primarily used. Given the success of the physical optics approximation in matching numerical results up to 20 degrees, the primary issue in the 0 to 30 degree region concerns the accuracy of the GO approximation, which is required for non-power law spectra due to the difficulty in evaluating

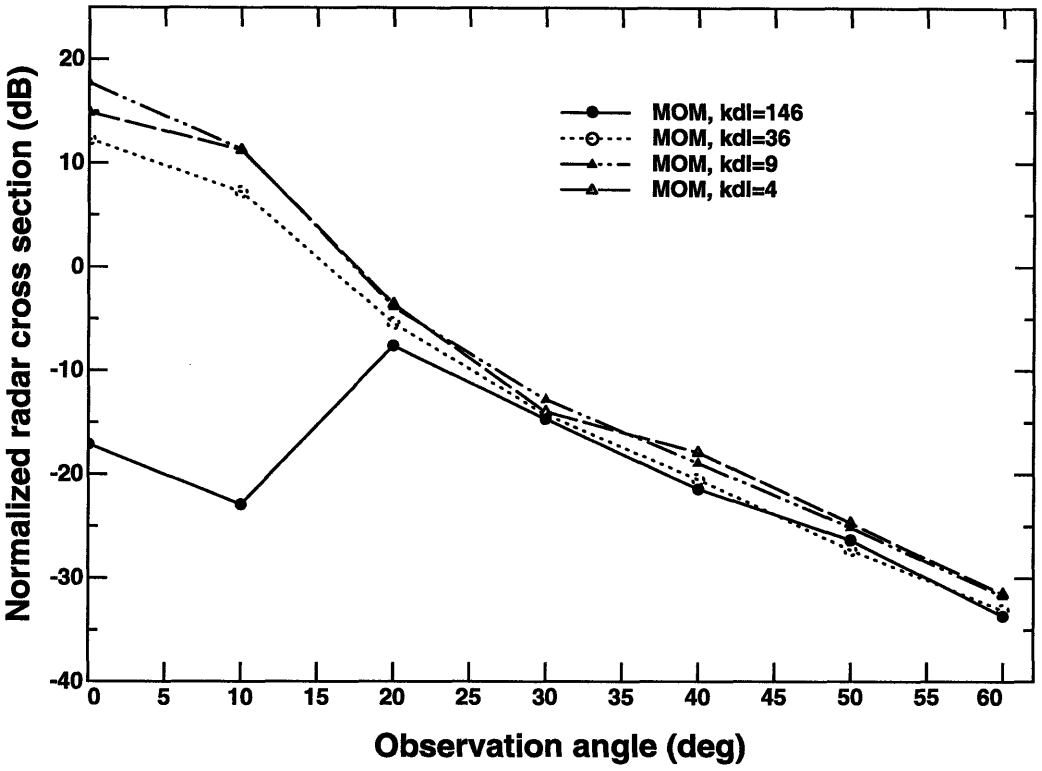

Figure 5.12: Variation in hh backscatter cross sections with low frequency cutoff

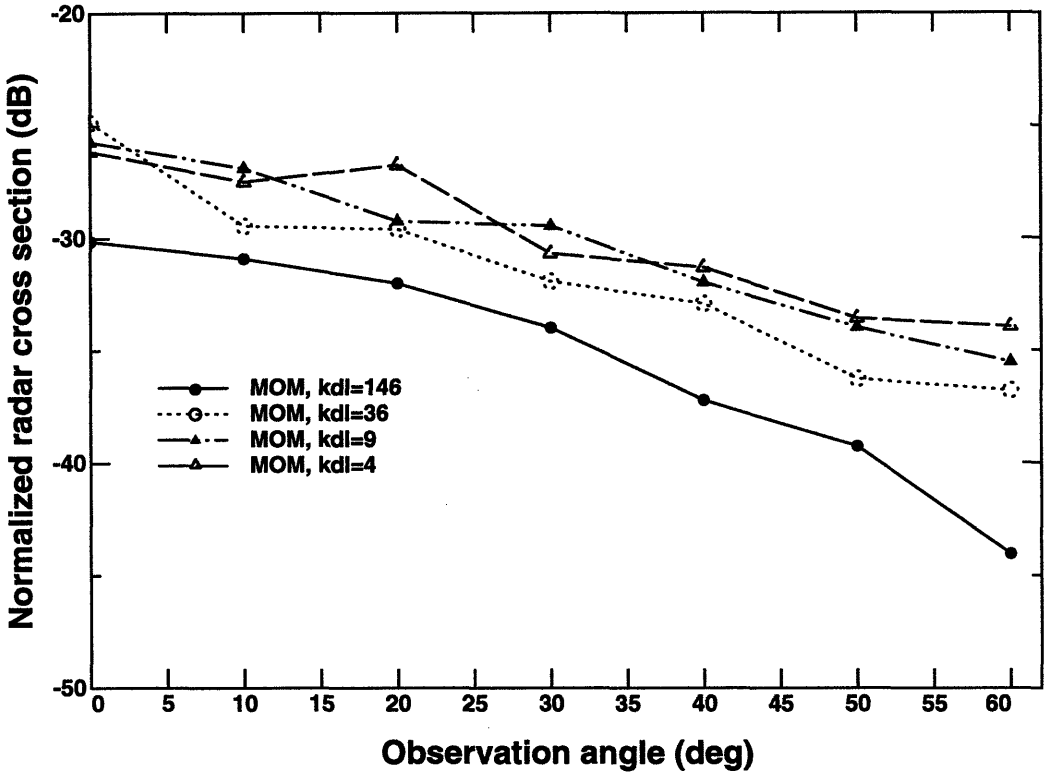

Figure 5.13: Variation in *hv* backscatter cross sections with low frequency cutoff

the full PO integral. Figure 5.14 compares physical/geometric optics results for four power law spectra, which begin with the numerically validated $k_{dl} = 4.58$ case and extend the low frequency cutoff below regions where numerical simulations could be run and correspondingly increase surface rms height so that GO predictions should become more valid. The full surface spectrum was used in defining surface rms slope for use in the geometrical optics approximation, corresponding to choosing a composite surface model cutoff of $K_d = k_{du}$. Geometric optics predictions in this case are seen to agree with the physical optics approximation very poorly over the entire range of incidence angles, indicating a poor choice of the K_d parameter. Figure 5.15 presents the same comparison using a cutoff wavenumber of $K_d = k/2$ for the GO predictions, and is seen to produce a very good comparison with PO predictions up to approximately 20 degrees for the rough surfaces simulated. Alternate choices of K_d were found to produce inferior results, so a choice of $K_d = k/2$ seems optimal for backscattering predictions from a perfectly conducting power law surface. This choice is in agreement with [140], and results in a $k\sigma$ product of 0.126 for the small scale portion of the spectrum, slightly less than 0.158 value suggested by [15]. Note that even when including the entire slope variance of the surface as in Figure 5.14, GO predictions fail to match the incidence angle dependence of PO results beyond 20 degrees, indicating the inherent limitations of the GO approximation in this region. However, since two scale SPM predictions produce reasonable agreement for large incidence angles, these limitations should not influence composite surface model accuracy.

Comparisons between method of moments results and composite surface model

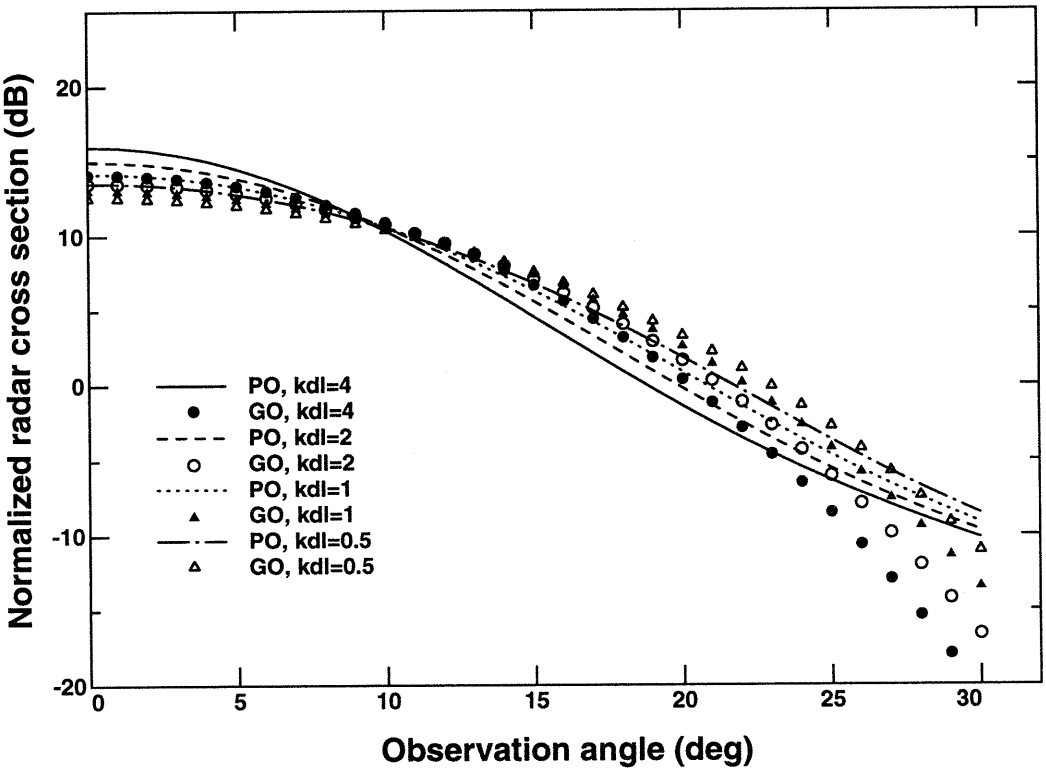

Figure 5.14: Comparison of PO and GO backscattering predictions using $K_d = 2k$

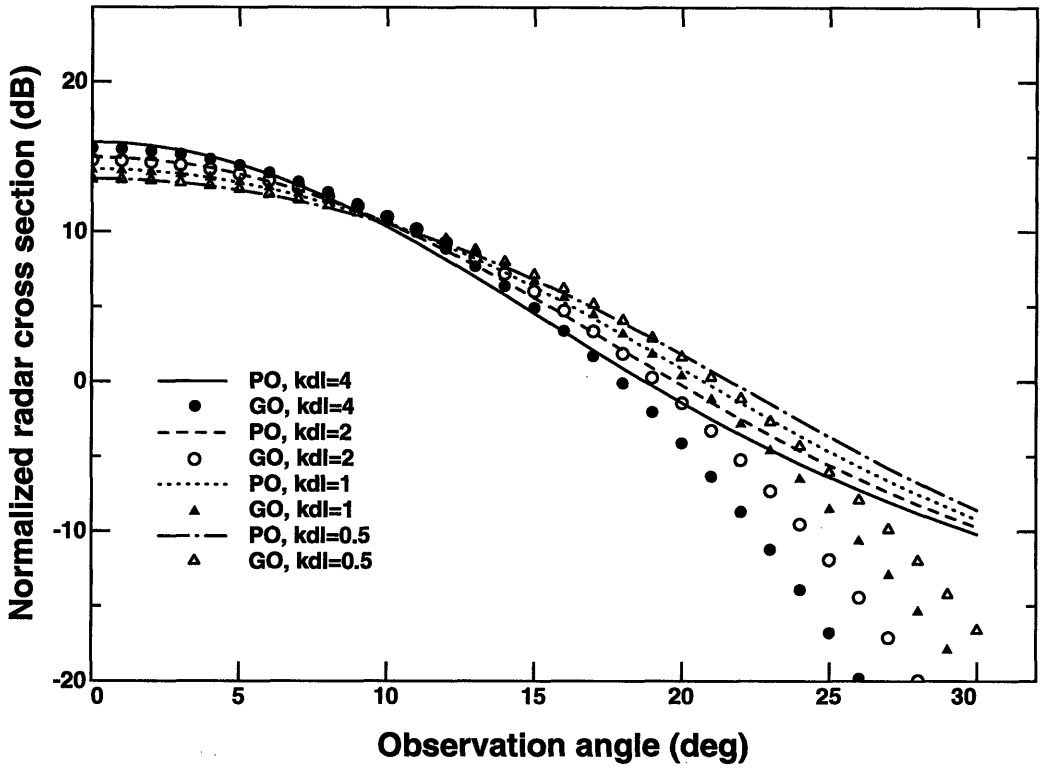

Figure 5.15: Comparison of PO and GO backscattering predictions using $K_d = k/2$

predictions for incidence angles between 30 and 60 degrees are shown in Figure 5.16 for three of the simulated surfaces. Also included is the corresponding untilted SPM result. A slight underestimation of vv cross sections by the numerical model is observed at higher incidence angles as with PO predictions. However, the small variations in vv results with increases in surface slope agree well with the composite surface model. The magnitude of hh variations also agree well with the composite surface model, although again these variations are small enough to make an thorough quantitative assessment difficult. Overall, however, the composite surface model is qualitatively validated by these comparisons. As mentioned previously, the greatest sensitivity to tilting effects was observed in the cross polarized numerical results. However, comparison with the composite surface model is complicated by the fact that SPM predicted cross polarized cross sections are singular for a perfectly conducting surface [7]. Comparisons between numerical results and untilted SPM predictions are made in Figure 5.17 with a surface conductivity of 10^8 S-m used in the SPM, chosen to set the level of SPM results near the numerical simulations. No tilting is performed for the cross polarized predictions, due to computational complexity of evaluating the SPM second order cross polarized results and the relatively flat curves for which tilting should have little effect. The comparison shows a reasonable agreement between SPM predictions alone and numerical results for incidence angles greater than 20 degrees where SPM predictions are expected to be valid. Note that the SPM alone reproduces variations with low frequency cutoff for cross polarization since second order fields involve a convolution of scales within the surface spectrum rather than the single surface scale of first order predictions. Performance for angles less than 20 degrees is seen to be much worse, as with co-polarized cross sections, indicating

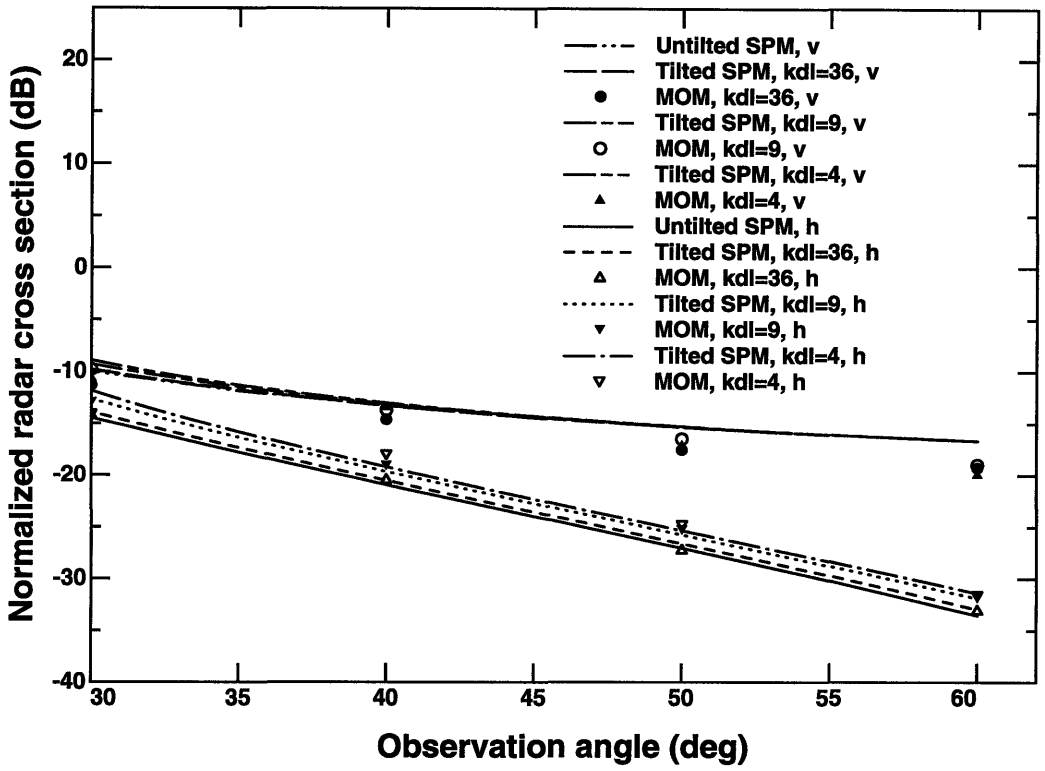

Figure 5.16: Comparison of MOM and composite surface model co-pol backscatter results

the inaccuracy of SPM predictions for this region. Note that geometrical optics predictions also produce no cross polarization for backscattering, so that near-normal incidence cross polarized backscattering is inaccurately predicted by the composite surface model. However, given the success of the composite model in all the other regions studied, this limitation seems relatively minor.

5.5.3 Comparison with Neumann iteration results

A final subject of interest involves the accuracy of single Neumann iteration results for the power law spectrum. Since the majority of attempts to extend analytical surface scattering theories beyond the physical optics limit are based on a single

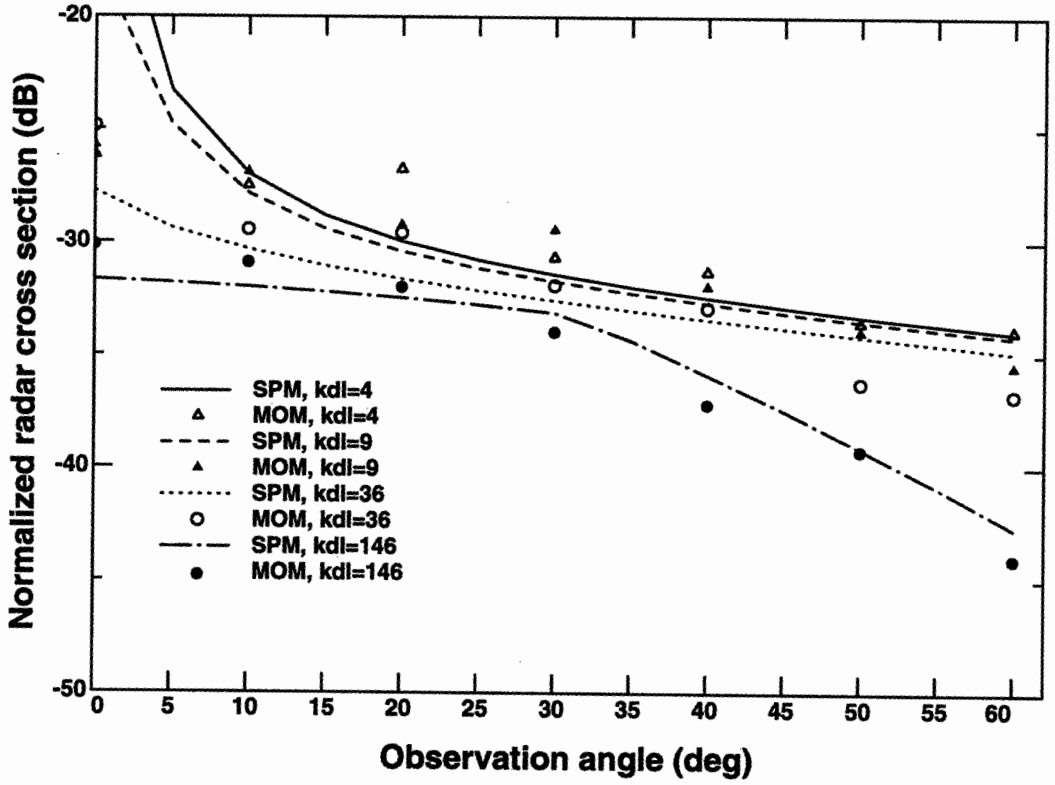

Figure 5.17: Comparison of MOM and SPM cross-pol backscatter results using a conductivity of 10^8 S-m in the SPM

Neumann iteration [19]-[20],[27], a numerical study of the accuracy allowed by this approach should allow some insight into the potential success or failure of these extended theories. Figure 5.18 compares backscattering cross sections for the same set of 20 surface realizations using both the method of moments and a single Neumann iteration for a low frequency cutoff of $k_{dl} = 9$ ($k\sigma = 2.02$). The comparison shows that a single Neumann iteration extends physical optics results to include the polarization difference predicted by the SPM. This fact has been demonstrated analytically by Holliday in [28] for surfaces with small rms heights and slopes, and the good agreement obtained between MOM and Neumann results shows this conclusion to hold for power law surfaces with larger rms heights. The accuracy of Neumann iteration cross polarized predictions indicates the second order scattering nature of cross polarized fields. Some inaccuracies are observed, however, which seem to increase with incidence angle. As mentioned previously, numerical simulations for 1-D surfaces have been performed which show similar phenomena, including a divergence of the Neumann series as surface slopes and incidence angles increase to larger values than the simulations performed here. However, the results of this comparison demonstrate that an analytical solution with accurately calculated single Neumann iterated cross sections should produce very good results for incidence angles up to 60 degrees and could potentially eliminate the need for the heuristic composite surface theory presently used. The development of such a theory, along with a detailed evaluation of the approximate Neumann iterated theories of [19]-[20],[27], remains a subject for further study.

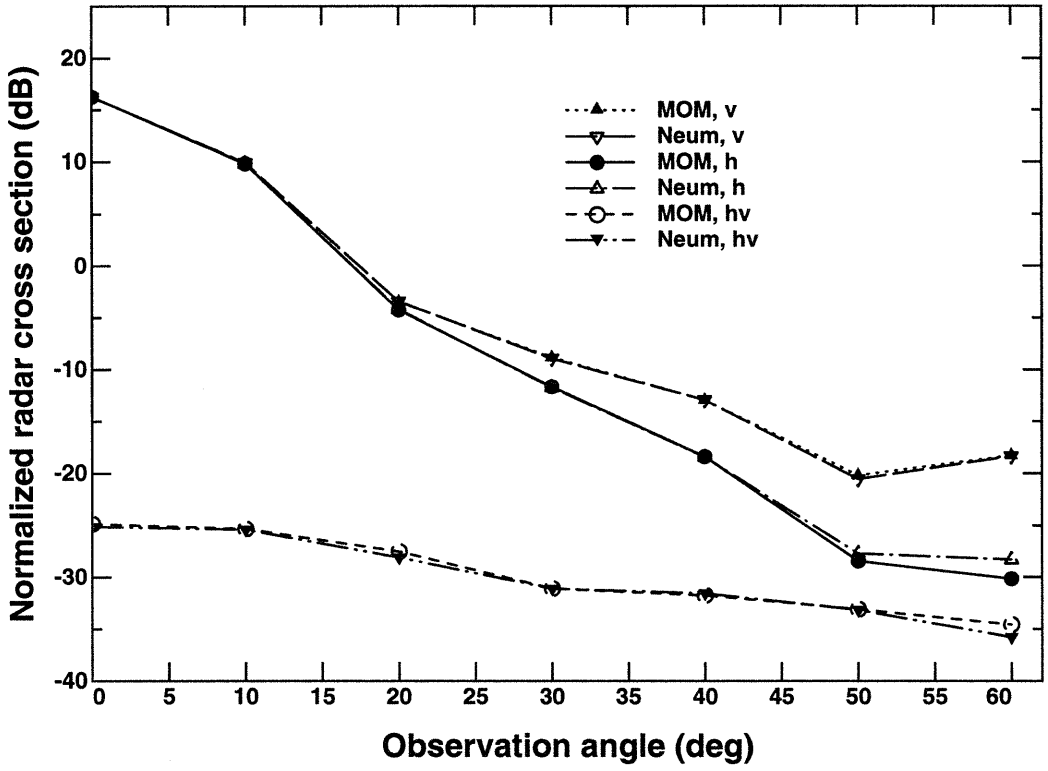

Figure 5.18: Comparison of MOM and single Neumann iteration backscattering predictions, $k_{dl} = 9.16$

5.6 Forward Scattering

As mentioned previously, predicting forward scattering from the ocean is important in understanding multipath interference effects for communication and radar systems operating in a sea environment. For HF and lower frequencies, the large electromagnetic wavelengths make the ocean appear as an almost specular reflector, so that a strong coherent reflected wave is obtained. In the microwave frequency range, however, multipath interference is clearly incoherent for most wind speeds, as the small wavelengths of microwaves make even small gravity-capillary type ocean waves appear large on an electromagnetic scale. Important issues to be considered are the accuracy of standard approximate methods for forward scattering as well as the effect of parameters such as incidence angle, polarization, frequency, wind speed, and ocean spectrum model on forward scattered bistatic cross sections.

Numerical results presented in this section were calculated concurrently with the backscattering predictions of the previous section. As discussed previously and observed for backscattering, the physical optics approximation is expected to produce accurate predictions for near forward scattering. Figure 5.19 is an example of the accuracy of PO results: plotted are the method of moments, Monte Carlo PO, and analytical PO results for the same power law spectrum as the previous section with high and low frequency cutoffs of $k_{dl} = 4.58\ (64\lambda)$ and $k_{du} = 586.4\ (\lambda/2)$ at a frequency of 14 GHz. The three plots of Figure 5.19 represent azimuthal cuts through the bistatic scattering pattern centered on the specular direction of $\theta_s = 60, \phi_s = 0$ for the $g' = 16\lambda$ tapered beam incident field. Only hh cross sections are plotted in Figure 5.19, as vv and hh results are similar to within 0.5 dB. Figure 5.19 clearly

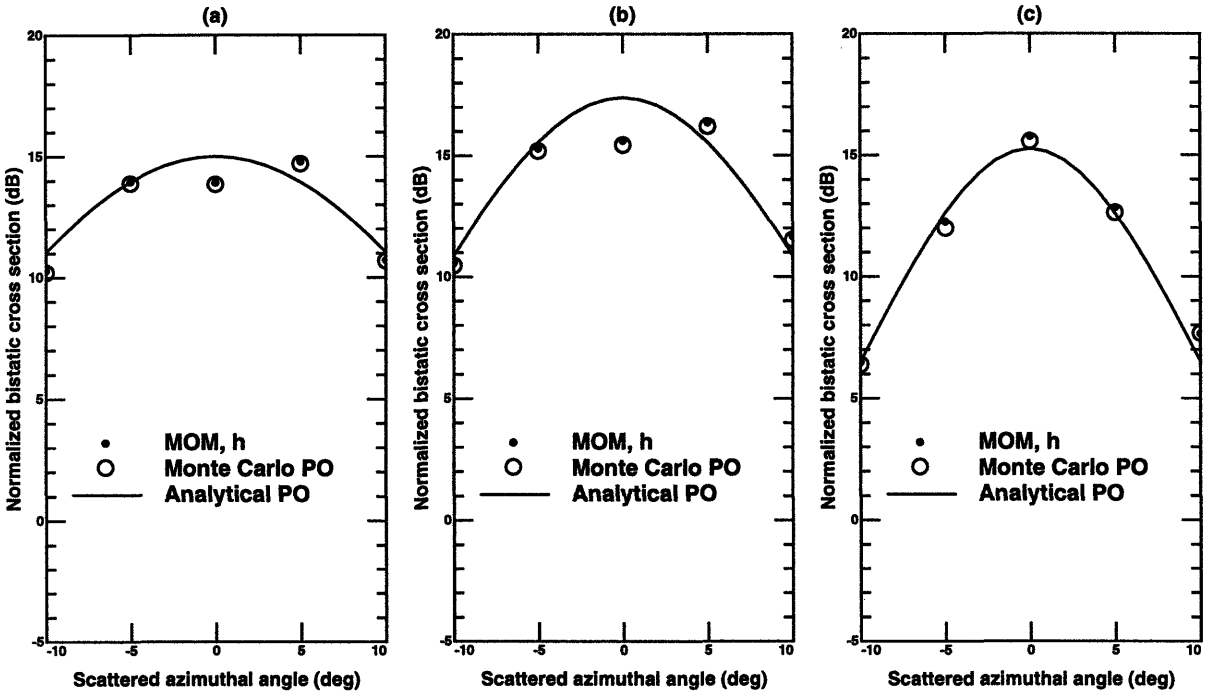

Figure 5.19: Cutoff wavenumber $k_{dl} = 4.58$, $k\sigma = 4.0$: Comparison of MOM, Monte Carlo PO, and analytical PO forward scatter co-pol cross sections for 60 degree incidence (a) $\theta_s = 50$ deg (b) $\theta_s = 60$ deg (c) $\theta_s = 70$ deg

illustrates that Monte Carlo PO and method of moments results are in agreement, so that the physical optics approximation is validated. Small differences within 2 dB from analytical PO results are due to the finite surface size, tapered incident field, and finite number of realizations in the simulation. Overall, however, the agreement between Monte Carlo PO and MOM results and analytical PO results validates the numerical approach.

5.6.1 Power law spectrum

As in the backscatter case, only variations of the low frequency cutoff wave number will be considered due to the simplicity of the power law spectrum. Figures 5.19 through 5.22 illustrate Monte Carlo MOM, Monte Carlo PO, and analytical PO co-polarized results for low frequency cutoff wavenumbers ranging from 4.58 to 36.6 for an incidence angle of 60 degrees. Cross-polarized comparisons are shown in Figures 5.23 through 5.26. Forward scattering at large incidence angles is of most interest due to the near grazing angle operation of many ocean borne radar and communication systems. However, surface size limitations prevent angles closer to grazing from being simulated, so that a compromise angle of 60 degrees results. Throughout Figures 5.19 to 5.26, Monte Carlo PO and MOM results are seen to be within 1 dB except for a few isolated cases both in co and cross polarizations, and a good general agreement with analytical PO results is also obtained. Note the dramatic changes in forward scattered incoherent cross sections as surface rms height is decreased. This is similar to the changes in near-normal incidence backscatter predictions previously observed, and indicates the gradual transfer of energy between coherent and incoherent cross sections. Minor differences between PO and MOM results are observed in the "cutoff" regions, especially at azimuth angle 0 degrees for which analytical (plane wave incidence) PO predictions yield no cross polarized scattering. Monte Carlo PO results, however, yield some cross polarized amplitudes in this region due to the tapered beam incident field, which effectively averages scattered fields over a small angular region. MOM cross polarized fields are observed to exceed PO values by approximately 5 dB, however, indicating that the PO approximation is inadequate for cross pol predictions

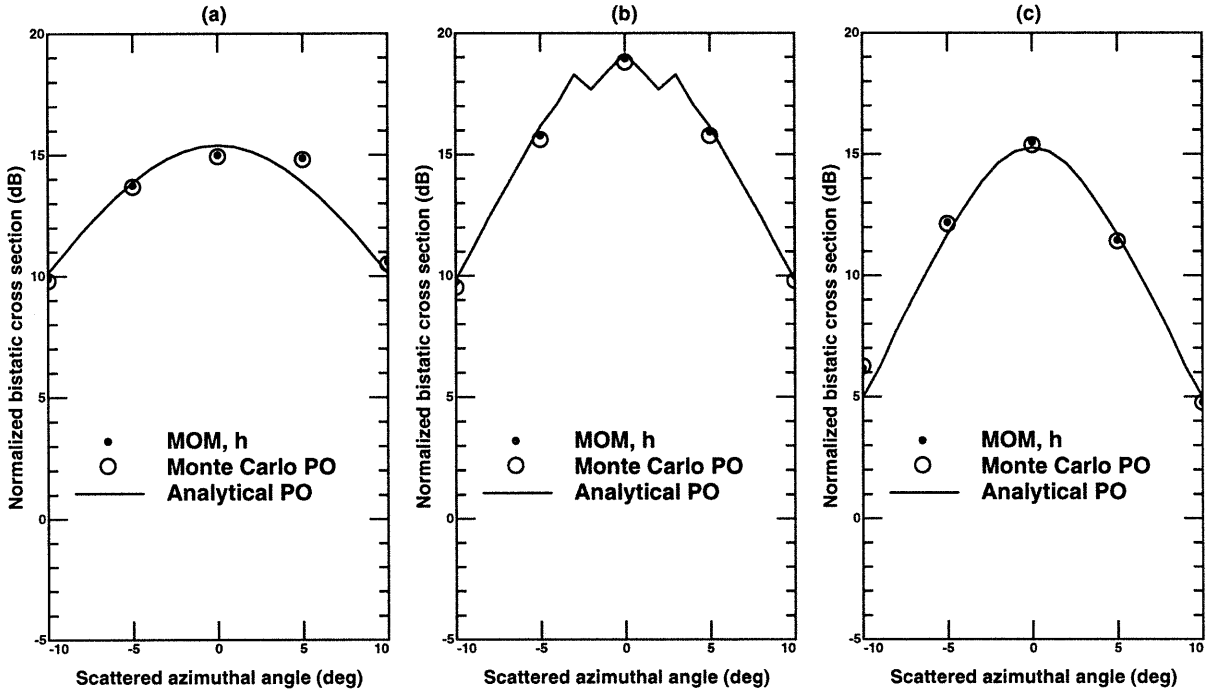

Figure 5.20: Cutoff wavenumber $k_{dl} = 9.16$, $k\sigma = 2.0$: Comparison of MOM, Monte Carlo PO, and analytical PO forward scatter co-pol cross sections for 60 degree incidence (a) $\theta_s = 50$ deg (b) $\theta_s = 60$ deg (c) $\theta_s = 70$ deg

in this region.

Figure 5.27 and 5.28 plot co-polarized cross sections for incidence angles of 0 and 30 degrees respectively and $k_{dl} = 9.16$, and again demonstrate that physical optics predictions remain valid at these incidence angles. Figure 5.29 and 5.30 illustrate the variation in predicted PO co-pol and cross-pol cross sections respectively for an incidence angle of 60 degrees, and clearly shows that particular angular portions of the near forward scattered fields are dominated by corresponding portions of the spectrum, in agreement with a Bragg scatter mechanism but modified to some degree by the presence of other spectral scales.

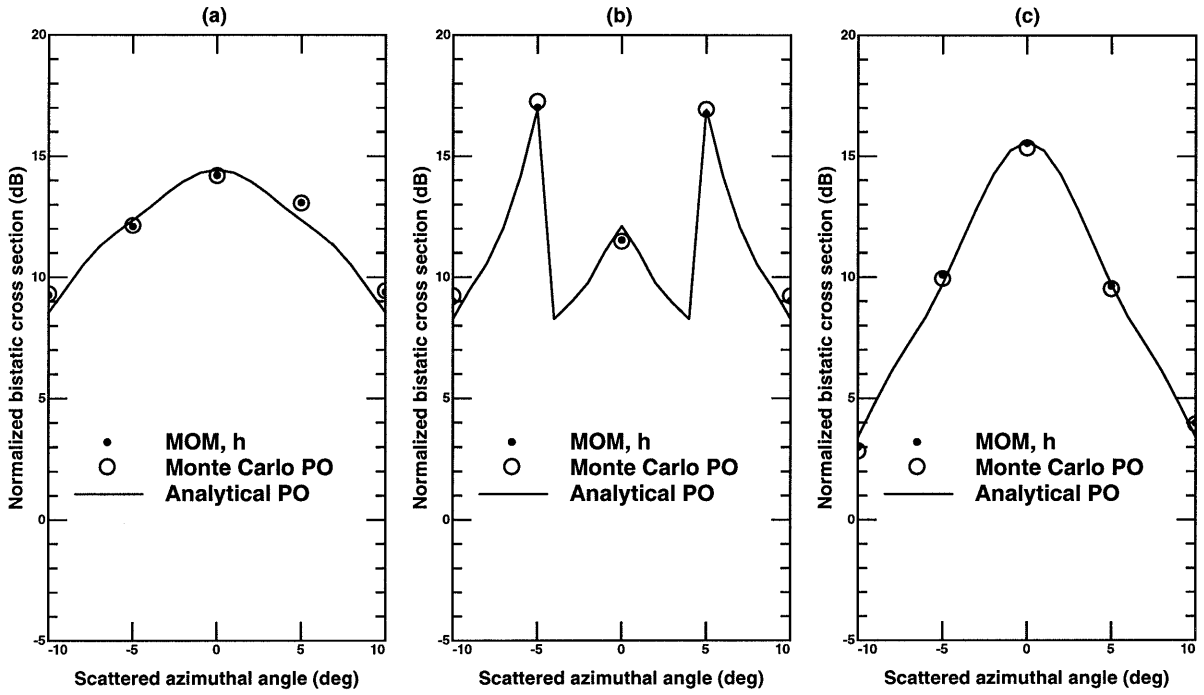

Figure 5.21: Cutoff wavenumber $k_{dl} = 18.32$, $k\sigma = 1.0$: Comparison of MOM, Monte Carlo PO, and analytical PO forward scatter co-pol cross sections for 60 degree incidence (a) $\theta_s = 50$ deg (b) $\theta_s = 60$ deg (c) $\theta_s = 70$ deg

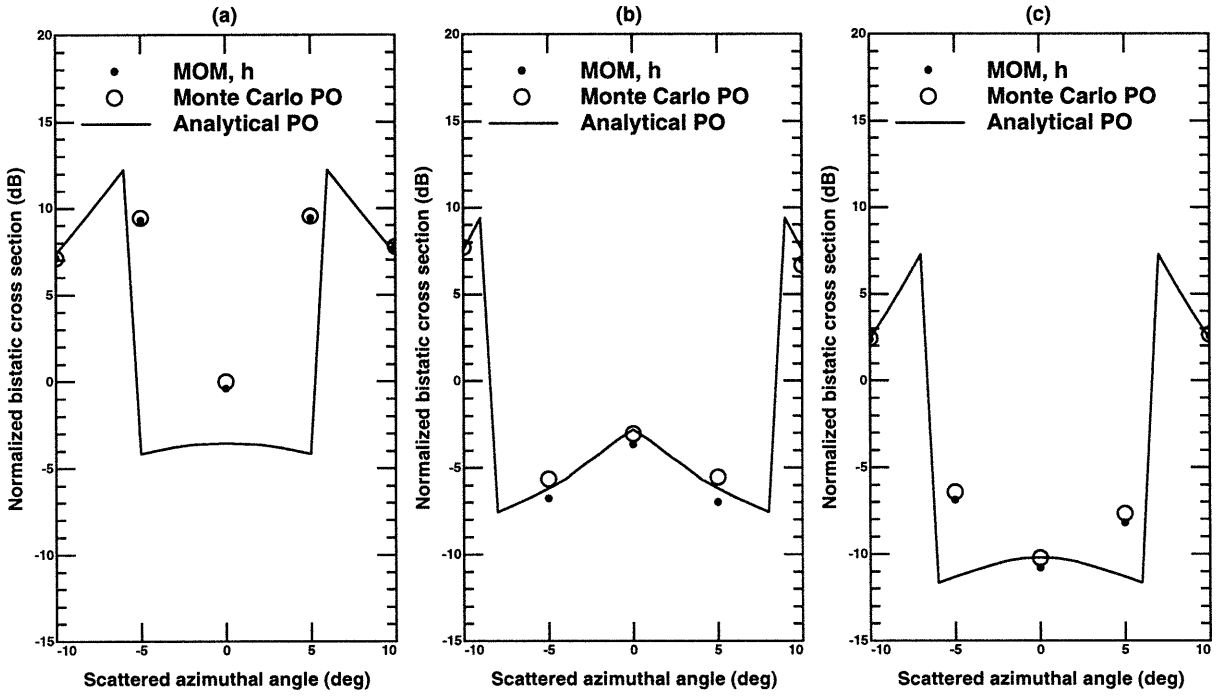

Figure 5.22: Cutoff wavenumber $k_{dl} = 36.65$, $k\sigma = 0.5$: Comparison of MOM, Monte Carlo PO, and analytical PO forward scatter co-pol cross sections for 60 degree incidence (a) $\theta_s = 50$ deg (b) $\theta_s = 60$ deg (c) $\theta_s = 70$ deg

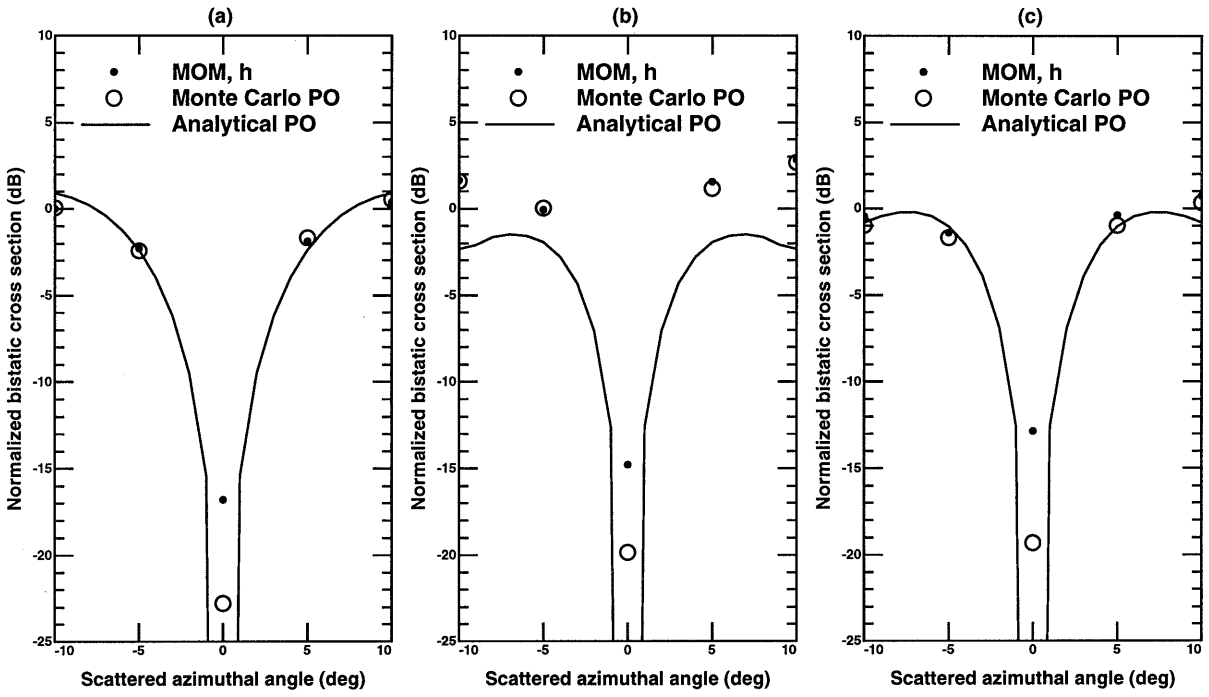

Figure 5.23: Cutoff wavenumber $k_{dl} = 4.58$, $k\sigma = 4.0$: Comparison of MOM, Monte Carlo PO, and analytical PO forward scatter cross-pol cross sections for 60 degree incidence (a) $\theta_s = 50$ deg (b) $\theta_s = 60$ deg (c) $\theta_s = 70$ deg

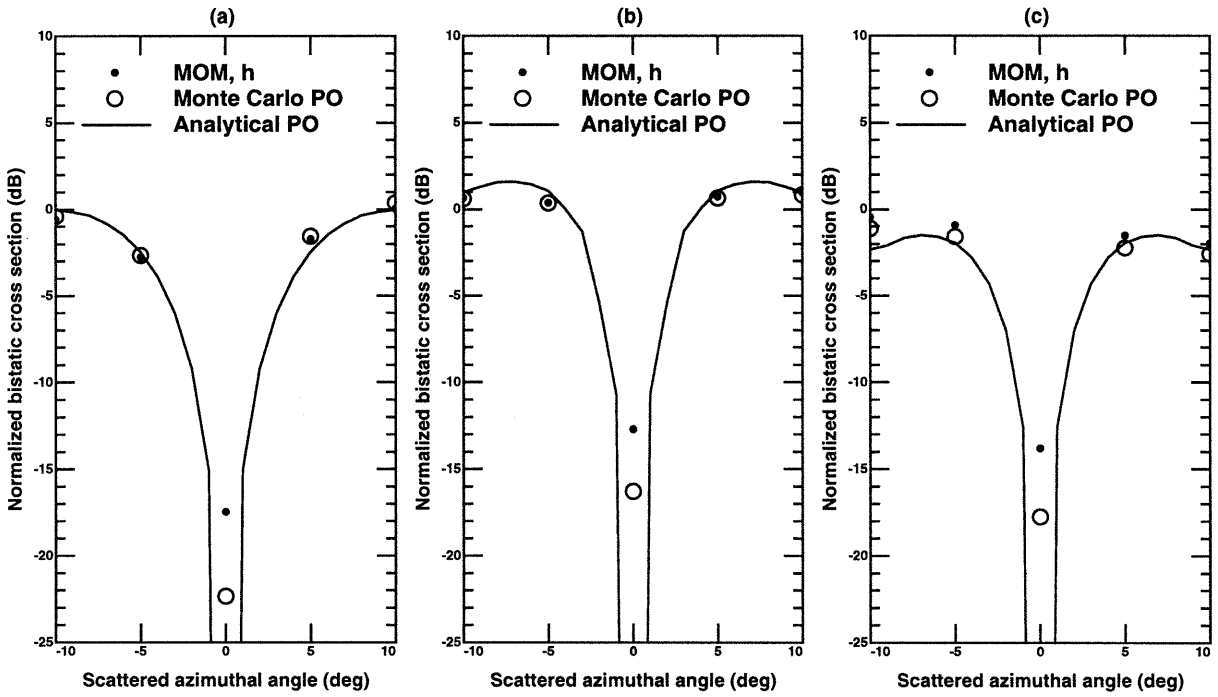

Figure 5.24: Cutoff wavenumber $k_{dl} = 9.16$, $k\sigma = 2.0$: Comparison of MOM, Monte Carlo PO, and analytical PO forward scatter cross-pol cross sections for 60 degree incidence (a) $\theta_s = 50$ deg (b) $\theta_s = 60$ deg (c) $\theta_s = 70$ deg

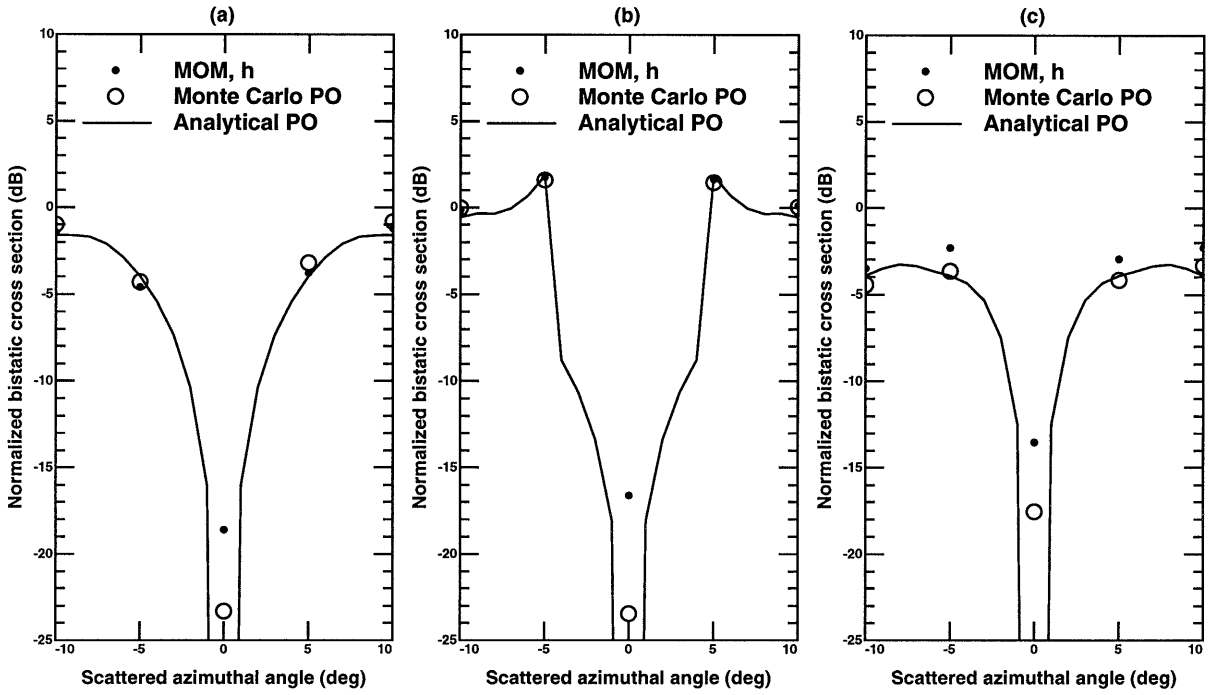

Figure 5.25: Cutoff wavenumber $k_{dl} = 18.32$, $k\sigma = 1.0$: Comparison of MOM, Monte Carlo PO, and analytical PO forward scatter cross-pol cross sections for 60 degree incidence (a) $\theta_s = 50$ deg (b) $\theta_s = 60$ deg (c) $\theta_s = 70$ deg

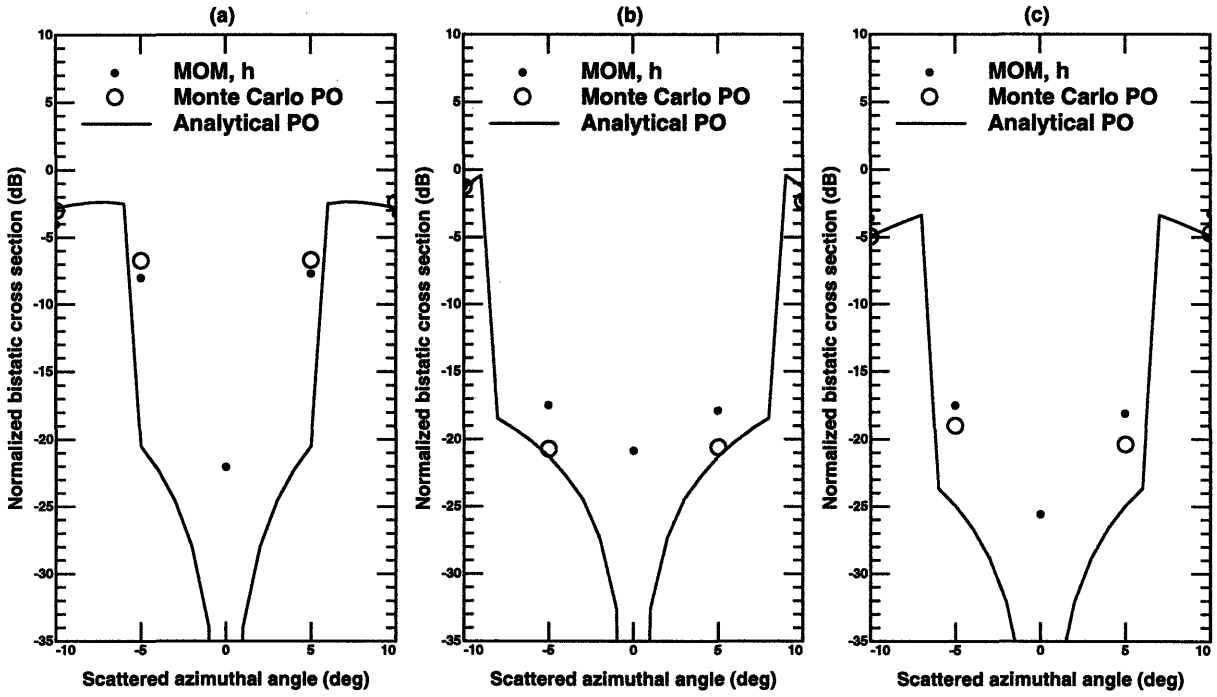

Figure 5.26: Cutoff wavenumber $k_{dl} = 36.65$, $k\sigma = 0.5$: Comparison of MOM, Monte Carlo PO, and analytical PO forward scatter cross-pol cross sections for 60 degree incidence (a) $\theta_s = 50$ deg (b) $\theta_s = 60$ deg (c) $\theta_s = 70$ deg

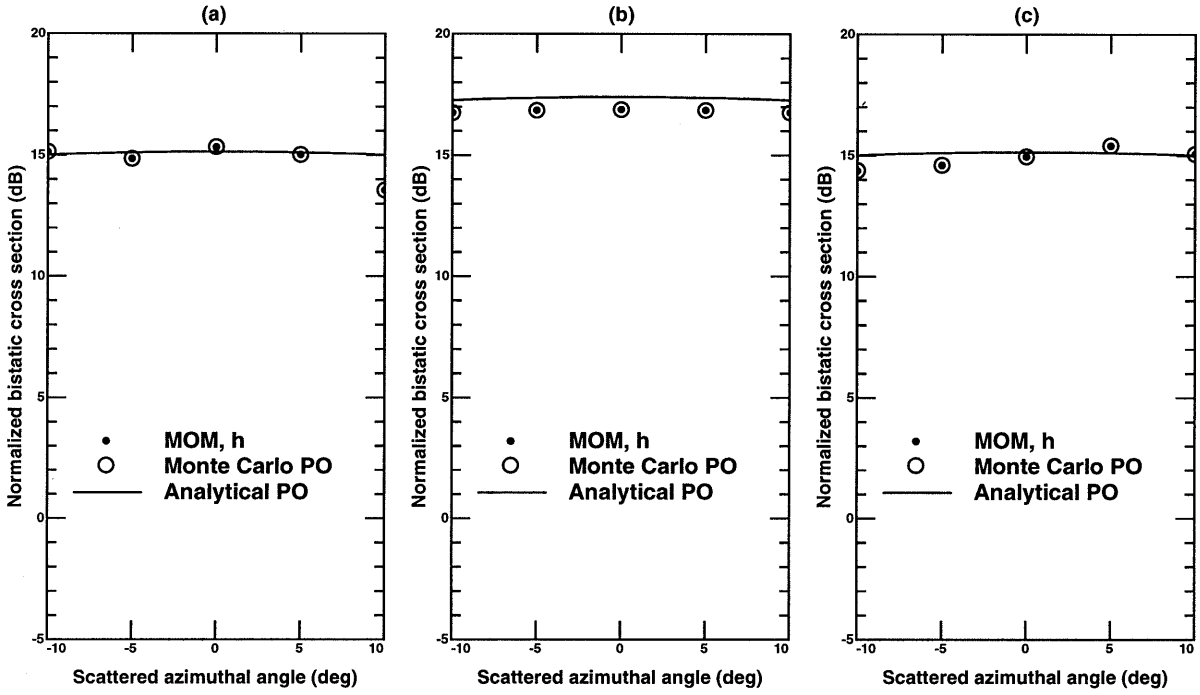

Figure 5.27: Comparison of MOM, Monte Carlo PO, and analytical PO forward scatter co-pol cross sections for 0 degree incidence with cutoff wavenumber $k_{dl} = 9.16$, $k\sigma = 2.0$ (a) $\theta_s = -10$ deg (b) $\theta_s = 0$ deg (c) $\theta_s = 10$ deg

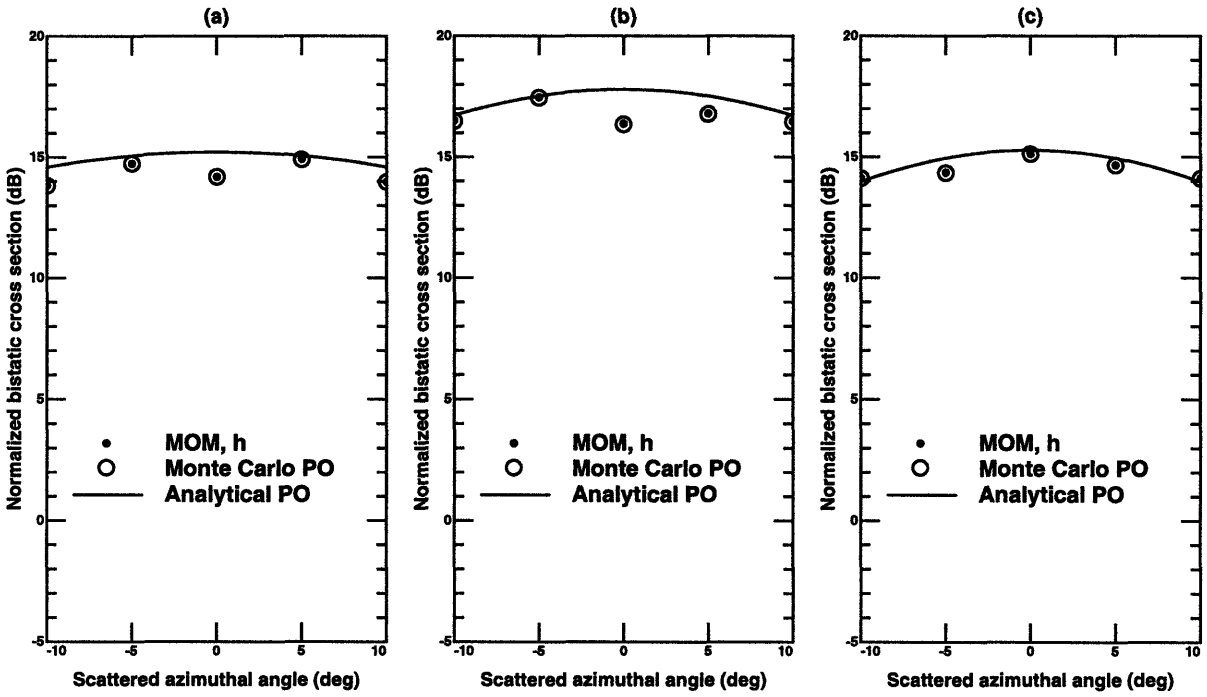

Figure 5.28: Comparison of MOM, Monte Carlo PO, and analytical PO forward scatter co-pol cross sections for 30 degree incidence with cutoff wavenumber $k_{dl} = 9.16$, $k\sigma = 2.0$ (a) $\theta_s = 20$ deg (b) $\theta_s = 30$ deg (c) $\theta_s = 40$ deg

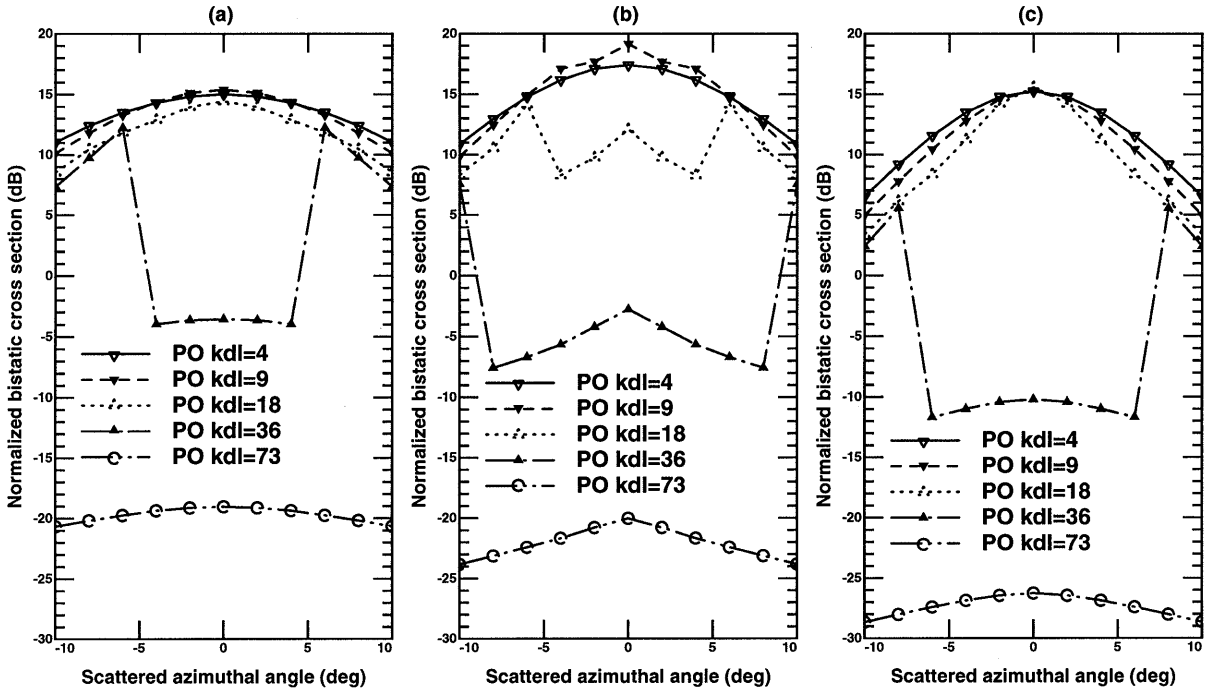

Figure 5.29: Variation in analytical PO forward scatter cross sections with low frequency cutoff at 60 degree incidence: co-pol cross sections (a) $\theta_s = 50$ deg (b) $\theta_s = 60$ deg (c) $\theta_s = 70$ deg

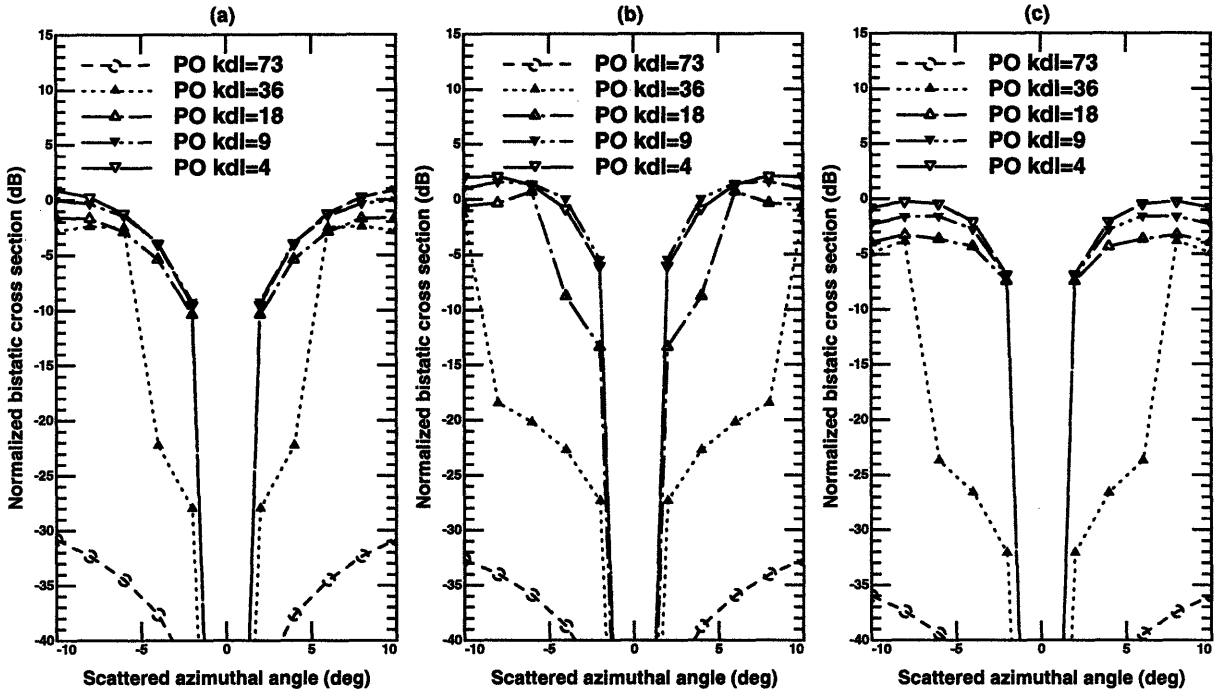

Figure 5.30: Variation in analytical PO forward scatter cross sections with low frequency cutoff at 60 degree incidence: cross-pol cross sections (a) $\theta_s = 50$ deg (b) $\theta_s = 60$ deg (c) $\theta_s = 70$ deg

As in the case of near normal incidence backscatter, calculation of forward scattered cross sections for realistic ocean spectra requires use of the geometric optics approximation due to difficulties associated with evaluating the full physical optics integral. Figure 5.31 investigates GO accuracy by comparing PO and GO results in the near forward region for an incidence angle of 60 degrees. A good agreement is obtained in both co- and cross polarized predictions especially as surface rms height is increased, but requires use of a different cutoff wavenumber, $K_d = k/4$, from the backscattering case. Figure 5.32 plots the same comparisons for an incidence angle of 0 degrees, and again illustrates a good agreement but through use of the backscattering cutoff $K_d = k/2$ as in the previous section. A more detailed study of forward scattering for the $k_{dl} = 1.145$ case showed that an reasonable agreement can be obtained for near forward scattering at incidence angles between 0 and 70 degrees by using a cutoff wavenumber of $K_d = k/2 \cos\theta_i$ in the geometric optics approximation. Suggested values from the literature are not available for the non-normal incidence forward scattering configurations considered.

5.7 Composite Surface Model for Non-power Law Spectra

Based on the results of the previous sections, the composite surface model should provide reasonable predictions for ocean surface forward and back scattering given an appropriate choice of the cutoff wavenumber. To consider scattering from surfaces modeled by the more realistic Durden-Vesecky and Donelan-Banner-Jahne spectra, the composite surface model is applied in this section and results are compared with

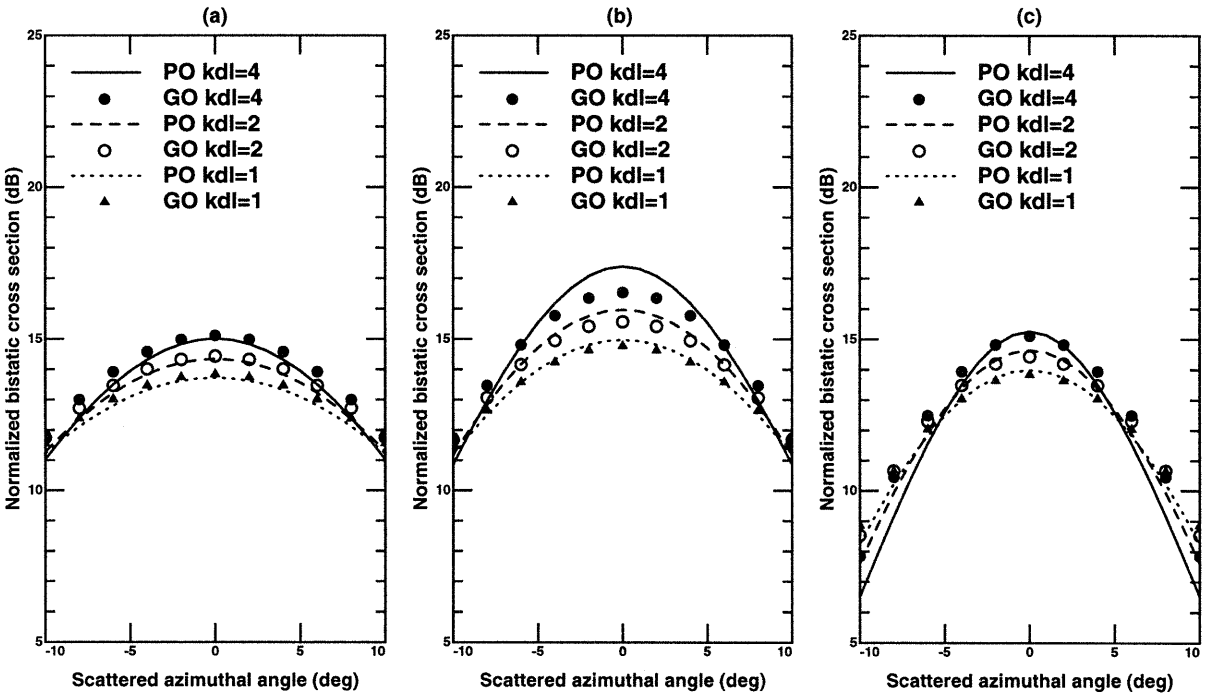

Figure 5.31: Comparison of analytical PO and GO forward scatter co-pol cross sections for 60 degree incidence with varying low frequency cutoffs, $K_d = k/4$ (a) $\theta_s = 50$ deg (b) $\theta_s = 60$ deg (c) $\theta_s = 70$ deg

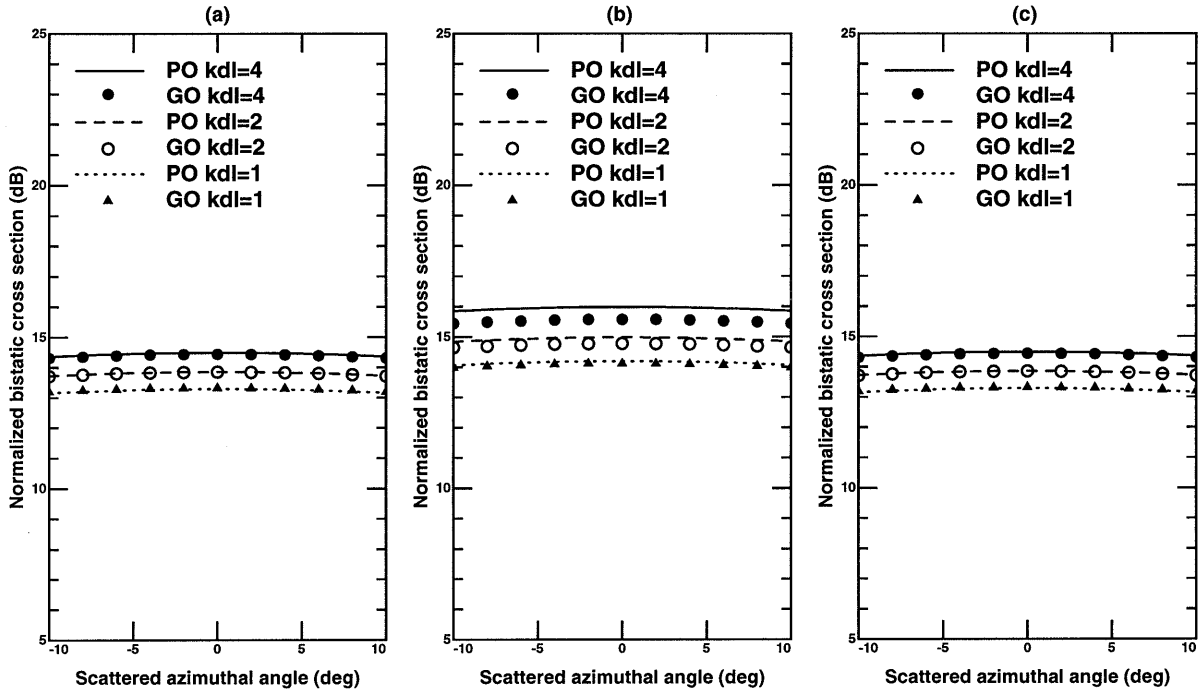

Figure 5.32: Comparison of analytical PO and GO forward scatter co-pol cross sections for 0 degree incidence with varying low frequency cutoffs, $K_d = k/2$ (a) $\theta_s = -10$ deg (b) $\theta_s = 0$ deg (c) $\theta_s = 10$ deg

the AAFE backscatter data of [116]. Predictions for forward scatter using the geometric optics approximation with these spectra are also presented, although no experimental data is currently available for non-normal incidence forward scattering with which to compare model predictions. A finitely conducting ocean surface is considered in this section, with a permittivity described by the model of [139].

Figure 5.33 illustrates composite surface model results for backscattering using the DBJ spectrum and compares these results with the AAFE 13.9 GHz upwind data [116] at four different wind speeds. Geometrical optics, untilted SPM, and tilted SPM results are all included on the plots so that individual components of the composite model can be resolved. The model is observed to produce a reasonable match to this experimental data for both polarizations over the entire range of wind speeds, although cross sections near 15 degrees are overestimated by the GO for lower wind speeds and the greatly reduced polarization ratio at 23.6 m/s is not reproduced. Similar comparisons were made in [130] for vertical polarization, but the slope variance of the entire spectrum was used for GO predictions and found to produce inaccurate predictions near normal incidence. The good comparison obtained here gives further credence to the choice of $K_d = k/2$ obtained from the numerical model. The obtained slope variance is also seen to provide a reasonable increase in hh cross sections for incidence angles of 20 degrees or larger at the lower wind speeds.

Figure 5.34 presents the same comparisons using the Durden-Vesecky spectrum in the composite surface model with a spectrum amplitude of $a_0 = 0.008$. A similar agreement is observed in Figure 5.34 to that of Figure 5.33, indicating the accuracy of the Durden-Vesecky spectrum when used in the composite model. This is not surpris-

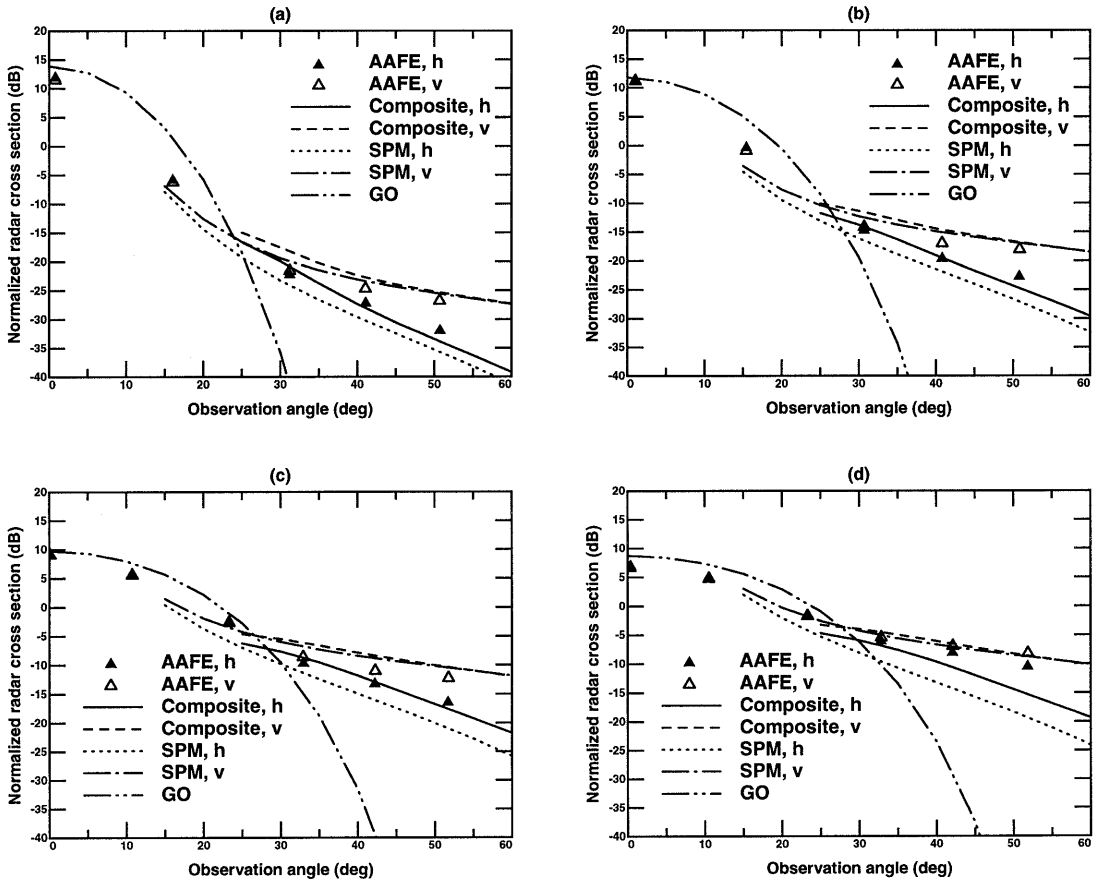

Figure 5.33: Composite surface model with DBJ spectrum: Comparison with AAFE experimental backscatter data (a) Wind speed 3.0 m/s (b) 6.5 m/s (c) 13.5 m/s (d) 23.6 m/s

ing since this spectrum was derived based on fits to AAFE and similar backscattering data under a composite surface model [135]. However, the original spectrum chose a cutoff wavenumber based on limiting the RMS height of the SPM portion of the spectrum to a specified constant, so that K_d was not equal to $k/2$ as in Figure 5.34, and used $a_0 = 0.004$. Use of $a_0 = 0.008$ as suggested by [93] and $K_d = k/2$ yields more reasonable slope variances for the "long" wave portion of the spectrum, as indicated by the good agreement between theory and experiment near normal incidence. Tilted SPM predictions are also seen to be in better agreement for all but the lowest wind speed and again indicate reasonable slope variances for the spectrum. AAFE hh cross sections remain somewhat underpredicted at the highest incidence angles however. Although the DBJ spectrum has a more sound basis since it is derived from wavetank measurements of capillary wave spectra, the comparisons of Figure 5.33 and 5.34 indicate that both the DBJ and Durden-Vesecky spectra provide reasonable predictions when used in the composite surface model, and minor differences between their predictions emphasize the importance of obtaining an accurate model for the ocean surface observed at the time and location of scattering experiments.

Figure 5.35 illustrates predicted forward scatter cross sections for the Durden-Vesecky spectrum at an incidence angle of 60 degrees as a function of wind speed, using the GO approximation with a cutoff wavenumber of $K_d = k/4$. Both hh and vv cross sections are included, as Brewster angle effects begin to introduce a polarization difference for 60 degree incidence. Results show the sensitivity of forward scatter cross sections to wind speed, as the changing slope variances in the "long" wave portion of the spectrum reduce direct forward scatter and increase width of the quasi-specular

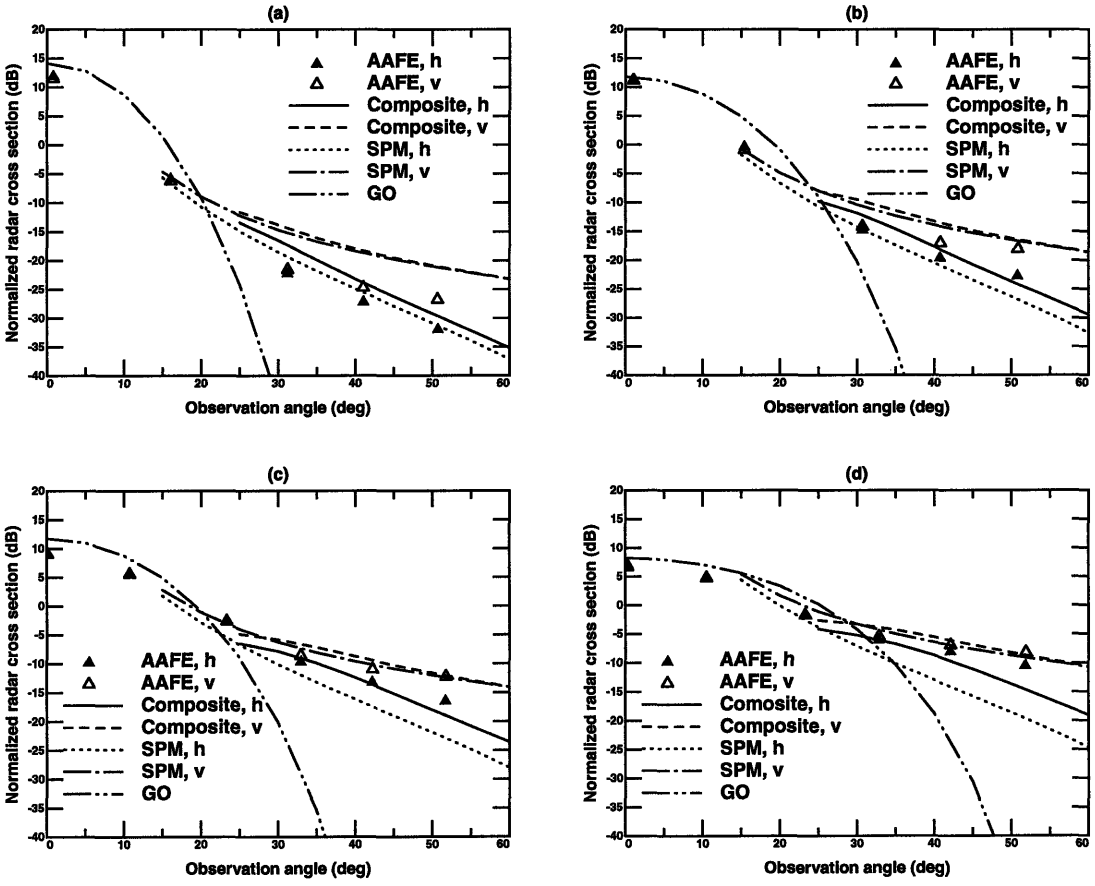

Figure 5.34: Composite surface model with Durden-Vesecky spectrum: Comparison with AAFE experimental backscatter data (a) Wind speed 3.0 m/s (b) 6.5 m/s (c) 13.5 m/s (d) 23.6 m/s

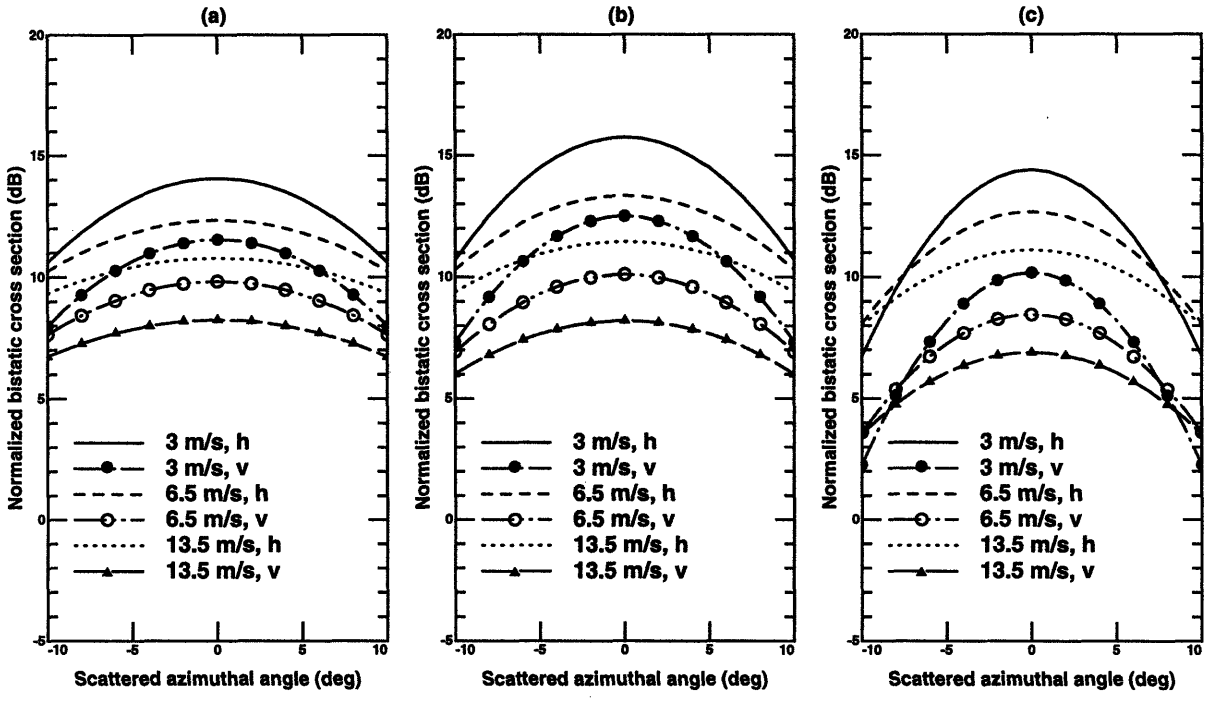

Figure 5.35: GO co-pol forward scatter with Durden-Vesecky spectrum for incidence angle 60 degrees and $K_d = k/4$: Variation with wind speed (a) $\theta_s = 50$ deg (b) $\theta_s = 60$ deg (c) $\theta_s = 70$ deg

pattern as in the backscatter case. Comparison of these predictions with experimental measurements remains a subject for future study as bistatic ocean scattering data becomes available.

5.8 Conclusions

A numerical model for ocean scattering has been developed and applied in a study of forward and backscattering from a perfectly conducting power law ocean surface. The SMFSIA/CAG approach allowed surfaces of $64\lambda \times 64\lambda$ to be included in the numerical simulation, with a matrix size of 524,288, so that edge uncertainties could

be reduced and backscattering simulations performed at incidence angles up to 60 degrees with a resulting model uncertainty of approximately 2.5 dB. Comparisons with analytical theories show the physical optics approximation to work well in the forward scatter direction and for backscattering up to 20 degree incidence. SPM predictions were also found to be valid for higher incidence angles as surface rms height increased beyond typical SPM limits, and slight increases in hh cross sections were also observed as predicted by the composite surface model. Cross polarized results were well fit by the standard SPM model as well after the inclusion of a finite surface conductivity to avoid the singularity in SPM predictions for a perfectly conducting surface. Further comparisons between analytically evaluated PO and GO predictions showed an appropriate choice of cutoff wavenumber to be $K_d = k/2$ for backscattering and $K_d = k/2 \cos\theta$ for forward scattering in the composite surface model. The validated composite surface model was then used with the more realistic DBJ and Durden-Vesecky spectra in a comparison with experimental data, which showed both the DBJ and Durden-Vesecky spectra to provide adequate predictions of backscattered experimental data. Forward scattering simulations were also performed which illustrated the sensitivity of forward scatter cross sections to wind speed over the ocean.

The results of this study demonstrate the importance of an accurate model for the ocean spectrum. Further research into this area continues, as there are many models in the literature which are at variance with one another as evidenced by the DBJ and Durden-Vesecky spectra of this chapter. Overall, the success of the composite surface model when compared to numerical simulations, however, validates

this approach for prediction of ocean scattering.

5.9 Appendix - Physical Optics for Ocean Scattering

As discussed in Chapter one, the physical optics scattering cross section for a Gaussian random process is given by

$$\sigma_{aa}(\theta_i,\theta_s,\phi_s) = \frac{k^2}{\pi}\left|\frac{(1+\cos\theta_i+\cos\theta_s)\cos\phi_s-\sin\theta_i\sin\theta_s}{\cos\theta_i+\cos\theta_s}\right|^2 \int dx'\int dy' e^{-\sigma^2k_{dz}^2}\left\{e^{\sigma^2k_{dz}^2C(x',y')}-1\right\}e^{ik_{dx}x'+ik_{dy}y'} \quad (5.23)$$

where $\overline{k}_d = \overline{k}_i - \overline{k}_s$, σ is the rms height of the surface, and $C(x,y)$ is the correlation function of the random process, defined in terms of the surface spectrum as

$$C(x,y) = \frac{1}{\sigma^2}\int_{-\infty}^{\infty}dk_x\int_{-\infty}^{\infty}dk_y\Psi(k_x,k_y)e^{-ik_xx-ik_yy} \quad (5.24)$$

For an isotropic, k^{-4} spectrum, the above integrals can be simplified by integrating out the azimuthal dependence. Resulting expressions are

$$\sigma_{aa}(\theta_i,\theta_s,\phi_s) = \frac{k^2}{\pi}\left|\frac{(1+\cos\theta_i+\cos\theta_s)\cos\phi_s-\sin\theta_i\sin\theta_s}{\cos\theta_i+\cos\theta_s}\right|^2 \int d\rho'\rho' e^{-\sigma^2k_{dz}^2}\left\{e^{\sigma^2k_{dz}^2C(\rho')}-1\right\}J_0(k_{d\perp}) \quad (5.25)$$

where J_0 indicates the zeroth order Bessel function, $k_{d\perp} = \sqrt{k_{dx}^2 + k_{dy}^2}$, and

$$C(\rho) = \frac{2\pi a_0}{\sigma^2} \int_{k_{dl}}^{k_{du}} dk_\rho \; k_\rho^{-3} \; J_0(k_\rho \rho) \tag{5.26}$$

Some analytical progress can be made with the above expression for the correlation function at large values of ρ by approximating the Bessel function by its sinusoidal asymptotic series. The resulting form is

$$\begin{aligned} C(\rho) \approx & \frac{2k_{dl}^2 k_{du}^2}{k_{du}^2 - k_{dl}^2} \frac{1}{\sqrt{\pi\rho}} \left[\frac{\sqrt{2}}{28} \frac{\sin(k_\rho \rho - \pi/4)}{k_\rho^{4.5}} + \frac{29}{28} \left\{ \frac{-2}{5k_\rho^{2.5}} \right.\right. \\ & (\cos(k_\rho\rho)[1 + \frac{2}{3}k_\rho\rho - \frac{4}{3}(k_\rho\rho)^2] + \sin(k_\rho\rho)[1 - \frac{2}{3}k_\rho\rho - \frac{4}{3}(k_\rho\rho)^2]) \\ & \left.\left. + \frac{8}{15}\sqrt{2\pi}\rho^{2.5}[s(\sqrt{2k_\rho\rho/\pi}) - c(\sqrt{2k_\rho\rho/\pi})] \right\} \right]_{k_{dl}}^{k_{du}} \end{aligned}$$

where $s(\cdot)$ and $c(\cdot)$ are the standard Fresnel sine and cosine integrals respectively. This expression can be further simplified for large values of ρ by expanding the s and c functions into their sinusoidal asymptotic series, with the resulting leading order term

$$C(\rho) \approx \left(\frac{2}{k_{dl}\rho}\right)^{1.5} \frac{1}{\sqrt{\pi}} \cos(k_{dl}\rho + \pi/4) \tag{5.27}$$

where it has been assumed that $k_{du} >> k_{dl}$. However, analytical progress with the physical optics integral is much more difficult, so that a numerical evaluation is required.

To evaulate the physical optics integral numerically, a term proportional to the

Bragg scatter cross section is added and subtracted as

$$\begin{aligned}\sigma_{aa}(\theta_i,\theta_s,\phi_s) &= \frac{k^2}{\pi}\left|\frac{(1+\cos\theta_i+\cos\theta_s)\cos\phi_s-\sin\theta_i\sin\theta_s}{\cos\theta_i+\cos\theta_s}\right|^2 \\ &\left\{(2\pi k_{dz})^2 e^{-\sigma^2 k_{dz}^2}\Psi(k_{dx},k_{dy})+\right. \\ &\left.\int d\rho'\rho' e^{-\sigma^2 k_{dz}^2}\left\{e^{\sigma^2 k_{dz}^2 C(\rho')}-1-\sigma^2 k_{dz}^2 C(\rho')\right\}J_0(k_{d\perp})\right\} \quad (5.28)\end{aligned}$$

This subtraction enables much of the contribution to the integral from large values of ρ to be eliminated. The above integral is evaluated by Gaussian quadrature integration over a finite range, with the upper limit extended to infinity in an iterative fashion until convergence in the cross section is observed. Correlation function values are calculated using a Gaussian quadrature integration of (5.26) and tabled so that repeated integrations are not performed. Resulting calculations require only a few seconds on a DEC AXP 3000 workstation for a full set of 60 backscatter calculations. However, the method breaks down for large rms height surfaces ($k\sigma$ greater than approximately 30) due to a loss of precision in the numerical calculations. Methods for PO integral evaluation in this limit have been discussed by [141] and [27].

Chapter 6

A Numerical Study of Ocean Thermal Emission

6.1 Introduction

Models for the prediction of ocean surface polarimetric thermal emission are currently of interest for the interpretation of data from recent airborne microwave radiometer flights. As discussed in Chapter 3, brightness temperatures of azimuthally anisotropic media are expected to vary with azimuth angle, and to contain signals in the third and fourth Stokes parameters, U_B and V_B. Since a wind generated ocean surface has such azimuthally anisotropic properties, polarimetric passive remote sensing should be useful for the remote sensing of ocean winds and is currently under investigation by a number of organizations [91],[92]-[94],[159]. Although experimental data has been taken and reveals azimuthal variations similar to those observed in Chapter 3, a fully validated model for the prediction of ocean polarimetric brightnesses does not presently exist.

In this chapter, an initial numerical study of ocean polarimetric brightness tem-

peratures is performed using a penetrable surface version of the SMFSIA of Chapters 4 and 5. Monte Carlo simulations are performed for the Durden-Vesecky ocean model discussed in the Chapter 5 since this spectrum has been used in previous studies [92]-[93], and since an azimuthally anisotropic surface model is necessary to obtain U_B and V_B brightnesses. Predictions are compared with experimental data and with predictions of the standard approximate theories, although the larger computational requirements associated with penetrable surface simulations limit maximum SMFSIA surface sizes to 8 by 8 electromagnetic wavelengths, and the small azimuthal variations which occur (usually less than 1.5 K) make accurate calculations difficult. Although these limitations prevent a thorough quantitative numerical study, the simulations performed give some indication that present approximate theories yield reasonable results, and a more detailed study of the influence of ocean spectral models on polarimetric brightness temperatures is performed using the composite surface model approach.

The next section provides a brief review of previous studies of ocean thermal emission, and Section 6.3 discusses the application of the standard approximate theories to this problem. The formulation of the penetrable surface SMFSIA is presented in detail in Section 6.4, and a technique for treating highly lossy media such as sea water without greatly increasing the number of unknowns required is discussed. Section 6.5 compares model predictions with experimental data and with the approximate theories, and the composite surface model is applied to assess variations with ocean spectrum models in Section 6.6

6.2 Previous studies of ocean thermal emission

Interest in passive remote sensing of the ocean at microwave frequencies developed in the late 1960's, with early ground based experiments demonstrating the sensitivity of ocean brightnesses to sea surface temperature, salinity, and wind speed [142]-[143]. Models based upon a geometrical optics formulation [144] were proposed, but found inadequate when compared with experimental data at frequencies ranging from 1.81 to 19.3 GHz. The availability of passive microwave data from the Electrically Scanning Microwave Radiometer (ESMR) on board the Nimbus 5 and 6 satellites and the Scanning Multifrequency Microwave Radiometer (SMMR) onboard the Nimbus 7 and Seasat-A satellites led to further interest in the improvement of theoretical models for ocean brightness temperatures [145] through the mid to late 1970's. Extensions of the standard composite surface scattering theory to the prediction of brightness temperatures were made by [146] and [147], and found to provide more reasonable predictions of variations with incidence angle and wind speed. The importance of an anisotropic ocean spectrum model in these references was still not recognized, as the circluar active flights of [116] had yet to be performed. Sufficient experimental data existed, however, for sensitivities with respect to many physical parameters to be determined and for retrieval algorithms to be developed [145],[148]-[151]. In addition, the importance of the contributions of sea surface foam and atmospheric emissions was recognized, and empirical models for these contributions were derived [152]-[155].

As interest in anisotropic ocean surface models developed, ocean brightness temperature variations with azimuth observation angle began to be considered. Results in [156] showed that variations with azimuth angle at normal incidence (equivalent

to polarization variations as well) could be as large as 5 K. Experimental studies [157] confirmed these variations, and demonstrated the potential for remote sensing of both ocean wind speed and direction from passive measurements assuming that radiometers sensitive enough to detect these relatively small variations are employed. Studies of data from the Special Sensor Microwave/Imager (SSM/I), a more sensitive microwave radiometer flown on several Defense Meteorological Satellite Program (DMSP) satellites through the 1980's, further illustrated the wind direction dependence of ocean brightnesses, and analysis of this data enabled global scale mean ocean wind vector maps to be created [158].

Interest in improvement of accuracy for the ocean wind vector retrievals of [158] has led to the development of polarimetric techniques for ocean passive remote sensing. Since measurement of the U_B parameter corresponds to a third polarization measurement for normally incident observations, the additional information in measured in polarimetric remote sensing can potentially achieve some improvement in retrieval accuracy. Methods for the application of this information are discussed in [92], where an SPM emission model is applied with the Durden-Vesecky ocean spectrum to produce predictions of ocean surface polarimetric brightness temperatures. Comparisons with the 14 GHz, nadir polarimetric passive data of [91] show the SPM to yield reasonable predictions for azimuthal variations of the U_B brightness, and model sensitivities with respect to various parameters were discussed. A composite surface model has also been proposed in [93], and compared with experimental data from an experiment performed by the WINDRAD sensor of the Jet Propusion Laboratory (JPL) in 1994 [94] in which polarimetric brightness temperatures were

measured at 30, 40, and 50 degree incidence angles at 19.35 GHz for a wind speed of 12 m/s. Experimental data has also been measured at 92 GHz in [89],[159]-[160] and was fit with a geometric optics model. Currently, [91],[94], and [159] form the only exisiting polarimetric measurements of ocean emission although more experiments are planned for the future. Accurate theoretical models are thus of interest for the design of these experiments and for predicting behaviors with various ocean parameters. The studies of this chapter should allow some insight into the approximate theoretical models proposed to date.

6.3 Approximate methods

As mentioned previously, all three of the approximate theories discussed in Chapter 1 have been applied to the prediction of thermal emission from the ocean surface. Geometrical optics [144],[159], SPM [92], and composite surface [93],[146]-[147], models have all shown some degree of success, with the SPM and composite surface models compared most extensively with experimental data. It should be noted that no models have been based on a full physical optics method, again due to the difficulties associated with physical optics integral evaluation. An additional problem with analytical evaluation of the physical optics integral arises for penetrable surfaces, since the Fresnel reflection coefficients vary as a function of incidence angle. Monte Carlo simulations, however, are not limited by this problem since local incidence angles can be determined for a given surface realization. All of these methods require integration of the bistatic cross sections predicted by a given approximate scattering theory as discussed in Chapter 1, making approximate emission models more computationally

involved than their scattering counterparts. These integrals are usually performed numerically, as their evaluation can be difficult for an arbitrary ocean spectrum.

The SPM based emission model of [92] was found to produce reasonable comparisons with the experimental data of [91] using the Durden Vesecky spectrum once second order contributions to the coherent reflection coefficient were taken into account. It should be noted that a truncated Durden Vesecky spectrum was used, with the cutoff wavenumber chosen to insure that rms heights of surfaces simulated remained within limits (approximately $k\sigma < 0.4$) validated for 1-D periodic power law spectrum surfaces through comparison with a Monte Carlo method of moments solution. In addition, comparisons with experimental data were performed only for the U_B and $Q = T_{Bv} - T_{Bh}$ brightnesses, so that absolute levels of linearly polarized temperatures were not illustrated. Use of the SPM implies that these simulations modeled the bistatic cross section of the ocean as including a specularly reflected coherent term at 14 GHz, which is clearly at odds with the large $k\sigma$ product when the entire ocean spectrum is considered.

To address this issue, a composite surface model based on the original formulation of [146] was developed for the anisotropic Durden Vesecky spectrum, and predictions were compared with WINDRAD experimental data [93] in T_{Bh}, T_{Bv} and U_B brightnesses. The composite surface model results in the specular coherent wave of the SPM being tilted over the slope distribution of the long waves, with a more realistic geometrical optics type behavior resulting for the near forward scattered region. Again, overall agreement in the azimuthal variations of polarimetric brightness temperatures was found to be good, although experimental data in the linearly po-

larized brightnesses exceeded model predictions by as much as 25 K and an empirical weighting function was included in the model to obtain the observed up-down wind brghtness asymmetry. Only minor differences between brightnesses predicted by the composite surface and SPM alone models were observed, indicating that tilting effects have little influence on azimuthal variations of ocean brightness temperatures. Differences between experimental and theoretical linear brightnesses were explained due to effects of foam and atmospheric emissions, which were not included in the theoretical model. Simulations were also performed using a geometrical optics model with the Cox and Munk derived slope variances for an ocean surface, and predicted azimuthal variations were found smaller than those of the composite surface model. Thus, reference [93] concludes that the most significant source of azimuthal variations in ocean surface emission is the SPM Bragg scattering contribution.

In contrast, references [89] and [159] propose a GO based model which includes both shadowing and multiple scattering effects, and obtain reasonable agreement with measured data from ground based observations of mechanically generated water waves at 91.65 GHz. Experimental flights of this sensor also were performed, although data has yet to be fully published. As discussed in Chapter 5, a geometrical optics model for the ocean emphasizes the long wave portion of the spectrum, since near forward scattering, where GO predictions are expected to be valid, is dominated by surface low frequencies. The distinction between these references and [93] emphasizes the limited state of current knowledge in polarimetric passive remote sensing, and motivates the numerical simulations of this chapter. Comparisons will be made with both SPM and Monte Carlo physical optics predictions to obtain some insight into the differences

between these references.

6.4 Derivation of Penetrable Surface SMFSIA

Calculation of scattering from a penetrable rough surface involves use of one or a combination of equations (1.6-1.7) along with one of a combination of equations (1.8-1.9), as discussed in Chapter 1. Since the ocean is a highly lossy dielectric surface at microwave frequencies, a formulation similar to that of the perfectly conducting surface case in Chapters 4 and 5 is adopted, although the free space MFIE of this approach is augmented through use of the EFIE in the lower medium. The integral equations to be used are thus

$$\begin{aligned}\frac{\bar{n}\times\overline{H}_0(\overline{r})}{2} &= \bar{n}\times\overline{H}_{inc}+\bar{n}\times\int dS'\left\{-i\omega\epsilon_0\overline{\overline{G}}_0(\overline{r},\overline{r}')\cdot[\hat{n}'\times\overline{E}(\overline{r}')]\right.\\ &\left.+\nabla\times\overline{\overline{G}}_0\cdot[\hat{n}'\times\overline{H}(\overline{r}')]\right\} \qquad (6.1)\end{aligned}$$

in region 0 above the surface profile and

$$\begin{aligned}-\frac{\bar{n}\times\overline{E}_1(\overline{r})}{2} &= \bar{n}\times\int dS'\left\{i\omega\mu_1\overline{\overline{G}}_1(\overline{r},\overline{r}')\cdot[\hat{n}'\times\overline{H}(\overline{r}')]\right.\\ &\left.+\ \nabla\times\overline{\overline{G}}_1\cdot[\hat{n}'\times\overline{E}(\overline{r}')]\right\} \qquad (6.2)\end{aligned}$$

in region 1 below, where $\bar{n}$ is the vector $= \left(\hat{z}-\frac{\partial f}{\partial x}\hat{x}-\frac{\partial f}{\partial y}\hat{y}\right)$. In contrast to the EBC formulation of Chapter 3, however, these integral equations are now to be tested and solved at points on the surface profile, so that the above integrals are principle value integrals and the factor of 1/2 results from the contribution of the Green's function

singularity.

Difficulties associated with principle value integration of the self terms in the above formulation motivate a transformation to the Stratton-Chu integral equations, as discussed in [1]. The equations then become

$$\frac{\bar{n}\times\overline{H}_0(\bar{r})}{2} = \bar{n}\times\overline{H}_{inc}+\bar{n}\times\int dS'\left\{-i\omega\epsilon_0 g_0(\bar{r},\bar{r}')[\hat{n}'\times\overline{E}(\bar{r}')]\right.$$
$$\left.+(\nabla\times g_0)\cdot[\hat{n}'\times\overline{H}(\bar{r}')]-\frac{i}{\omega\mu_0}\nabla'_s\cdot[\hat{n}'\times\overline{E}(\bar{r}')]\nabla g_0\right\} \quad (6.3)$$

in region 0 above the surface profile and

$$-\frac{\bar{n}\times\overline{E}_1(\bar{r})}{2} = \bar{n}\times\int dS'\left\{i\omega\mu_1 g_1(\bar{r},\bar{r}')\cdot[\hat{n}'\times\overline{H}(\bar{r}')]\right.$$
$$\left.+\ (\nabla\times g_1)\cdot[\hat{n}'\times\overline{E}(\bar{r}')]+\frac{i}{\omega\epsilon_1}\nabla'_s\cdot[\hat{n}'\times\overline{H}(\bar{r}')]\nabla g_1\right\} \quad (6.4)$$

where g_j is the scalar Green's function as defined in Chapter 3.

Applying the method of moments to these equations requires expansion of the four unknown scalar functions on the surface into pulse basis functions, as

$$F_x=\hat{x}\cdot\left[\hat{n}\times\overline{H}(\bar{r})\right] = \sum_m\sum_n F_x^{mn}P_{mn}(\bar{r}) \quad (6.5)$$

$$F_y=\hat{y}\cdot\left[\hat{n}\times\overline{H}(\bar{r})\right] = \sum_m\sum_n F_y^{mn}P_{mn}(\bar{r}) \quad (6.6)$$

$$G_x=\hat{x}\cdot\left[\hat{n}\times\overline{E}(\bar{r})\right] = \sum_m\sum_n G_x^{mn}P_{mn}(\bar{r}) \quad (6.7)$$

$$G_y=\hat{y}\cdot\left[\hat{n}\times\overline{E}(\bar{r})\right] = \sum_m\sum_n G_y^{mn}P_{mn}(\bar{r}) \quad (6.8)$$

and substituting these expansions into dot products of equations (6.3) and (6.4) with $\hat{x}$ and $\hat{y}$ respectively. The resulting four scalar equations are

$$H_{iy} + \frac{\partial f}{\partial y} H_{iz} = -\frac{F_x \sqrt{1 + \left(\frac{\partial f}{\partial x}\right)^2 + \left(\frac{\partial f}{\partial y}\right)^2}}{2} + \int\int dx'\, dy' \sqrt{1 + \left(\frac{\partial f}{\partial x'}\right)^2 + \left(\frac{\partial f}{\partial y'}\right)^2}$$
$$\left\{ -i\omega\epsilon_0 g_0 \left[-G_x \frac{\partial f}{\partial y}\frac{\partial f}{\partial x'} - G_y(1 + \frac{\partial f}{\partial y}\frac{\partial f}{\partial y'}) \right] \right.$$
$$+G_{30}\left[F_x(dy\frac{\partial f}{\partial y'} + dx\frac{\partial f}{\partial x'} - dz) + F_y(\frac{\partial f}{\partial y'} - \frac{\partial f}{\partial y})dx \right]$$
$$\left. +\frac{i}{\omega\mu_0}\nabla_s' \cdot \overline{G}\left[dy + \frac{\partial f}{\partial y}dz \right] G_{30} \right\} \tag{6.9}$$

$$-H_{ix} - \frac{\partial f}{\partial x} H_{iz} = -F_y \sqrt{1 + \left(\frac{\partial f}{\partial x}\right)^2 + \left(\frac{\partial f}{\partial y}\right)^2}/2 +$$
$$\int\int dx'\, dy' \sqrt{1 + \left(\frac{\partial f}{\partial x'}\right)^2 + \left(\frac{\partial f}{\partial y'}\right)^2} \left\{ -i\omega\epsilon_0 g_0 \left[G_x(1 + \frac{\partial f}{\partial x}\frac{\partial f}{\partial x'}) + G_y \frac{\partial f}{\partial y'}\frac{\partial f}{\partial x} \right] \right.$$
$$+G_{30}\left[F_x(\frac{\partial f}{\partial x'} - \frac{\partial f}{\partial x})dy + F_y(dy\frac{\partial f}{\partial y'} + dx\frac{\partial f}{\partial x'} - dz) \right]$$
$$\left. -\frac{i}{\omega\mu_0}\nabla_s' \cdot \overline{G}\left[dx + \frac{\partial f}{\partial x}dz \right] G_{30} \right\} \tag{6.10}$$

$$0 = G_x \sqrt{1 + \left(\frac{\partial f}{\partial x}\right)^2 + \left(\frac{\partial f}{\partial y}\right)^2}/2 + \int\int dx'\, dy' \sqrt{1 + \left(\frac{\partial f}{\partial x'}\right)^2 + \left(\frac{\partial f}{\partial y'}\right)^2}$$
$$\left\{ i\omega\mu_0 g_1 \left[-F_x \frac{\partial f}{\partial y}\frac{\partial f}{\partial x'} - F_y(1 + \frac{\partial f}{\partial y}\frac{\partial f}{\partial y'}) \right] \right.$$
$$+G_{31}\left[G_x(dy\frac{\partial f}{\partial y'} + dx\frac{\partial f}{\partial x'} - dz) + G_y(\frac{\partial f}{\partial y'} - \frac{\partial f}{\partial y})dx \right]$$

$$-\frac{i}{\omega\epsilon_1}\nabla_s' \cdot \overline{F}\left[dy + \frac{\partial f}{\partial y}dz\right] G_{31}\Bigg\} \tag{6.11}$$

$$\begin{aligned}
0 = {} & G_y\sqrt{1+\left(\frac{\partial f}{\partial x}\right)^2+\left(\frac{\partial f}{\partial y}\right)^2}/2 + \int\int dx'\, dy'\sqrt{1+\left(\frac{\partial f}{\partial x'}\right)^2+\left(\frac{\partial f}{\partial y'}\right)^2} \\
& \Bigg\{ i\omega\mu_0 g_1 \left[F_x(1+\frac{\partial f}{\partial x}\frac{\partial f}{\partial x'}) + F_y\frac{\partial f}{\partial y'}\frac{\partial f}{\partial x}\right] \\
& + G_{31}\left[G_x(\frac{\partial f}{\partial x'} - \frac{\partial f}{\partial x})dy + G_y(dy\frac{\partial f}{\partial y'} + dx\frac{\partial f}{\partial x'} - dz)\right] \\
& + \frac{i}{\omega\epsilon_1}\nabla_s' \cdot \overline{F}\left[dx + \frac{\partial f}{\partial x}dz\right] G_{31}\Bigg\}
\end{aligned} \tag{6.12}$$

which are then tested at the center points of the pulse basis functions to form the matrix equation of the method of moments. In the above equation,

$$\begin{aligned}
\nabla g_j(\overline{r},\overline{r}') &= \overline{R}\frac{e^{ik_j|\overline{r}-\overline{r}'|}}{4\pi|\overline{r}-\overline{r}'|^2}(ik_j - \frac{1}{|\overline{r}-\overline{r}'|}) \\
&= \overline{R}G_{3j}
\end{aligned}$$

where

$$\begin{aligned}
\overline{R} &= \hat{x}(x-x') + \hat{y}(y-y') + \hat{z}\,(f(x,y) - f(x',y')) \\
&= \hat{x}dx + \hat{y}dy + \hat{z}dz
\end{aligned} \tag{6.13}$$

Note that the $\nabla_s' \cdot \overline{G}$ and $\nabla_s' \cdot \overline{F}$ terms require a numerical differentiation of these

unknown functions, and are calculated as

$$\begin{aligned} \nabla'_s \cdot \overline{A} &\approx \frac{\partial}{\partial x'} A_x + \frac{\partial}{\partial y'} A_y \\ &\approx \left(F_x^{n+1,m} - F_x^{n-1,m} \right) / (2\Delta x) + \left(F_y^{n,m+1} - F_y^{n,m-1} \right) / (2\Delta y) \end{aligned} \quad (6.14)$$

where n and m refer to the x and y indices of the pulse basis functions used on the surface rectangular grid, and Δx and Δy refer to the spacing between these basis functions in the x and y directions. Surfaces in this formulation are approximated as a collection of planes, with their heights and first derivatives specified on a rectangular grid. For basis functions lying on the edge of the surface profile, field unknowns on adjacent points were approximated as being equal to those at the edges. The above procedure for the calculation of surface field divergences effectively assumes that adjacent field values are averaged with the center point to obtain values for surface fields at the edges of the center pulse basis function, and these values then derive the divergence through a centered difference derivative. The accuracy of this approximation was investigated through comparison of results with a 6 unknown function penetrable code, where surface field divergences were retained as unknown functions also. Obtained values were found to correspond well with equation (6.14), and computed scattering coefficients showed only minor differences.

Note also that the g_j and $\nabla'_s \cdot \overline{A}$ functions have self term contributions which require careful consideration. A small argument expansion of these terms was analytically integrated, and remaining portions of the ~~these~~ functions were integrated numerically to insure accurate self term calculations. Principle value self terms in-

volving $\nabla \times \underline{\underline{g}}_j$ are zero for surfaces approximated by collections of planes, as can be seen in equations (6.9-6.12), due to the fact that MFIE matrix elements vanish for flat surfaces.

The above formulation holds for a lower medium with arbitrary dielectric properties. Other choices of integral equations could be used as well, but note that the choice illustrated results in the $\sqrt{1+\left(\frac{\partial f}{\partial x}\right)^2+\left(\frac{\partial f}{\partial y}\right)^2}/2$ terms always located on matrix diagonals if sets of four equations (6.9- 6.12) are taken together for individual testing points to construct the matrix equation, and if unknown amplitudes are taken as sets of four in the column vector multiplied by the matrix. Since the $\sqrt{1+\left(\frac{\partial f}{\partial x}\right)^2+\left(\frac{\partial f}{\partial y}\right)^2}/2$ terms are usually the largest matrix elements obtained, their inclusion on matrix diagonals improves matrix conditioning properties and iterative method convergence. The SMFSIA and CAG techniques of Chapters 4 and 5 can be directly applied to this formulation to obtain an iterative penetrable surface solution. However, a problem arises for high dielectric constant materials that is addressed in the next section.

6.4.1 Numerical impedance boundary condition (NIBC)

As discussed in Chapter 1, the method of moments requires sampling at a rate ranging from 4 to 10 points per wavelength of the surface sampled if all surface spatial scales are properly resolved with this discretization. For materials with high dielectric constants, the short wavelengths obtained inside the dielectric material can therefore cause great increases in the number of unknowns required to solve a fixed physical size problem. However, it is clear that a limit to the discretization level needed should be obtained for highly lossy media, since solutions for a perfectly conducting surface

require sampling only on the scale of the free space wavelength.

In the past, the standard impedance boundary condition (IBC) approach has been applied with both the MFIE and EFIE to address this problem for highly conducting media. The IBC [161] approximates electric fields on the surface profile as

$$\overline{E} = Z[\hat{n} \times \overline{H}] \tag{6.15}$$

where Z is the characteristic impedance of the lower medium, and is derived from standard integral equations by assuming a very small skin depth compared with any of the surface dimensions of interest. The IBC can be related to the matrix equation of the MOM by observing that it corresponds to ignoring any phase variations of either surface fields or Green's functions on the scale of the lower medium wavelength, and approximates equations (6.11) and (6.12) by a single point relationship between the $\overline{G}$ and $\overline{F}$ unknown functions. While the IBC has been successfully applied to the prediction of scattering from finitely conducting metallic media, its application to ocean scattering is not directly warranted since sea water conductivities, though high, are much less than those of metallic materials. Also, the large range of spatial scales in the ocean spectrum allows surface variations to occur over lengths comparable to those of the dielectric wavelength, even when a high frequency surface cutoff as in Chapter 5 is used. Thus, an improved approach is needed for the penetrable ocean surface case.

Formulation

The formulation of an improved technique begins by considering equations (6.11) and (6.12) alone. Clearly, the rapid decay of the Green's function in the lower medium allows matrix elements beyond a certain distance from the testing point to be completely neglected, so that weak and flat surface matrix contributions for the lower region in the SMFSIA can be ignored if a large enough bandwidth is included in the strong matrix. For example, results presented in this chapter will use an ocean permittivity of $\epsilon = (39.7, 40.2)$ at 14 GHz, which corresponds to that of sea water at 10 degrees C with a salinity of 30 parts per thousand obtained from the model of [139]. The resulting wave vector inside the ocean is $k = (2033.6, 849.8)$, which decays to less than one percent in a distance of 5.42 mm, or 0.253 free space wavelengths. Thus, if a sampling rate of 8 points per free space wavelength were to be used, a bandwidth of only 2 points in the strong matrix is needed to include contributions to one percent accuracy. However, this sampling rate still fails to capture the rapidly decaying behavior of the lower Green's function within the included region.

To address this issue, the matrix equation of the EFIE portion in the method of moments is written as

$$\begin{bmatrix} \overline{\overline{A}} & \overline{\overline{B}} & \overline{\overline{C}} & \overline{\overline{D}} \\ \overline{\overline{E}} & \overline{\overline{F}} & \overline{\overline{G}} & \overline{\overline{H}} \end{bmatrix} \begin{bmatrix} \overline{F_x} \\ \overline{F_y} \\ \overline{G_x} \\ \overline{G_y} \end{bmatrix} = \begin{bmatrix} \overline{0} \\ \overline{0} \end{bmatrix} \tag{6.16}$$

where the $\overline{\overline{A}}$ to $\overline{\overline{H}}$ matrices refer to the corresponding Green's functions integrals in (6.11) and (6.12), $\overline{F_x}$ through $\overline{G_y}$ represent vectors made up of the unknown constant

amplitudes of the pulse basis functions, and $\overline{0}$ is a null vector. This matrix is actually rearranged as mentioned previously so that individual 2×4 submatrices are placed adjacently for each testing-integration point combination. The notation above will be used for convenience however in the following equations.

An equation similar to (6.15) can be obtained by solving (6.16) for $\overline{G}$ as

$$\begin{bmatrix} \overline{G_x} \\ \overline{G_y} \end{bmatrix} = -\overline{\overline{R}}^{-1}\overline{\overline{S}} \begin{bmatrix} \overline{F_x} \\ \overline{F_y} \end{bmatrix} \tag{6.17}$$

where

$$\overline{\overline{R}} = \begin{bmatrix} \overline{\overline{C}} & \overline{\overline{D}} \\ \overline{\overline{G}} & \overline{\overline{H}} \end{bmatrix} \tag{6.18}$$

and

$$\overline{\overline{S}} = \begin{bmatrix} \overline{\overline{A}} & \overline{\overline{B}} \\ \overline{\overline{E}} & \overline{\overline{F}} \end{bmatrix} \tag{6.19}$$

except that variations of Green's functions and surface fields are now included. Rewriting the MFIE portion of the method of moments matrix equation as

$$\begin{bmatrix} \overline{\overline{I}} & \overline{\overline{J}} & \overline{\overline{K}} & \overline{\overline{L}} \\ \overline{\overline{M}} & \overline{\overline{N}} & \overline{\overline{O}} & \overline{\overline{P}} \end{bmatrix} \begin{bmatrix} \overline{F_x} \\ \overline{F_y} \\ \overline{G_x} \\ \overline{G_y} \end{bmatrix} = \begin{bmatrix} -\overline{F}_x^{inc} \\ -\overline{F}_y^{inc} \end{bmatrix} \tag{6.20}$$

and substituting in (6.17) for $\overline{G}$ yields

$$\left\{\overline{\overline{T}} - \overline{\overline{U}}\,\overline{\overline{R}}^{-1}\overline{\overline{S}}\right\} \begin{bmatrix} \overline{F_x} \\ \overline{F_y} \end{bmatrix} = \begin{bmatrix} -\overline{F}_x^{inc} \\ -\overline{F}_y^{inc} \end{bmatrix} \tag{6.21}$$

where

$$\overline{\overline{T}} = \begin{bmatrix} \overline{\overline{I}} & \overline{\overline{J}} \\ \overline{\overline{M}} & \overline{\overline{N}} \end{bmatrix} \tag{6.22}$$

and

$$\overline{\overline{U}} = \begin{bmatrix} \overline{\overline{K}} & \overline{\overline{L}} \\ \overline{\overline{O}} & \overline{\overline{P}} \end{bmatrix} \tag{6.23}$$

where now only the $\overline{\overline{A}}$ through $\overline{\overline{H}}$ terms contain the lower medium Green's function, while the $\overline{\overline{I}}$ through $\overline{\overline{P}}$ terms involve the upper medium Green's function only. The first $\overline{\overline{T}}$ matrix of this equation is exactly that of the MFIE for perfectly conducting surfaces, so the second product of three matrices modifies the MFIE to include the effects of finite surface conductivity.

Element averaging

The NIBC approach is based on an assumption that variations of tangential surface fields on the scale of the lower medium wavelength do not contribute significantly to scattered fields. Consider equation (6.21) with sampling on the scale of the lower medium wavelength under this assumption. Since the $\overline{\overline{T}}$ matrix contains only free space Green's functions, any small scale variations in $\overline{F}_x$ and $\overline{F}_y$ are effectively averaged by the slowly varying free space Green's function to the free space scale, which implies that an average over matrix columns is reasonable. In addition, an average over matrix rows is also possible given that the right hand side of the matrix equation contains only slowly varying incident fields as well. These averages should be approx-

imately equal to the free space sampled MFIE elements, again since only the free space Green's function is averaged. A similar argument can be applied to illustrate that an average over the columns of the $\overline{\overline{S}}$ matrix and an average over rows of the $\overline{\overline{U}}$ matrix should not introduce significant error, although in these cases the average should be significantly different from a free space sampling rate since lower medium Green's functions are involved in this product. Methods for the $\overline{\overline{R}}$ matrix are not as clear since properties of its inverse, which is involved in the matrix product needed, are more difficult to quantify. A more detailed consideration of this matrix (which contains the same terms as the MFIE free space matrix except with the lower medium Green's function), however, reveals it to be well approximated as a diagonal matrix if the surface is assumed to be made up of planes passing through each free space scale testing point. This is due to the fact again that MFIE matrix elements are zero for points located on the same plane, so that most of the near diagonal points when sampled on the lower medium wavelength scale are zero, and the matrix is dominated by the $\sqrt{1+\left(\frac{\partial f}{\partial x}\right)^2+\left(\frac{\partial f}{\partial y}\right)^2}/2$ diagonal terms. An average over the rows $\overline{\overline{S}}$ is then possible, since it again multiplies a matrix involving free space Green's functions which should effectively average out the small scale variations.

Thus, the final NIBC approach samples the $\overline{\overline{T}}$,$\overline{\overline{U}}$ and $\overline{\overline{R}}$ matrices on the free space scale as in the perfectly conducting case, with the lower medium Green's function $\overline{\overline{R}}$ matrix being dominated by the self terms so that only minor errors should be incurred. The $\overline{\overline{S}}$ matrix is generated as if the entire problem were sampled on the lower medium scale, and then averaged over both rows and columns to free space scale to use in the matrix products required.

The SMFSIA is applied for the solution of matrix equation (6.21) once the appropriate submatrices are generated. As discussed previously, weak and flat surface terms are neglected for the $\overline{\overline{A}}$ through $\overline{\overline{H}}$ matrices, so that weak iterations are performed only on the free space Green's function contributions. Since the BICGSTAB solver requires a product of the entire matrix of (6.21) with a vector, individual routines for sub-matrix products are used in succession, and another BICGSTAB routine is used to obtain the $\overline{\overline{R}}^{-1}$ product by solving

$$\overline{\overline{R}} \begin{bmatrix} \overline{Q_x} \\ \overline{Q_y} \end{bmatrix} = \overline{\overline{S}} \begin{bmatrix} \overline{F_x} \\ \overline{F_y} \end{bmatrix} \tag{6.24}$$

where $\overline{Q}$ is the desired product with the matrix inverse, and the right hand side of the equation is known from earlier multiplications.

Verification

A verification of the accuracy of this technique was performed through a study of a two basis function problem, with matrix products for various averaging methods compared with those retaining all elements on the lower medium scale and averaging after all products had been formed. Results showed the above procedure to cause a greater than 10 percent error in obtained product vector norms, which was reduced to 1.3 percent by using a row and column averaged $\overline{\overline{U}}$ matrix as well. The numerical differentiation performed by the terms of this matrix evidently requires significant oversampling in order to obtain accurate results. Use of a row and column averaged $\overline{\overline{R}}$ matrix was not found to cause any improvement in accuracy, nor did use of a row and column averaged version of the free space MFIE matrix, $\overline{\overline{T}}$. Thus, the NIBC

approach averages the g_j and $\nabla'_s \cdot \overline{A}$ terms over rows and columns on the small scale, and samples $\nabla g \times \overline{A}$ terms on free space scale. Verification of the technique for larger problems is complicated by the much greater number of unknowns required to sample problems on the lower medium scale. Comparisons with analytical models will be presented in Section 6.5 which illustrate that the technique yields reasonable accuracy.

Calculation of brightness temperatures

As discussed in Chapters one and three, brightness temperatures emitted by a medium are proportional to the physical temperature of the medium and to its emissivity. Emissivities are calculated by determining the total power absorbed into the medium for a specified incident field and incidence direction, and can also be calculated as one minus the total power reflected if power conservation is satisfied. To avoid a time consuming numerical integration of bistatic scattering coefficients over the upper hemisphere as in Chapter 1, an integration of the Poynting vector obtained from the method of moments over the surface profile is used to calculate both reflected and transmitted powers. This approach has the advantage of allowing a power conservation check on numerical results, which is not possible by integrating scattering coefficients for a lossy medium since transmitted far field propagation is exponentially attenuated. Power transmitted into the lower medium is computed as

$$P_t = -\int dS' \frac{1}{2} Re\left\{\hat{n} \cdot \left(\overline{E} \times \overline{H}^*\right)\right\} \tag{6.25}$$

$$= -\int dx' \int dy' \left(\sqrt{1 + \left(\frac{\partial f}{\partial x'}\right)^2 + \left(\frac{\partial f}{\partial y'}\right)^2} \right)^2 \frac{1}{2} Re\left\{ G_x \, F_y^* - G_y \, F_x^* \right\} \quad (6.26)$$

and reflected power in calculated as

$$P_r = \int dS' \frac{1}{2} Re\left\{ \hat{n} \cdot \left(\left(\overline{E} - \overline{E}_{inc}\right) \times \left(\overline{H} - \overline{H}_{inc}\right)^* \right) \right\} \quad (6.27)$$

$$= \int dx' \int dy' \left(\sqrt{1 + \left(\frac{\partial f}{\partial x'}\right)^2 + \left(\frac{\partial f}{\partial y'}\right)^2} \right)^2 \frac{1}{2} Re\left\{ (G_x - G_{xinc}) \, (F_y - F_{yinc})^* \right.$$

$$\left. -(G_y - G_{yinc}) \, (F_x^* - F_{xinc}) \right\} \quad (6.28)$$

where $\hat{n}$ is assumed to be upward pointing. Power incident on the surface profile, P_{inc}, is computed as in equation (6.25) with total fields on the surface profile replaced by incident fields alone. The sum of P_t/P_{inc} and P_r/P_{inc} from the above equations should be unity if power conservation is satisfied, and any deviations from unity give an estimation of the magnitude of numerical error in obtained brightness temperatures. For the SMFSIA/NIBC results to be presented in this chapter, power conservation within one percent was observed, with resulting errors in brightness temperatures of less than 2.8 K for an assumed 283 K surface temperature. While one percent is a reasonable accuracy for a numerical simulation, azimuthal variations to be studied for the ocean surface are typically less than 1.5 K, so that a precise quantitative assessment from numerical results is difficult. Variations in numerical results with ocean spectrum cutoffs, however, will still allow insight into the importance of spectral regions in ocean thermal emission.

Implementation

The results to be shown in this chapter will use a surface size of 8 by 8 electromagnetic wavelengths with a total of 64 by 64 free space scale unknowns in the simulation. An ocean permittivity with $|\epsilon| = 56.5$ implies a scale difference of 7.5 between free space and the lower medium. Thus, matrix elements for the $\overline{\overline{U}}$ and $\overline{\overline{S}}$ matrices are generated over a 512 by 512 grid (the 7.5 factor is rounded to 8) covering a surface profile generated by linearly interpolating the 64 by 64 profile within the pulse basis functions, and then averaged back to 64 by 64 scale. Note that this procedure is performed only within a small bandwidth of the testing point, since lower medium Green's functions rapidly decay with distance. Simulations with varying bandwidths and scaling factor ratios were performed, and showed brightness temperatures variations to be within 0.5 K of results obtained using a scale factor of 8 and averaging bandwidth of 3 free space scale points. A larger bandwidth of 30 points is used to separate the weak and strong matrix terms in the $\overline{\overline{T}}$ and $\overline{\overline{U}}$ matrices, since free space element contributions remain significant for much larger distances.

Averaged matrix elements are stored in the NIBC to avoid their calculation as part of each matrix vector product required in the SMFSIA. Non-averaged elements of the $\overline{\overline{R}}$ matrix are also stored, since a larger number of multiplies with this matrix are needed in the new BICGSTAB $\overline{\overline{R}}^{-1}$ routine. This storage requirement introduces potential computer memory limitations as both the averaging bandwidth and surface size are increased. The 64 by 64 point surface size and averaging bandwidth of 3 points used approached the 128 megabyte memory limitations of individual SP/2 nodes at the Maui High Performance Computing center, so that computations for

larger surface sizes, though desirable for investigation of edge effects in the simulation, were not possible with present computational resources. Effects of these contributions will be assessed through use of a Monte Carlo PO simulation discussed in Section 6.5. A plane wave incident field will be used for the simulations of this chapter, due to the normally incident configuration to be studied.

Parallel algorithm

In addition to the increased memory requirements of the NIBC, computational requirements are also larger than the simulations of Chapters 4 and 5 due to the row and column averaging of $\overline{\overline{U}}$ and $\overline{\overline{S}}$ performed in the simulation, which dominates all other sections of the code in terms of CPU time. The greater number of matrix vector products required at each BICGSTAB iteration and the new BICGSTAB iterations required for the calculation of $\overline{\overline{R}}^{-1}$ further increase the computational time needed to near allowed limits on the IBM SP/2 by its job queueing system. To reduce matrix generation time so that calculations could be accomplished more efficiently, a parallel algorithm was developed and implemented with the SP/2. This algorithm is specifically designed for the simulations of this chapter, in which polarimetric brightness temperatures at 7 azimuth angles ranging from 0 to 90 degrees will be presented.

Since brightness temperatures for a single surface realization can be calculated at varying observation angles by changing only the right hand side (incident field) in equation (6.21), a group of 7 SP/2 nodes was used with identical surface profiles and varying incident fields to obtain predictions at the 7 azimuth angles desired. Since all 7 nodes share the same matrix, generation of the row and column averaged $\overline{\overline{U}}$ and $\overline{\overline{S}}$

matrices is performed in parallel, with each node performing calculations for 1/7 of matrix rows and communicating the results to the other 6 processes to generate the full averaged matrices. This parallel algorithm was found to reduce computational time to within allowed process limits, so that Monte Carlo simulations with the SP/2 could be performed.

6.5 Results

Figure 6.1 illustrates the comparison between SMFSIA/NIBC, Monte Carlo PO and SPM predictions for 14 GHz nadir observation of a Durden-Vesecky ocean surface at a wind speed of $U_{19.5} = 10$ m/s. A lower cutoff wavenumber of 73.3 and a higher cutoff of 1172.9 are used in the numerical simulation, which result in a $k\sigma$ product of approximately 0.29, so that SPM predictions should be accurate. The three plots of Figure 6.1 show the T_{Bh}, T_{Bu}, and U_B brightnesses for azimuth angles ranging from 0 (upwind) to 90 (crosswind) degrees. V_B brightnesses are not plotted, since all three models predict negligible V_B temperatures for nadir observation. A total of nine realizations were averaged for the SMFSIA results, and brightness temperatures were calculated using the total power transmitted into the lower medium. Figure 6.2 illustrates the same comparison, but with brightness temperatures calculated as one minus the reflectivity of the medium. A comparison of Figures 6.1 and 6.2 shows differences in linear brightness temperatures to be within 1.5 K, and changes in azimuthal variations and U_B brightness temperatures to be within 0.5 K, all consistent with a numerical accuracy of better than one percent. SMFSIA/NIBC results are observed to be matched well by both SPM and PO predictions, (all within 3 K of one

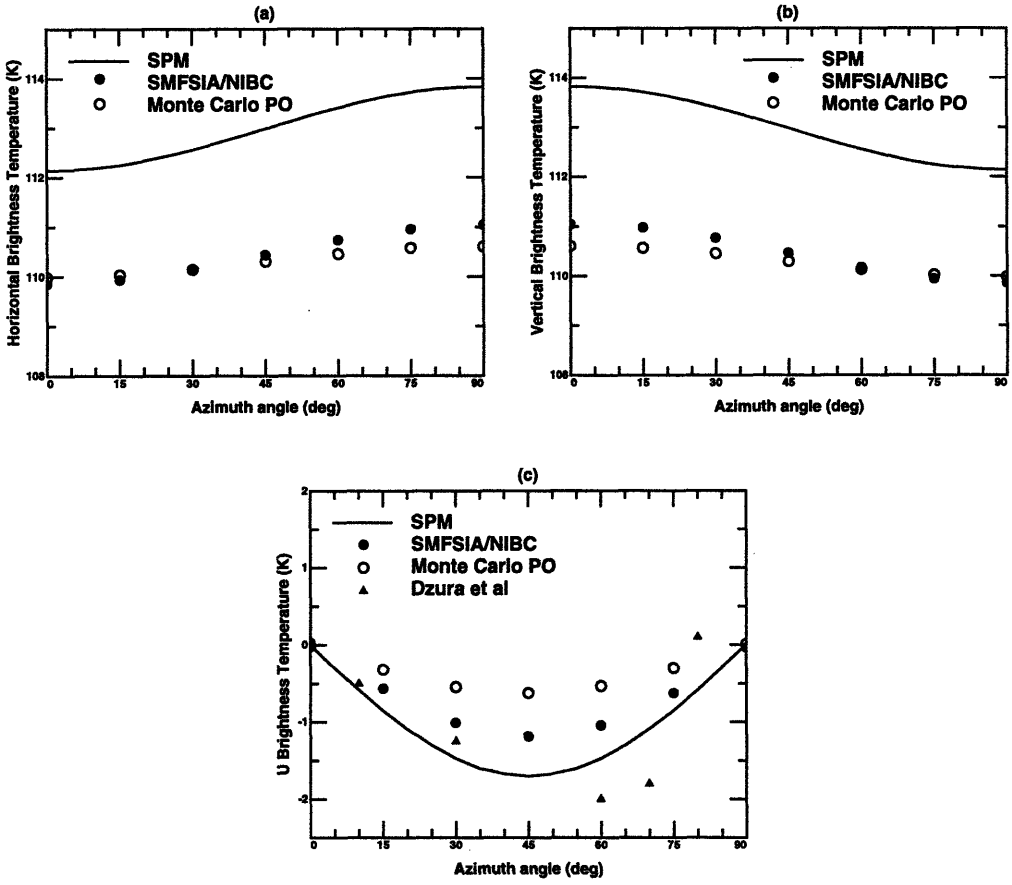

Figure 6.1: Comparison of SMFSIA/NIBC, Monte Carlo PO, SPM, and measured (U_B only) brightness temperatures: 14 GHz, nadir looking, Durden-Vesecky spectrum, $U_{19.5} = 10$ m/s, surface temperature 283 K, $k_{dl} = 73.3$, $k_{du} = 1172.9$, emissivity calculated as absorbed power (a) T_{Bh} (b) T_{Bv} (c) U_B

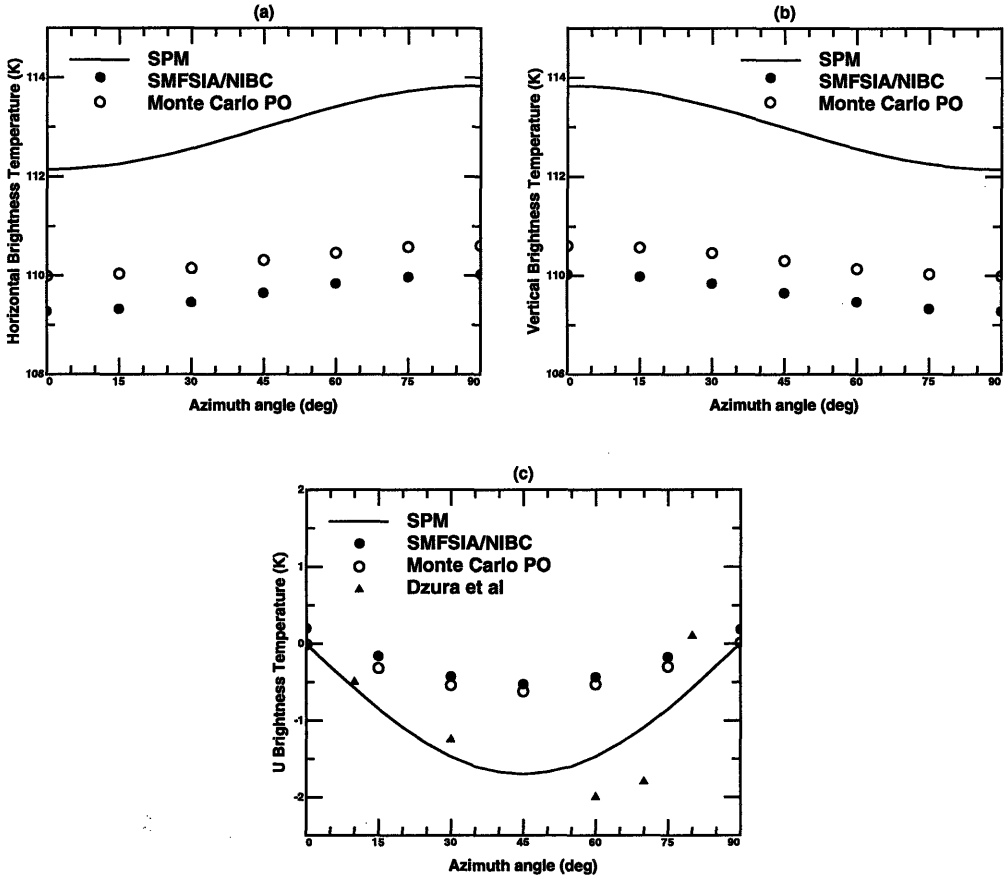

Figure 6.2: Comparison of SMFSIA/NIBC, Monte Carlo PO, SPM, and measured brightness temperatures: 14 GHz, nadir looking, Durden-Vesecky spectrum, $U_{19.5} =$ 10 m/s, surface temperature 283 K, $k_{dl} = 73.3$, $k_{du} = 1172.9$, emissivity calculated as one minus reflected power (a) T_{Bh} (b) T_{Bv} (c) U_B

another), although PO predictions match linear brightnesses levels better than the SPM, but seemingly underestimate azimuthal obtained azimuthal variations. Such comparisons are similar to those reported in [93], where SPM azimuthal variations were found to be under predicted by a geometrical optics formulation, although a full ocean spectrum was considered in this case. SPM results are observed to overpredict both linear and U_B brightness temperatures and their azimuthal variations, although again within a one percent accuracy level. Also included in Figures 6.1 and 6.2 is the U_B experimental data of [91], which was taken for the specified configuration. Measured U_B brightnesses are seen to be slightly larger than those obtained by the SMFSIA/NIBC method, with the small magnitude of these differences making detailed assessments difficult. Effects of finite surface size on both SMFSIA/NIBC and PO results are also difficult to assess, but Monte Carlo PO simulations with larger surface sizes or using tapered incident fields showed brightness temperature variations to be within 0.1 K.

Although Figures 6.1 and 6.2 clearly show SMFSIA/NIBC accuracy to be insufficient for a detailed study of ocean brightnesses, variations in SMFSIA/NIBC predictions with spectrum cutoffs can give some indication as to the importance of spectral regions in ocean thermal emission. Figure 6.3 plots variations in predicted brightness temperatures with high frequency cutoff wavenumber. SMFSIA/NIBC results are included for a low frequency cutoff of 73.3 and high frequency cutoffs of 586.5 and 1172.9 in the numerical simulation. Figure 6.3 demonstrates the importance of the high frequency component in Durden-Vesecky spectrum brightness temperature azimuthal variations, a result also predicted by PO and SPM. SMFSIA brightness

temperatures calculated as one minus reflectivity are shown in Figure 6.4 and also yield a similar conclusion.

Figure 6.5 plots brightness temperatures for the configuration of Figures 6.1 and 6.2 with low frequency cutoffs of 73.3 and 36.6 and with a high frequency cutoff of 586.5. Brightness temperatures are calculated as the power absorbed. Figure 6.5 indicates that low frequency components have little effect on brightness temperatures with the Durden-Vesecky spectrum, also as obtained by both the PO and SPM approximations and as discussed in [92] and [93]. Brightness temperatures calculated as one minus the reflectivity are illustrated in Figure 6.6, and again yield a similar result.

Further SMFSIA/NIBC simulations were prohibited by limitations on computational resources. Although the SMFSIA results presented represent only an initial step in the development of the SMFSIA/NIBC approach for the calculation of ocean brightness temperatures, the simulations performed demonstrate that the approximate models applied to date should yield reasonable predictions. Variations with low and high frequency ocean spectrum cutoffs were found to be in qualitative agreement with all of the models, again providing some validation for the approximate theories applied to date. The remaining section of this chapter will study the influence of different ocean spectrum models in the composite theory, and will emphasize the limited state of current knowledge of ocean polarimetric thermal emission, even with a fully validated electromagnetic model.

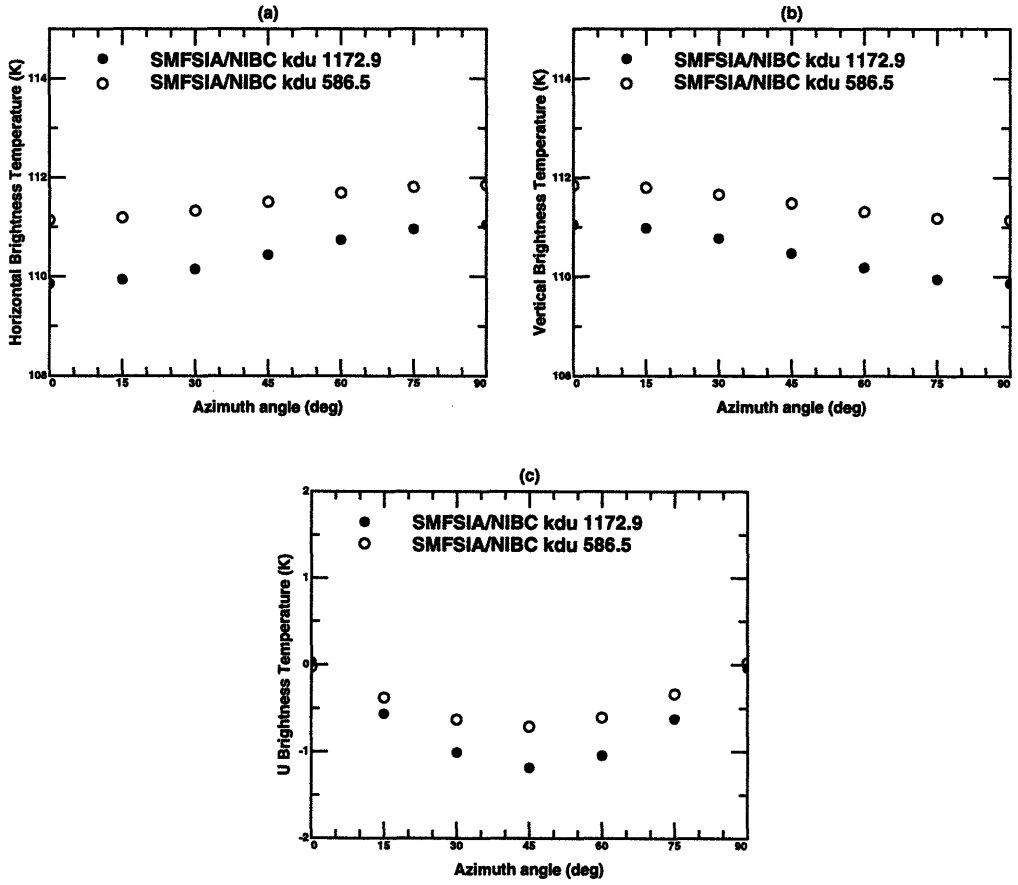

Figure 6.3: Variation of SMFSIA/NIBC brightness temperatures with high frequency cutoff: 14 GHz, nadir looking, Durden-Vesecky spectrum, $U_{19.5} = 10$ m/s, surface temperature 283 K, $k_{dl} = 73.3$, emissivity calculated as absorbed power (a) T_{Bh} (b) T_{Bv} (c) U_B

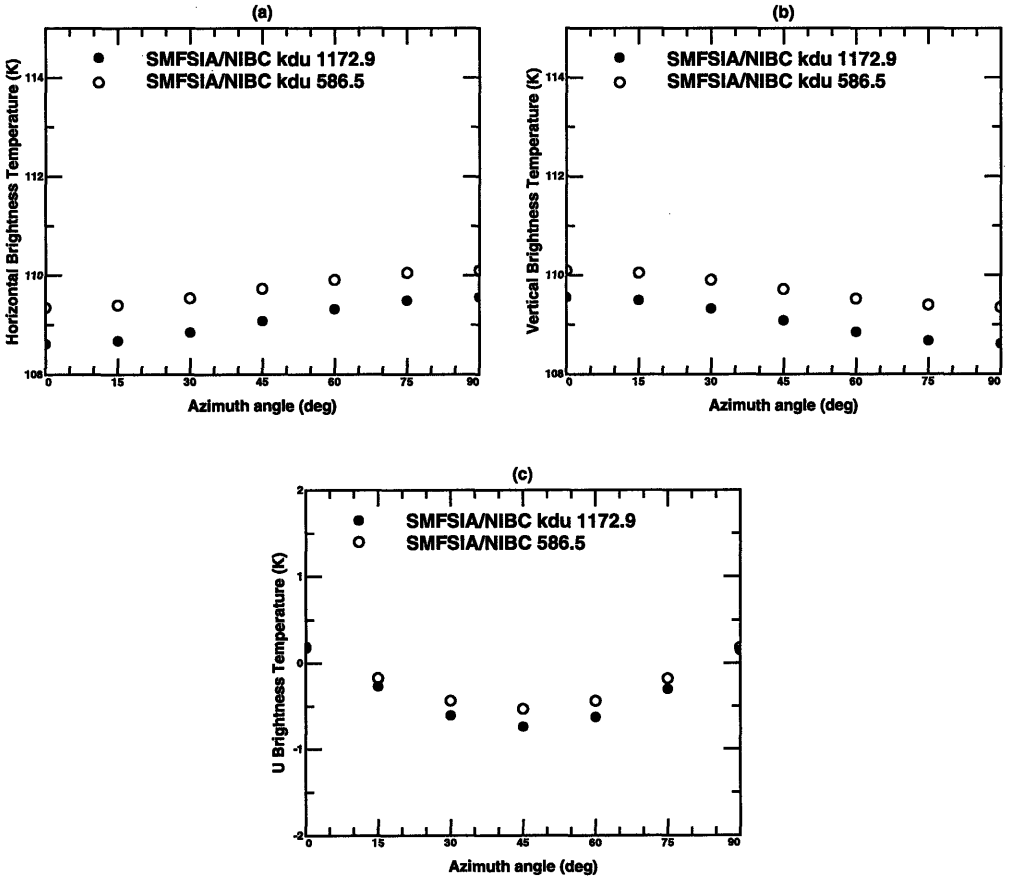

Figure 6.4: Variation of SMFSIA/NIBC brightness temperatures with high frequency cutoff: 14 GHz, nadir looking, Durden-Vesecky spectrum, $U_{19.5} = 10$ m/s, surface temperature 283 K, $k_{dl} = 73.3$, emissivity calculated as one minus reflectivity (a) T_{Bh} (b) T_{Bv} (c) U_B

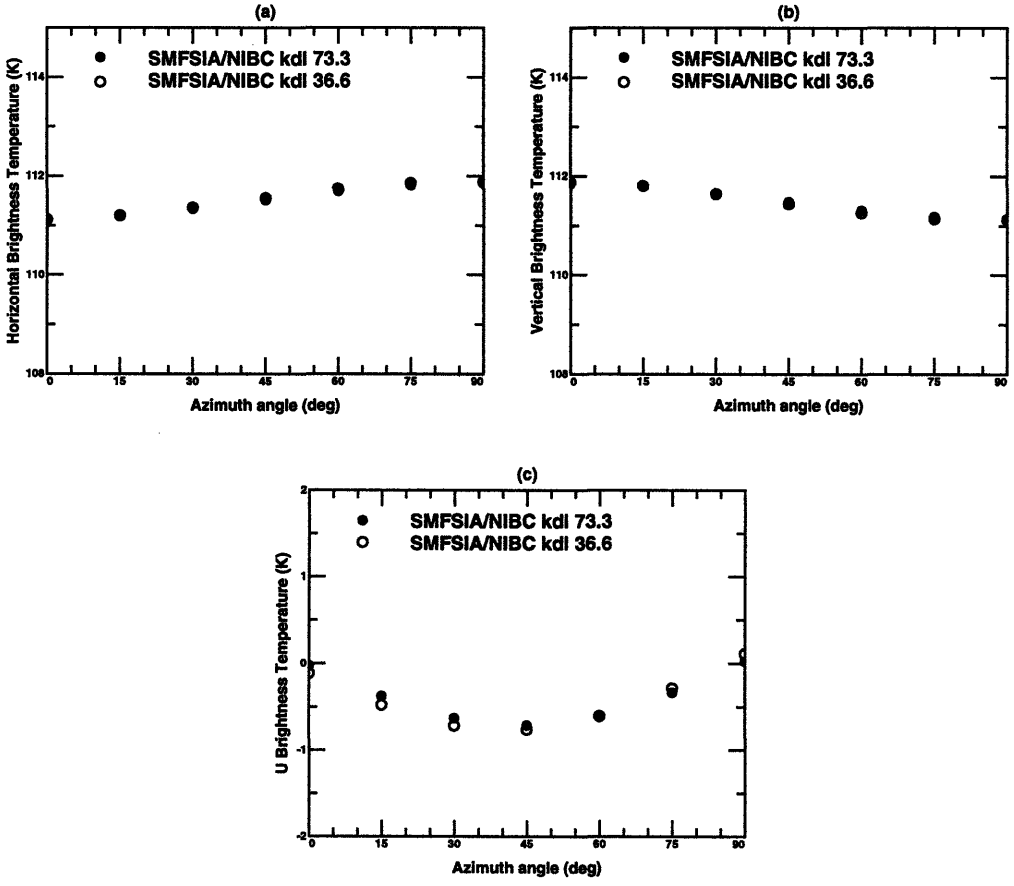

Figure 6.5: Variation of SMFSIA/NIBC brightness temperatures with low frequency cutoff: 14 GHz, nadir looking, Durden-Vesecky spectrum, $U_{19.5} = 10$ m/s, surface temperature 283 K, $k_{du} = 1172.9$, emissivity calculated as absorbed power (a) T_{Bh} (b) T_{Bv} (c) U_B

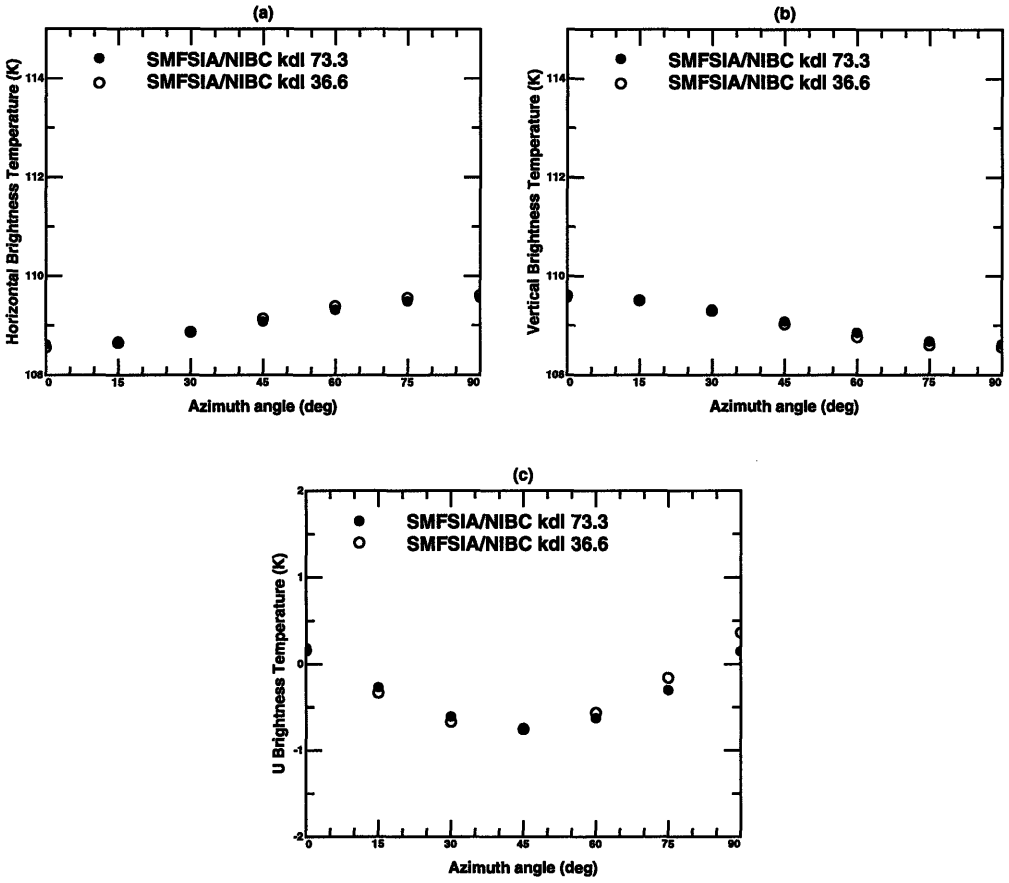

Figure 6.6: Variation of SMFSIA/NIBC brightness temperatures with low frequency cutoff: 14 GHz, nadir looking, Durden-Vesecky spectrum, $U_{19.5} = 10$ m/s, surface temperature 283 K, $k_{du} = 1172.9$, emissivity calculated as one minus reflectivity (a) T_{Bh} (b) T_{Bv} (c) U_B

6.6 Sensitivity to Ocean Spectrum Model

The SMFSIA/NIBC simulations presented in Section 6.5 illustrated that azimuthal variations of polarimetric brightness temperatures were influenced primarily by the high frequency portion of the ocean spectrum, and that lower frequencies, corresponding to wavelengths in the ocean longer than a few electromagnetic wavelengths, had little effect. This conclusion parallels that of [93], where the inclusion of lower ocean frequencies through a composite surface model caused only extremely small deviations from SPM predictions alone. However, it should be noted that the ocean spectrum model used, that of Durden and Vesecky, places the azimuthally anisotropic portion of the spectrum in the high frequency region, so that lower frequencies are almost isotropic and therefore inherently do not contribute to brightness temperature azimuthal variations. In contrast, the Donelan-Banner-Jahne spectrum of [130] places the azimuthal anisotropy into the lower frequency ocean waves, which can potentially allow a different conclusion regarding the source of azimuthal variations to be obtained. In this section, comparisons of Durden-Vececky and DBJ ocean spectrum brightness temperatures under the SPM and composite surface models will be made to address this issue. The DBJ spectrum used is modified slightly from that of Chapter 5 in that the spectrum is made origin symmetric by reflecting the first quadrant over appropriate axes to generate all four quadrants of the spectrum. An appropriate scaling factor is used to maintain a constant surface rms height. This procedure was necessary to symmetrize the DBJ spectrum while maintaining a maximum amplitude in the up-down wind direction. Issues to be discussed in this section depend primarily on the variation of spectrum anisotropy with ocean wavenumber,

so that this symmetrization should not strongly influence the conclusions drawn.

Figure 6.7 illustrates variations in polarimetric brightness temperatures with high frequency cutoff wavenumber predicted by the SPM with the Durden-Vesecky ocean spectrum model. This plot is similar to Figure 6.3, except that more curves are included for the much less computationally complex SPM results, and shows the discussed sensitivity to short ocean wavelengths. Figure 6.8 presents the same comparison for the DBJ ocean spectrum model, and shows a similar result, although predicted linear brightnesses are somewhat larger than those of the Durden-Vesecky spectrum as well as their variations with high frequency cutoff. Azimuthal variations are also somewhat smaller for the DBJ apectrum, since the high frequencies of this spectrum are less azimuthally anisotropic than the low frequencies.

Figure 6.9 illustrates the effect of longer ocean scales, as composite surface model and SPM predictions are compared for both the Durden-Vesecky and DBJ spectra. Composite surface model predictions used the $K_d = k/2$ cutoff wavenumber suggested in Chapter 5. The contrasting locations of the azimuthally anisotropic spectral portions in these two models lead to contrasting results. Longer ocean scales in the Durden-Vesecky spectrum are observed to have almost no effect, while those in the DBJ spectrum cause a significant increase in azimuthal variations. Azimuthal variations with the DBJ spectrum are observed to be smaller than those with the Durden-Vesecky spectrum, although an assessment of the accuracy of the composite surface model for long ocean scale modeling has yet to be obtained due to the necessity of numerically modeling scales much larger than an electromagnetic wavelength. This simulations of this section, however, show that a better understading of ocean wave

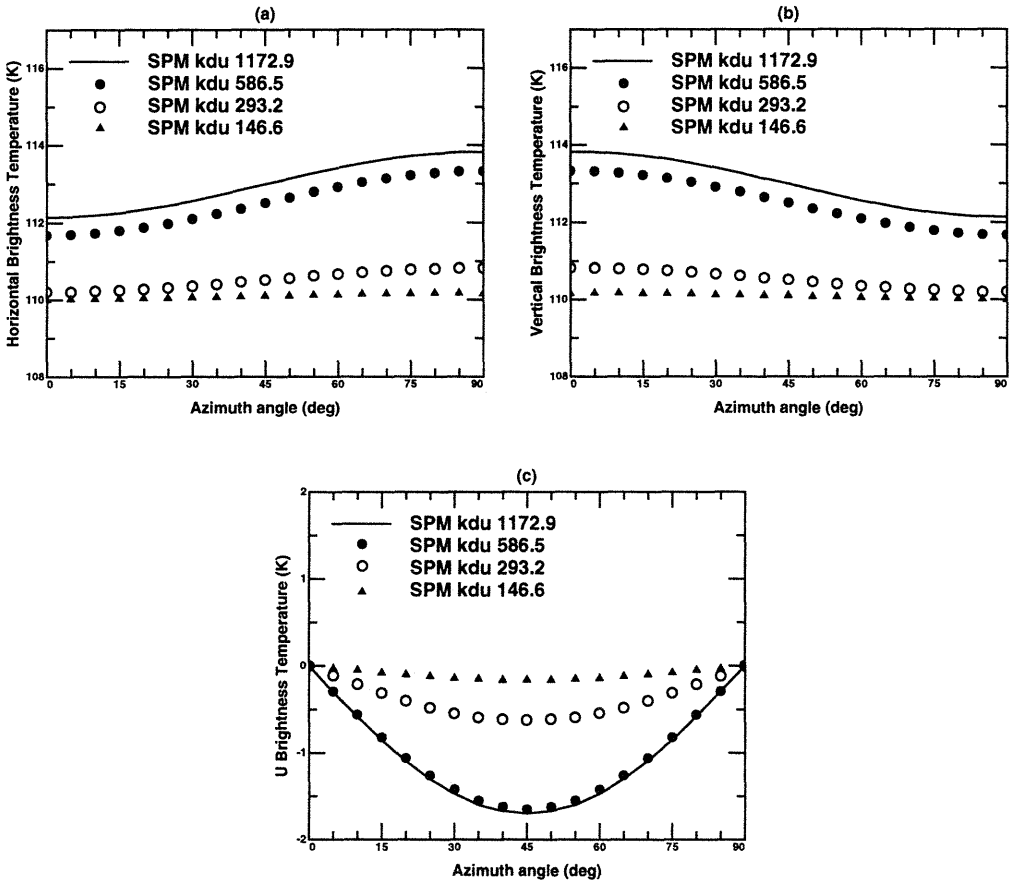

Figure 6.7: Variation of SPM brightness temperatures with high frequency cutoff: 14 GHz, nadir looking, Durden-Vesecky spectrum, $U_{19.5} = 10$ m/s, surface temperature 283 K, $k_{dl} = 73.3$ (a) T_{Bh} (b) T_{Bv} (c) U_B

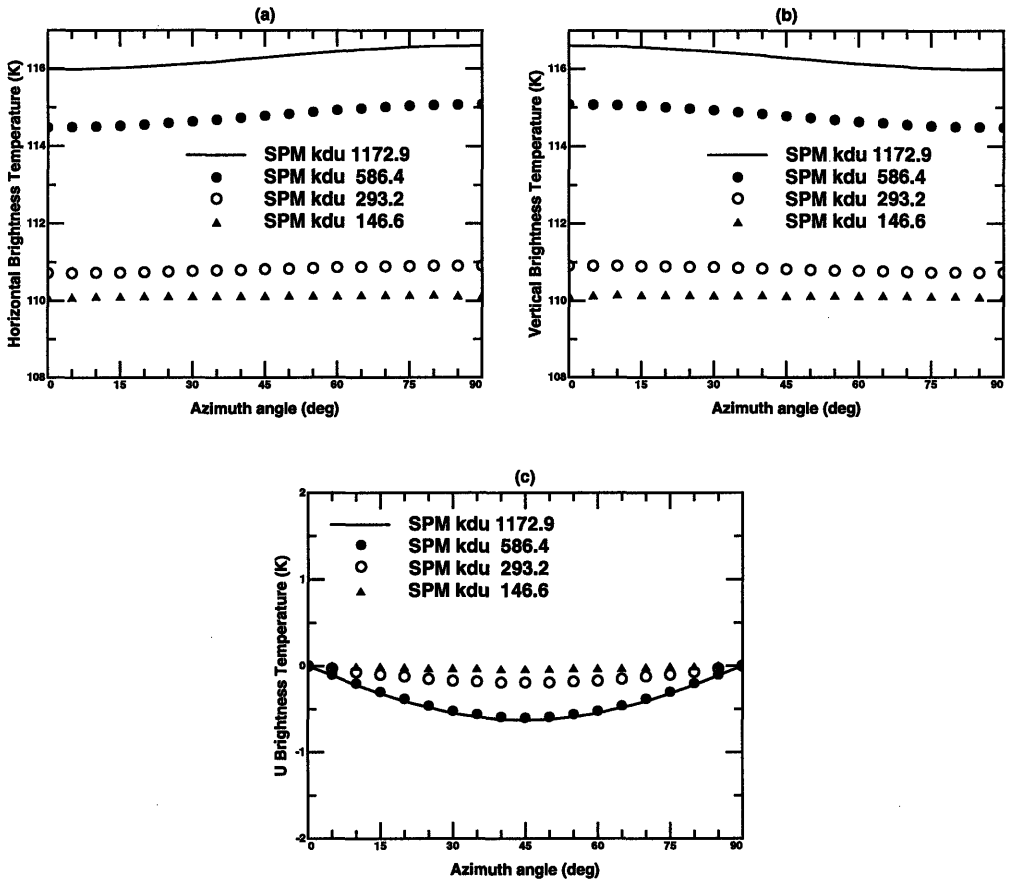

Figure 6.8: Variation of SPM brightness temperatures with high frequency cutoff: 14 GHz, nadir looking, DBJ spectrum, $U_{19.5} = 10$ m/s, surface temperature 283 K, $k_{dl} = 73.3$ (a) T_{Bh} (b) T_{Bv} (c) U_B

azimuthal anisotropy is needed before realistic models of ocean polarimetric thermal emission can be developed.

6.7 Conclusions

An initial numerical study of ocean polarimetric thermal emission has been performed using the SMFSIA/NIBC approach. The derivation of the NIBC method was presented, and comparisons with brightness temperatures predicted by the SPM and Monte Carlo PO models showed SMFSIA/NIBC accuracy to be within one percent emissivity. Since the azimuthal variations of ocean brightness temperatures obtained were smaller than this uncertainty, a quantitative assessment was not possible given the present computational limitations. However, variations in polarimetric brightness temperatures with spectral cutoffs were illustrated, and found similar to those predicted by the analytical models. In particular, high frequency components in the Durden-Vesecky ocean spectrum were found to be the principle sources of azimuthal variations in ocean emission, as predicted by the SPM and PO methods. A further application of the composite surface model with both the Durden-Vesecky and Donelan-Banner-Jahne spectra, however, showed these two spectra to yield conflicting predictions of the sources of azimuthal variations, as DBJ spectrum results were strongly influenced by low frequency contributions. Thus, the development of future models for ocean polarimetric thermal emission will require a better understanding of the azimuthal properties of the ocean spectrum. In addition, improvements to the SMFSIA/NIBC are necessary before a full numerical validation of the composite surface model can be performed. An application of the canonical grid method to the

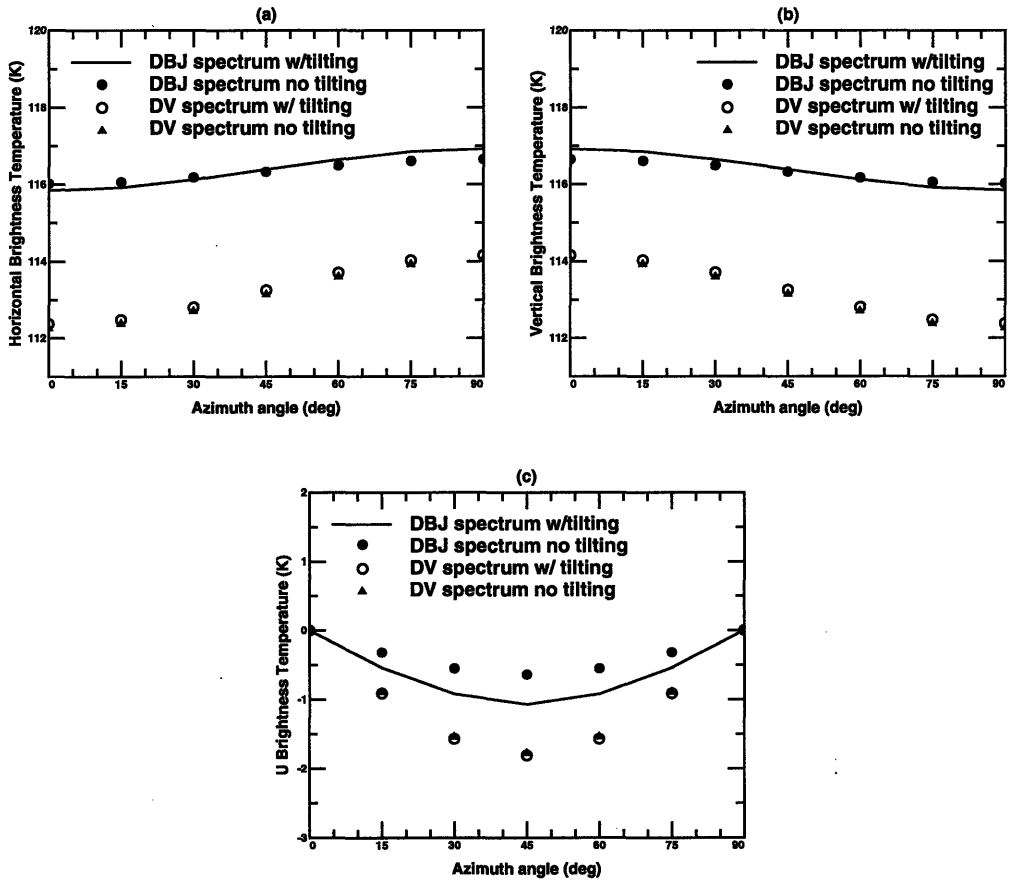

Figure 6.9: Comparison of composite surface and SPM brightness temperatures: 14 GHz, nadir looking, $U_{19.5} = 10$ m/s, surface temperature 283 K, (a) T_{Bh} (b) T_{Bv} (c) U_B

SMFSIA/NIBC could potentially alleviate some of the problems associated with computational time limitations, and a more detailed validation study could demonstrate potential approximate methods to further reduce storage and time requirements. The study of ocean polarimetric thermal emission remains a challenging problem, given the small magnitude of brightness temperature azimuthal variations, but the future development of improved ocean passive sensors continues to motivate this area.

Chapter 7

Conclusions

This thesis has demonstrated the application of improved numerical algorithms and parallel computing techniques to surface scattering problems which have enabled large one dimensional and two dimensional surface profiles to be treated. Results have shown the accuracy of the numerical approach, and have allowed studies of phenomena not predicted by any analytical models to be performed, as well as studies of analytical model accuracy in appropriate cases. General conclusions show numerical models to be useful tools for obtaining a better understanding of surface scattering physics, which can potentially lead to future improved analytical and numerical solutions. In addition, the more efficient numerical models developed are themselves of interest, as they allow accurate simulations of realistic two dimensional surface scattering configurations to be performed without simultaneous uncertainties in both surface specification and electromagnetic approximations. Future work in general should concentrate on more detailed studies of surface scattering with these numerical models, as well as further improvements to the numerical algorithms themselves for specific cases. Individual chapter conclusions and suggestions for future work are

detailed below.

A method of moments simulation of one dimensional surface VHF propagation showed good agreement with measured data and with the approximate SEKE and PWE methods. Use of the parallel BMFSIA method allowed very large surface profiles (up to 20,000 wavelengths) to be considered, so that realistic propagation geometries could be considered. Results showed the sensitivity of propagation models to input terrain profiles, and illustrated some of the limitations of the analytical algorithms which comprise the SEKE model. Agreement with the numerical PWE model was seen to be excellent, so that greater emphasis should be placed on the improvement and application of this technique in the future. Further extensions to this study should involve comparisons for a larger set of terrain profiles so that a more thorough assessment of any limitations of the PWE model can be obtained. In addition, the method of moments approach can potentially be made even more efficient through the use of the CAG method for applicable surface profiles or through the neglect of coupling between some surface regions when appropriate. A more efficient method of moments model could replace the PWE approach as the solution of choice in the future.

Chapter three considered scattering and thermal emission from two dimensional periodic surfaces. The EBC model developed was found to be relatively efficient for surfaces made up of a small number of facets, although the method was limited to surfaces with small slopes. Simulations of periodic pyramidal surface polarimetric thermal emission showed that properties observed in the one dimensional periodic surface case remain similar for two dimensional periodic surfaces. U_B was also found

to respond to the level of medium anisotropy, as expected. Further work in this area should concentrate on more detailed studies of periodic surface scattering and emission, and on the extension of the model developed to more general rough surface profiles. Scattering from periodic surfaces is currently of interest, as periodic surfaces are believed to eliminate finite surface size effects in grazing angle scattering simulations, such as those which required the large surface sizes in the ocean scattering study of Chapter 5. Extensions to the EBC model developed should be based on an FFT expansion of required integrals, which should be more efficient for surfaces made up of a large number of facets.

Backscattering enhancement from two dimensional perfectly conducting random rough surfaces was studied in Chapter four using the SMFSIA, and Monte Carlo simulations and experimental data were found to be in good agreement. A tapered beam incident field was introduced to avoid finite surface size effects on the simulation, although the relatively small incidence angle (20 degrees) of the study made tapered beam use less critical. Results illustrated the validity of the numerical model in backscattering enhancement predictions, so that more detailed future studies of backscattering enhancement physics can be studied with this approach. Future work should concentrate on performing these more detailed studies, as well as the potential application of the CAG approach to this problem. In addition, the accuracy of recently developed analytical models based on Neumann iteration should be considered.

Ocean forward and back scattering was studied in Chapter 5 using the SMFSIA for perfectly conducting surfaces in a simulation of power law surface scattering. Results of the study qualitatively validated the composite surface model approach

to ocean scattering, as variations with power law spectrum low frequency cutoff illustrated the dependencies predicted by the composite model. Choices of the cutoff wavenumber K_d as $k/2$ for backscattering and as $k/2\ \cos\theta$ in forward scattering were found to provide reasonable predictions for the GO and tilted SPM portions of the composite model. Comparison of composite surface model predictions with the AAFE RADSCAT data showed good agreement using this choice the cutoff parameter. Further studies in this area should concentrate on more thorough Monte Carlo simulations, perhaps using a more realistic ocean model than the power law spectrum applied, and should investigate the validity again of the recently developed analytical models based on Neumann iteration. The results of Chapter 5 show that an accurately evaluated single Neumann iteration result should provide reasonable predictions of ocean backscattering for a range of surface heights, and could therefore potentially eliminate the need for the heuristic composite surface model.

Polarimetric thermal emission from the ocean surface was considered in Chapter 6, and an extension of the SMFSIA model of Chapter 5 to the case of highly lossy dielectric media such as sea water was developed. Computational limitations prevented a detailed numerical study of ocean emission, but some initial simulations showed the composite surface model to provide correct predictions of the influence of different spectral regions on ocean brightness temperature azimuthal variations, at least for the Durden Vesecky ocean spectrum model used in Monte Carlo simulations. A comparison of composite surface model results with the Durden Vesecky and DBJ spectra, however, emphasized that the differing azimuthal variations of these spectra lead to differing conclusions regarding the importance of waves much larger than an

electromagnetic wavelength on azimuthal variations. A clarification of this issue will require a better understanding of the true azimuthal properties of a wind generated ocean surface. Simulations with the SMFSIA should also be continued, and appropriate methods for improving the accuracy and efficiency of the method should be considered, perhaps based on the canonical grid approach or on approximations to the time consuming numerical integrals of lower medium matrix elements currently implemented. Simulations with an improved SMFSIA should lead to a better understanding of composite surface model accuracy, at least for a given ocean spectrum model.

The calculation of electromagnetic fields scattered by an arbitrary rough surface profile remains a challenging problem. The numerical models presented in this thesis have enabled some previously unanswered questions to be addressed, but many issues still remain. The development of improved analytical theories remains the principle goal of surface scattering research, and numerical models form one of the building blocks, along with experiments and improved analytical methods, for the attainment of this goal.

Bibliography

[1] Kong, J. A. *Electromagnetic Wave Theory,* Second edition, Wiley, New York, 1990.

[2] Poggio, A. J. and E. K. Miller, "Integral equation solutions of three-dimensional scattering problems," Ch. 4 of *Computer Techniques for Electromagnetics,* R. Mittra, ed., Hemisphere, Washington, 1973.

[3] Wang, J. J. H., *Generalized Moment Methods in Electromagnetics,* Wiley, New York, 1991.

[4] Lee, C. F., "Radar cross section prediction using a hybrid method," S. M. Thesis, Dept. of Electrical Engineering and Computer Science, Mass. Inst. of Technology, 1987.

[5] Tsang, L., "Polarimetric passive microwave remote sensing of random discrete scatterers and rough surfaces," *J. of Electromag. Waves Applic.,* vol. 5, pp. 41–57, 1991.

[6] Tsang, L., J. A. Kong, and R. T. Shin, *Theory of Microwave Remote Sensing,* Wiley, New York, 1985.

[7] Rice, S. O., "Reflection of electromagnetic waves from slightly rough surfaces," *Commun. Pure Appl. Math,* vol. 4, pp. 361–378, 1951.

[8] Beckmann, P. and A. Spizzichino, *The Scattering of Electromagnetic Waves from Rough Surfaces,* Pergamon Press, New York, 1963.

[9] Stogryn, A., "Electromagnetic scattering from rough, finitely conducting surfaces," *Radio Science,* vol. 2, pp. 415–428, 1967.

[10] Lynch, P. J. and R. J. Wagner, "Rough surface scattering: shadowing, multiple scatter, and energy conservation," *J. of Math. Phys.,* vol. 11, pp. 3032–3042, 1970.

[11] Leader, J. C., "Bi-directional scattering of electromagnetic waves from rough surfaces," *J. of Appl. Phys.,* vol. 42, pp. 4808–4815, 1971.

[12] Zipfel, G. G. and J. A. Desanto, "Scattering of a scalar wave from a random rough surface: a diagrammatic approach," *J. of Math. Phys.,* vol. 13, pp. 1903–1911, 1972.

[13] Desanto, J. A., "Green's function for electromagnetic scattering from a random rough surfaces," *J. of Math. Phys.,* vol. 15, pp. 283–288, 1974.

[14] Gray, E. P., R. W. Hart, and R. A. Farrell, "An application of a variational principle for scattering by random rough surfaces," *Radio Science,* vol. 13, pp. 333–343, 1978.

[15] Brown, G. S., "Backscattering from a Gaussian distributed perfectly conducting rough surface," *IEEE Trans. Ant. Prop.,* vol. AP-26, pp. 472–482, 1978.

[16] Brown, G. S., "A stochastic Fourier transform approach to scattering from a perfectly conducting randomly rough surfaces," *IEEE Trans. Ant. Prop.,* vol. AP-30, pp. 1135-1144, 1982.

[17] Weinbrenner, D. and A. Ishimaru, "Investigation of a surface field phase perturbation technique for scattering from rough surfaces," *Radio Science,* vol. 20, pp. 161–170, 1985.

[18] Belobrov, A. V. and I. M. Fuks, "Short wave asymptotic analysis of the problem of acoustic wave diffraction by a rough surface," *Sov. Phys. Acoust.,* vol. 31, pp. 442–445, 1985.

[19] Fung, A. K. and G. W. Pan, "A scattering model for perfectly conducting random surfaces: I. Model development," *Int. J. Remote Sens,* vol. 8, pp. 1579–1593, 1987.

[20] Ishimaru, A. and J. S. Chen, "Scattering from very rough surfaces based on the modified second order Kirchhoff approximation with angular and propagation shadowing," *J. Acoust. Soc. Am.,* vol. 88, pp. 1877-1888, 1990.

[21] Rodriguez, E., "Beyond the Kirchhoff approximation," *Radio Science,* vol. 24, pp. 681–693, 1989.

[22] Rodriguez, E., "Beyond the Kirchhoff approximation II: electromagnetic scattering," *Radio Science,* vol. 26, pp. 121–132, 1991.

[23] Rodriguez, E. and Y. Kim, "A unified pertubation expansion for surface scattering," *Radio Science,* vol. 27, pp. 79–93, 1992.

[24] Yordanov, O. I., K. Ivanova, and M. A. Michalev, "On the Lynch variational method for scattering of waves by randomly rough surfaces," *J. Acoust. Soc. Am.,* vol. 89, pp. 2104–2110, 1991.

[25] A. K. Fung, Z. Li, and K. S. Chen, "Backscattering from a randomly rough dielectric interface," *IEEE Trans. Geosc. Remote Sens.,* vol. 30, pp. 356–369, 1992.

[26] Collin, R. E., "Full wave theories for rough surface scattering: an updated assessment," *Radio Science,* vol. 29, pp. 1237–1254, 1994.

[27] Fung, A. K., *Microwave Scattering and Emission Models and Their Applications,* Artech House, Boston, 1994.

[28] Holliday, D., "Resolution of a controversy surrounding the Kirchhoff approach and the small perturbation method in rough surface scattering theory," *IEEE Trans. Ant. Prop.,* vol. AP-35, pp. 120–122, 1987.

[29] Chan, H. L. and A. K. Fung, "A numerical study of the Kirchhoff approximation in horizontally polarized backscattering from a random surface," *Radio Science,* vol. 13, pp. 811–818, 1978.

[30] Thorsos, E. I., "The validity of the Kirchhoff approximation for rough surface scattering using a Gaussian roughness spectrum," *J. Acoust. Soc. Am,* vol. 83., pp. 78–92, 1988.

[31] Chen, M. F. and A. K. Fung, "A numerical study of the regions of validity of the Kirchhoff and small perturbation rough surface scattering models," *Radio Science,* vol. 23, pp. 163–170, 1988.

[32] Rodriguez, E., Y. Kim, and S. L. Durden, "A numerical assessment of rough surface scattering theories: horizontal polarization," *Radio Science,* vol. 27, pp. 497–513, 1992.

[33] Kim, Y., E. Rodriguez, and S. L. Durden, "A numerical assessment of rough surface scattering theories: vertical polarization," *Radio Science,* vol. 27, pp. 515–527, 1992.

[34] Valenzuela, G., "Depolarization of EM waves by slightly rough surfaces," *IEEE Trans. Ant. Prop.,* vol. AP-15, pp. 552-557, 1967.

[35] Thorsos, E. I. and D. R. Jackson, "The validity of the perturbation approximation for rough surface scattering using a Gaussian roughness spectrum," *J. Acoust. Soc. Am,* vol. 86, pp. 261–277, 1989.

[36] Wright, J. W., "A new model for sea clutter," *IEEE Trans. Ant. Prop.,* vol. AP-16, pp. 217-223, 1968.

[37] Bass, F. G., I. M. Fuks, A. I. Kalmykov, I. E. Ostruvsky, and A. D. Rosenberg, "Very high frequency radio wave scattering by a disturbed sea surface," *IEEE Trans. Ant. Prop.,* vol. AP-16, pp. 554–568, 1968.

[38] Barrick, D. and W. Peake, "A review of scattering from surfaces with different roughness scales," *Radio Science,* vol. 3, pp. 865–868, 1968.

[39] Valenzuela, G. R., "Scattering of electromagnetic waves from a tilted slightly rough surface," *Radio Science,* vol. 3, pp. 1057–1066, 1968.

[40] Valenzuela, G. R., "Ocean spectra for the high frequency waves as determined from airborne radar measurements," *J. Marine Res.,* vol. 29, pp. 69–84, 1971.

[41] Chan, H. L., and A. K. Fung, "A theory of sea scatter at large incident angles," *J. Geophys. Res.,* vol. 82, pp. 3439–3444, 1977.

[42] Valenzuela, G. R., "Theories for the interaction of electromagnetic and oceanic waves: a review," *Bound. Layer Meteorology,* vol. 13, pp. 61–85, 1978.

[43] Fung, A. K. and K. K. Lee, "A semi-empirical sea spectrum model for scattering coefficient estimation," *IEEE J. Oceanic Eng.,* vol. OE-7, pp. 166–176, 1982.

[44] J. H. Richmond, "Digital Computer Solutions of the Rigorous Equations for Scattering Problems," Proc. IEEE, Vol. 53, pp. 796, 1965.

[45] R. F. Harrington, "Matrix Methods for Field Problems," Proc. IEEE, Vol. 55, pp. 136, 1967.

[46] K. S. Yee, "Numerical Solution of Initial Boundary Value Problems Involving Maxwell's Equations in Isotropic Media," IEEE Trans. Antennas and Propagation, Vol. 14, No. 3, pp. 302-307, May 1966.

[47] *11th Annual Review of Progress in Applied Computational Electromagnetics,* Proceedings, Applied Computational Electromagnetics Society, Mar. 1995.

[48] Lou, S. H., L. Tsang, and C. H. Chan, "Application of the finite element method to Monte Carlo simulations of scattering of waves by random rough surfaces:

penetrable case," *Waves in Random Media,* vol. 1, pp. 287–307, 1991.

[49] Lou, S. H., L. Tsang, C. H. Chan, and A. Ishimaru, "Application of the finite element method to Monte Carlo simulations of scattering of waves by random rough surfaces with periodic boundary conditions," *J. Electromag. Waves Applic.,* vol. 5, pp. 835–855, 1991.

[50] C. H. Chan, S. H. Lou, L. Tsang, and J. A. Kong, "Electromagnetic scattering of waves by random rough surfaces: a finite difference time domain approach," *Microwave and Optical Technology Letters,* vol. 4, pp. 355–359, 1991.

[51] Fung, A. K., M. R. Shah, and S. Tjuatja, "Numerical simulation of scattering from three dimensional randomly rough surfaces," *IEEE Trans. Geosc. Remote Sens.,* vol. 32, pp. 986–994, 1994.

[52] Lentz, R. R., "A numerical study of electromagnetic scattering from ocean-like surfaces," *Radio Science,* vol. 9, pp. 1139–1146, 1974.

[53] Axline, R. M. and A. K. Fung, "Numerical computation of scattering from a perfectly conducting random surface," *IEEE Trans. Ant. Prop.,* vol. 26, pp. 482–488, 1978.

[54] Fung, A. K. and M. F. Chen, "Numerical simulation of scattering from simple and composite random surfaces," *J. Opt. Soc. Am. A,* vol. 2, pp. 2274–2284, 1985.

[55] Nieto-Vesperinas, M. and J. A. Sanchez-Gil, "Intensity angular correlation of light multiply scattered from random rough surfaces," *J. Opt. Soc. Am. A*, vol. 10, pp. 150–157, 1993.

[56] Thorsos, E. I. and D. R. Jackson, "Studies of scattering theory using numerical methods," *Waves in Random Media,* vol. 1, pp. 165–190, 1991.

[57] Tsang, L., C. H. Chan, K. Pak, H. Sangani, A. Ishimaru, and P. Phu, "Monte Carlo simulations of large scale composite random rough surface scattering based on the banded matrix iterative approach," *J. Opt. Soc. of Am.*, vol. 11, pp. 691-696, 1994.

[58] Chan, C. H., L. Li, and L. Tsang, "A banded matrix iterative approach to Monte Carlo simulations of large scale random rough surface scattering: penetrable case," *Ninth Annual Review of Progress in Applied Computational Electromagnetics*, Conference Proceedings, pp. 391-397, 1993.

[59] Tsang, L., C. H. Chan, K. Pak, "Monte Carlo simulations of a two-dimensional random rough surface using the sparse matrix flat surface iterative approach," *Electronics Letters,* vol. 29, pp. 1153-1154, 1993.

[60] Pak, K., L. Tsang, C. H. Chan, and J. T. Johnson, "Backscattering enhancement of electromagnetic waves from two dimensional perfectly conducting random rough surfaces based on Monte Carlo simulations," *J. Optical Soc. of America,* vol. 12, 1995.

[61] Press, W. H., S. A. Teukolsky, W. T. Vetterling, and B. P. Flannery, *Numerical Recipes: The Art of Scientific Computing,* second edition, Cambridge Univ. Press, New York, 1992.

[62] Barrett, R., M. Berry, T. Chan, J. Demmel, J. Donato, J. Dongarra, V. Eijkhout, R. Pozo, C. Romine, and H. van der Vorst, *Templates for the Solution of Linear Systems: Building Blocks for Iterative Methods,* available by *ftp* from *netlib2.cs.utk.edu,* 1993.

[63] Hestenes, M. R. and E. Stiefel, "Methods of conjugate gradients for solving linear systems," *J. Res. Nat. Bur. Standards,* vol. 49, pp. 409–436, 1952.

[64] Au, W. C., *Computational electromagnetics in microwave remote sensing,* Ph. D. thesis, Dept. of Aeronautics and Astronautics, 1994.

[65] *Maui High Performance Computing Center World Wide Web Site,* on the World Wide Web at *http:www.mhpcc.edu,* 1995.

[66] Geist, A., A. Beguelin, J. Dongarra, W. Jiang, R. Manchek, and V. Sunderam, "PVM 3 user's guide and reference manual," Oak Ridge National Laboratory Report ORNL/TM-12187, 1994.

[67] Ayasli, S., "SEKE: A computer model for low altitude radar propagation over irregular terrain," *IEEE Trans. Ant. Prop.*, vol. AP-34, pp. 1013–1023, 1986.

[68] McDaniel, S. T., "Propagation of a normal mode in the parabolic approximation," *J. Acoust. Soc. Am.*, vol. 57, pp. 307–311, 1975.

[69] Barrios, A. E., "A terrain parabolic equation model for propagation in the troposphere," *IEEE Trans. Ant. Prop.*, vol. AP-42, pp. 90–98, 1994.

[70] Levy, M. F., "Horizontal parabolic equation solution of radiowave propagation problems on large domains," *IEEE Trans. Ant. Prop.*, vol. AP-43, pp. 137–144, 1995.

[71] Janaswamy, R., "A Fredholm integral equation method for propagation over small terrain irregularities," *IEEE Trans. Ant. Prop.*, vol. AP-40, pp. 1416–1422, 1992.

[72] Janaswamy, R., "A fast finite difference method for propagation predictions over irregular, inhomogeneous terrain," *IEEE Trans. Ant. Prop.*, vol. AP-42, pp. 1257–1267, 1994.

[73] Liepa, V.,"Numerical approach for predicting radiation patterns of HF-VHF antennas over irregular terrain," *IEEE Trans. Ant. Prop.*, vol. AP-16, pp. 273–274, 1968.

[74] Luebbers, R., "Finite conductivity uniform GTD versus knife edge diffraction in prediction of propagation path loss," *IEEE Trans. Ant. Prop.*, vol. AP-32, pp. 70–76, 1984.

[75] Huang, G. T. and R. T. Shin, "Theoretical Models for Low-Altitude Propagation over Terrain," *Progress in Electromagnetics Research Symposium,* Conference proceedings, pp. 931, 1993.

[76] Huang, G. T., *Propagation over knife edge obstacles on a spherical Earth,* S. M. Thesis, Dept. of Electrical Engineering and Computer Science, Massachusetts Institute of Technology, 1992.

[77] Chuang, S. L. and J. A. Kong, "Scattering of waves from periodic surfaces," *Proc. of the IEEE,* vol. 69, pp. 1132–1144, 1981.

[78] Zaki, K. A. and A. R. Neureuther, "Scattering from a perfectly conducting surface with a sinusoidal height profile: TE Polarization," *IEEE Trans. Ant. Prop.*, vol. AP-19, pp. 208–214, 1971.

[79] Waterman, P. C., "Scattering by periodic surfaces," *J. Acoust. Soc. Am.,* vol. 57, pp. 791–802, 1975.

[80] Maystre, D., "A new general integral theory for dielectric coated gratings," *J. Opt. Soc. Am.,* vol. 68, pp. 490–495, 1978.

[81] Chuang, S. L. and J. A. Kong, "Wave scattering from a periodic dielectric surface for a general angle of incidence," *Radio Science,* vol. 17, pp. 545–557, 1982.

[82] Moharam, M. G., and T. K. Gaylord, "Diffraction analysis of dielectric surface-relief gratings," *J. Opt. Soc. Am.,* vol. 72, pp. 1385–1392, 1982.

[83] Kong, J. A., S. L. Lin, and S. L. Chuang, "Microwave Thermal Emission from Periodic Surfaces," *IEEE Trans. Geosc. Electr.,* vol. GE-22, pp. 377–382, 1984.

[84] Barrick, D. E., "Near-grazing illumination and shadowing of rough surfaces," *Radio Science,* vol. 30, pp. 563–580, 1995.

[85] Veysoglu, M. E., H. A. Yueh, R. T. Shin, and J. A. Kong, "Polarimetric passive remote sensing of periodic surfaces," *J. Electromag. Waves Applic.,* vol. 5, pp. 267–280, 1991.

[86] Nghiem, S. V., M. E. Veysoglu, J. A. Kong, R. T. Shin, K. O'Neill, and A. W. Lohanick, "Polarimetric passive remote sensing of a periodic soil surface: microwave measurements and analysis," *J. Electromag. Waves Applic.,* vol. 5, pp. 997–1005, 1991.

[87] Johnson, J. T., J. A. Kong, R. T. Shin, D. H. Staelin, K. O'Neill, and A. Lohanick, "Third Stokes Parameter Emission from a Periodic Water Surface," *IEEE Trans. Geosc. Remote Sens.,* vol. 31, pp. 1066–1080, 1993.

[88] Yueh, S. H., S. V. Nghiem, W. Wilson, F. K. Li, J. T. Johnson, J. A. Kong, "Polarimetric Passive Remote Sensing of Periodic Water Surfaces," *Radio Science,* vol. 29, pp. 87–96, 1994.

[89] Gasiewski, A. J., and D. B. Kunkee, "Polarized Microwave Emission from Water Waves," *Radio Science,* vol. 29, pp. 1449–1465, 1994.

[90] Johnson, J. T., J. A. Kong, R. T. Shin, S. H. Yueh, S. V. Nghiem, and R. Kwok, "Polarimetric Thermal Emission from Rough Ocean Surfaces," *J. Electromag. Waves Applic.,* vol. 8, pp. 43–59, 1994.

[91] Dzura, M. S., V. S. Etkin, A. S. Khrupin, M. N. Pospelov, M. D. Raev, "Radiometers Polarimeters: Principles of Design and Applications for Sea Surface Microwave Emission Polarimetry," *IGARSS 92,* conference proceedings, pp. 1432–1434, 1992.

[92] Yueh, S. H., R. Kwok, F. K. Li, S. V. Nghiem, and W. J. Wilson, "Polarimetric passive remote sensing of ocean wind vectors," *Radio Science,* vol. 29, pp. 799–814, 1994.

[93] Yueh, S. H., S. V. Nghiem, and R. Kwok, "Comparison of a polarimetric scattering and emission model with ocean backscatter and brightness measurements," *IGARSS 94,* conference proceedings, 1994.

[94] Yueh, S. H., W. J. Wilson, F. K. Li, S. V. Nghiem, and W. B. Ricketts, "Polarimetric Measurements of Sea Surface Brightness Temperatures Using an Aircraft K-Band Radiometer," *IEEE Trans. Geosc. Remote Sens.,* vol. 33, pp. 85–92, 1995.

[95] Yang, C. F., W. D. Burnside, and R. C. Ruddock, "A doubly periodic moment method solution for the analysis and design of an absorber covered wall," *IEEE Trans. Ant. and Prop.,* vol. 41, pp. 600–609, 1993.

[96] Garcia, N., V. Celli, N. Hill, and N. Cabrera, "Ill conditioned matrices in the scattering of waves from hard corrugated surfaces," *Phys. Rev. B,* vol. 18, pp. 5184–5189, 1978.

[97] O'Donnell, K. and E. R. Mendez, "Experimental study of scattering from random rough surfaces," *J. Opt. Soc. Am. A*, vol. 4, pp. 1194–1205, 1987.

[98] Kim, M. J., J. Dainty, A. Friberg, and A. Sant, "Experimental study of enhanced backscattering from one- and two- dimensional random rough surfaces," *J. Opt. Soc. Am. A*, **7**, pp. 569-577, (1990).

[99] Knotts, M. E. and K. A. O'Donnell, "Backscattering enhancement from a conducting surface with isotropic roughness," *Opt. Comm.*, vol. 99, pp. 1-6, 1993.

[100] Phu, P., A. Ishimaru, and Y. Kuga, "Co-polarized and cross-polarized enhanced backscattering from two-dimensional very rough surfaces at millimeter wave frequencies," *Radio Science,* vol. 29, pp. 1275-1291, 1994.

[101] Kuga, Y., J. S. Colburn, and P. Phu, "Millimeter-wave scattering from one-dimensional surface of different surface correlation functions," *Waves in Random Media,* vol. 3, pp. 101-110, 1993.

[102] Kuga, Y. and P. Phu, "Experimental techniques in random media and rough surface," *Progress in Electromagnetics Research,* Vol. 9, Elsevier Science Publishers, Cambridge, Mass, in press 1995.

[103] Ishimaru, A., C. Le, Y. Kuga, L. Ailes-Sengers, and T.K. Chan, "Polarimetric scattering theory for large slope rough surfaces," *Progress in Electromagnetics Research,* Vol. 9, Elsevier Science Publishers, Cambridge, Mass, in press 1995.

[104] Wingham, D. J. and R. H. Devayya, "A note on the use of the Neumann expansion in calculating the scatter from rough surfaces," *IEEE Trans. Ant. Prop.*, vol. 40, pp. 560–563, 1992.

[105] Tran, P., V. Celli, and A. A. Maradudin, "Electromagnetic scattering from a two-dimensional, randomly rough, perfectly conducting surface: iterative methods," *J. Opt. Soc. Am. A.,* vol. 11, pp. 1686–1689, 1994.

[106] Tran, P. and A. A. Maradudin, "The scattering of electromagnetic waves from a randomly rough 2D metallic surface," *Opt. Comm.,* vol. 110, pp. 269–273, 1994.

[107] C. H. Chan and R. Mittra, "Some recent developments in iterative techniques for solving electromagnetic boundary value problems," *Radio Science,* vol. 22, pp. 929–934, 1987.

[108] Skolnik, M. I., *Introduction to Radar Systems,* Second edition, Mcgraw-Hill, New York, 1980.

[109] Ulaby, F. T., R. K. Moore, and A. K. Fung, *Microwave Remote Sensing,* vol. 3, Addison Wesley, Reading, 1982.

[110] Wetzel, L. B., "Sea Clutter," chapter 13 of *Radar Handbook,* second edition, M. Skolnik, ed., Mcgraw-Hill, New York, 1990.

[111] Crombie, D., "Doppler spectrum of sea echo at 13.56 Mc/s," *Nature,* vol. 175, pp. 681–683, 1955.

[112] Daley, J. C., J. T. Ransome, J. A. Burkett, and J. R. Duncan, "Sea clutter measurements on four frequencies," *Naval Res. Lab. Rept. 6806,* Nov. 1968.

[113] Valenzuela, G. R. and R. Laing, "On the statistics of sea clutter," *Naval Res. Lab. Rept. 7349,* Dec. 1971

[114] Guinard, N. W., J. T. Ransone, J. A. Burkett, and J. R. Duncan, "Variation of the NRCS of the sea with increasing roughness," *J. Geophys. Res.,* vol. 76, pp. 1525–1538, 1971.

[115] Daley, J. C., "Wind dependence of radar sea return," *J. Geophys. Res.,* vol. 76, pp. 7823–7833, 1973.

[116] Jones, W. L., L. C. Schroeder, and J. L. Mitchell, "Aircraft measurements of the microwaves scattering signature of the ocean," *IEEE Trans. Ant. Prop.,* vol. AP-25, pp. 52–61, 1977.

[117] Johnson, J. W., L. A. Williams, E. M. Bracalante, F. B. Beck, and W. L. Grantham, "Seasat-A satellite scatterometer instrument evaluation," *IEEE J. Oceanic Eng.,* vol. OE-5, pp. 138–144, 1980.

[118] Moore, R. K. and A. K. Fung, "Radar determination of winds at sea," *Proc. IEEE,* vol. 67, pp. 1504–1521, 1979.

[119] Brown, G. S., H. R. Stanley, and N. A. Roy, "The windspeed measurement capability of spaceborne radar altimeters," *IEEE J. Oceanic Eng.,* vol. OE-6, pp. 53–59, 1981.

[120] Wentz, F. J., S. Peteheryoh, and L. A. Thomas, "A model function for ocean radar cross sections at 14.6 GHz," *J. Geophys. Res.,* vol. 89, pp. 3689-3704, 1984.

[121] Chelton, D. B. and F. J. Wentz, "Further development of an improved altimeter wind speed algorithm," *J. Geophys. Res.,* vol. 91, pp. 14251-14260, 1986.

[122] Masuko, H., K. Okamoto, M. Shimada, and S. Niwa, "Measurement of microwave backscatter signatures of ocean surface using X band and K_a band airborne scatterometers," *J. Geophys. Res.,* vol. 91, pp. 13065-13083, 1986.

[123] Nghiem, S. V., F. K. Li, S. H. Lou, G. Neumann, R. E. McIntosh, S. C. Carson, J. R. Carswell, E. J. Walsh, M. A. Donelan, and W. M. Drennan, "Observations of radar backscatter at K_u and C bands in the presence of large waves during the surface wave dynamics experiment," *IEEE Trans. Geosc. Remote Sens.,* vol. 33, pp. 708–721, 1995.

[124] Alpers, W. and C. L. Rufenach, "The effect of orbital motions of synthetic aperture radar imagery of ocean waves," *IEEE. Trans. Ant. Prop.,* vol. AP-27, pp. 685–790, 1979.

[125] Jain, A., "SAR Imaging of ocean waves," *IEEE J. Oceanic Eng.,* vol. OE-6, pp. 130–139, 1981.

[126] Ivanov, A. V., "On the synthetic aperture imaging of ocean surface waves," *IEEE J. Oceanic Eng.,* vol. OE-7, pp. 96–103, 1982.

[127] Plane, W. J. and W. C. Keller, "The two-scale radar wave probe and SAR imagery of the ocean," *J. Geophys. Res.,* vol. 88, pp. 9776–9784, 1983.

[128] Phillips, O. M., *The Dynamics of the Upper Ocean,* second edition, Cambridge Univ. Press, Cambridge, 1977.

[129] Cox, C. S. and W. H. Munk, "Measurement of the roughness of the sea from photographs of the sun's glitter," *J. Opt. Soc. Am.,* vol. 44, pp. 838–850, 1954.

[130] Apel, J. R., "An improved model of the ocean surface wave vector spectrum and its effects on radar backscatter," *J. Geophys. Res.*, vol. 99, pp. 16269–16291, 1994.

[131] Guissard, A., "Directional spectrum of the sea surface and wind scatterometry," *Int. J. Remote Sens.*, vol. 14, pp. 1615-1633, 1993.

[132] Lleonart, G. T. and D. R. Blackman, "The spectral characteristics of wind generated capillary waves," *J. Fluid Mech.*, vol. 97, pp. 455–479, 1980.

[133] Pierson, W. J. and M. A. Donelan, "Radar scattering and equilibrium ranges in wind generated waves with application to scatterometry," *J. Geophys. Res,* vol. 91, pp. 4971–5029, 1987.

[134] Kitaigorodskii, S. A., "On the theory of the equilibrium range in the spectrum of wind generated gravity waves," *J. Phys. Oceanogr.*, vol. 13, pp. 816–827, 1983.

[135] Durden, S. L. and J. F. Vesecky, "A physical radar cross-section model for a wind driven sea with swell," *IEEE J. Oceanic Eng.*, vol. OE-10, pp. 445–451, 1985.

[136] Phillips, O. M., "Spectral and statistical properties of the equilibrium range in wind generated gravity waves," *J. Fluid Mech.*, vol. 156, pp. 505–531, 1986.

[137] Banner, M. L., "Equilibrium spectra of wind waves," *J. Phys. Oceanogr.*, vol. 20, pp. 966–984, 1990.

[138] Jahne, B. and K. S. Riemer, "Two dimensional wave number spectra of small scale water surface wavesa," *J. Geophys. Res,* vol. 95., pp. 11351-11546, 1990.

[139] Klein, L. A. and C. T. Swift, "An improved model for the dielectric constant of sea water at microwave frequencies," *IEEE Trans. Ant. Prop.*, vol. AP-25, pp. 104–111, 1977.

[140] Durden, S. L. and J. F. Vesecky, "A numerical study of the separation wavenumber in the two scale scattering approximation," *IEEE Trans. Geosc. Remote Sens,* vol. 28, pp. 271–272, 1990.

[141] Holliday, D., G. St-Cyr, and N. E. Woods, "A radar ocean imaging model for small to moderate incidence angles," *Int. J. Remote Sens.*, vol. 8, pp. 1323–1430, 1987. 1987.

[142] Hollinger, J. P., "Passive microwave measurements of sea surface roughness," *IEEE Trans. Geosc. Electr.,* vol. GE-9, pp. 165–169, 1971.

[143] VanMelle, M. J., H. H. Wang, and W. F. Hall, "Microwave radiometric observations of simulated sea surface conditions," *J. Geophys. Res.,* vol. 78, pp. 969–976, 1973.

[144] Stogryn, A., "The apparent temperature of the sea at microwave frequencies," *IEEE Trans. Ant. Prop,* vol. AP-15, pp. 278–286, 1967.

[145] Wilheit, T. T., "A review of applications of microwave radiometry to oceanography," *Bound. Layer Meteorology,* vol. 13, pp. 277–293, 1978.

[146] Wu, S. T. and A. K. Fung, "A noncoherent model for microwave emissions and backscattering from the sea surface," *J. of Geophys. Res.,* vol. 77, pp. 5917–5929, 1972.

[147] Wentz, F. J., "A two-scale scattering model for foam-free sea microwave brightness temperatures," *J. of Geophys. Res.,* vol. 80, pp. 3441–3446, 1975.

[148] Sasaki, Y., I. Asanuma, K. Muneyama, G. Naito, and T. Suzuki, "The dependence of sea surface microwave emission on wind speed, frequency, incidence angle, and polarization over the frequency range from 1 to 40 GHz," *IEEE Trans. on Geosc. and Remote Sens.,* vol. GE-25, pp. 138–146, 1987.

[149] Njoku, E. and L. Swanson, "Global measurements of sea surface temperature, wind speed, and atmospheric water content from satellite microwave radiometry," *Monthly Weather Review,* vol. 111, pp. 1977–1987, 1983.

[150] Wentz, F. J., "A model function for ocean microwave brightness temperatures," *J. Geophys. Res.,* vol. 88, pp. 1892–1908, 1983.

[151] Wilheit, T. T., J. R. Greaves, J. A. Gatlin, D. Han, B. M. Krupp, A. S. Milman, and E. S. Chang, "Retrieval of ocean surface parameters from the SMMR on the Nimbus-7 Satellite," *IEEE Trans. Geosc. Remote Sens.,* vol. GE-22, pp. 133–143, 1984.

[152] Stogryn, A., "The emissivity of sea foam at microwave frequencies," *J. Geophys. Res.,* vol. 77, pp. 1658–1666, 1972.

[153] Ross, D. B. and V. Cardone, "Observations of oceanic whitecaps and their relation to remote measurements of surface wind speed," *J. Geophys. Res.,* vol. 79, pp. 444–452, 1974.

[154] Rosenkranz, P. W. and D. H. Staelin, "Microwave emissivity of ocean foam and its effect on nadiral radiometric measurements," *J. Geophys. Res.,* vol. 77, pp. 6258–6537, 1983.

[155] Pandey, P. C. and R. K. Kakar, "An empirical microwave emissivity model for a foam covered sea," *IEEE J. Oceanic Eng.,* vol. OE-7, pp. 135–140, 1982.

[156] Kravtsov, Yu. A., Ye. A. Miroskaya, A. Ye. Popov, "Critical phenomena accompanying thermal radiation of periodically uneven water surface," *Izv. An SSSR: Ser. Fizika Atmosfery I Okeana,* vol. 14, pp. 733–739, 1978.

[157] Bespalova, Ye. A., V. M. Veselov, V. Ye. Gershenzon, "Determinating surface wind velocity by measurements of polarization anisotropy of natural and scattered microwave radiation," *Issledovaniye Zemli Iz Kosmosa,* pp. 87–94, 1982.

[158] Wentz, F. J., "Measurement of oceanic wind vector using satellite microwave radiometers," *IEEE Trans. Geosc. and Remote Sens.,* vol. 30, pp. 960–972, 1992.

[159] Kunkee, D. B. and A. J. Gasiewski, "Airborne passive polarimetric measurements of sea surface anisotropy at 92 GHz," *IGARSS '94,* conference proceedings, 1994.

[160] Kunkee, D. B. and A. J. Gasiewski, "Passive microwave wind direction signatures over the ocean: the importance of wave asymmetry and foam," *Progress in Electromagnetics Resarch Symposium 1995,* conference proceedings, 1995.

[161] Mitzner, K. M., "An integral equation approach to scattering from a body of finite conductivity," *Radio Science,* vol. 2, pp. 1459–1470, 1967.

5224-18